Chromophoric dissolved organic matter in the Athabasca Oil Sands Region, Alberta, Canada

A Thesis Submitted to the Committee on Graduate Studies in Partial Fulfillment of the Requirements for the Degree of Doctor of Philosophy in the Faculty of Arts and Science

TRENT UNIVERSITY

Peterborough, Ontario, Canada

Environmental and Life Sciences Ph.D. Graduate Program

April 2025

ABSTRACT

Chromophoric dissolved organic matter in the Athabasca Oil Sands Region, Alberta, Canada

Dane Blanchard

Chromophoric dissolved organic matter (CDOM), a chemically diverse family of organic compounds defined by their ability to absorb ultraviolet and visible light, is a critical constituent of numerous environmental systems, including freshwater lakes. Industrial operations in the Athabasca Oil Sands Region (AOSR, Alberta, Canada) are major sources of acidic inorganic gases and organic contaminants to the atmosphere, the subsequent deposition of which posed the potential to alter the composition of natural CDOM within surrounding lake surface-waters. The objective of this thesis was to determine if OS sources measurably impacted CDOM quality within 50 regionally monitored acid sensitive lakes by means of a) altered acid-base chemical processes or b) industrial atmospheric CDOM inputs. Ultraviolet-visible light spectroscopy and excitation emission matrix (EEM) fluorescence spectroscopy were applied to characterize CDOM within regional lake surface-waters to identify the primary sources (e.g., natural, anthropogenic) and process (e.g., acid-base chemistry) influencing chromophoric organic matter quality. These spectroscopic techniques were further used to evaluate industrial CDOM within atmospheric aerosols and deposition to assist with the identification of industrial CDOM within lake waters. Spectroscopic analysis of regional lake surface-water found weak associations between CDOM and acid-base variables, suggesting that acid inputs from OS sources would have limited influence over surface-water chromophoric organic matter. A

distinct fluorescent component (i.e., fluorophore) measured within the lake samples (C3) displayed decreasing emission intensity as a function of distance from OS sources and positive correlations with surface-water polycyclic aromatic compounds, implying industrial influence. Spectral similarity between C3 and industrial fluorophores observed from regional aerosol and atmospheric deposition samples further confirmed the lake fluorophore was linked to OS sources. This research suggests that EEM fluorescence spectroscopy could be used as a cost-effective technique to detect industrial pollution within lake surface-waters throughout the AOSR.

Keywords: Dissolved organic matter; lake chemistry; atmospheric deposition; atmospheric pollution; atmospheric brown carbon; oil and gas industry; fluorescence spectroscopy; Parallel Factor Analysis

Acknowledgments

This thesis is far too long already (sorry) so I will keep this brief. I would first like to thank my parents, Anne and Steve, for all the parenting things, of course – but I am also grateful that they nurtured my early interest in science and the environment. Without their gentle encouragement I would not have entered academia. I am deeply appreciative of friends, family, and road bikes (in alphabetical order): Anna, Brett, Diana, Giant TCR [2025], Ian, Kimber, Krystle, Mac, Matt, Mo, Ruth, Scott, Specialized Allez Sprint [2021], Tazrian, Todd, and Viv – thank you all for your support over the years. To my friends, Rishabh and Varsha, thank you so much for accommodating (and feeding) me during my trips to Peterborough. Although brief, the time spent in your home was always the highlight of my visit. I would like to thank my co-supervisors, Julian and Mark, as well as my research committee member, Huy, for their support and mentorship over the years – this thesis would have obviously not been possible without their involvement.

Table of Contents

List of Figures

List of Tables

List of Abbreviations

Abbreviation	Full name
AOSR	Athabasca Oil Sands Region
ASL	Acid Sensitive Lakes
a_{254}	Naperian absorption coefficient at 254 nm
A_{254}	Absorbance at 254 nm
Abs_{λ}	Aerosol light absorption coefficient
BIX	Biological index
BrC	Brown carbon
C	Carbon
CC	Core consistency
CDOM	Chromophoric dissolved organic carbon
CV	Coefficient of variation
DOC	Dissolved organic carbon
DOM	Dissolved organic matter
EEM	Excitation-emission matrix
FA	Fulvic acid
FI	Fluorescence index
GEM-MACH	Global Environmental Multi-scale - Modelling air quality and Chemistry
HA	Humic acid
HIX	Humification index
HOMO	Highest occupied molecular orbital

HULIS	Humic-like substances
IFE	Inner filter effect
l	Transmitted light
l_o	Incident light
LUMO	Lowest occupied molecular orbital
MAC_{365}	Mass absorption cross section at 365 nm
MAE_{365}	Mass absorption efficiency at 365 nm
MFT	Mature fine tailings
n	Non-bonding orbital
NADP	National Atmospheric Deposition Program
NMAD	Normalized median absolute deviation
NO_x	Nitrogen oxides
O_a	Organic anions
OS	Oil sands
PAC	Polycyclic aromatic compounds
PARAFAC	Parallel Factor Analysis
PAH	Polycyclic aromatic hydrocarbon
PCA	Principal component analysis
PLS-R	Partial least squares regression
$PM_{2.5}$	Fine particulate matter
PRLIS	Protein-like substances
QSU	Quinine sulphate units
RAMP	Regional Aquatic Monitoring Program

SO_x	Sulphur oxides
SO_2	Sulphur dioxide
SO_4^{2-}	Sulphate
$SUVA_{254}$	Specific UV absorbance at 254 nm
SWE	Snow water equivalence
S_0	Ground-state orbital
S_1	First excited-state orbital
TC	True colour
TCC	Tucker Congruence Coefficient
T_{OS}	Oil sands transport frequency
TSP	Total suspended particulate
UV-Vis	Ultraviolet – visible light
VWA	Volume-weighted average
WBEA	Wood Buffalo Environmental Association
WPSCF	Weighted potential source contribution function
WS-BrC	Water soluble brown carbon
WSOC	Water soluble organic carbon
π	Bonding Pi orbital
π^*	Antibonding Pi orbital
λ	Wavelength

1. Chapter One: General Introduction

1.1 Chromophoric dissolved organic matter in the aquatic environment

Dissolved organic matter (DOM) consists of a complex mixture of carbon (C) rich molecules that are abundant throughout the natural world. Water-soluble organic matter is a major constituent of the global C cycle (Battin et al., 2009) and moderates numerous processes critical to the function of aquatic environments, including freshwater lake systems (Creed et al., 2018; Solomon et al., 2015). A major fraction of environmental DOM is comprised of chromophoric dissolved organic matter (CDOM), a broad class of molecules that absorb light in the visible and ultraviolet wavelength range (100 – 800 nm) (Del Vecchio and Blough, 2004). The CDOM fraction is ubiquitous throughout freshwater and marine environments and plays a critical role in the transport of nutrients and trace elements, acts as a medium for biological activity, and can limit the primary productivity of autotrophs (Dodds and Whiles, 2010; Fisher and Likens, 1973). Chromophoric organic matter is introduced to aquatic environments through sources located outside (allochthonous) or within (autochthonous) the system (Coble, 2007). Organic matter originating from allochthonous or terrestrial sources is typically composed of large, highly polymerized aromatic molecules often classified as humic substances (HS), which broadly consist of humic acids (HA) and fulvic acids (FA) (Thurman, 1985). Organic matter originating from in-lake materials and processes often consist of smaller, less aromatic compounds, such as amino acids and proteins (Zhang et al., 2011).

The initial composition of aquatic CDOM is determined by the primary allochthonous and autochthonous sources (e.g., foliage, soil, macrophyte, microbial metabolism) contributing

to the system; however, numerous other environmental processes can subsequently alter organic matter composition (Huang et al., 2022; Olefeldt et al., 2013). Biological and photochemical reactions fundamentally alter CDOM quality within natural waters through degradation, mineralization, and sedimentation (Olefeldt et al., 2013). Hydrological conditions such as catchment runoff and residence times play a key role in organic matter transport and within lake processing waters (Kellerman et al., 2014; Kothawala et al., 2013).

The abundance and quality of surface-water CDOM is inexorably linked to the acid-base conditions of the surrounding environment. Shifting surface-water pH can directly alter the protonation state of humic and fulvic acids, which further impacts species' physical properties and reaction chemistry (Lan et al., 2022). Various environmental processes responsible for the production and transport of allochthonous and autochthonous CDOM are similarly sensitive to pH; for instance, pH-sensitive autochthonous processes can alter the in-situ production and removal of CDOM within surface-waters (Anesio & Granéli, 2003; Dillon & Molot, 1997; Gu et al., 2017), and catchment acidification can inhibit DOM flux to aqueous systems (Schindler, 1998). Owing to their abundance of carboxyl and phenolic functional groups, chromophoric humic and fulvic acids can conversely influence the acid-base chemistry of the aquatic environment (Oliver et al., 1983), which depending on organic acid strength can contribute to pH and acid neutralization capacity (Castrillon-Munoz et al., 2022; Driscoll et al., 1994; Munson & Gherini, 1993).

1.2 Chromophoric dissolved organic matter in the atmospheric environment

Many studies have focused on CDOM within aquatic systems (Del Vecchio and Blough, 2004; Kothawala et al 2014); however, coloured organic matter is also recognized as an important chemical constituent of the atmospheric environment (Chakrabarty et al., 2016; Facchini et al., 1999). Atmospehric CDOM is highly diverse and can consist of polymerized aromatic structures similar to humic acids, as well as relatively low molecular weight compounds such as nitrocatechols, aromatic acids, and polycyclic aromatic hydrocarbons (PAHs) (Claeys et al., 2012). These chemical species can persist within both the gas and aerosol-phase (Chen et al., 2021); however, most research to date has focused on the latter, which is conventionally referred to as water-soluble brown carbon (WS-BrC) (Fuzzi et al., 2002; Lin et al., 2012; Stone et al., 2009).

Given that the chromophoric fraction can contain environmentally toxic compounds like heterocyclic PAHs, previous analysis has suggested that atmospheric CDOM and WS-BrC can be harmful to human and environmental health (Ma et al., 2019; Maulderly and Chow, 2008). Owing to their light absorbing properties and capacity as cloud condensation nuclei, gas and aerosol phase CDOM can directly and indirectly influence planetary albedo and solar radiation budgets (Facchini et al., 1999). Specifically, WS-BrC has been increasingly recognized as an important factor contributing to regional and global climate change (Chakrabarty et al., 2016; Gustafsson et al., 2009). The environmental sources of atmospheric CDOM and WS-BrC are diverse: fungi, plant debris, soil erosion (Andreae et al., 1997; Rizzo et al., 2013), biomass burning (Ramanathan et al., 2007), and fossil fuel combustion (Bond, 2001; Shen et al., 2023; Yan et al., 2017) can all influence the concentration and composition of CDOM in the ambient atmosphere.

Atmospheric CDOM eventually re-enter the planetary surface through wet and dry deposition. This process can impact the surrounding environment. Atmospheric inputs have been found to measurably alter the composition of natural CDOM within aquatic systems; for example, dry deposition of BrC to alpine lakes near the Mediterranean Sea significantly altered surface-water optical properties and light penetration (Mladenov et al., 2011; Zang et al., 2013). Moreover, WS-BrC deposition onto snow- and ice-covered surfaces can enhance warming and thaw rates (Zhou et al., 2022).

1.3 Ultraviolet – visible light spectroscopy

Optical evaluation techniques including ultraviolet-visible (UV-Vis) and fluorescence spectroscopy are widely applied in the study of environmental DOM and CDOM given their analytical versatility, chemical sensitivity, and low operational costs. Ultraviolet-visible light spectroscopy relies upon the interaction of incoming (incident) light radiation (l_o) and molecules within a sample, which temporarily increases the orbital, vibrational, and rotational energy state of electrons within sample compounds (Schulman et al., 2017). These three states exist as a discrete series of energy levels, where the kinetic input required for an orbital transition is comparably larger than jumps in vibrational and rotational state. Moreover, each orbital state has its own set of vibrational and rotational energy levels. Owing to the discrete number of available energy states within a molecule, l_o of a specific wavelength (λ, nm) is required for any possible energy transition (Akash & Rehman, 2020).

Incident photons with high-enough kinetic energy ($h\nu_A$), including light in the UV and visible wavelength range (100–800 nm), can promote an electron from its ground-state (S_0) to a vibrational sublevel of a new excited orbital state (e.g., S_1). This excited electron

conserves the spin orientation from its initial ground orbit (which spins antiparallel to a second-paired ground-state electron) and as such is considered part of a singlet system (Akash & Rehman, 2020). The wavelength of light absorbed by a molecule in the UV-Vis range is largely dependent upon the type of electronic transitions between molecular orbitals, the most important being:

a) bonding pi to antibonding pi ($\pi \rightarrow \pi^*$)

b) non-bonding to antibonding pi ($n \rightarrow \pi^*$)

Where the hv_A required to promote an electron from its highest occupied molecular orbital (HOMO) in the ground-state to the lowest un-occupied molecular orbital (LUMO) corresponds to the wavelength of light absorbed by a molecule (Schulman et al., 2017). The distance between the HOMO and LUMO is determined by a molecule's resonance structure configuration, where enhanced stability via electron delocalization reduces the energy gap between molecular orbitals. Both $\pi \rightarrow \pi^*$ and $n \rightarrow \pi^*$ transitions occur in stable, conjugated systems such as carbon-carbon (C = C) and carbon-oxygen (C = O) double bonds (Akash & Rehman, 2020). Higher degrees of conjugation (alternating single and double C bonds) increase the stability of a molecule, which in turn reduces the HOMO – LUMO energy difference. Due to the lower hv_A required for electronic transitions, increasingly conjugated molecules absorb l_o at progressively longer wavelengths (Schulman et al., 2017). As such, aromatic compounds like HA, FA, and PAHs are effective at absorbing light in the UV-Vis range. The addition of functional groups to an aromatic structure typically decreases the HOMO – LUMO energy gap; as such, substituted aromatic molecules absorb at longer wavelengths than their unsubstituted counterparts.

Singlet state transitions produce primary absorption bands while lower/higher l_o wavelengths can excite electrons to adjacent vibrational and rotational sub-states, broadening the initial absorption bands. In spectroscopy analysis, absorbance (A) is reported as the log transformed fraction of light radiation transmitted through (l), and the l_o directed into the sample. In accordance with the Beer-Lambert law, measured A is directly proportional to the concentration of the absorbing molecule and sample path length (Akash & Rehman, 2020). Although spectroscopic analysis of individual molecules may produce distinct absorbance peaks, chemically heterogeneous environmental samples present a broadened spectrum reflecting the combined absorbance bands of all chromophoric compounds. Through the application of UV-Vis spectrophotometers, absorbance measured as a function of λ (100–800 nm) can provide valuable insights regarding the bulk properties of CDOM within a sample. For example, absorbance at 254 nm (A_{254}) is frequently used as a general proxy for DOM in terrestrial and aquatic environments (Brandstetter et al., 1996). Additional diagnostic metrics derived from the absorbance spectra can provide further information regarding the compositional structure of environmental DOM. Specific UV absorbance at 254 nm ($SUVA_{254}$), derived via normalizing A_{254} by DOC concentration (mgC L^{-1}), generally represents the degree of aromaticity within a sample (Weishaar et al., 2003).

1.4 Fluorescence spectroscopy

Following initial l_o absorption, an excited electron rapidly returns to the lowest vibrational state of S_1 via processes of non-radiative decay, including vibrational heat transfer (vibrational relaxation) and energy transfers between excited singlet states (internal conversion) (Valeur & Berberan-Santos, 2013). Upon reaching S_1 the electron can continue

to decay to S_0 through non-radiative energy transfer, or it can jump to a vibrational sub-level of S_0 by emitting a photon in a process identified as fluorescence (Figure 1.1). Owing to the energy lost through non-radiative decay, the singlet system emits a photon of a wavelength longer than the excitation light; this difference in wavelength is termed the Stokes shift (Wolfbeis, 1985). The degree of Stokes shift is dictated by the competition between non-radiative and radiative decay processes, which in turn is determined by solvent conditions and the vibrational freedom of a molecule. As a rule of thumb, molecules of increased conjugation (such as HA and FA) display absorbance and fluorescence peaks at correspondingly longer wavelengths, while higher solvent polarity increases Stokes shift.

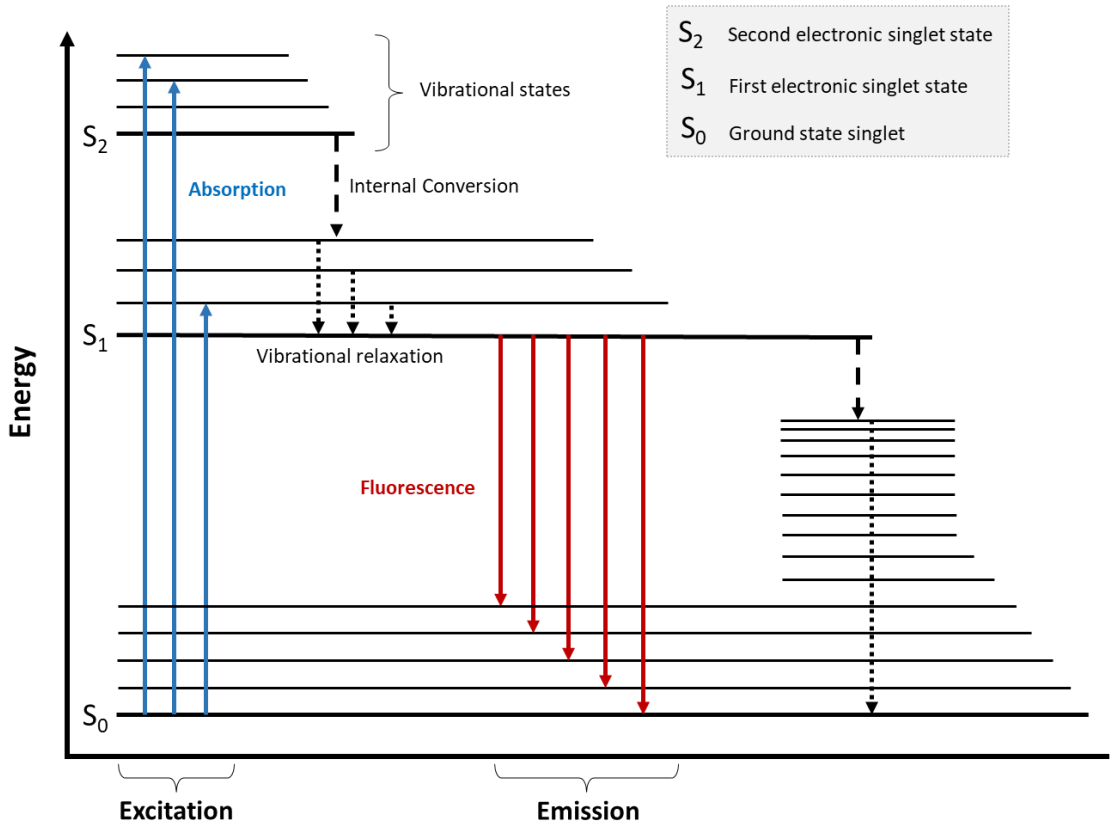

Figure 1.1. Perrin-Jablonski diagram illustrating the energy transitions between electronic singlet states and vibrational levels that occur during the processes of molecular absorbance

and fluorescence. Non-radiative energy transitions, including internal conversion and vibrational relaxation are shown.

The wavelength coordinates and intensity of the excitation (λ_{Ex}, absorbance) and emission (λ_{Em}, fluorescence) spectra can offer insights to the chemical structure and concentration of one or multiple fluorescent molecules (fluorophores) (Valeur & Berberan-Santos, 2013). Spectrofluorometers are capable of excitation emission matrix (EEM) measurements, a three-dimensional scan that plots fluorescence intensity against a range of excitation and emission wavelengths (Figure 1.2). These contour plots enable direct comparison of the excitation and emission spectra, where identifiable peaks can represent individual, or spectrally overlapping groups of fluorophores within the sample. Fluorescence EEM analysis is a relatively sensitive technique and can detect fluorophores in the parts-per-billion (ppb) range (Jiji et al., 2000).

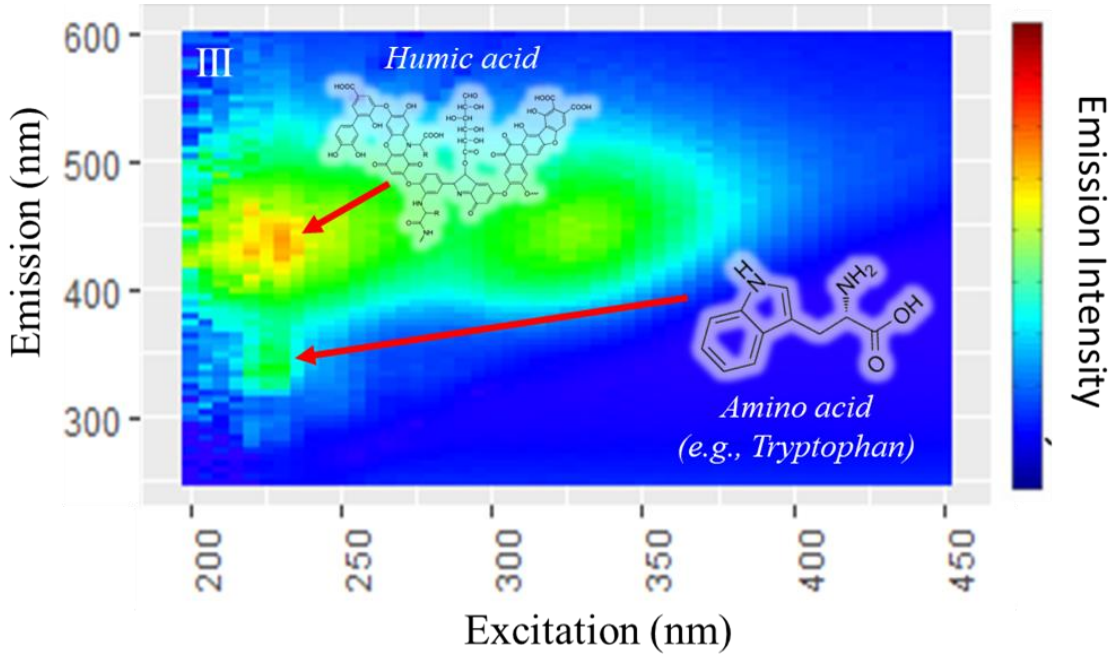

Figure 1.2 Example of an excitation emission matrix (EEM) scan of an environmental sample (lake surface-water from northern Alberta, Canada). Example fluorophore species responsible for the primary fluorescent peaks are illustrated.

1.5 Processing and interpretation of EEM data

The compilation of multiple EEM scans produces a three-way array (X) with dimensions i, j, k; i represents the number of EEM samples, while j and k reflect the number of emission and excitation wavelengths, respectively. One of the earliest methods employed to identify and evaluate fluorophore species from EEM scans relied upon manual "peak-picking" techniques (Sgroi et al., 2017); however, visual identification is generally inadequate when processing large EEM arrays containing spectrally complex information. Multivariable decomposition techniques such as principal component analysis (PCA) and PARAllel FACtor analysis (PARAFAC) have been widely adopted to evaluate expansive EEM data arrays.

Dimension reduction methods are intended to simplify complex multivariable datasets into a reduced set of components. Principal component analysis calculates linear combinations of the original variables to generate new orthogonal variables (C_1, ..., C_N) called principal components (PC). Each PC represents an eigenvector from the covariance matrix, where each corresponding eigenvalue represents the dataset variance explained by the respective PC (Miller & Miller, 2002). The bilinear nature of PCA models results in the loss of dimensionality from the three-way EEM array, which limits chemical interpretation of fluorescent species within the samples. Alternatively, PARAFAC offers a multi-way method that conserves the dimensions of the original data array. The resulting model decomposes EEM arrays (x_{ijk}) into a score matrix (**A**) and two loadings' matrices (**B** and **C**) with corresponding trilinear elements a_{if}, b_{if}, and c_{kf}:

$$x_{ijk} = \sum_{f=1}^{F} a_{if} b_{jf} c_{kf} + e_{ijk} \qquad \textbf{Eq. 1.1)}$$

Score values in a_{if} represent the relative fluorescence intensity of analyte f in sample i. Given that emission intensity is proportional to fluorophore abundance (Valeur, 2002), **A** scores can be interpreted as concentration data. The elements b_{if} and c_{kf} represent the modelled emission (j) and excitation (k) spectrum of analyte f, while F is the total number of modelled chemical components. Each modelled component represents the distinct spectra of an individual or a group of similar fluorescent molecules (Figure 1.3). Utilizing the residual element e_{ijk}, the PARAFAC model applies an alternating least-squares optimization technique to find the function that best approximates the dataset (Bro, 1997).

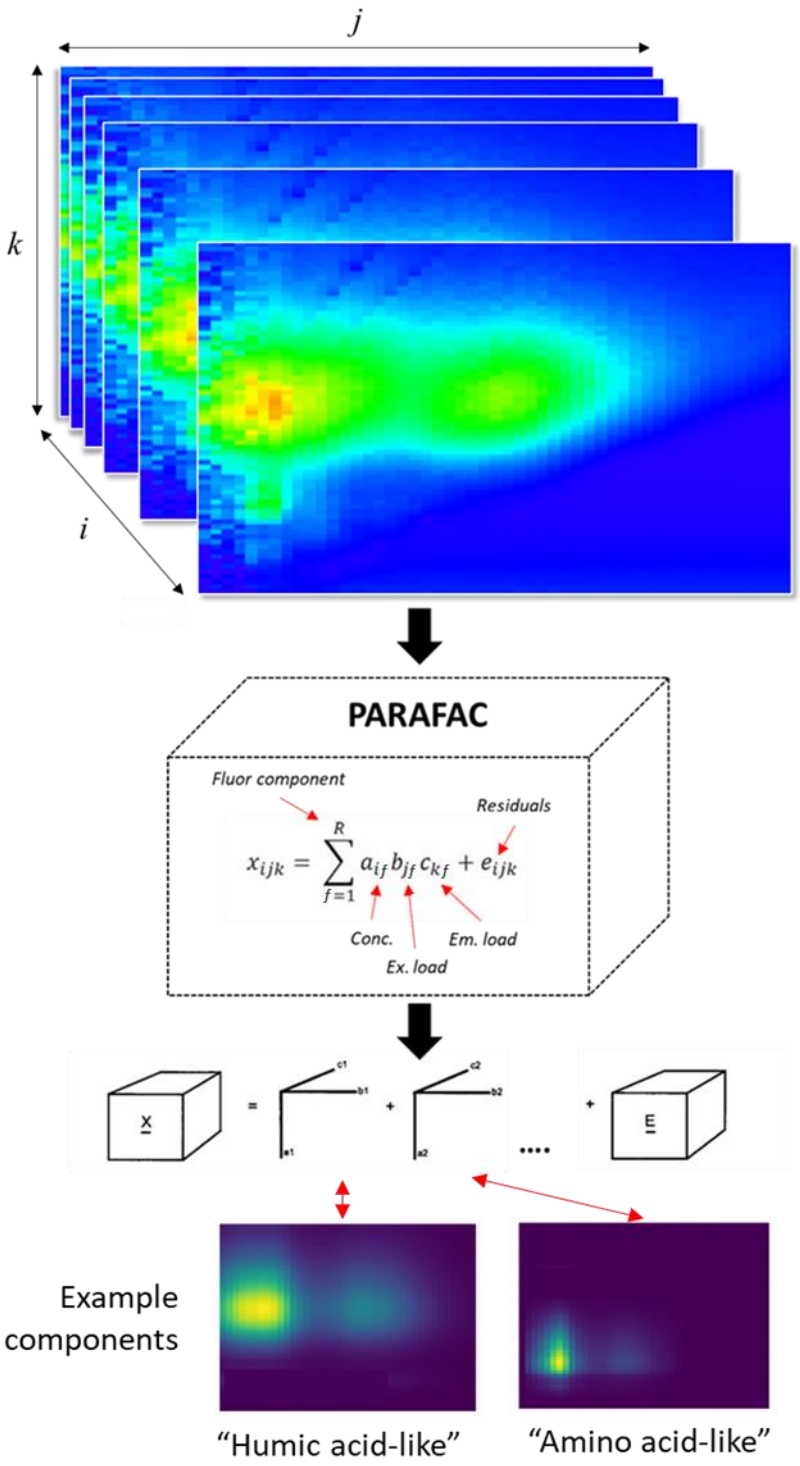

Figure 1.3 Conceptual diagram illustrating the key steps involved in the PARAFAC modelling process.

It is imperative that the operator selects the appropriate number of fluorescent components (also identified as model rank) included in the PARAFAC model, as an insufficient or excess number of components risks under or overfitting the EEM dataset, respectively. Several accepted validation techniques can be applied to assist with model rank selection, including: 1) visual peak inspection, 2) EEM residual plots, 3) split-half analysis, and 4) core consistency (CC). These validation tools and their corresponding procedures are described in detail in Chapter 3, section 2.4. Due to its analytical advantages, the PARAFAC technique has been widely adopted as a tool to evaluate EEM fluorescence data. The development of user-friendly software packages, such as the MATLAB toolbox "drEEM" (Murphy et al., 2013) and R package "staRdom" (Pucher et al., 2021) has improved the accessibility of the PARAFAC method to the broader scientific community.

The combined EEM-PARAFAC method is frequently utilized to evaluate naturally occurring CDOM within aquatic and terrestrial systems, where multi-way modelling can aid in the identification of distinct fluorophores such as HA, FA, protein, and amino acid like compounds (Coble, 1996). The λ_{Ex} and λ_{Em} spectra of each modelled component can be manually compared to EEM data in the literature to assist with fluorophore characterization.

Numerous studies have applied EEM-PARAFAC analysis across a wide range of environmental mediums and regions (Fu et al., 2015; Sgroi et al., 2017); further, a selection of studies have successfully identified the fluorescent constituents of anthropogenic organic pollutants of pyrogenic and petrogenic origin (Mendoza et al., 2013). For example, EEM analysis of aquatic samples have identified a variety of fluorescent peaks associated with

PAHs, PACs, and naphthenic acids (Kaur et al., 2014; Mahamuni et al., 2019). Further, fluorescence spectroscopy has been used to evaluate the composition of WS-BrC extracted from active sampler mediums. The resulting analysis of these samples, accompanied by external pollutant and meteorological variables, successfully identified several fluorescent

Although EEM-PARAFAC offers useful information regarding the optical structure of organic matter within a sample, complimentary environmental data is frequently used to further characterize CDOM. A variety of statistical techniques are applied for such analysis, one of the most common is partial least squares regression (PLS-R). Partial least squares regression is a multivariable technique effective at decomposing large numbers of colinear predictor variables (X) into a smaller set of uncorrelated orthogonal components (Eriksson et al., 2013). The PLS-R model attempts to explain the maximum variability between X and response variables (Y) through a least-squares regression method. By assigning EEM-PARAFAC fluorescent components as the Y variables and supplementary environmental data as X, PLS-R can help identify the primary sources and processes influencing CDOM structure and variation within an environment (Kothawala et al., 2014).

1.6 Athabasca Oil Sands Region

The Athabasca Oil Sands Region (AOSR) is a boreal landscape in northern Alberta, Canada, where peatlands and boreal forests are the dominant landscape features. Largely because of its northern – inland geographical location, the region typically experiences warm summers and cold, dry winters (ECCC, 2024). Beneath the boreal landscape lies the Athabasca oil sands deposit, the world's largest known bitumen reserve which covers a surface area of ~ 140,200 km^2. Beginning in the mid-20^{th} century, oil and gas companies

such as Syncrude, Suncor, and Imperial Oil have established industrial facilities over these deposits to extract and upgrade crude oil material. Industrial production has expanded continuously; for example, between 2013 and 2023, crude oil production from the AOSR increased from 2.1 to 3.4 million barrels per day (data available via the Canadian Association of Petroleum Producers and Canada Energy Regulator). The major oil sands (OS) facilities are located along the east and western banks of the Athabasca River, which flows north through the AOSR. The largest municipalities in the region are Fort McMurray and Fort McKay; the former is located ~50 km south of OS operations while Fort McKay sits along the western bank of the Athabasca River, situated between several major industrial facilities (Figure 1.4).

Oil sands mining and upgrading processes are a major source of sulphur dioxide (SO_2) and oxidized nitrogen species (NO_x) (ECCC & AEP, 2016). Due to the acidic potential of these inorganic species, atmospheric deposition of sulphur and nitrogen has been the focus of extensive regional evaluations (Bennet et al., 2008; Cathcart et al., 2016). Past studies have highlighted the prevalence of acid-sensitive soils throughout the AOSR, raising concerns regarding the impact of acidic inputs to surrounding ecosystems, including lakes (Cathcart et al., 2016).

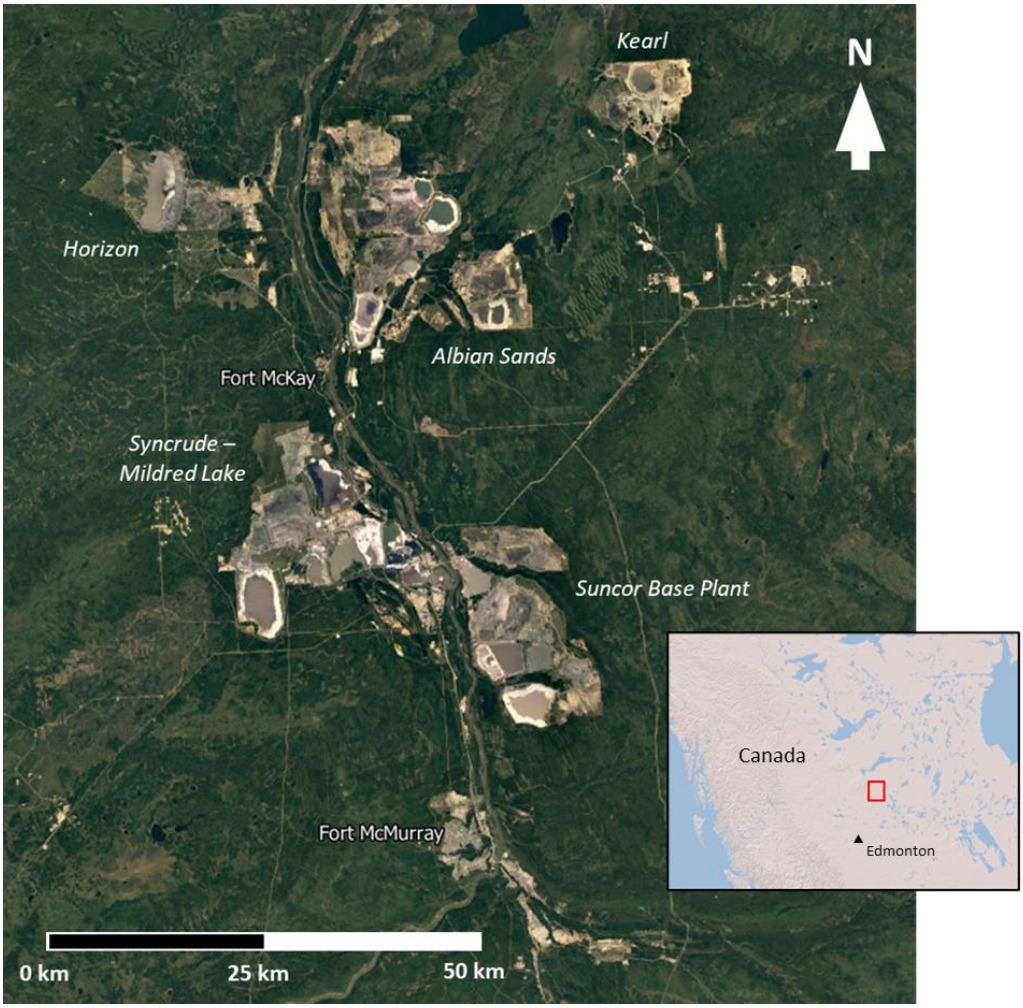

Figure 1.4 Overview of the Athabasca Oil Sands Region (AOSR) identifying local municipalities (Fort McMurray and McKay) and the location and scale of the major oil sands industrial facilities. The inset map displays the broader geographical location of the AOSR study area.

The AOSR contains an abundance of boreal lake systems, which owing to the prominence of organic soils and peatlands throughout the landscape, possess surface-waters uniquely high in DOC. Between 2015 and 2017, the median DOC concentration among a selection of 50 annually monitored acid sensitive lakes (ASL; www.ramp.org) throughout the AOSR was 22.0 mg C L^{-1}, considerably higher than globally reported values (median = 5.7 mg C L^{-1}, n ≈ 7500) (Sobek et al., 2007). Moreover, lake surface-waters throughout the AOSR

often display a high degree of colouration, which indicates the presence of CDOM within the water column. There is limited data describing the composition of lake CDOM throughout the AOSR; further, the sources and environmental processes influencing the organic matter fraction within regional surface-waters are not well understood. Given the established link between CDOM and acid-base chemistry it is expected that acidification will alter the organic matter fraction within regional lake surface-waters; this process could substantially impact numerous aquatic system functions.

Industrial operations in the AOSR are a major source of organic emissions to the atmosphere. Exposed bitumen, tailings ponds, petroleum coke (petcoke) stockpiles, and upgrading facilities emit gaseous polycyclic aromatic compounds (PAC) (Jariyasopit et al., 2018; Qiu et al., 2018), while open pit mines, mining fleet emissions, and petcoke generate organic-rich particulate matter containing high PAC loadings (Jariyasopit et al., 2021; Landis et al., 2019a). Oil sands emissions subsequently contribute to high organic deposition flux to the surrounding surface-environment, this process has been shown capable of impacting surface-water quality throughout the region (Kelly et al., 2009). Using the Global Environmental Multiscale–Modelling Air-quality and Chemistry model, Liggio et al. (2025) found that annual gas-phase organic carbon deposition from OS emissions theoretically exceeded the DOC catchment flux (excluding gas-phase DOC) of lakes within 200 km of major OS facilities. The OS-sourced organic matter entering aquatic systems in the AOSR is chemically diverse and largely undefined, which in turn presents a challenge to environmental monitoring efforts, given conventional forms of mass spectrometry analysis are limited by high operational costs (Frysinger et al., 2003)

A substantial portion of organic emissions and deposition from the OS industry likely possess light-absorbing and fluorescing properties, generally due to the presence of conjugated aromatic structures (Yamaguchi et al., 2008). As such, OS operations likely contributed to the emission and subsequent deposition of CDOM and WS-BrC throughout the AOSR. Owing to its light absorbing properties, CDOM aerosols and deposition could measurably impact radiative forcing within the regional atmospheric and surface environment. However, no studies have evaluated atmospheric CDOM throughout the AOSR.

Considering that industrial pollutants are observable within AOSR surface-waters (Kelly et al., 2009) and that atmospheric inputs are capable of influencing lake CDOM (Mladenov et al., 2011; Zang et al., 2014), it was suspected that atmospheric CDOM deposition from OS industry could alter the chromophoric fraction within regional lake surface-waters. Altered surface water CDOM quality due to OS inputs could have real-world implications for lake functions, as variable light absorbance could directly impact aquatic system energy budgets and productivity. Moreover, a clearly observable link between industrial operations and lake CDOM would demonstrate that relatively accessible spectroscopy techniques (UV-Vis, EEM-PARAFAC) equipped to measure CDOM could provide a cost-effective means to detect industrial pollution within regional surface-waters.

1.7 Research objectives and study design

The first overarching objective of this thesis was to determine if acidic atmospheric input from OS emissions could impact CDOM within regional lake surface-waters by altering acid-base and CDOM interactions. However, to approach this question, it was first

necessary to confirm that acid-base chemistry and CDOM shared an influential link within regional waters. Given the bidirectional associations between freshwater CDOM and acid-base chemistry established in the literature, the first hypothesis (H_1: a) predicted that variables reflective of chromophoric organic matter would be statistically associated with variables reflective of acid-base chemistry (e.g., pH and alkalinity). The corresponding null hypothesis (H_0: a) was: "CDOM and acid-base variables are not significantly associated".

The second objective was to establish whether organic inputs from OS emissions contributed to surface-water CDOM within lakes throughout the AOSR. Aerosol, snowpack, and precipitation samples collected throughout the AOSR were analyzed using spectroscopy techniques to characterize the optical properties of industrial CDOM, the resulting knowledge was then applied to search for similar spectral signals within regional lakes. The observations produced from this work were then used to answer the second hypothesis (H_1: b), which predicted that local industry would measurably alter CDOM quality within lake surface-waters. The corresponding null hypothesis (H_0: b) was: "Industrial emissions do not measurably contribute to CDOM within regional lake surface-waters"

Five complimentary studies were conducted to fulfill both research objectives, the contents of each are presented as standalone chapters written in the style of a peer-reviewed journal article (Figure 1.5):

a) The first research chapter (Chapter 2) was intended to provide a preliminary assessment of DOM spatiotemporal variation among regional lake surface-waters. This work involved the analysis of historical water quality data (1999–2017) available through the ASL

monitoring program, which represented 50 boreal lakes throughout the broader AOSR. Variables known to be associated with DOM and CDOM variation were the focus of analysis, while Lagrangian trajectory modelling was applied to explore the potential link of OS emissions with lake DOM and acid sensitivity. In 2021, the study corresponding to this chapter was published as a scientific paper in the journal of Environmental Science and Technology (Blanchard et al., 2021).

b) The objective of Chapter 3 was to characterize CDOM within ASL surface-waters (collected during the summer of 2021) through the application of UV-Vis and EEM fluorescence spectroscopy, paired with PARAFAC modelling. This analysis offered the first evaluation of CDOM composition and further explored the environmental sources and processes influencing the organic matter fraction within the regional lakes, including the potential relationship between CDOM and acid-base chemistry. Absorbance and fluorescence variables (including fluorophores identified via EEM-PARAFAC) were compared against corresponding lake water quality, morphological, and hydrological data for the purpose of CDOM characterization. At the time of completing this thesis (2025), this work was submitted to the journal, Science of the Total Environment, for peer review.

c) Chapter 4 was designed to evaluate the composition and spatial variation of atmospheric WS-BrC in the AOSR airshed, ultimately to determine how OS operations contributed to aerosol - phase CDOM. During the summer of 2021 active filter-pack samplers were deployed throughout the AOSR to collect total suspended particulate samples, which were subsequently submitted for absorbance and fluorescence spectroscopy analysis to characterize CDOM and identify fluorophore signals linked to OS operations. Supplementary filter-pack elemental analysis, continuous air quality data, and back-

trajectory modelling were employed to characterize the primary WS-BrC sources. This investigation was published as a scientific article in the journal of Atmospheric Chemistry and Physics February 2025 (Blanchard et al., 2025a).

d) Chapter 5 explored the spatial and temporal variation of CDOM within atmospheric deposition in the AOSR through the optical analysis of regional snowpack (Spring 2023) and weekly precipitation (2021 meteorological year) samples. Absorbance and EEM fluorescence spectroscopy analysis, complemented by elemental and continuous air quality variables were applied to characterize CDOM deposition and identify fluorophores specifically linked to OS sources. The study corresponding to this chapter was published (February 2025) in the journal, Environmental Pollution (Blanchard et al., 2025b).

e) The purpose of the final chapter (6) was to determine if OS emissions and deposition contributed to surface-water CDOM within regional lakes in the AOSR. This work involved a reanalysis of the EEM – PARAFAC dataset from the 2021 ASL samples, where the modelled fluorescent components were evaluated against surface-water PACs to assist with characterization. Moreover, the fluorescent spectra were compared against the petrogenic fluorophores observed within regional WS-BrC (Chapter 4) and deposition (Chapter 5) to determine if industrial CDOM in the atmosphere was observable within lake surface-waters. Following completion of this thesis, the findings from Chapter 6 will be submitted to a scientific journal.

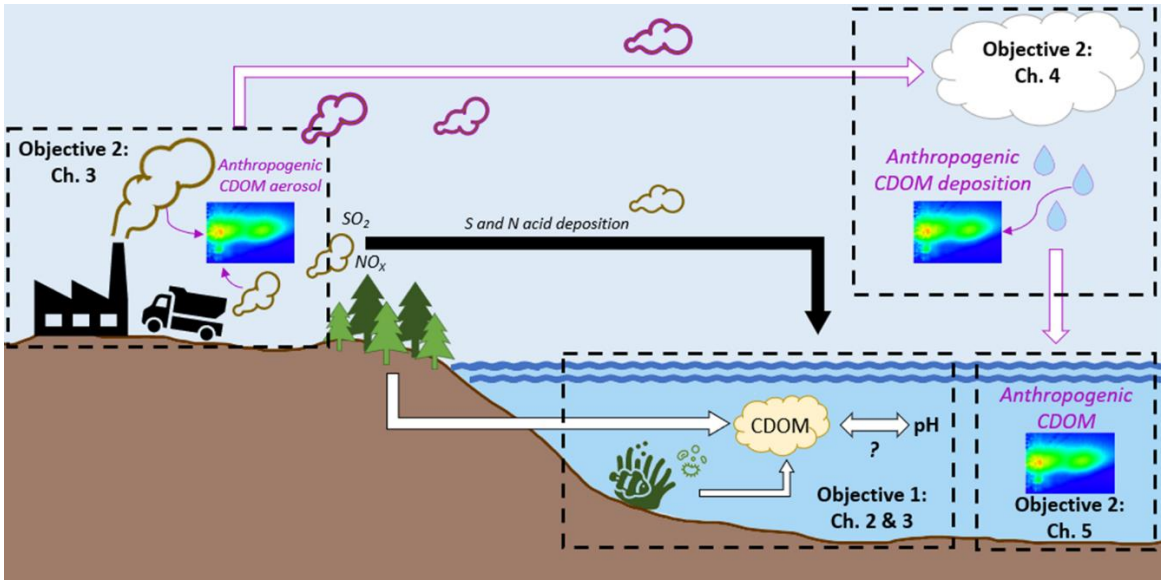

Figure 1.5 Conceptual diagram illustrating the key processes corresponding to each research chapter within the thesis.

2. Chapter Two: Dissolved Organic Carbon in lakes of the Athabasca Oil Sands Region: Is colour an indicator of acid sensitivity?[1]

2.1 Introduction

Dissolved Organic Carbon (DOC) consists of a complex mixture of carbon-rich compounds suspended in aqueous solution, which can pass through a 0.45 μm filter. This organic fraction is prevalent throughout the natural world and acts as a significant carbon (C) reservoir for numerous aquatic environmental systems (Hansel et al., 2009), including freshwater lakes. Dissolved organic carbon has a limiting influence over lake productivity partially owing to its UV-absorptive properties, which can inhibit photosynthesis (Jones, 1998; Snucins and Gunn, 2000; Toming et al., 2020). Depending on chemical composition and concentration, DOC can alter lake chemistry through the introduction of weak or strong organic acids (Köhler et al., 1999; Mattsson et al., 1995; Oliver et al., 1983). Organic compounds can complex with metals and nutrients including iron (Fe), copper (Cu), and phosphate (PO_4^{3-}), which in addition to altering the solubility and transport of organic species (Maranger and Pullin, 2003; Mierle and Ingram, 1991) can also influence the optical properties of DOC (Maloney et al., 2005; Xiao et al., 2013).

Optical properties of water samples are often analyzed to characterize the chromophoric fraction of DOC (CDOC). Humic substances are the most common constituents of CDOC in freshwater lakes (Thurman, 1985), however, they present a high degree of complexity in

[1] Blanchard, D., Aherne, J., Makar, P. (2021). Dissolved Organic Carbon in Lakes of the Athabasca Oil Sands Region: Is Color an Indicator of Acid Sensitivity?. *Environmental Science and Technology*, 55(10), 6791-6803, https://doi.org/10.1021/acs.est.1c00507

their chemical speciation. The optical metric, 'true colour' (TC) is a standard–calibrated measure of UV-absorbance often used to evaluate CDOC in aquatic systems. Owing to the prominence of the CDOC fraction within organic pools, TC is often employed as a proxy for DOC within aqueous samples. Previous research in Canada has found that TC is correlated with average DOC over extended periods in lakes (Molot, 2009; Molot and Dillion, 1997). However, this TC–DOC relationship often becomes more complicated in the presence of dissolved (d)-Fe owing to the formation of coloured Fe-DOC complexes (Heikkinen, 1990; Kutser et al., 2015). An extensive evaluation of freshwater systems throughout boreal regions in Canada and Sweden by Weyhenmeyer et al. (2014) observed that the relative fraction of absorptive DOC increased in response to elevated Fe concentrations, indicating a biogeochemical coupling between the two.

Biological decomposition is the primary known contributor to lake DOC, which is introduced via sources located outside (allochthonous) or within (autochthonous) the aquatic system. Anthropogenic sources (such as fossil fuel combustion and the processing or municipal wastewater) are known to contribute to freshwater DOC via both atmospheric and aquatic transport (Kritzberg et al., 2017; Pemberton et al., 2019; Siudek et al., 2015). Acidification of aquatic systems influences the concentration and composition of organic matter through altering in-situ removal and autochthonous production mechanisms (Anesio and Granéli, 2003; Dillion and Molot. 1997), allochthonous flux (Schindler, 1998), and the abundance of metals available for complexation (Schindler et al., 1992). Furthermore, processes of acidification (including acid deposition) can have substantial influence over ecosystem chemistry and function (Holt et al., 2003; Koptsik et al., 2001; Likens et al., 1998). North America and Europe have experienced a gradual increase in lake organic

content over recent decades, which is thought to be the combined result of decreasing mineral acidic deposition and the ongoing influence of climate change (Kritzberg et al., 2020; Meyer-Jacob et al., 2019). These trends are concerning as the acidic constituents of DOC can depress the acid neutralizing capacity (ANC) of poorly buffered lakes, retarding pH recovery from previous mineral acidification (Erlandsson et al., 2010).

The Athabasca Oil Sands Region (AOSR) in north-eastern Alberta, Canada, contains the world's third largest known bitumen deposit. Oil sands (OS) industrial processes are a major source of oxidized sulphur (SO_x) and nitrogen (NO_x) species, which have been the focus of previous evaluations owing to their acidifying potential through atmospheric deposition (Bennett et al., 2008; Carou et al., 2008; Cathcart et al., 2016; Hazewinkel et al., 2008). These studies have highlighted the prevalence of acid-sensitive soils throughout the AOSR, raising concerns regarding the sensitivity of surrounding lakes to acidifying inputs. There is limited evidence to suggest that OS-sourced deposition is acidifying lakes in the region, but there is suspicion this is partially due to the unique biogeochemistry of the lakes in question – convoluting any comparison against the thoroughly-studied acid-sensitive lakes of northern Europe and Eastern North America (Hazewinkel et al., 2008). Furthermore, these assessments largely discounted the influence of organic deposition over environmental chemistry. The Athabasca Oil Sands have been frequently identified as a significant source of gaseous volatile organic compounds (VOC) (Bari et al., 2018), organic species known to contribute to secondary organic aerosol (SOA) and secondary organic acid formation downwind of OS operations (Liggio et al., 2016; 2017). These findings, further supplemented by numerous prior studies (Cho et al., 2014; Kurek et al., 2013; Landis et al., 2019c), indicate the OS as a major source of organic deposition to the AOSR,

which raises concern regarding the combined impact of inorganic and organic acid inputs on freshwater acid-base chemistry and DOC variability. Despite this possibility, there are limited studies that have evaluated the characteristics and variability of DOC throughout the AOSR.

Beginning in 1999, the Acid Sensitive Lakes (ASL) program (operated through the Regional Aquatic Monitoring Program [RAMP]) has conducted annual monitoring of surface water chemistry for approximately 50 lakes throughout the AOSR. Here, we analyzed this historical (1999–2017) dataset to assess the spatial and temporal variation of lake DOC in the AOSR, and to investigate the potential influence of OS atmospheric deposition on lake chemical characteristics. Select water-quality variables known to be associated with freshwater CDOC (including TC, pH, alkalinity, major ions and select metals) were evaluated to interpret DOC variability among lakes throughout the study region. Dissociated organic anions (O_a), estimated via ion balance deficit were included in the dataset analysis. The Lagrangian trajectory model, HYSPLIT was employed to investigate the potential linkages between OS emissions and lake acid sensitivity.

2.2 Methods

2.2.1 Study region

The AOSR is located within the broader Wood Buffalo municipal region, which is in north-eastern Alberta, Canada (Figure 2.1). Primary oil sands operations (owned by Syncrude, Suncor Energy, Imperial Oil, etc.), consisting of open pit/in-situ excavation, upgraders, and steam-assisted gravity drainage have been established over major bitumen deposits, which combined cover a surface area of 140,200 km^2. Oil sands operations have been growing

steadily; between 1999 and 2017, production increased from 32.9 to 155.2 million m^3 of crude oil per year (CAPP, 2019; Natural Resources Canada, 2020).

The ASL program conducts annual monitoring of approximately 50 lakes throughout the AOSR, which are categorized according to their approximate geographical subregion, including: North-east of Fort McMurray (NE), West of Fort McMurray (WF), Birch Mountains (BM), Canadian Shield (CS), Caribou Mountains (CM), and Stoney Mountains (SM). The majority of ASL lakes (including subregions NE, WF, SM, BM) are located within a ~200 km radius surrounding the general epicenter of OS operations (north of the town of Fort McMurray), named AR6 (Figure 2.1). The remaining lakes are in the further-distant subregions CM and CS, which are located north-east and north-west of AR6, respectively (Figure 2.1). Samples were collected once a year during late summer–autumn (August–October) via float plane or helicopter. The ASL program was implemented via RAMP to monitor the long-term variation of surface-water chemistry among lakes throughout the AOSR, with specific interest in evaluating the potential influence of OS operations over surrounding lakes encompassing variable levels of acid sensitivity.

Bedrock geology is heterogeneous throughout the AOSR; most formations surrounding the OS and southern/central AOSR originate from the cretaceous period. The dominant formations throughout the SM and NE subregions contain shales and sandstones with variable moderate calcareous content. Bedrock underlying the lakes throughout the BM region consisted of a mixture of non- to variably calcareous mudstone and shale layers. The Cretaceous and Paleogene formations throughout the CM region consisted of sandstone, mudstone, shale, and upland gravel, while the bedrock above Lake Athabasca (CS region) is dominated by exposed granite (Prior et al., 2013). Located beneath the WF subregion are

the highly bituminous and calcareous McMurray and Waterways formations known to be associated with carbonate-rich groundwaters (Cowie et al., 2015). Surface materials throughout the region are primarily comprised of tills, and till veneers, while soils are classified as organics (primarily mesisols), luvisols, brunisols, and cryosols (Fulton et al., 1996; Agriculture and Agri-food Canada, 2005).

The AOSR is situated primarily within the Boreal Plains ecozone, which is composed of muskeg peatlands, poor fens, and forested ecosystems. Approximately 54% of total land cover in the AOSR consists of wetlands, the most prominent of which are fens (AEP, 2018). Poor fens, characterized by low ion concentrations and depressed pH are common among elevated headwater areas (including SM, BM, and CM) in addition to regions with acidic bedrock/surficial deposits (CS). Poor fens can become further acidified from surface inputs from surrounding bogs (ESRD, 2015), which are prominent within the BM and CM watershed (44% and 76% of median lake catchment area, respectively) (Gibson et al., 2020). Medium to rich fens, characterized by elevated ion and pH levels, are more abundant along low-elevation areas, including the WF subregion (ERSD, 2015). Owing to the prevalence of organic rich soils and extensive wetland complexes, lakes throughout the AOSR often present high DOC concentrations.

The AOSR experiences cold winters and warm summers, owing to its northern continental climate. The monthly climate normals (1981–2010) for Fort McMurray indicate that daily average temperature ranges from –17.4°C (January) to 17.1°C (July) while monthly precipitation varies between 13.2 mm (February) to 80.7 mm (July) (ECCC, 2020). Permafrost is prevalent throughout mid to high-altitude sub-regions, where 44, 76, and 7% of the median lake watershed is affected within the BM, CM, and NE subregions,

respectively. The remaining watersheds throughout the study region experience minimal permafrost (median watershed coverage <1%) (Gibson et al., 2020).

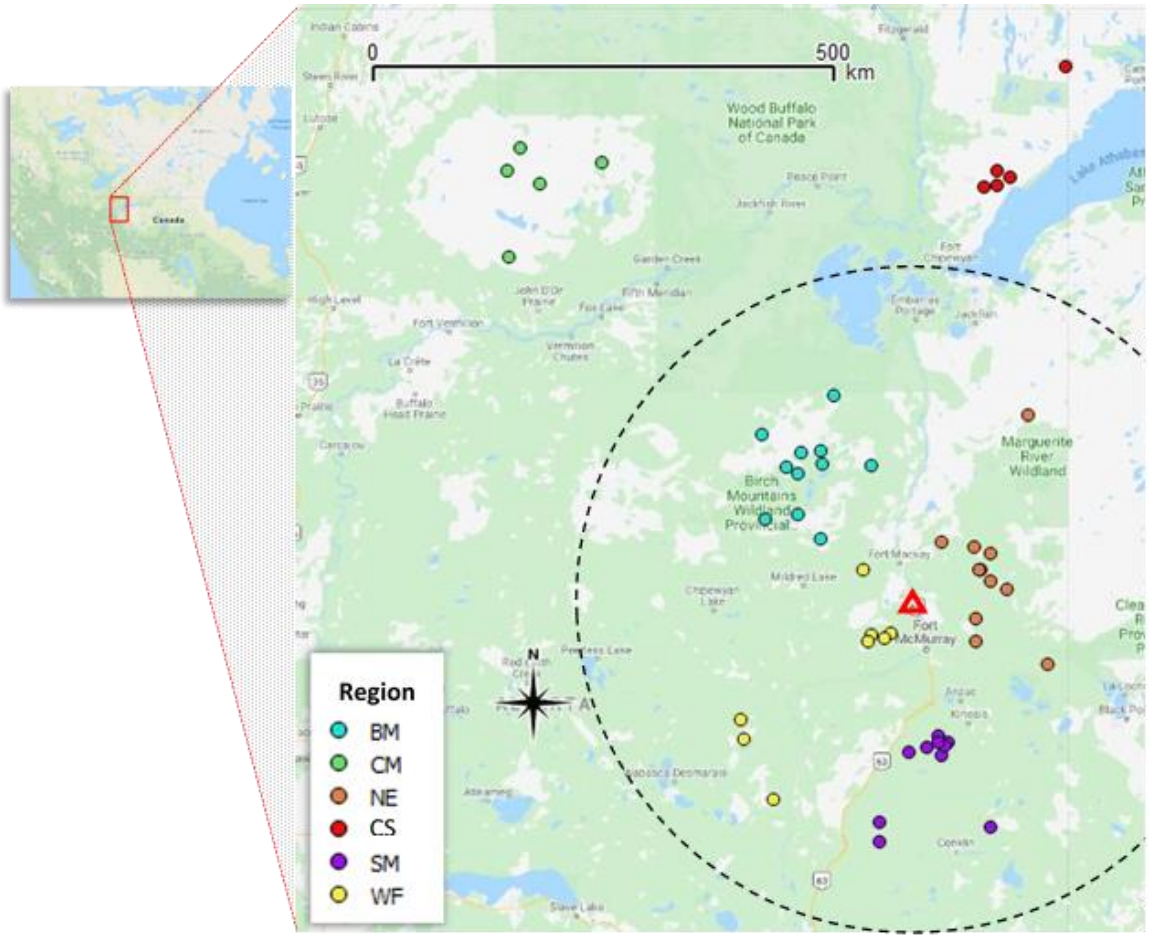

Figure 2.1 Overview of the ASOR study region and ASL lakes; coloured points identify the six geographical lake regions. Inset map displays the broader geographical location of the AOSR study area while the red triangle and black circle indicate the location of AR6 and the surrounding 200 km radius (source: Google Maps).

2.2.2 Dataset analysis

The ASL provided a long-term (1999–2017) dataset of annually monitored water-quality variables including: pH, TC, total and gran alkalinity, conductivity, chlorophyll-a, major

ions, nutrients, and metal species (dataset access: www.ramp-alberta.org). Additional information detailing the physical characteristics of individual ASL lakes (including lake depth, volume, surface area, and watershed area) was available through the program (Bennett et al., 2008). Past studies investigating the role of organic acids over lake acid-base chemistry have estimated the concentration of organic anions (O_a) in solution based on the discrepancy of a solution's charge balance (Driscoll et al., 1989; Hruška et al., 2001). Following the methods outlined in these studies, O_a (μeq L^{-1}) was estimated for each available surface-water observation within the dataset. Given the retroactive nature of this analysis, samples were unavailable to determine the average charge of monomeric Al. Therefore, it was assumed Al had a valence charge of +3, error associated with this generalization was likely minor considering Al concentrations are relatively low (Table 2.1). To evaluate the contribution of O_a to total ion abundance, the relative concentration of O_a in each sample was calculated as:

$$O_aR = 100 * \frac{O_a}{[C+A]} \qquad \textbf{Eq. 2.1)}$$

Where O_aR is the O_a fraction (%), C and A are sum concentrations (μeq L^{-1}) of cation and anion species (including O_a).

The available water-quality and physical variables for the ASL lakes were non-normal in distribution, as determined via Shapiro-Wilk test ($\alpha < 0.05$), thus non-parametric statistical tests were employed for analysis. Median observations were used as a measure of central tendency. The variability of median lake data was evaluated using the normalized median absolute deviation (NMAD). Spearman's Rank Order correlation tests were applied to assess bivariate associations between ASL physical and chemical variables, and the Mann-

Whitney U test was used to determine significant differences between subpopulations. Generalized least-squares models were employed to test significant differences between regression slopes (of similar variables) by comparing respective residual error values. Principal component analysis (PCA) was employed for exploratory evaluation of the large multivariable dataset. The resulting analysis generated linear combinations of select variables, identified as principal components (PC), which explained a portion of the total variance within the dataset. Our initial analysis primarily focused on the three most-recent years of ASL observations, which spanned from 2015–2017. Further, the Mann-Kendall test was applied to detect significant historical trends (1999–2017) in water-quality variables for individual lakes (Libiseller and Grimvall, 2002).

Potential correlations between DOC and TC were evaluated to reclassify lakes into subpopulations according to their shared chromophoric properties. These populations underwent independent evaluation (as described above), with focused interest in variables associated with the CDOC fraction (including DOC, TC, d-Fe, Fe, and PO_4^{3-}).

The atmospheric transport model, HYSPLIT was applied to predict the movement of OS emissions (AR6 was assigned as the central source of emissions) using the National Centers for Environmental Prediction / National Center for Atmospheric Research global reanalysis data archive (2.5 × 2.5-degree resolution) from 2005. Archived data from 2005 was selected for analysis as it was found to be representative of median-meteorological variation for the region during the 1999–2017 study period. Twenty-four-hour forward trajectories (operating at a 6-hour frequency) were projected from AR6 (with a starting elevation of 1 km above sea level) for the entirety of the 2005 meteorological year. Using the geographic information system (GIS) based software, TrajStat (Wang et al., 2009), the study region

was divided into grid cells identified by the variables i (latitude) and j (longitude). TrajStat recorded the frequency at which trajectory endpoints passed through each cell, denoted by n_{ij}. The resulting values were assigned a corresponding weighting function $w(n_{ij})$ (here on referred to as a weighted potential source contribution function [WPSCF]), that represented the deviation of individual n_{ij} estimates from the average number of endpoints (n_{mean}) intersecting each cell: (Polissar et al., 2001)[56]

$$W(n_{ij}) = \begin{cases} 1.00, 3n_{mean} < n_{ij} \\ 0.70, 1.5n_{mean} < n_{ij} \leq 3n_{ij} \\ 0.40, n_{mean} < n_{ij} \leq 1.5n_{ij} \\ 0.20, n_{ij} < n_{mean} \end{cases}$$

Eq. 2.2)

Each lake was assigned a WPSCF class corresponding to the nearest n_{ij} cell value, effectively classifying individual ASL sites according to their likelihood of receiving OS emissions. Refer to Wang and Polissar for further details regarding TrajStat analysis (Wang et al., 2009; Polissar et al., 2001). The ASL dataset was subsequently assessed to evaluate the variability of water-quality variables between ASL sites assigned to different WPSCF classes. These variable trends were visualized via box-plots charts proceeded by stepwise Mann-Whitney U tests to determine significant differences between lakes of differing WPSCF class.

The resulting WPSCF ASL classifications were compared against corresponding annual estimates of total S deposition previously generated via the GEM-MACH model provided by Environment and Climate Change Canada (ECCC). The model estimated total annual S and nitrogen (N) deposition (μeq m^{-2} yr) on a 2.5 × 2.5 km regional grid between August 1, 2013 – July 31, 2014 (Makar et al., 2018). The deposition model provided independent

data to determine if the HYSPLIT trajectories were representative of atmospheric transport and deposition variability in the AOSR. Mann-Whitney U tests were employed to assess significant differences between modelled S deposition and ASL WPSCF classification groups.

2.3 Results

2.3.1 Lake subregion summary

Lake physical/hydrological characteristics, including max depth, surface area, and catchment area, were comparatively low in lakes located within the SM and WF subregions (Table 2.1); median-lake observations ranged from 1.5–1.9 m, 1.1–1.4 km^2, and 10.8–12.8 km^2, respectively. The CS region displayed the highest median maximum lake depth and catchment area, while BM and CM lakes had the highest median volume and surface area. In general, the deepest ASL sites (ranging from 6.0–27.4 m) were located among the subregions furthest from primary OS operations, including CS and CM (Table 2.1).

Median inter-regional observations or estimates of surface water pH, DOC, O_a, TC, d-Fe, and PO_4^{3-}, from the recent sampling periods (2015–2017) ranged from 6.0–7.5 pH, 12.8–31.9 mg L^{-1}, 117.2–263.9 µeq L^{-1}, 54.4–218.9 mg L^{-1} Pt, 31.5–648.0 µg L^{-1}, and 0.1–1.1 µeq L^{-1}, respectively. The WF subregion presented the highest median DOC (Figure 2.2) and O_a, while the CM and BM subregions displayed the highest TC and d-Fe (Table 2.1). It should be noted that the observed water quality parameters experienced a high degree of variability among lakes within each geographical subregion, as indicated by the respective NMAD values. Future regional monitoring efforts should be cognizant of this heterogeneity if the ASL sites are categorized according to these established subregions.

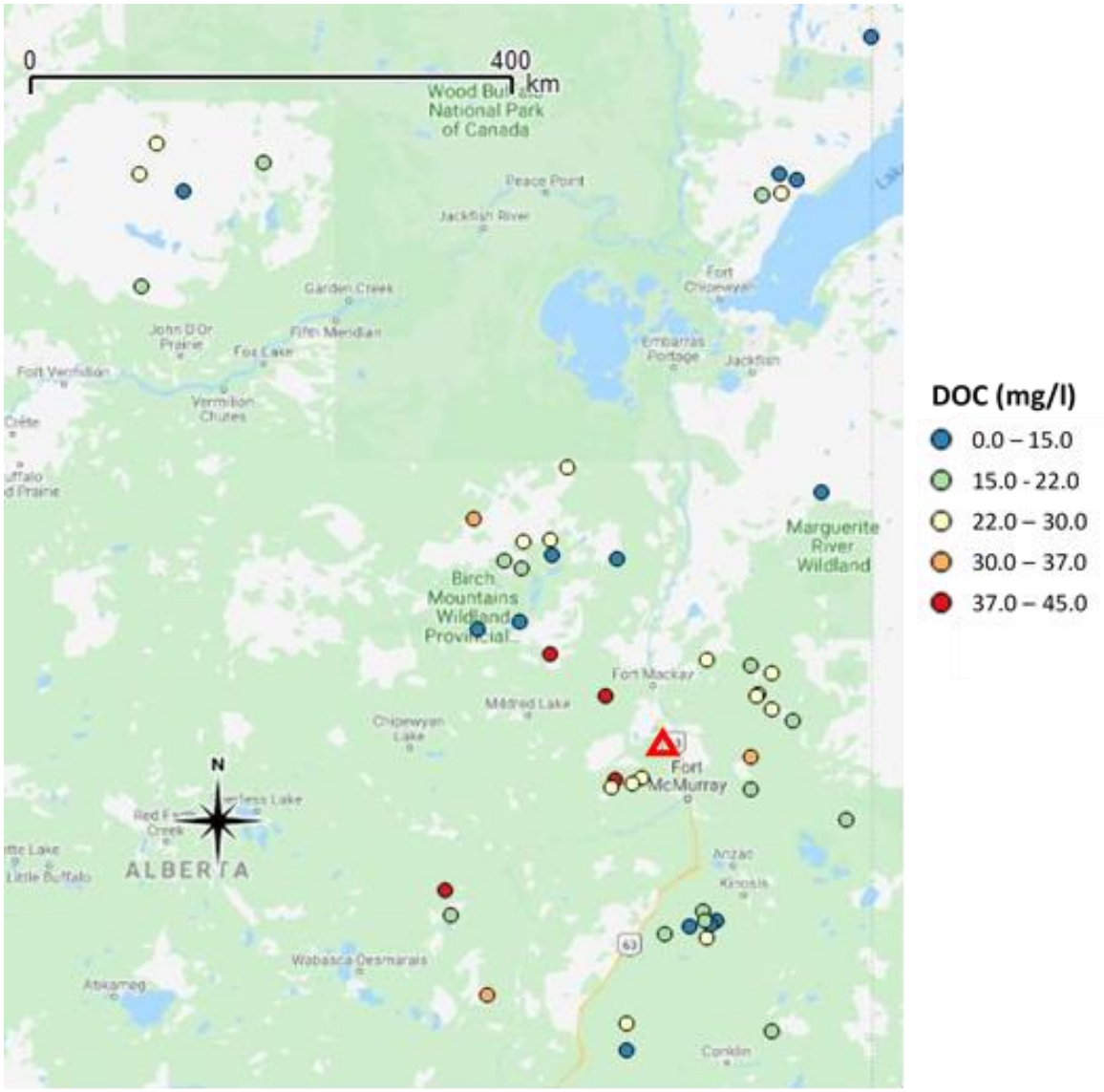

Figure 2.2 Average DOC (mgC L^{-1}) measured at individual ASL lakes during the 2015–2017 sampling period. The red outlined triangle indicates the location of the primary OS operations (AR6). The dotted-vertical line indicates the Alberta-Saskatchewan border (source: Google Maps).

.

Table 2.1 Median measured surface water variables among the ASL sampling regions (see Figure 2.1) during the recent (2015–2017) sampling periods. Values in parenthesis display normalized median absolute deviation (NMAD) between lakes within each subregion.

Region[a]	BM	CS	CM	NE	SM	WF
# of lakes	11	5	5	11	10	8
DOC (mgC L^{-1})	19.5 (47.7)	12.8 (31.3)	22.4 (12.9)	22.5 (21.3)	16.9 (30.2)	31.9 (19.1)
DIC (µeq L^{-1})	205.4 (114.2)	377.4 (24.0)	188.7 (73.0)	263.7 (158.5)	41.6 (107.5)	360.8 (58.2)
Oa (µeq L^{-1})	142.0 (59.0)	117.2 (36.7)	163.5 (14.2)	196.5 (18.7)	128.4 (137.5)	263.9 (23.1)
O_aR (%)	14.6 (29.4)	12.0 (31.8)	17.8 (16.7)	13.8 (55.3)	29.6 (18.6)	17.1 (20.7)
SO_4^{2-} (µeq L^{-1})	119.7 (65.4)	12.6 (32.5)	39.6 (61.6)	9.2 (102.2)	19.2 (53.2)	33.8 (43.8)
PO_4^{3-} (µeq L^{-1})	4.3 (81.7)	0.5 (34.8)	2.0 (32.9)	1.0 (37.4)	1.6 (70.0)	1.9 (66.9)
NO_3^- (µeq L^{-1})	< 0.1 (0.3)	< 0.1 (< 0.1)	< 0.1 (0.1)	0.1 (0.0)	< 0.1 (0.1)	< 0.1 (0.3)
Cl^- (µeq L^{-1})	2.6 (65.4)	32.5 (36.6)	2.4 (16.7)	4.0 (162.5)	2.9 (34.5)	5.3 (41.5)
Ca^{2+} (µeq L^{-1})	349.0 (43.5)	329.4 (19.7)	282.3 (43.4)	337.0 (81.6)	116.9 (171.1)	454.1 (37.0)
Na^+ (µeq L^{-1})	134.7 (59.4)	88.3 (28.7)	27.4 (69.7)	63.2 (126.1)	38.7 (30.5)	70.3 (82.9)
K^+ (µeq L^{-1})	20.3 (43.4)	16.5 (35.8)	8.0 (37.5)	5.8 (131.0)	8.1 (72.8)	24.0 (57.9)
Mg^{2+} (µeq L^{-1})	170.1 (58.8)	142.4 (19.7)	118.8 (43.1)	138.0 (90.2)	46.5 (57.9)	251.3 (49.9)
Al^{3+} (µeq L^{-1})	3.6 (98.5)	0.7 (44.6)	7.9 (27.5)	1.9 (93.5)	6.1 (73.6)	1.2 (36.9)
NH_4^+ (µeq L^{-1})	0.6 (166.7)	0.15 (66.7)	0.8 (25.0)	0.5 (40.0)	0.6 (66.7)	0.6 (283.3)
Anion sum (µeq L^{-1})	487.2 (54.9)	510.8 (19.1)	268.8 (62.8)	417.2 (111.7)	74.6 (82.0)	525.8 (56.3)
Cation sum (µeq L^{-1})	723.6 (41.4)	636.4 (10.0)	432.3 (41.4)	659.0 (73.6)	254.8 (88.3)	830.9 (37.8)
Alkalinity (µeq L^{-1})	268.5 (95.9)	449.8 (19.0)	226.5 (63.8)	405.3 (113.1)	58.4 (108.7)	472.9 (55.8)
pH (pH units)	7.1 (11.3)	7.5 (2.7)	7.1 (2.8)	7.3 (9.6)	6.0 (11.7)	7.3 (6.9)
Fe (µg L^{-1})	400.0 (97.5)	60.0 (83.3)	648.0 (29.1)	165.0 (93.9)	135.0 (61.1)	31.5 (134.9)
Conductivity (µs cm^{-1})	67.1 (37.6)	57.9 (15.9)	34.7 (48.1)	49.2 (85.4)	16.3 (34.4)	62.6 (43.3)
TC (mg L^{-1} pt)	139.1 (75.2)	54.4 (54.0)	218.5 (25.1)	87.8 (89.9)	90.3 (61.7)	120.6 (44.6)
Max depth (m)	6.4 (89.1)	13.6 (40.4)	6.7 (65.7)	2.0 (20.0)	1.9 (31.6)	1.5 (13.3)
Lake area (km^2)	8.9 (112.4)	1.5 (53.3)	3.3 (75.8)	2.2 (77.3)	1.4 (35.7)	1.1 (100.0)
Catchment area (km^2)	6.4 (104.7)	56.8 (80.6)	28.0 (41.4)	21.5 (67.4)	10.8 (31.5)	12.8 (96.1)

[a]BM – Birch Mountains; CS – Canadian Shield; CM – Caribou Mountains; NE – Northeast of Fort McMurray; SM – Stoney Mountains; WF – West of Fort McMurray.

2.3.2 DOC and TC analysis

Annual measured DOC presented relatively weak and insignificant correlations with the other available water quality variables among the ASL lakes. However, comparison of median lake DOC and TC (including both 2015–2017 and 1999–2017) revealed two visually distinct data groupings in relation to linear fit (Figure 2.3), which were re-classified as 'High' (H; n = 35) and 'Low' (L; n = 15), indicative of the relative difference in TC. The H and L subpopulations had significantly different slope coefficients (Generalized least-squares model analysis; $\alpha < 0.5$). Further comparison of lake populations revealed a significant difference in multiple water quality variables (Mann-Whitney; $\alpha < 0.05$), where the H group presented notably higher TC, SO_4^{2-}, dissolved PO_4^{3-}, and total/dissolved fractions of Al, and Fe. Lakes in the L group displayed significantly higher DOC, DIC, total alkalinity, major ions (with exception of SO_4^{2-}), and conductivity (Table 2.2). No significant differences in physical characteristics were detected between the two subpopulations.

All but one of the ASL sites assigned to the L subpopulation were located within the 200 km perimeter surrounding OS operations (Figure 2.1). Nonetheless, each subregion consisted of a mixture of H and L lakes, except for CM (Figure 2.4).

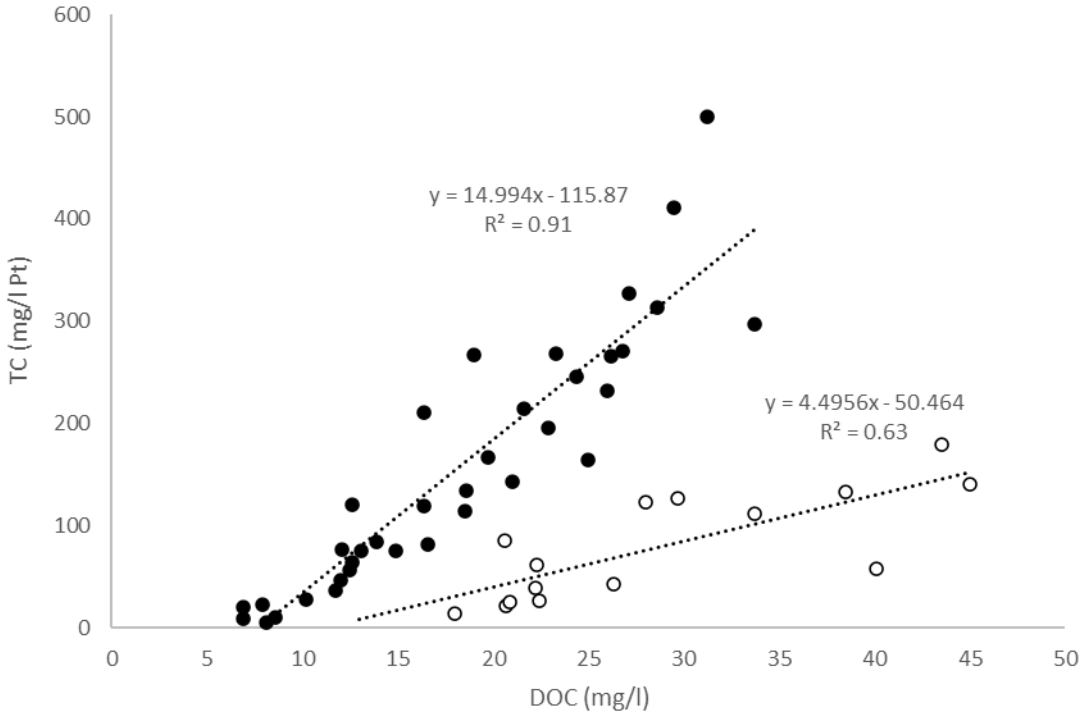

Figure 2.3 Median DOC (mg L^{-1}) and TC (mg L^{-1} Pt) measured at individual ASL sites (2015-2017). The black and white circles indicate lakes corresponding with the H and L sub-populations, respectively. The line of best fit and corresponding regression equations with coefficient of determination are displayed for each ASL cohort.

Table 2.2 Summary comparison of H and L ASL cohorts (see Figure 2.3), displaying the cross-population median of recent (2015–2017) lake observations. The normalized median absolute deviation (NMAD; %) is displayed for each cohort, while significant ($\alpha < 0.05$) Mann–Whitney U test results (comparing H and L subpopulations) are indicated for each variable ("Yes" indicates significant difference).

	High (n = 186)		**Low (n = 74)**		
	Median	**NMAD**	**Median**	**NMAD**	**$\alpha < 0.05$**
DOC ($mg\ L^{-1}$)	18.5	32.4	26.3	21.9	Yes
DIC ($\mu eq\ L^{-1}$)	141.5	64.7	441.3	54.7	Yes
TC ($mg\ L^{-1}$ Pt)	134.7	65.9	60.8	64.5	Yes
pH	7.0	9.3	7.5	5.6	Yes
Gran Alkalinity ($\mu eq\ L^{-1}$)	197.2	65.7	586.2	57.4	Yes
Conductivity (µS/cm)	30.6	47.1	73.4	46.5	Yes
NH_4^+ ($\mu eq\ L^{-1}$)	0.4	50.0	0.4	25.0	-
Ca^{2+} ($\mu eq\ L^{-1}$)	219.6	49.6	503.0	44.8	Yes
Cl^- ($\mu eq\ L^{-1}$)	2.8	40.0	5.6	50.0	Yes
Mg^{2+} ($\mu eq\ L^{-1}$)	114.4	43.9	297.9	51.9	Yes
NO_3^- ($\mu eq\ L^{-1}$)	< 0.1	< 0.1	< 0.1	< 0.1	-
K^+ ($\mu eq\ L^{-1}$)	11.3	56.8	19.7	59.7	Yes
Na^+ ($\mu eq\ L^{-1}$)	50.0	60.0	84.4	66.0	Yes
SO_4^{2-} ($\mu eq\ L^{-1}$)	23.9	52.2	11.7	92.9	Yes
d-P ($\mu eq\ L^{-1}$)	1.1	62.3	0.8	25.1	-
Total P ($\mu eq\ L^{-1}$)	3.5	15.9	3.8	17.2	-
d-Al ($\mu g\ L^{-1}$)	54.1	140.9	10.9	12.8	Yes
Total Al ($\mu g\ L^{-1}$)	83.0	740.3	28.3	34.7	Yes
d-Cu ($\mu g\ L^{-1}$)	0.3	0.4	0.2	0.4	-
Total Cu ($\mu g\ L^{-1}$)	0.4	0.8	0.2	1.9	-
d-Fe ($\mu g\ L^{-1}$)	252.0	213.6	15.7	6.2	Yes
Total Fe ($\mu g\ L^{-1}$)	334.5	249.5	29.0	14.0	Yes
O_a ($\mu eq\ L^{-1}$)	141.6	30.8	243.7	28.6	Yes
O_aR (%)	17.8	42.3	14.6	35.2	Yes
Max depth (m)	1.9	6.9	1.5	1.9	-
Lake volume (m^3)	1277.0	76506.3	1292.0	2065.3	-
Lake area (km^2)	1.3	7.6	1.9	1.8	-
Catchment area (km^2)	16.0	35.6	8.5	19.3	-

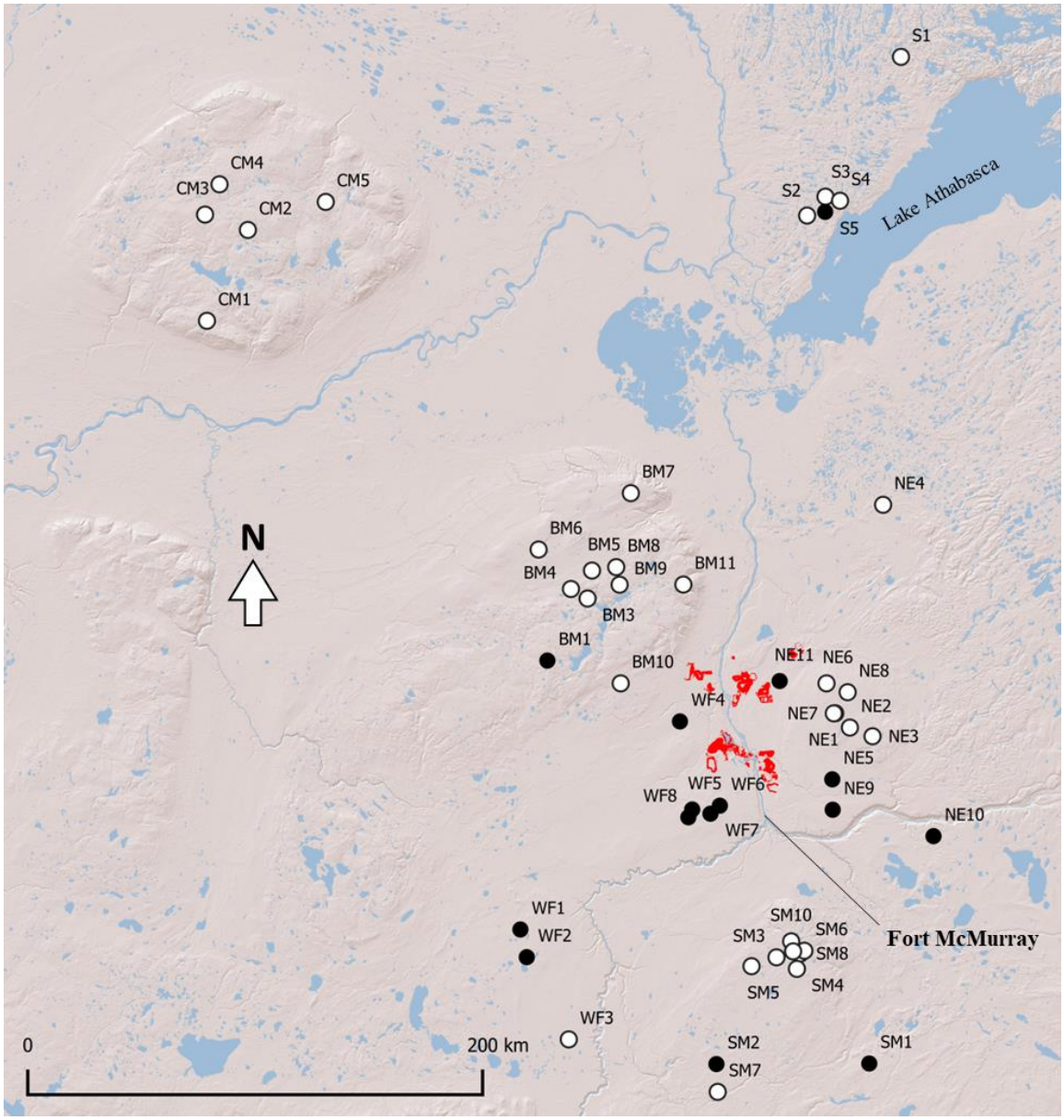

Figure 2.4 Reclassification of Acid Sensitive Lakes (n = 50) into "Low" (black; n = 15) and "High" (White; n = 35) true colour lake subpopulations, as displayed in Figure 2.3. Red outlined regions identify the boundaries of major oil sands facilities (ESRI 1995-2024).

The majority of variation within the complete ASL dataset (1999–2015) was explained by two principal components (PC), which combined represented 61.4% of total variance. The

first PC (explaining 34.1% variation) was characterized by positively correlated variables including: dissolved fractions of Fe, Al, V, PO_4^{3-}, and TC; possibly representing high colour surface waters associated with CDOC. PC2 (27.3%) consisted of positively correlated variables including: Ca^{2+}, Mg^{2+}, Na^{2+}, K^+, DIC, conductivity, alkalinity, and pH, which indicate well-buffered lakes with abundant groundwater and/or atmospheric alkaline inputs. A third PC (representing 5.9% total variance) was characterized by positively correlated total nitrogen (TN) and DOC. Two distinct data clusters consistent with the two subpopulations were observed within the PCA biplot (Figure 2.5), where the H and L clusters appeared consistent with PC1 and PC2, independently. Previous modelling work has suggested that atmospheric alkaline deposition is strongly dependent on distance, with most of the deposition of base cations occurring close to OS sources (Makar et al., 2018).

Bivariate comparison of log-transformed d-Fe and TC among TC–DOC subpopulations revealed a moderate correlation within the H cohort ($R^2 = 0.62$) only. Dissolved PO_4^{3-} was a comparatively weaker linear predictor of TC owing to high data scatter at high concentration (High $R^2 = 0.48$; Low $R^2 = 0.49$). Dissolved Fe and PO_4^{3-} fractions displayed stronger correlations with TC compared to their respective total concentrations. Both total and dissolved Cu displayed insignificant or weak correlations with DOC and TC.

Figure 2.5 Biplot of PC1 and PC2 from PCA of the complete ASL dataset, including all available water-quality variables. Datapoints have been categorized according to their H (red) and L (blue) lake subpopulation; the coloured ovals highlight these respective data clusters.

Total and d-Fe presented associations with few additional variables, including select trace metals, including V and Al. Irrespective of lake TC–DOC class, neither total nor d-Fe were significantly correlated with surface water pH (Figure A1 and A2). At low pH (~ 4.0–6.5, predominantly H lakes), a large portion of Fe (~ 60–90%) persisted as a dissolved fraction,

while at high pH ranges (~ 7.5–9.0, predominantly L lakes), d-Fe fell to a relative fraction ranging between 5–30%. Dissolved Fe fractions were highly variable near circumneutral lake pH levels, ranging between ~ 5 to 90 % of total Fe (Figure 2.6).

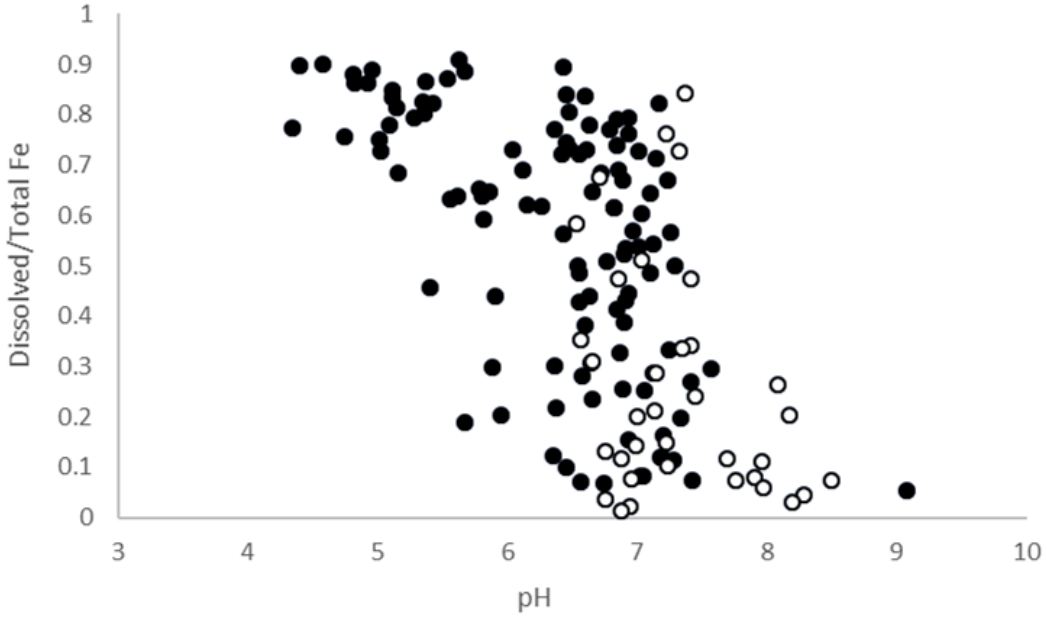

Figure 2.6 Annual-observed pH plotted against the relative fraction of d-Fe (%) at H (black points) and L (white points) ASL sites.

Annual estimated O_a presented a moderate positive correlation with DOC ($R^2 = 0.51$), with increased scattering at higher values. Estimated O_a presented relatively weak and/or insignificant correlations with the remaining water quality variables (Figure A1 and A2). However, O_aR presented a strong negative correlation with annual lake pH ($R^2 = 0.83$). Similar evaluation of the remaining measured ion species (including SO_4^{2-} and Cl^-) revealed comparatively weaker correlations with the aforementioned variables (Table A1).

Few significant correlations were observed between ASL physical and chemical variables; however, the deepest ASL sites (> 3 m) were predominantly circumneutral (Figure A3),

possibly owing to mineral-rich ground water inputs (and/or increased lake mixing) to deeper water bodies.

2.3.3 Atmospheric transport

Comparison of annual trajectory estimates with corresponding GEM-MACH deposition outputs revealed ASL sites that were assigned higher WPSCF values (1 – 0.7) experienced significantly higher ($\alpha < 0.05$) total S deposition relative to low WPSCF lakes (0.4 – 0.2) (Figure A4). The subregions NE, SM, and WF displayed the highest WPSCF values per lake (the majority receiving values 1.0–0.7), while the remaining regions were assigned comparatively lower weightings (Figure A5). Higher transport probability generally increased relative to lake proximity to the OS operation. The most predominant trends between transport probability and surface water variables were apparent within the separate H and L lake subpopulations. Among ASL sites within the H cohort, significantly ($\alpha < 0.05$) lower pH corresponded with greater WPSCF values – the inverse of which was observed for L lakes. This is consistent with differences in modelled deposition rates of anion source gases (SO_2, NO_x) and base cations emitted by OS sources (Makar et al., 2018).

Within the H subpopulation, O_aR fractions were significantly larger among lakes with high WPSCF scores, the opposite occurred for the L subpopulation (Figure 2.7). Among H lakes, the most prominent stepwise differences in pH and O_aR were observed between lakes with WPCSF scores of 0.7 and 0.4. Exclusion of ASL lakes with maximum depth > 3 m (to remove possible disproportionate influence of ground-water inputs / lake mixing) resulted in only minor deviations from the above trends.

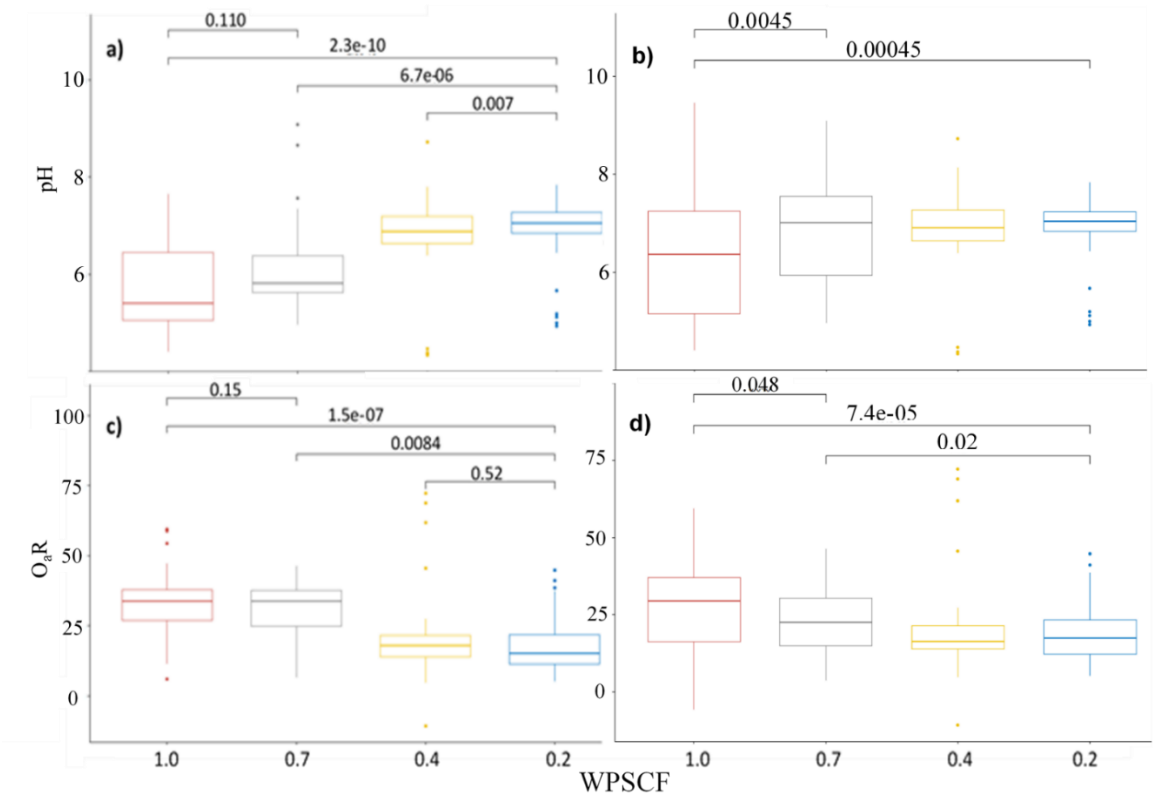

Figure 2.7 Boxplot comparing the distribution of annual pH and *OaR* in relation to lake WPSCF categories (1.0, 0.7, 0.4, and 0.2) among H lakes (a & c) and complete ASL dataset (b & d). Mann-Whitney U test p-values are presented for significantly different samples.

2.3.4 Long-term trend analysis

There were few significant long-term trends in DOC, O_a, and TC among the ASL sites (Table 2.3). The majority of lakes among the BM, CS, CM, and NE subregions presented significant – positive temporal trends in surface water alkalinity and pH. Anion species including SO_4^{2-}, Cl^-, NO_3^- presented a notable frequency of significantly decreasing trends (12-38% of total dataset), while DIC and anion sum displayed several positive trends. Select subregions presented an elevated frequency of significantly decreasing Cl^- and PO_4^{3-}

concentrations. The Birch Mountains were the only subregion which presented significantly increasing DOC. Positive long-term trends in pH (69%) and alkalinity (58%) were most prevalent among H lakes, while decreasing trends in DOC (29%), SO_4^{2-} (50%), and PO_4^{3-} (79%) were prominent among the L subgroup (Table A2). Among the H classified lakes, high WPSCF rated lakes (0.7-1.0) expressed a lower frequency of increasing pH trends (57% of lake subset) relative to low transport probability lakes (WPSCF 0.0-0.4) (81% of lake subset) (Table A2).

Table 2.3 Summary of Mann-Kendal monotonic trend analysis (1999–2017) for individual lakes within primary ASL subregions (see Figure 2.1). The number lakes presenting significant positive (+) and negative (–) Z test statistic values are presented for each variable and subregion. The total proportion (%) of lakes experiencing significant trends is displayed for each variable.

Region[a]	BM	CS	CM	NE	SM	WF	% - Significant
# of lakes	**11**	**5**	**5**	**11**	**10**	**8**	**N = 50**
TC (mg L^{-1} Pt)	+2		-1	-1			**8**
DOC (µmol L^{-1})	+1	-2		-2	-2	-1	**16**
DIC (µeq L^{-1})	+1	+1	+3	+2-1	-2	+2	**24**
O_a **(µeq L^{-1})**					-1	+1	**4**
O_aR	-3		-3	-2	-1	-1	**20**
SO_4^{2-} (µeq L^{-1})	-2		+2-1	-4	-4	+1-1	**30**
PO_4^{3-} (µeq L^{-1})		-1	-4	-3	-5	-5	**36**
NO_3^- (µeq L^{-1})	-1	-1	-1	-1	-1	-1	**12**
Cl^- (µeq L^{-1})	-4	-1	-2	+1-4	-7	-1	**40**
Ca^{2+} (µeq L^{-1})	+1		+3		+1-1	+2	**16**
Na^+ (µeq L^{-1})	+3		+1	+1-2	-1	+1	**18**
K^+ (µeq L^{-1})	+2	+1	+1	+2-1	-2	+1	**20**
Mg^{2+} (µeq L^{-1})	+1		+3	+3-1	-1	+3	**24**
Al^{3+} (µeq L^{-1})				+1	+1		**4**
Anion sum (µeq L^{-1})	+4	+3	+3	+2-1	+3-1	+4	**42**
Cation sum (µeq L^{-1})	+3-1		+3	+1-1	-2	+3	**28**
d-Fe (µg L^{-1})	+2		-1	+1	+1	+1	**12**
Alkalinity (µeq L^{-1})	+6	+5	+5	+8-1	+3	+2	**60**
pH (pH units)	+6	+5	+5	+8-1	+3	+5	**66**
Conductivity (µs/cm)	+2		-1	-1		+2	**12**

[a]BM – Birch Mountains; CS – Canadian Shield; CM – Caribou Mountains; NE – Northeast of Fort McMurray; SM – Stoney Mountains; WF – West of Fort McMurray.

2.4 Discussion

2.4.1 Evaluation of ASL surface-water characteristics

Metadata analysis of ~7,500 lakes from across the globe (Sobek et al., 2005) has previously reported a median DOC concentration of 5.7 mg L^{-1} while recent modelling efforts

predicted that global and North American lakes experience an average DOC of 3.8 mg L^{-1} and 3.3 mg L^{-1}, respectively (Toming et al., 2020). In contrast, average and median DOC concentrations among ASL sites during the 2015–2017 period was 20.8 and 22.0 mg L^{-1}, with a NMAD of 30%. Lakes with the highest DOC were generally located close to AR6 (relative to the remaining ASL sites). The observed spatial variability of lake DOC is likely the combined result of multiple environmental factors, including soil composition, lake physical characteristics, wetland inputs, and surrounding topography.

The weak linear correlation between surface water DOC and TC across the ASL dataset was inconsistent with the findings of previous studies (Molot et al., 1997). However, the significant correlations observed within separate H and L subpopulations suggested these lakes possessed unique chomophoric properties. It was uncertain what mechanisms were responsible for this divergence, and/or whether these lakes possessed CDOC of unique quality and source. Considering the majority of ASL geographical subregions contained a mixture of H and L classified lakes, the regional groupings were not representative of the two chromophoric populations. Subsequent evaluation via Mann-Whitney U test and PCA revealed distinct characteristics unique to each of the two ASL cohorts. Namely, H-lakes appeared to experience significantly higher levels of TC, d-Fe, PO_4^{3-}, V, and Al (Table 2.2). Many of these variables are known to be associated with CDOC complexation in boreal lakes (Maloney et al., 2005; Weyhenmeyer et al., 2014).

The significant correlation observed between d-Fe and TC (among H-lakes) was similar to previous studies, which found Fe-DOC complexation exaggerated the absorptive properties of organic matter within boreal lakes (Maloney et al., 2005; Weyhenmeyer et al., 2014). Iron exhibits an affinity to bind with organic matter owing to its high valence, and often

outcompetes other potential binding species (i.e., Al, Cu, and Mn) (Maloney et al., 2005).[10] Competitive Fe-DOC complexation may explain the limited associations between DOC and other metal species throughout the ASL dataset. The lack of significant d-Fe-TC correlation among L lakes suggested that similar processes of complexation was limited.

The observed relationship between the relative fraction of d-Fe (%) and lake pH suggested that surface water acidity impacted d-Fe-availability and subsequently Fe-DOC complexation. The oxidation state of Fe in natural waters is influenced in-part by pH, where Fe^{2+} to Fe^{3+} oxidation rates increase with rising pH (Ilbert and Bonnefoy, 2013). Compared to its reduced state, Fe^{3+} is highly insoluble in water, and often precipitates out of solution as an inorganic or organic complex (Nierop et al., 2002). The larger relative fraction of insoluble Fe among L lakes with elevated pH (Figure 2.6) may represent a higher abundance of Fe^{3+}, where rapid complexation and subsequent flocculation may explain the low concentrations of total Fe among these lakes. Lake pH was likely not the sole factor influencing d-Fe availability, as indicated by the high variability of d-Fe fractions among circumneutral lakes. The availability and composition of Fe-enriched soils, bedrock, and groundwater may play a role in determining the availability of Fe within lake systems.

As highlighted above, lake pH appeared to play a substantial role in defining the chromophoric properties of H and L classified lakes. Furthermore, it was suspected that local environmental factors have a large influence over lake acid-base chemistry. The McMurray and Waterways formations are associated with carbonate-rich ground water that encompasses a region largely populated by L lakes (Cooke et al., 2017; Cowie et al., 2015); given such a correspondence, these sources are likely first-order determinants of H and L classification. Many sites within the L subpopulation were in near-field regions (< 50 km

from AR6) known to receive S and nitrogen (N) deposition, in addition to elevated base cation (BC) inputs linked to short-range dust emissions from OS operations (Edgerton et al., 2020; Makar et al., 2018). Disproportionately alkaline deposition (associated with BC-rich particulate matter [PM]) could further compound the influence of enriched ground-water inputs to L classified lakes (Cowie et al., 2015; Watmough et al., 2014). In contrast, the magnitude of BC deposition was likely too low to notably influence the chemistry of H lakes, which do not receive the enriched groundwater of the McMurray and Waterways formations.

Estimated O_aR increased relative to declining pH among ASL sites, which suggest an association between organic matter and acid/base chemistry. Extensive wetlands and organic-rich soils contribute to the large DOC pool within lake systems throughout the AOSR, while an unknown mass of petrogenic organic carbon enters these systems via atmospheric deposition. Is it possible the combined acidity of these organic inputs could place further stress onto poorly buffered lakes simultaneously pressured by inorganic acid inputs. However, it is important to emphasize that the correlation between O_aR and pH also corresponded with increasing ion concentrations – which would systematically lower the O_aR fraction.

It should be established that these newly defined ASL subpopulations were categorized based on a visual analysis of surface-water DOC and TC. However, the multiple water-quality variables found to be significantly different between subpopulations supports the division of these lake types (Table 2). The analysis conducted in this study has strongly indicated that lakes within the ASL dataset do not present uniform associations between

DOC and TC, which may be an indicator of broader chemical processes partially dependent upon carbonate ground-water inputs.

2.4.2 WPSCF and lake pH trend analysis

The tentative agreement between WPSCF and GEM-MACH estimates suggested that trajectory analysis serves as a general surrogate for atmospheric deposition. Low pH among H lakes with higher transport probability suggested a potential linkage between OS emissions and lake acid status. Owing to their lower relative buffering capacity (Table 2.2), H lakes may be more susceptible to acidic deposition sourced from OS operations. However, it is critical to consider the influence heterogeneous soil and bedrock composition imposes over lake acidity, as these environmental factors could explain the co-variation observed between surface-water pH and WPSCF.

As previously established, much of the bedrock material underlying far-field lakes (CM, CS, BM) in the study region are carbonate poor, while near-field bedrock formations (NE, WF, SM) are variably calcareous (Fulton, 1996; Prior et al., 2013). In an extensive regional survey prepared by Palmer and Trew (1987), numerous geological datasets detailing Albertan soil and bedrock composition were compiled to map the potential for surface materials to reduce incoming acidic atmospheric deposition. Geology throughout CM, CS, and parts of BM presented the lowest potential to reduce inputs, regions largely encompassing the NE and SM lakes displayed medium capacity, while land surrounding the WF lake subregion presented the highest acid reduction potential (likely owing to the carbonate-rich groundwaters associated with the McMurray formation [Cowie et al., 2015]). Based on the above-mentioned factors, it would be assumed that lake regions

nearest to the OS are more suited to suppress acid inputs compared to far-field regions. These assumptions are largely incompatible with the inverse association observed between lake pH and WPSCF among H classified lakes. Organic-rich Mesisols are prevalent throughout the NE and SM subregions, especially in comparison to the remaining ASL regions. Mesisols are variably acidic, however there was no consistent difference when comparing the pH of H-classified lakes located within and outside of Mesisol-dominated catchments in the NE and SM regions (Agriculture and agri-food Canada, 2005). A negative association between H-lake pH and WPSCF was still apparent following the exclusion of Mesisol-encompassed ASL sites. Furthermore, the prevalence of poor (acidic) fens and bogs among further-field lake regions (excluding SM) de-emphasizes the potential influence wetlands may have over the observed pH trends. In summation, the variation of regional geology and wetland composition (among H-lakes) does not fully explain the negative relationship between pH and WPSCF.

The observed trends among H lakes contrast the findings of previous studies in the AOSR, which found little evidence to indicate OS emissions contributed to lake acidification (Curtis et al., 2010; Hazewinkel et al., 2008; Laird et al., 2013). Considering these previous studies did not independently evaluate the two subpopulations identified in the current investigation, the mixture of H and L lakes throughout the AOSR may have confounded the apparent associations between pH and OS emission transport. Future studies should consider these unique subsets of lakes (high, low), as there are likely unknown lake-specific factors (permafrost and wetland inputs, DOC composition) that may further explain the observed spatial trends throughout the region.

2.4.3 Monotonic trends

During the observed period, 64% and 58% of ASL sites presented significance increases in surface water pH and alkalinity (respectively), decreasing SO_4^{2-}, Cl^-, and NO_3^- (24%, 38%, and 12% of ASL sites, respectively) may further indicate that select lakes are responding to declining atmospheric deposition due to regional/local emission reductions. However, the lower-relative frequency of SO_4^{2-} trends cannot fully explain the observed increase in pH/alkalinity. In their 2020 study, Gibson et al. (2020) indicated that long-term climactic warming (further escalated by climate change) has resulted in gradual permafrost thaw throughout the AOSR, which has increased the water-yields of lakes primarily located within the CM, BM, and NE subregions. Higher water-yields may influence lake chemistry and could further explain increasing pH trends among select lakes. Low-classified lakes presented a reduced frequency of increasing pH and alkalinity trends relative to the H subpopulation, possibly owing to the elevated alkalinity within L lakes (Table 2.2) – which could resist shifting acid/base chemistry. The lower relative frequency of increasing surface-water pH among high WPSCF (0.7-1.0) H-lakes may suggest that on a localized level, OS emissions and deposition can disrupt the broader temporal trends observed throughout the study region.

Lake DOC remained largely unchanged (16% significant trends) throughout the study period, an observation contrary to the widely reported inverse correlation between declining S deposition and increasing lake DOC concentrations (Erlandsson et al., 2010; Monteith et al., 2007; Oni et al., 2013). Declining trends in surface water PO_4^{3-}, as observed among 36% of ASL sites, has been similarly identified among boreal lakes across northern Europe and Canada (Huser et al., 2018).

2.5.0 Conclusions and potential sensitivity of lakes to atmospheric inputs

Comparison of DOC and TC revealed two distinct lake populations in the AOSR, which represented the variation of surface-water absorptive properties more effectively than the previous geographical subregion classification. These newly defined populations may provide a novel perspective to evaluate AOSR surface-water chemistry in future studies. The differing optical properties between H and L lakes were partially characterized by d-Fe, which in its complexed-state can alter lake TC. Dissolved Fe availability was dependent upon surface-water pH, which may be influenced by the carbonate-rich groundwaters associated with the McMurray and Waterways formations (as observed throughout the WF subregion). Future studies should consider the geochemical influence of these inputs when evaluating the variability of lake acid/base chemistry and DOC throughout the AOSR.

Initial WPSCF analysis revealed that H-lakes with a higher probability of receiving OS polluted air-masses experienced significantly lower pH compared with distant sites. The observed chemistry among H-lakes contrasted previous regional studies, which found little indication that OS-sourced deposition contributed to lake acidification. Given these findings, there may be reason to reevaluate the previously assumed influence of OS emissions over lake chemistry in the AOSR; this is made more apparent in the wake of recent studies that have raised suspicious regarding OS-sourced organic acid deposition.

3. Chapter Three: Chromophoric dissolved organic matter in the Athabasca Oil Sands Region, Canada, and its association to lake acid sensitivity[2]

3.1 Introduction

In aquatic environments, chromophoric dissolved organic matter (CDOM) represents a broad class of complex organic compounds that absorb light in the visible and ultraviolet (UV) wavelength range (Del Vecchio & Blough, 2004). The CDOM fraction plays a critical role in the transport of nutrient and metal species, acts as a medium for biological activity, and directly influences solar radiation budgets (Dodds & Whiles, 2010; Fisher & Likens, 1973). Chromophoric DOM may be introduced from sources located outside (allochthonous) or within (autochthonous) aqueous systems (Thurman, 1985). Organic matter originating from allochthonous / terrestrial sources are typically large, highly aromatic molecules often classified as humic substances (HS), which broadly consist of humic (HA) and fulvic acids (FA) (Coble, 2007). Organic matter originating from in-lake materials and processes (i.e., biological metabolism) are often smaller, less aromatic species such as amino acids (Zhang et al., 2011).

The composition of CDOM within an aquatic system is dependent upon numerous factors, noting that allochthonous / autochthonous source characteristics (i.e., catchment landscape composition, resident macrophytes) dictate the organic matter initially introduced to a system (Huang et al., 2022; Olefeldt et al., 2013). Biological and photochemical processes fundamentally alter CDOM quality within natural waters through degradation,

[2] The contents of Chapter 3 were submitted for review by Science of the Total Environment in 2025. Manuscript number: STOTEN-D-25-04319

mineralization, and sedimentation processes (Olefeldt et al., 2013). Hydrological conditions, such as catchment runoff and residence times, play a key role in organic matter transport and in-situ processing within lake waters (Kellerman et al., 2014; Kothawala et al., 2013). Metal species such as iron (Fe) can readily form organo-metallic complexes with DOM, a process which often influences the optical properties of CDOM (Maloney et al., 2005).

Acid-base chemistry can influence CDOM quality within aquatic systems. For instance, pH-sensitive autochthonous processes can alter the in-situ production and removal of CDOM within surface-waters (Anesio & Granéli, 2003; Dillon & Molot, 1997; Gu et al., 2017), catchment acidification can inhibit organic matter flux to aqueous systems (Schindler, 1998), and DOM - metal interactions are often influenced by pH (Schindler et al., 1992). Conversely, chromophoric humic and fulvic acids can impact lake acid-base chemistry owing to their abundance of acid functional groups (Oliver et al., 1983). Depending on the strength and density of functional groups, organic acids can both increase or decrease surface-water pH and acid neutralizing capacity (Castrillon-Munoz et al., 2022; Driscoll et al., 1994; Munson & Gherini, 1993).

The Athabasca Oil Sands Region (AOSR) in northeastern Alberta, Canada, contain a high number of DOM-rich (Agriculture and Agri-Food Canada, 2005; Gibson et al., 2019) and potentially acid-sensitive boreal lakes (Cathcart et al., 2016). In Chapter 2, the reanalysis of 50 AOSR lakes with nearly 20 years of observations (1999–2017; Acid Sensitive Lake [ASL] network, www.ramp-alberta.org) (Blanchard et al., 2021) identified two distinct lake populations, including a cohort (titled High, or “H”; n = 35) characterized by high relative true colour (TC), dissolved Fe, and comparatively low dissolved organic carbon (DOC),

pH, and alkalinity, while a smaller (titled Low, or "L"; n = 15) lake population displayed the inverse properties. The authors postulated that the H population contained elevated concentrations of CDOM and Fe – CDOM complexes, the presence of which could explain the high surface-water colour. As far as the authors are aware no previous studies have detailed the quality of CDOM within lake surface-waters in the AOSR, and consequently, the sources and environmental processes influencing this organic matter fraction are unknown.

Oil sands (OS) industrial operations in the AOSR are a major emission source of sulphur dioxide and oxidized nitrogen species which pose the potential to acidify surrounding surface-waters via atmospheric deposition (Cathcart et al., 2016). Analysis in Chapter 2 reported that H classified lakes, which were most likely to receive OS emissions, displayed significantly lower surface-water pH and alkalinity, potentially indicating CDOM-rich lakes were sensitive to industrial acid inputs (Blanchard et al., 2021). However, long-term monitoring (2002–2017) suggested that many lakes throughout the AOSR have experienced monotonic increases in pH, possibly because of bicarbonate inputs from elevated permafrost thaw (Gibson et al., 2019; Gibson et al., 2020). Either lake acidification or recovery could affect the environmental processes linked to CDOM quality and abundance (Anesio & Granéli, 2003; Dillon & Molot, 1997; Gu et al., 2017; Schindler, 1998; Schindler et al., 1992) which could lead to cascading ecological impacts as a result of shifting primary productivity and nutrient cycling (Dodds & Whiles, 2010; Fisher & Likens, 1973; Rautio et al., 2011; Sweetman et al., 2010).

The objective of this study was to evaluate CDOM quality within ASL surface-waters and to identify the environmental sources. In addition, this study evaluated the potential link

between CDOM and acid-base chemistry within the AOSR. Ultraviolet – visible (UV-Vis) light spectroscopy and excitation emission matrix (EEM) fluorescence spectroscopy, paired with Parallel Factor Analysis (PARAFAC) modelling techniques were applied to characterize CDOM within ASL surface-water samples collected during August 2021. To identify the prominent sources and processes influencing CDOM variability, multivariate analysis of optical and supplementary water quality, hydrological, and morphometric variables was employed. These novel observations were intended to improve our understanding of DOM and CDOM cycling among regional lakes, which is critical given the shifting hydrological and water quality conditions throughout the AOSR (Gibson et al., 2019).

3.2 Methods

3.2.1 Study region

The ASL sites (n = 50) are dispersed throughout the Wood Buffalo municipality in northeastern Alberta, Canada (Figure 3.1). The lakes are categorized by their geographical subregion, including Northeast of Fort McMurray (NE; n = 11), West of Fort McMurray (WF; n = 8), Birch Mountains (BM; n = 11), Canadian Shield (CS; n = 5), Caribou Mountains (CM; n = 5), and Stony Mountains (SM; n = 10). Bedrock geology is heterogeneous throughout the area; dominant formations underlying the SM and NE subregions contain shales and sandstones with variable moderate calcareous content (Prior et al., 2013). Bedrock underlying the BM region consists of a mixture of non-to variably calcareous mudstone and shale layers. The Cretaceous and Paleogene formations in the CM region consist of sandstone, mudstone, shale, and upland gravel, while the bedrock above Lake Athabasca (CS region) is dominated by exposed granite (Prior et al., 2013). Located

beneath the WF subregion are the highly bituminous and calcareous McMurray and Waterways formations known to be associated with carbonate-rich groundwaters. Surface materials throughout the region are primarily comprised of tills, and till veneers, while soils are classified as organics (primarily mesisols), luvisols, brunisols, and cryosols (Agriculture and Agri-Food Canada, 2005; Fulton, 1996). Approximately 54% of total land cover in the AOSR consists of wetlands, which are dominated by fens and bogs (AEP, 2018; ESRD, 2015; Sweetman et al., 2010).

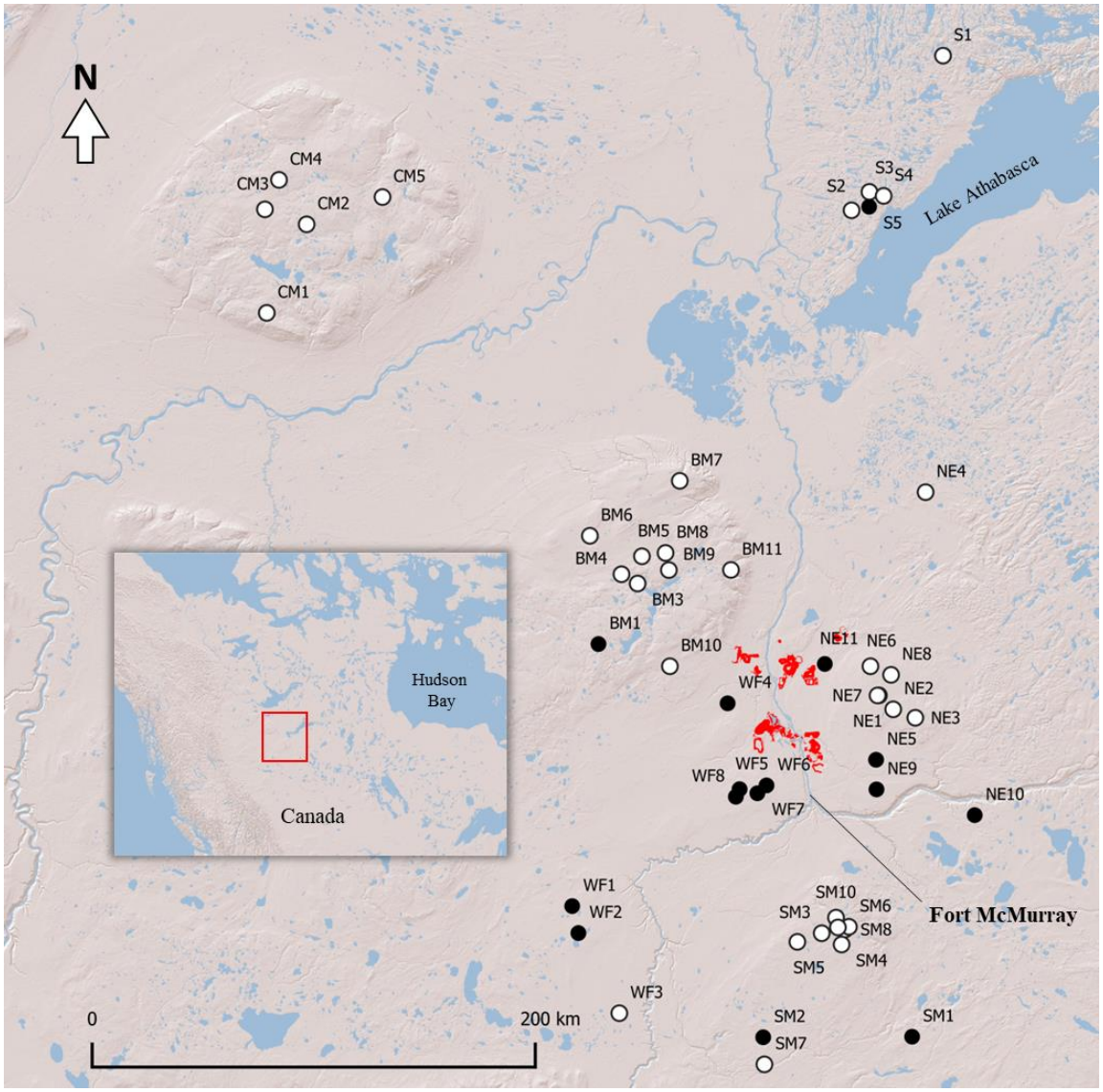

Figure 3.1 Overview of the Athabasca Oil Sands Region (ASOR) study area and Acid Sensitive Lakes network (n = 50); black and white circles represent "Low" (L; n = 15) and "High" (H; n = 35) true colour lake subpopulations, respectively, as identified in Chapter 2. Inset map displays the broader geographical location of the AOSR study area, while the red outlined regions identify the boundaries of major oil sands facilities (ESRI 1995-2024).

3.2.2 Surface-water sampling and analysis

Lake water quality samples were collected via float plane and helicopter over a five-day period in August 2021; water chemistry from the survey are publicly available through the joint Oil Sands Monitoring Program (Data portal: https://osmdataportal.alberta.ca/applications/public.html?publicuser=Guest#waterdata/stationoverview). At the approximate center of each lake, a multiprobe instrument (YSI EXO) was used to measure several physical parameters down the water column (pH, dissolved oxygen [DO], redox potential, turbidity, and temperature [temp]) and a Secchi disk was deployed to estimate euphotic zone depth. Integrated water samples were taken from multiple euphotic zone depths within each lake using a Tygon sampling tube equipped with a one-way valve (Emmerton et al., 2018). Lake water from the vertical profile was decanted into an acid-washed (HCl) plastic carboy and mixed, the subsequent bulk sample was then poured into individual acid-washed bottles and shipped to Bureau Veritas Labs (Calgary, Alberta) for a wide range of biogeochemical analysis including cations, anions, total alkalinity (Alk-T), dissolved inorganic carbon (DIC), total organic carbon (TOC), dissolved organic carbon (DOC), dissolved Kjeldahl nitrogen (DKN), ammonia, ammonium, total phosphorous (TP), total dissolved phosphorous (TDP), chlorophyll-a (chl-a), and TC (Table B1). Dissolved organic nitrogen (DON) was additionally calculated by subtracting ammonia and ammonium from DKN (mgN L^{-1}). The molecular ratio of DOC:DON was included in this analysis, as previous studies have used the metric to evaluate the sources and processes altering the composition of aquatic DOM (Evans et al., 2024).

Additional sample aliquots (preserved in 1% nitric acid) were sent to InnoTech Alberta (ISO/IEC 17025:2017 accredited laboratory), where they were microwave digested in Teflon vessels and analyzed for total iron (Fe), aluminum (Al), zinc (Zn), nickel (Ni), and copper (Cu) by inductively coupled mass spectrometry (using either a Perkin Elmer NexION 300D or Agilent 8900 ICP-QQQ) following InnoTech's "AC-038" laboratory method, which is based on the EPA method 200.8 (USEPA, 1994). A separate set of non-digested lake samples were filtered (0.45 μm) and submitted for analysis of dissolved elements (denoted by the prefix, "d"). The elements listed above were chosen for this study as many can readily form metal-DOM complexes within freshwater environments and are associated with OS industrial activities (Luider et al., 2003; Mantoura et al., 1978; Paul & Skrzypek, 2006). Refer to Appendix section B1 for elemental analysis QA/QC results.

Sample aliquots were shipped to InnoTech for the determination of hydrogen-2 (^{2}H) and oxygen-18 (^{18}O) stable isotope abundance via a Delta V Thermo Fisher Scientific Isotope Ratio Mass Spectrometer interfaced with a Gasbench peripheral, following the laboratory methods described by Paul and Skrzypek (2006). Stable isotope results were reported in delta (δ) notation in permil (‰) relative to Vienna Standard Mean Ocean Water (V-SMOW). Hydrogen-2 and oxygen-18 isotope abundances have been used to provide insight to lake hydrology as various environmental sources (i.e., precipitation, groundwater) and fractionation processes (i.e., evaporative loss) uniquely influence isotopic composition (Olefeldt et al., 2013). The isotope abundance variables displayed a very strong positive correlation ($R_S = 0.97$), so only ^{18}O was included in the ASL dataset to avoid redundancy.

An aliquot of the bulk sample from each lake was decanted into a 250 ml amber glass bottle (zero headspace) and shipped to Trent University, ON, for optical analysis. Prior to sampling, each amber glass bottle was thoroughly washed in a hydrochloric acid (HCl) bath for 24 h, after which they were rinsed in ultra-pure water (Milli-Q), combusted at 550 °C for 6 h, and rinsed again in ultra-pure water (Chen et al., 2018). A total of five field blank samples (prewashed amber glass bottles filled with Milli-Q) and five duplicate samples were included in the field campaign.

3.2.3 UV-Vis and fluorescence spectroscopy

Surface-water absorbance was measured along a range of wavelengths (λ) between 200 to 800 nm (1 nm intervals) using a Cary 100 UV-Vis spectrophotometer from Agilent Technologies. Lake samples were allowed to warm to room temperature (~ 21°C), filtered through a 0.45 µm nylon membrane, then placed in a 1 cm (3.5 ml) Hellma® Suprasil® quartz cuvette (Hellma 101-QS) for analysis. A blank sample of Milli-Q water was first used to establish an instrument baseline, after which blanks were measured as every fifth sample. To clean, cuvettes were soaked in a 2 M HCl bath for ten minutes followed by subsequent rinses in Milli-Q water, 95% ethyl alcohol, and a final rinse in Milli-Q.

Select optical metrics were derived from the UV-Vis scans (Table 3.1), including the absorbance coefficient at 254 nm (a_{254}; m^{-1}) and specific UV absorbance at 254 nm ($SUVA_{254}$). The a_{254} coeffecient is generally used as a proxy for DOM abundance within aquatic systems (Brandstetter et al., 1996), and is further calculated as:

$$a_{254} = 2.303 \frac{A(254\ nm)}{l} \qquad \textbf{Eq. 3.1)}$$

Where A is the raw absorbance (unitless) measured by the UV-Vis spectrophotometer at 254 nm and l is the path length (m) (Green & Blough 1994). Moreover, the $SUVA_{254}$ (L mg m^{-1}) metric was calculated as:

$$SUVA_{254}\left(\frac{L}{mg\ m^{-1}}\right) = \frac{A_{254}(m^{-1})}{DOC\ (\frac{mg}{L})} \quad \textbf{Eq. 3.2)}$$

Where A_{254} is the absorbance at 254 nm (m^{-1}), and DOC (mg L^{-1}) is measured within the corresponding sample (Weishaar et al., 2003). Typically, $SUVA_{254}$ values range between 1.0 to 6.0 (L mg^{-1} m^{-1}) within surface-water environments, where larger values reflect increasingly aromatic DOM (Brezonik et al., 2019; Weishaar et al., 2003).

Fluorescence spectroscopy is a widely practiced method in the field of CDOM analysis owing to its rapid and cost-effective operation, high sensitivity, and broad chemical selectivity (Bro 1997; Coble, 1996). Fluorescence analyses were conducted using a Cary Eclipse spectrophotometer set to three-dimensional EEM and signal to reference (S/R) acquisition modes (Kothawala et al., 2013). To avoid fluorescence spectrum skewing due to variable pH and the inner-filter effect (IFE), lake samples were diluted 1:10 in a phosphate buffer solution (pH ~ 6.5) to achieve an absorbance < 0.05 at 270 nm (Frysinger et al., 2003; Lakowicz, 2006). A second set of samples for were diluted (1:10) in Milli-Q water to maintain closer-to-native pH. Diluted lake samples were allowed to warm to room temperature (~ 21°C), filtered through a 0.45 µm nylon membrane, and subsequently placed in a 1 cm (3.5 ml) Hellma® Suprasil® quartz cuvette (Hellma 101-QS) for analysis. Excitation and emission scans (both measured at 5 nm intervals) ranged from 200–450 nm and 250–600 nm, respectively. An ultrapure blank was first measured to zero the fluorometer, then subsequent blanks were scanned as every fifth sample. During each day

of analysis, a set of quinine sulphate standards were prepared to create a calibration curve (1–100 ppb quinine sulphate in 0.5 M sulphuric acid) to convert fluorescence intensity measurements into quinine sulphate units (QSU) (Ferretto et al., 2014; Sui et al., 2017).

Post-processing and analysis were conducted with the R analytical package "staRdom" for EEM correction and PARAFAC modelling (Pucher et al., 2021). Surface-water EEMs received IFE corrections, while Rayleigh and Raman light scattering bands were removed from each scan. The lake dataset displayed limited fluorescence within the 540–600 λ_{Em} and 400–450 λ_{Ex} wavelength ranges, thus these regions were removed prior to PARAFAC modeling. The R package was further employed to determine additional fluorescence metrics including the humification (HIX), fluorescence (FI), and biological (BIX) indices (Table 3.1) (Coble, 1996; Hansen et al., 2016). The humification index is often employed as an indicator of DOM humic content, where high values represent increasing humification (Ohno, 2002). The biological index is representative of aquatic autotrophic productivity, and values > 1 indicate that the majority of CDOM originates from in-situ biological processes (Huguet et al., 2009). The fluorescence index is commonly employed to assess DOM source, where a high FI value (~1.8) is often associated with DOM derived from microbial processes, while a low value (~1.2) often indicates a terrestrial source (Cory & McKnight, 2005; Wilson & Xenopoulos, 2009).

Table 3.1 Description and interpretation of key optical metrics (along with corresponding references) used in the current study.

Metric	Method	Interpretation	Reference
a_{254}	Absorbance at 254 nm, normalized by pathlength	Proxy for DOC in aquatic environments	Brandstetter et al., 1996
$SUVA_{254}$	Absorbance coefficient at 254 divided by DOC (mgC L^{-1})	Positive association with DOM aromatic content	Weishaar et al., 2003
BIX	Ratio of fluorescence intensity at λ_{Ex}: 310, λ_{Em}: 380 and λ_{Ex}: 310, λ_{Em}: 430	High values correspond to DOM originating from autochthonous (autotrophic) sources	Huguet et al., 2009
HIX	Area under the 435–480 nm λ_{Em} spectra divided by the 300–345 + 435–480 nm λ_{Em} spectra (measured at λ_{Ex}: 254 nm)	High values indicate greater degree of humic content within DOM pool	Ohno, 2002
FI	Ratio of fluorescence intensity at λ_{Ex}: 370, λ_{Em}: 470 and λ_{Ex}: 370, λ_{Em}: 520	Indicates the relative contribution of terrestrial and microbial sources to DOM	Cory & McKnight, 2005; Wilson & Xenopoulos, 2009

* λ_{Ex} = excitation wavelength (nm); λ_{Em} = emission wavelength (nm)

3.2.4 PARAFAC Modelling

Combined EEM and PARAFAC analysis is commonly used to evaluate the optical and structural characteristics of environmental CDOM, as the modelling technique can identify the excitation and emission peaks of multiple spectrally distinct fluorophores (i.e., HULIS, PRLIS) within EEM scans (Bro, 1997). Here, the staRdom package was used to generate a PARAFAC model, which decomposed the data array of compiled EEM samples (x_{ijk}; consisting of the buffered and non-buffered ASL sample sets, separately) into a score matrix (**A**) and two loadings' matrices (**B** and **C**) with corresponding tri-linear elements a_{if}, b_{if}, and c_{kf} (Bro, 1997):

$$x_{ijk} = \sum_{f=1}^{F} a_{if} b_{jf} c_{kf} + e_{ijk} \quad \textbf{Eq. 3.3)}$$

Where x_{ijk} represented fluorescent data of the i^{th} sample, j^{th} emission, and k^{th} excitation wavelengths. Score values in a_{if} represented the relative fluorescence intensity of fluorophore f in sample i, the elements b_{if} and c_{kf} represented the modelled emission (j) and excitation (k) loadings (i.e., wavelength coordinates) of f, while F is the total number of modelled fluorophores. Utilizing the residual element e_{ijk}, the PARAFAC model applied an alternating least-squares optimization technique to find the function that best approximated the dataset (Bro, 1997; Murphy et al., 2014).

The appropriate number of modelled fluorescent components (also referred to as model rank) was selected based on four validation tools, including: 1) visual peak inspection, 2) EEM residual plots, 3) split-half analysis, and 4) core consistency (CC). Visual inspection provides an initial check to confirm the modelled components present well-defined emission peaks, which suggests that the spectra represent a distinct fluorophore or a group of similarly fluorescing species. The model residuals corresponding to each sample (e_{ijk}) can be plotted as a function of λ_{Ex} and λ_{Em}. These plots can be visually inspected to identify potential peaks, where a high abundance of such features across the dataset would indicate that the model rank is not representative of the array (Driskill et al., 2018; Murphy et al., 2014). Split-half analysis involved division of the EEM dataset into a set of four equal-sized groups, where independent PARAFAC models were generated for each subgroup and the resulting fluorescent components compared to measure spectral similarity via Tucker Congruence Coefficient (TCC) (Pucher et al., 2019). A high TCC similarity score (~ 1) suggested the model was representative of the true variation within the fluorescence dataset. The model rank that produced the highest TCC score was most likely the appropriate selection (Bro, 1997; Stedmon et al., 2003). Core consistency is a measure of the regression

between the three-way array of the PARAFAC model and the core array of a Tucker3 model generated from the corresponding EEM data. A CC score between 90% to 100% indicated a strong model, while values ≤ 50% suggested a problematic output. Generally, the largest model rank preceding an abrupt decline in CC should be selected (Bro and Kiers, 2003).

The fluorescent components generated from the lake dataset were compared against similar PARAFAC models published in the online database OpenFluor to assist with fluorophore characterization (Murphy et al., 2014). Model components with high similarity scores (> 0.95) along both excitation and emission spectrum were selected for further evaluation. Individual components within each sample were reported as maximum fluorescence emission intensity (F_{MAX}; QSU) and relative fluorescence (single component divided by the total sum of components; %C). Previous studies have utilized fluorescence ratios (C_x:C_y) to evaluate the relative concentrations of specific PARAFAC components of interest, where subsequent comparison to environmental data can provide useful insights to CDOM processing within aquatic systems (Huang et al., 2022). As such, fluorescent ratios comparing modelled components were included in the current study.

3.2.5 Geophysical variables

Lake and catchment physical / hydrological properties, including lake elevation (meters above sea level), lake volume (m^3) lake depth (m), lake surface area (m^2), drainage basin area (DBA; m^2), lake catchment wetland coverage (%bog, %fen; % of catchment area), and permafrost coverage (% of catchment area) were taken from Gibson et al. (2020; 2015). Average evaporation to lake inflow ratios (E:I) and water yield (WY; mm) values,

estimated via isotopic mass balance model between 2002–2017 were further obtained from Gibson et al. (2020). The ratios of lake surface area:DBA and DBA:lake volume were included in the analysis to further assess variability in lake catchment characteristics.

A lichen biomonitoring study by Landis et al. (2019) identified 19 emission sources (i.e., upgrader facilities, active mines, petroleum coke stockpiles) that likely contributed to pollutant deposition throughout the AOSR (source names and coordinates are listed in Supporting Information Table B4). The linear distance between each ASL site and the nearest OS source (km) was additionally included to identify potential links between OS emissions and lake CDOM.

3.2.6 Data analysis

Blank samples were used to determine method detection limits (MDL), which were calculated as: standard deviation [n samples] × t-value 99.0% confidence critical value (3.747). Data variability was assessed by calculating the RPD (%) from the duplicate samples. Lake water-quality and catchment physical variables displayed a non-normal distribution as determined via a Shapiro-Wilk test ($\alpha < 0.05$); thus, non-parametric statistical tests were employed for subsequent analysis. Median values were used as a measure of central tendency and environmental variability was evaluated using normalized median absolute deviation (NMAD). Spearman's Rank Order correlation tests were applied to assess bivariate associations between ASL environmental variables, and the Kruskal-Wallis test was used to determine significant differences between H and L lake groups. To maintain continuity with the historical data, the ASL sites from 2023 were labelled as either members of the H or L lake subpopulation based on their classification in Chapter 2.

To identify underlying trends within the dataset, principal component analysis (PCA) was employed for initial evaluation. To further identify key variables that explained the sources and environmental processes influencing CDOM in the study lakes, partial least squares regression (PLS-R) analysis was applied following Kothawala et al. (2013; 2014). The PLS-R technique attempts to relate predictor (X) and response (Y) variable matrices by decomposing each into a smaller set of orthogonal principal components (PC) and subsequently regressing PC scores (X vs. Y) via a least-squares method (Eriksson et al., 2013; Wold et al., 2001). Modelled PARAFAC components (F_{MAX}) were assigned as Y variables while physical, biological, and chemical lake (and lake catchment) variables were designated as X. Relative fluorescence (%C) values of PARAFAC components were assigned as the Y variables in a separate PLS-R model, while surface-water pH and alkalinity were assigned as predictors in a third model. The appropriate number of components for each model was determined via internal cross-validation, where a random subset of lake samples (~ 10% of dataset) was removed from the training dataset to evaluate the regression model. The resulting comparisons were evaluated based on cumulative goodness of fit (explained Y variation; R^2Y) and cumulative goodness of prediction (Q^2), where values approaching 1 indicated a stronger model. The relative influence of X variables over the model was interpreted using variable influence on projection scores (VIP), where values ≥ 1 and < 0.8 signified highly and less influential predictor variables, respectively (Eriksson et al., 2013). The spatial proximity of plotted variables served as a visual indicator of X and Y associations, while variable distance from the origin indicated the level of correlation with each component.

3.3 Results

3.3.1 Water quality and optical metrics

Lakes within the WF and NE subregions had relatively high pH, alkalinity, major ions, and DKN concentrations (Table B2), while those within the BM and SM regions displayed comparatively low values, e.g., median pH across WF and NE lakes was 6.89 compared with 6.32 among BM and SM sites. Median DOC was highest among the WF and CM subregions (25 and 26 mg C L^{-1}, respectively), while the lowest concentrations occurred within BM and SM (20 and 14 mg C L^{-1}, respectively). Conversely, TC was elevated among BM lakes (140 mg L^{-1} Pt) compared with WF surface-waters (70 mg L^{-1} Pt).

Similar to the H and L subpopulations identified in Chapter 2 (Blanchard et al., 2021), comparison of surface-water DOC and TC measurements from 2021 revealed two lake populations distinguished by diverging slopes (Figure 3.2). However, there was a notable overlap between subpopulations at lower DOC concentrations (< 20 mg C L^{-1}). Interannual variation of surface-water chemistry likely explained the inconsistency between the long-term (1999–2017) and 2021 ASL data; the comparatively distinct DOC-TC trends from the long-term ASL data benefitted from temporal smoothing. To maintain continuity with the historical data, subsequent comparisons of H and L populations were based on the classifications established in Chapter 2.

Significant differences (Kruskal-Wallis; $\alpha < 0.05$) in numerous water quality variables were observed between lake populations. In general, H classified lakes possessed comparatively higher SO_4^{2-} select metals (Fe, Al, Zn, Ni, Cu), and DOC:DON, but relatively depressed alkalinity, pH, and conductivity. Conversely, L lakes generally displayed high alkalinity,

pH, major ions (excluding SO_4^{2-}), DIC, DOC, and DON (Table 3.2). The H classified lakes displayed significantly higher lake surface area:DBA, E:I, and isotope enrichment ($\delta^{18}O$) compared with the L population (Table 3.2). The highest median a_{254}, and $SUVA_{254}$were observed among H surface-waters, while FI and BIX were elevated among L lakes (Table 3.2).

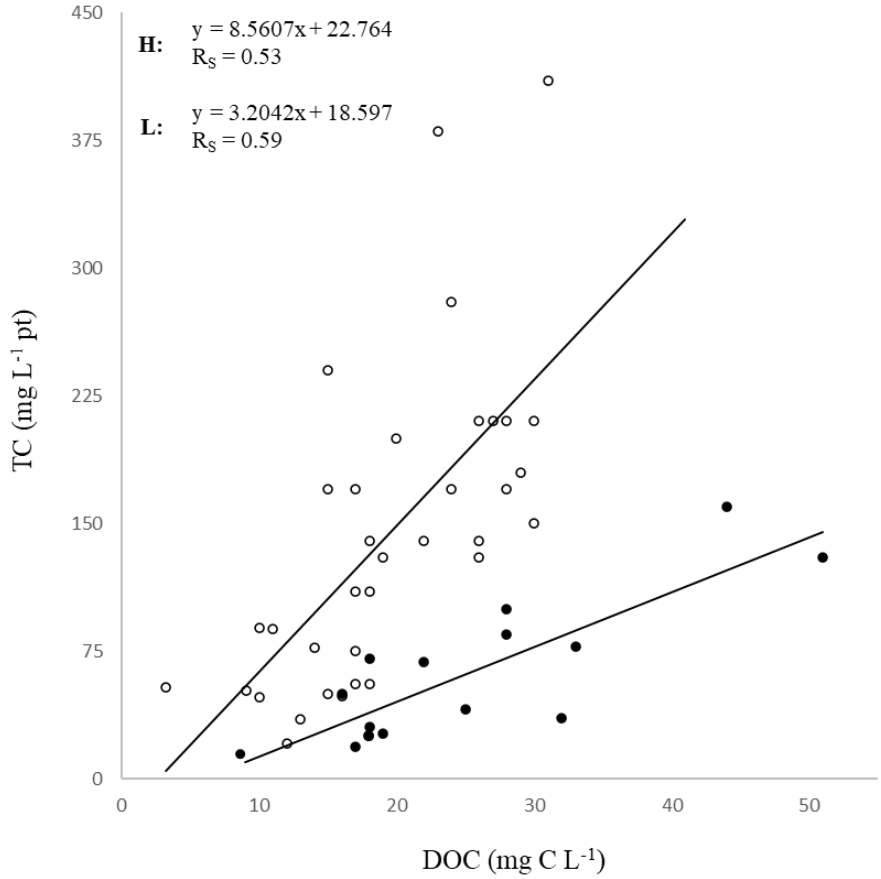

Figure 3.2 Comparison of surface-water DOC (mg C L^{-1}) and TC (mg L^{-1} Pt) measured at individual Acid Sensitive Lakes (ASL; 2021 sample data). The white and black circles correspond to the H (n = 35) and L (n = 15) lake subpopulations (respectively) established in Chapter 2 (Figure 3.1). The line of best fit and corresponding regression equations with coefficient of determination is displayed for each ASL cohort.

Table 3.2 Comparison of median values from the H (n = 35) and L (n = 15) lake subpopulations established in Chapter 2 (Figure 3.1). The normalized median absolute deviation (NMAD; %) is displayed for each cohort, while significant ($\alpha < 0.05$) Kruskal-Wallis test results (comparing H and L subpopulations) are indicated for each variable.

Variable	High (n = 35)		Low (n = 15)		Kruskal-Wallis
	Median	NMAD	Median	NMAD	$\alpha < 0.05$
Bog (%)	4.69	97.7	2.96	79.5	-
Fen (%)	56.87	39.4	52.01	32.3	-
Permafrost (%)	0.8	93.4	0.00	71.2	-
WY (mm yr^{-1})	221.91	43.7	121.06	47.6	-
E:I (%)	20.26	35.4	40.75	19.7	Yes
$\delta^{18}O$ (‰)	-14.22	8.7	-11.51	15.0	Yes
Temp (°C)	14.87	8.1	15.80	7.7	-
pH	6.58	5.8	7.16	4.6	Yes
Redox potential (mV^{-1})	333.0	7.3	258.9	21.9	Yes
Total alkalinity (mg L^{-1})	6.80	72.1	27.00	50.0	Yes
Total cations (meq L^{-1})	0.30	46.7	0.77	51.0	Yes
Total anions (meq L^{-1})	0.18	66.7	0.59	58.5	Yes
Ion deficit (meq L^{-1})	0.12	33.3	0.16	36.4	Yes
DIC (mgC L^{-1})	1.0	57.3	5.2	77.8	Yes
DOC (mgC L^{-1})	18.0	33.3	22.0	23.4	Yes
DON (mgN L^{-1})	0.57	20.5	0.82	16.9	Yes
DOC:DON	37.4	38.4	29.4	95.2	Yes
TP (mgP L^{-1})	0.04	48.6	0.03	43.1	-
TDP (mgP L^{-1})	0.01	63.6	<0.01	<0.1	Yes
Al (µg L^{-1})	78.60	74.2	24.30	68.7	Yes
d-Al (µg L^{-1})	52.05	72.5	10.10	72.8	Yes
Fe (µg L^{-1})	698.00	54.4	153.50	67.8	Yes
d-Fe (µg L^{-1})	334.00	79.6	16.50	66.7	Yes
Cu (µg L^{-1})	0.23	47.3	0.15	32.5	Yes
d-Cu (µg L^{-1})	0.21	42.4	0.14	39.1	Yes
Ni (µg L^{-1})	0.53	50.9	0.24	59.6	Yes
d-Ni (µg L^{-1})	0.42	59.5	0.13	72.0	Yes
Chl-a (mg m^{-3})	19.6	67.9	23.4	56.4	-
DO (mg L^{-1})	9.1	3.3	9.3	7.0	-
TC (pt Co^{-1})	135.0	46.4	70.0	45.7	Yes
a_{254} (m^{-1})	30.0	83.4	20.5	64.1	Yes
$SUVA_{254}$ (L mg^{-1} m^{-1})	1.26	89.0	0.79	96.1	Yes
HIX	0.74	8.8	0.71	8.5	-
BIX	0.44	4.9	0.54	9.5	Yes
FI	1.14	5.1	1.19	4.9	Yes

3.3.2 Modelled fluorescent components

Analysis of multiple PARAFAC models ranging from two to six components indicated that a model rank of four was most appropriate for further evaluation. In addition to a high

degree of fit (0.98), the four-component model displayed strong CC (83.5) and split-half validation (0.98) scores. The components generated from the selected model displayed clearly defined fluorescent peaks/regions, while no distinct and/or recuring residual peaks were observed within the model output.

The first fluorescent component (C1) presented two emission peaks at λ_{Ex}: 240, $\lambda_{Em:}$ 460, and λ_{Ex}:340, λ_{Em}: 460 nm, respectively (Figure 3.3). In the OpenFluor database, C1 is frequently characterized as humic acid-like DOM (Table 3.3), often originating from soil and terrestrial sources (Dalmagro et al., 2019; Garcia et al., 2018; Kothawala et al., 2014; Osburn et al., 2016). Component two (C2: λ_{Ex}: 225, λ_{Em}: 400 and λ_{Ex}: 310, λ_{Em}: 400 nm) was classified as photochemically/biologically processed humic matter (Garcia et al., 2018; Hansen et al., 2016; Murphy et al., 2014; Soto Cárdenas et al., 2017). Component three's (C3; λ_{Ex}: 205, λ_{Em}: 305 and λ_{Ex}: 215, λ_{Em}: 305 nm) spectral loadings were similar to the fluorescence of amino acid (Retelletti Brogi et al., 2019; Santana-Casiano et al., 2022; Yamashita et al., 2011) and anthropogenic (PAH) compounds (Retelletti Brogi et al., 2022; Zito et al., 2019). The final component (C4: λ_{Ex}: 210, λ_{Em}: 290 nm) presented limited matches in the OpenFluor database, where the only model with a similarity score > 0.95 characterized the component as the amino acid phenylalanine (Wünsch et al., 2015).

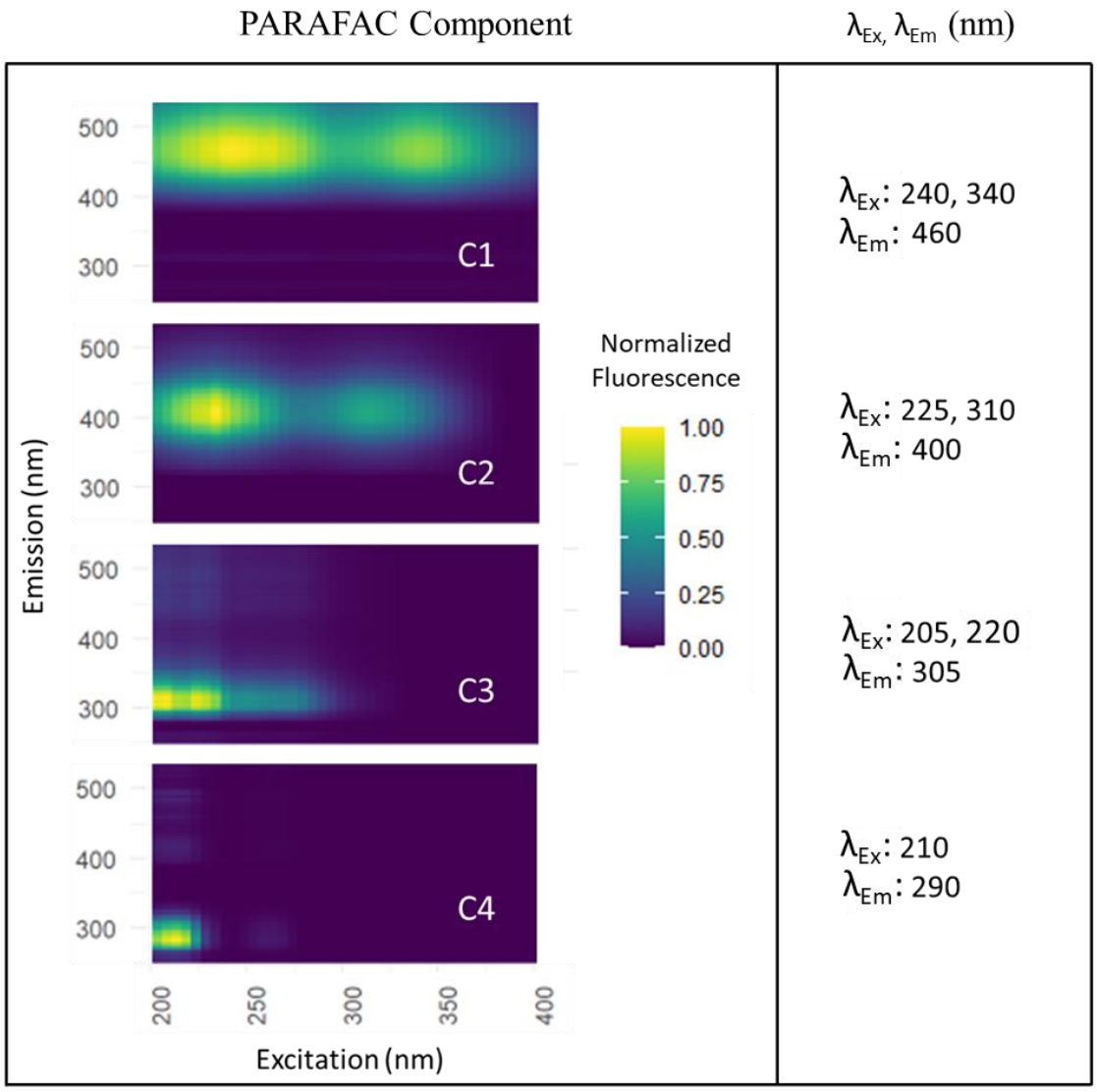

Figure 3.3 Visualization of the four PARAFAC components (C1–C4) generated from the lake EEM samples. Emission intensity values are normalized according to max component fluorescence. Fluorescent-peak excitation (λ_{Ex}) and emission (λ_{Em}) coordinates (nm) are displayed for each component.

Table 3.3 Comparison of PARAFAC model components (C1–C4) against the OpenFluor online database.[a] The number of highly similar components ($r > 0.95$), general fluorophore classifications based on the cited studies, and corresponding references (with modelled component number) are shown.

Component	Openfluor matches ($r > 0.95$)	Fluorophore Characterization	Reference and PARAFAC Component
C1	76	Lake humic acid	C1: Kothawala et al., 2013
		Soil derived humic / fulvic acid	C1: Osburn et al., 2016 C1: Garcia et al., 2018
		Terrestrial humic acid	C1: Shutova et al., 2014 C1: Dalmagro et al., 2019 C3: Shutova et al., 2014
C2	126	Processed terrestrial humic acid	C2: Shutova et al., 2014
		Microbial / biological derived humic acid	C3: Garcia et al., 2018 C1: Hansen et al., 2016 C1: Soto Cárdenas et al., 2017
		Lake humic acid	C1: Eriksson et al., 2013
C3	20	Protein, amino acid – like	C1: Retelletti Brogi, 2019 C4: Santana-Casiano et al., 2022 C4: Yamashita et al., 2011 C5: Osburn et al., 2016
		Anthropogenic, PAH	C6: Retelletti Brogi et al., 2022 C5: Zito et al., 2019
C4	2	Amino acid – phenylalanine	C1: Wünsch et al., 2015

[a] https://openfluor.lablicate.com

Median F_{MAX} intensity for components one to four were 77.9, 96.6, 42.6, and 70.9 QSU, respectively. The majority of CDOM fluorescence was attributable to the humic acid components C1 and C2, where the median relative emission intensity of each component

was 26 % and 33 % of total sample fluorescence. The highest C1 loadings were measured among H lakes, while C2 loadings were elevated in the WF region. The strongest C3 fluorescence intensity was observed in the NE and WF subregions and L classified lakes, while C4 was elevated in the SM region. The ratio of humic acid components C1 and C2 (C1:C2) was generally elevated throughout the CM and BM regions (Figure 3.4) and significantly higher among the H subpopulation (Table 3.4). Both C1:C3 and C2:C3 ratios where generally elevated among BM and CM and depressed within SM lakes. Finally, C1:C4, C2:C4, and C3:C4 values were highest among WF and low among SM lakes. Given the prominence of the humic acid-like fluorescent components within the samples, the C1:C2 ratio was included in subsequent analysis to assist in identifying environmental sources or processes contributing to lake humic content.

A second PARAFAC model generated from the non-buffered lake samples displayed fluorescent components nearly identical to the initial model. Moreover, component emission intensities were relatively similar between lake samples (< 5% variation), suggesting pH adjustment had a minor influence over CDOM fluorescence. Subsequent analysis involving these two datasets produced highly similar results; hence, discussion hereafter references data from the buffered lake samples.

Table 3.4 Summary of median PARAFAC component F_{MAX} (C1–C4, QSU) and F_{MAX} ratios among the H (n = 35) and L (n = 15) lake subpopulations established in Blanchard et al.'s 2021 study. The normalized median absolute deviation (NMAD; %) is displayed for each cohort, while significant ($\alpha < 0.05$) Kruskal-Wallis test results (comparing H and L subpopulations) are indicated for each variable. The method detection limit (MDL; QSU) and average relative percent difference (RPD; %) corresponding the to total dataset are shown.

Component	MDL	RPD (%)	H (n = 35)		L (n = 15)		Kruskal-Wallis ($\alpha < 0.05$)
			Median	NMAD	Median	NMAD	
C1 (QSU)	< 1.0	4.0	79.2	43.0	68.8	31.4	Yes
C2 (QSU)	< 1.0	5.7	96.4	27.3	103.6	28.6	-
C3 (QSU)	4.4	6.2	39.1	9.1	50.2	8.2	Yes
C4 (QSU)	5.3	9.3	70.9	42.4	71.2	39.2	-
C1:C2	-	-	0.9	16.9	0.6	21.7	Yes
C1:C3	-	-	1.9	53.9	1.3	38.7	-
C1:C4	-	-	1.1	60.5	1.2	62.7	-
C2:C3	-	-	2.1	41.4	2.0	28.5	-
C2:C4	-	-	1.2	61.1	1.7	53.1	-
C3:C4	-	-	0.6	45.3	0.8	21.7	-

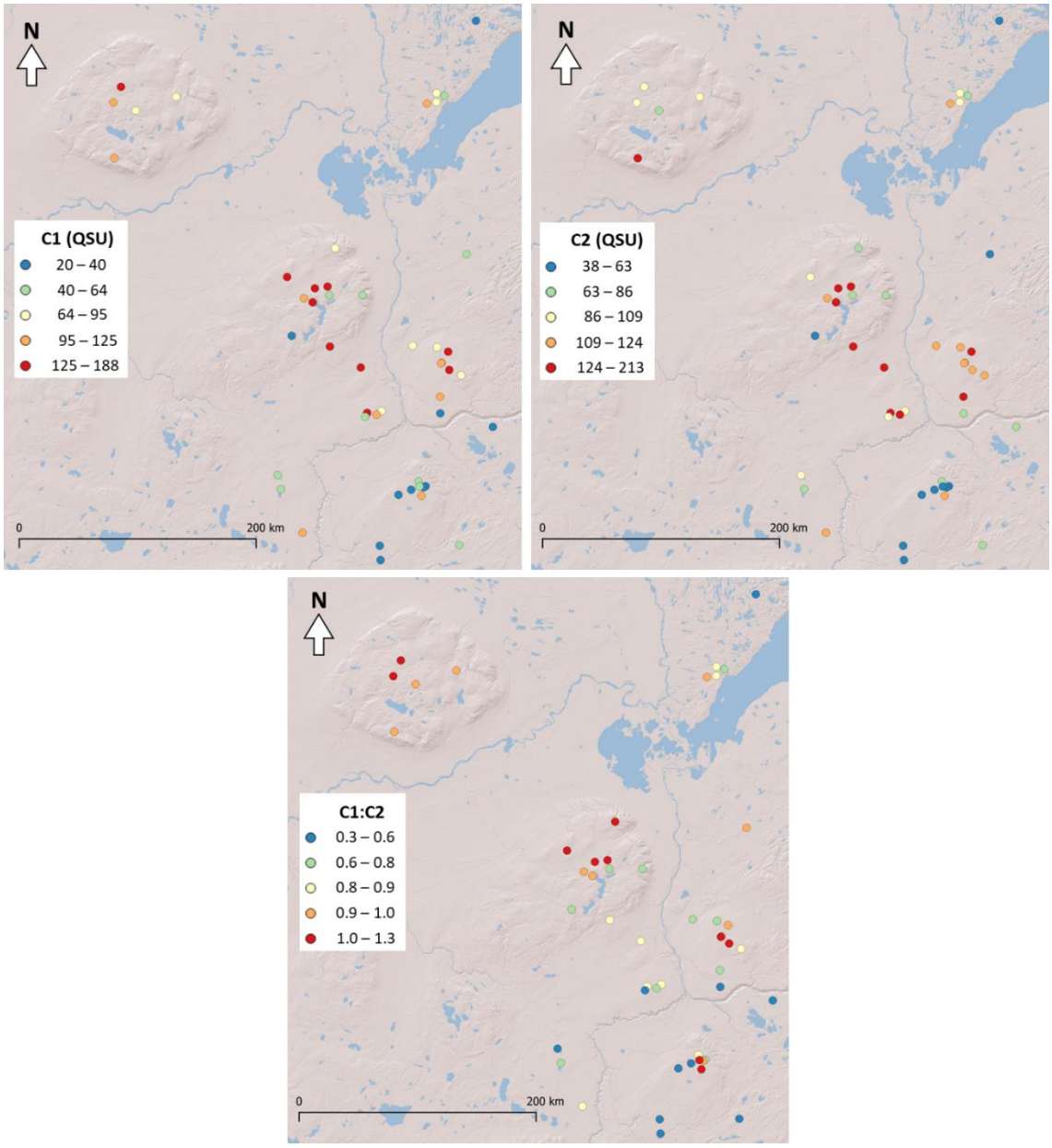

Figure 3.4 Spatial distribution of C1 and C2 F_{MAX} values (QSU) and C1:C2 ratios among Acid Sensitive Lake surface waters throughout the AOSR during the August 2021 sampling period.

3.3.3 Bivariate and multivariable analysis

There were significant positive correlations (R_S > 0.7; Spearman: α > 0.05) between C1 fluorescence intensity and C1:C2 with TC, DOC, d-Al, d-Fe, d-Ni, and d-Cu. Moreover, both C1 and C1:C2 displayed significant inverse correlations with $\delta^{18}O$ (R_S = 0.66) and temperature (R_S = 0.58). Component two (C2) presented significant positive correlations with total anions, total cations, DOC, and DON. Both C3 and C4 displayed few associations with the ASL dataset, except for a significant negative correlation (R_S = 0.55) between C3 and lake distance from the nearest OS source (Figure B1), and positive correlation of C3 with BIX and $\delta^{18}O$. Limited associations were observed between optical variables and surface water pH and alkalinity, including bivariate comparisons between observations within the H and L lake subpopulation, separately. It should be noted that the additional fluorophore ratios (i.e., C2:C3, C2:C4) presented limited correlations with the available variables, and were excluded from subsequent analysis.

The majority of variation within the combined ASL dataset was explained by four principal components (PC), which combined explained 62% of total variance (Table B3). Principal component one (PC1; 27%) displayed strong positive loadings (> 0.75) with C1, C1:C2, TC, HIX, a_{254}, TC, dissolved and total Fe, and Ni, while PC2 (15%) was positively associated (factor loadings > 0.7) with C2, pH, DOC, DON, total anions, total cations, and negatively correlated against redox potential. Biplot comparison of PC scores revealed a separate clustering of H and L classified lakes (Figure B2); thus, PC1 and PC2 appeared to describe the general characteristics of the previously established H and L lake subpopulations, respectively.[24] The third PC (10%) was positively associated (loadings > 0.6) with %bog, %permafrost, depth, volume, and negatively associated with %fen, while

the fourth component (PC4 = 9%) was positively associated with TP (loading = 0.7). Owing to its high loading value and proximity to lake variables (dissolved metals, TDP, %bog, %permafrost, TC) (Figure B2), C1:C2 was included as an additional Y variable in the PLS-R analysis.

Cross-validation confirmed that a two-component PLS-R model was most appropriate for further analysis, as it produced a relatively strong R^2Y (cumulative $R^2Y = 0.65$) and the highest increase in Q^2Y value (cumulative $Q^2Y = 0.55$). The first orthogonal component (PLS1: $R^2Y = 0.46$, $Q^2Y = 0.38$) was strongly influenced (VIP score ≥ 1) by DOC, DOC:DON, TDP, Al, Cu, Fe, Ni, d-Al, d-Cu, d-Fe, d-Ni, lake surface-area / DBA, $\delta^{18}O$, water temperature, TC, a_{254}, HIX, BIX, $SUVA_{254}$, %bog, %fen, and %permafrost landcover. Orthogonal component two (PLS2: $R^2Y = 0.19$, $Q^2Y = 0.17$) was largely influenced by TOC, DOC, and DON. Visualization of modelled components via correlation plot (Figure 3.5) displayed strong positive associations between C1 fluorescence and a_{254}, HIX, and $SUVA_{254}$, while C2 was plotted near TOC, DOC, and DON. Moreover, DOC:DON, TDP, Al, Cu, Fe, Ni, d-Fe, d-Ni, d-Cu, TC, %bog, and %permafrost was clustered in a region surrounding C1:C2 while BIX and $\delta^{18}O$ were located opposite of the Y variable. The variables TDP, total and dissolved metals, %bog, and %permafrost were plotted opposite of C3 along the PLS1 and PLS2 axes, although the Y variable displayed weaker correlations with both PLS components ($R < 0.50$). Limited predictor variables were plotted approximate to fluorescent component C4, which additionally presented weak correlations with both orthogonal components ($R < 0.4$). Notably, pH and alkalinity were assigned low VIP scores (< 0.8) and were relatively distant from the Y variables in the correlation plot. The second PLS-R model based on the relative fluorescence (%C) Y

matrix presented similar results, hence the former modelled output (F_{MAX}) will be referenced hereafter.

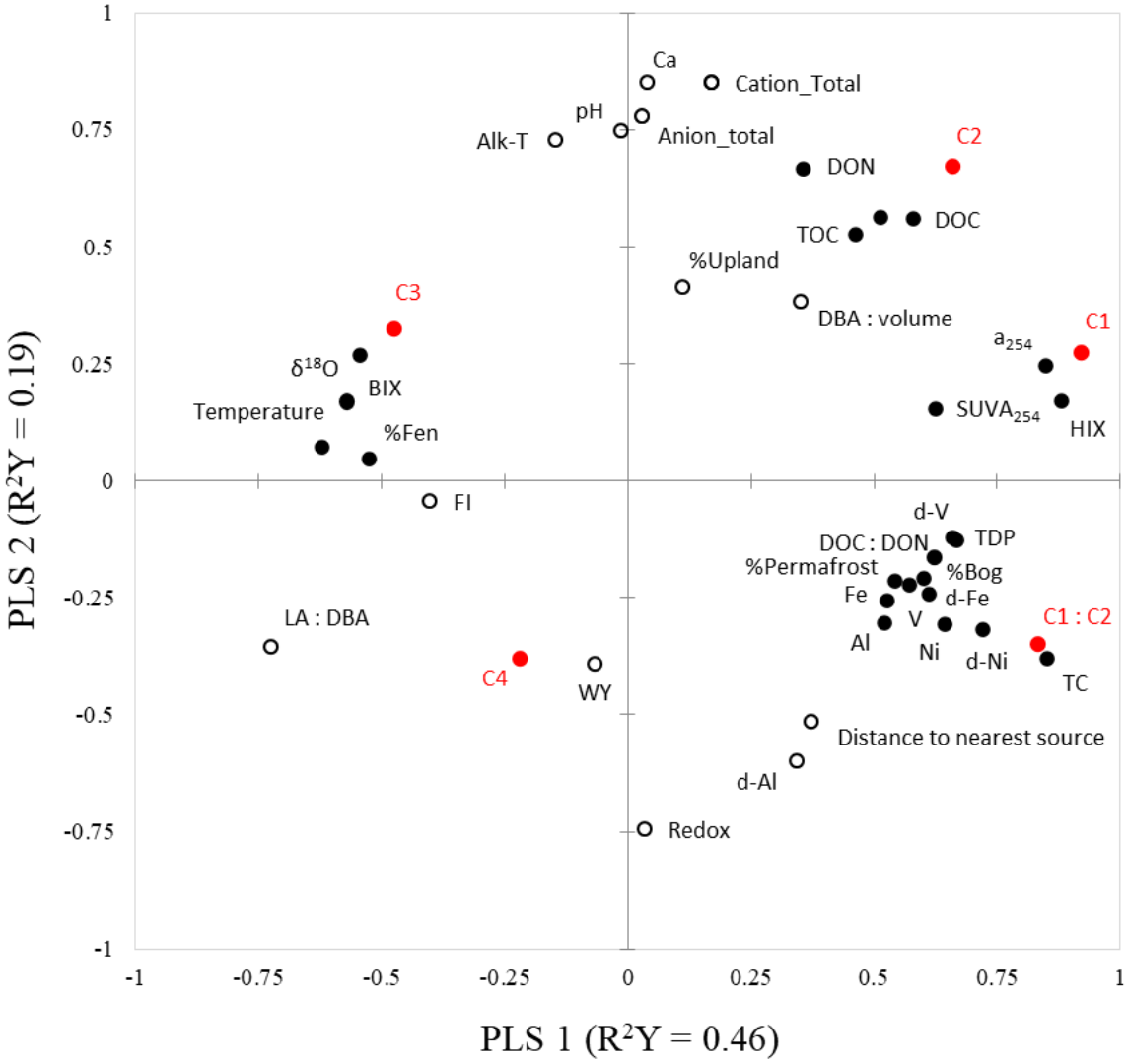

Figure 3.5 Correlation biplot displaying both X (black) and Y variables (red) in relation to partial least squares regression components one and two. The filled black and outlined black points indicate X variables with high (≥ 1) and low (< 1) variable influence over projection scores, respectively.

A two-component PLS-R model was most appropriate when pH and total alkalinity were assigned as predictor variables (cumulative R^2Y = 0.81; Q^2Y = 0.73). Correlation plot

visualization displayed that the Y variables were positively aligned with d-Ca, total cations, and total anions (Figure B3), which in turn received high VIP scores (> 1). Notably, absorbance and fluorescence variables were assigned low VIP scores (< 1) and plotted comparatively distant from pH and alkalinity.

3.4 Disscusion

3.4.1 Assessing the differences between ASL subpopulations

The distinct biogeochemical differences between the H and L populations was likely reflective of catchment properties, as perviously argued in Chapter 2 (Blanchard et al., 2021). The relatively high pH, alkalinity, and DIC among L-lakes was likely due to calcareous inputs from the underlying McMurray and Waterways bedrock formations; meanwhile, lower pH, alkalinity, and elevated metals (Fe, Al, Ni, Cu) among the H-lakes was likely linked to the metal-rich marine shales and organic soils prominent throughout their corresponding catchments (Blanchard et al., 2021; Emmerton et al., 2018). Significantly elevated E:I and $\delta^{18}O$ among the L subpopulation reflected enhanced evaporative losses within the corresponding catchments.

Measured absorbance within ASL waters agreed with the general range of values reported in the literature (e.g., the median a_{254} of 983 Swedish boreal lakes was 39.0 m^{-1}; Erlandsson et al., 2012). Significantly elevated a_{254} among H classified surface-waters supported Blanchard et al.'s (2021) assertion that the lake subpopulation contained high relative CDOM. The L lakes displayed comparatively low $SUVA_{254}$, indicating these surface waters contained less aromatic CDOM despite high DOC concentrations. Relative to the H-population, both FI and BIX metrics were higher among L lakes, suggesting a greater

proportion of autochthonous, biological CDOM production; however, these fluorescence metrics were low relative to the typical range reported in the literature (Cory et al., 2005; Huguet et al., 2009; Ohno, 2002; Wilson & Xenopoulos, 2009). The H lakes contained comparatively high molecular weight and aromatic organic matter as indicated by the elevated $SUVA_{254}$, while depressed FI and BIX indicated that the majority of CDOM was allochthonous in origin. Significantly different DOC:DON ratios between H and L lakes further confirmed that DOM contained within the two popluations was compositionally distinct. Highly aromatic organic matter derived from terrestrial sources typically present elevated DOC:DON (Yates et al., 2019), which possibly explained why the relatively aromatic (i.e., $SUVA_{254}$) H-lakes diplayed high DOC:DON values.

3.4.2 Characterization of fluorescent components

3.4.2.1 Humic acid C1

The strong associations between C1 and surface water a_{254}, $SUVA_{254}$, and HIX confirmed that the terrestrial humic matter was highly aromatic and linked to CDOM variation throughout the ASL dataset. The H-lake associated PC1 displayed high C1 and C1:C2 factor loadings, which suggested the humic fluorophore was partially responsible for the divergent characteristics of H and L lake surface-waters (Figure B2). Moreover, the strong positive correlation between C1 and TC indicated that the humic CDOM contributed to the hightened colour of H lakes.

The inverse association between C1 and LA:DBA (Figure 3.5 and B1) further affirmed the allochthonous origin of the fluorophore, as larger relative catchment areas contribute to greater terrestrial inputs. The organic-rich peatlands abundant throughout these catchments

(AEP, 2018; Strack et al., 2019) likely served as a key source of humic matter input to adjacent lakes, as has similarily been observed among other boreal lake systems in northern Albtera (Olefeldt et al., 2013). The importance of %bog as a predictor of C1:C2 suggested that humic matter composition was influenced by wetland composition within lake catchments (Dillon & Molot, 1997; Hosen et al., 2018), while the proximity of %permafrost relative to C1:C2 suggested the landscape feature may influence CDOM within ASL waters (Figure 3.5). Frozen peatlands are substantial reservoirs of humic organic matter, meltwater drainage from which can be a substantial source of terrestrial CDOM to connected freshwater systems (Wauthy et al., 2018). Increased warming and precipitation as a result of climate change and continued industrial land-development are expected to escalate ongoing rates of peatland degradation (Daniel et al., 2021; Price et al., 2013; Whittington & Price, 2012) and permafrost thaw (Dabros et al., 2018; Gibson et al., 2015, Gibson et al., 2019; Tarnocai, 2006) throughout the study region. Given the suspected link between these environmental sources and C1 fluorescence, shifting catchment conditions may impact (or continue to impact) lake CDOM composition over the coming decades.

Strong associations of C1 and C1:C2 with select dissolved metals (Fe, Ni, Cu) suggested that the humic-acid component played a role in the formation of organic-metal complexes, a process that could alter the mobility and bioavailability of dissolved metals in the environment (Luider et al., 2003; Mantoura et al., 1978). This was consistent with Guéguen et al. (2011), who found that peatland-derived humic-acids influenced metal mobility in sections of the Athabasca River throughout the AOSR. In the case of ASL surface-waters, the rate of CDOM-metal interactions may be controlled by lake-catchment characteristics, specifically features aligned with the chromophoric subpopulation. For instance,

catchments within the H subpopulation (which displayed significantly higher C1:C2 and dissolved metals than L lakes) contain peatlands and organic soils overlying metal-rich marine-shales (notably in the CM, SM, and BM regions) (AEP, 2018; Dufresne et al., 2001) which offer preferable conditions for organic-metal interactions, including the formation of Fe-DOM complexes. Increased rates of Fe-DOM complexation can enhance the absorbant properties of CDOM (Maloney et al., 2005), which would contribute to the high TC of H-classified lakes.

3.4.2.2 Humic acid C2

The strong positive associations between C2, DOC, and DON suggested that all three DOM constituents shared similar environmental origin (and processing), and that the C2 fluorescent component could serve as an optical proxy for bulk DOC and DON in ASL surface-waters. The spectral simlarity of C2 to allouchthonous humic organic matter reported in the literature suggested that the fluorophore originated from terrestrial sources surrounding the ASL sites (Shutova et al., 2014). The importance of %fen as an inverse predictor of C1:C2 suggested that these humics were more common among fen-dominated catchments.

Previous models uploaded to the OpenFluor database have defined similar fluorophores as terrestrial humic acids that have undergone microbial degradation (Garcia et al., 2018; Hansen et al., 2016). The strong correlation between C2 and DKN could indicate biological processing, as past studies have found that microbial consumption of organic matter is accelerated via nutrient availability (Tranvik et al., 1998). Microbial degradation can decrease the aromaticity and DOC:DON of DOM within aquatic systems (McDowell et al.,

2006; Koehler at al., 2012); as such, the positive association between the molar ratio and C1:C2, as well as the significanlty lower $SUVA_{254}$ and DOC:DON values among the L-lake subpopulation (characterized by elevated C2) further demonstrated that C2 may be linked to biological processing.

Through controlled incubation of boreal lake and groundwater samples, Olefeldt et al. (2013) found that increased evaporative losses due to solar irradiation and residence times (as indicated by $\delta^{18}O$) contributed to the preferential mineralization and sedimentation of highly aromatic DOM (von Wachenfeldt et al., 2008). Additional studies have demonstrated that photodegradation reduces the $SUVA_{254}$ and DOC:DON of aquatic DOM (Buffam and McGlathery, 2003; Fu et al., 2021). As such, the strong inverse correlation of E:I and $\delta^{18}O$ with DOC:DON, C1, C1:C2, and $SUVA_{254}$ (Figure 3.5) indicated that ASL waters experiencing elevated irradiation lost aromatic and carbon-enriched humic matter (i.e., C1) via photodegradation at a faster rate than the less aromatic and carbacious C2 molecules. Controlled photolytic incubations of regional surface-water CDOM would provide valuable insights regarding this potential process.

3.4.2.3. Amino acid C3 and C4

Although comparison to the OpenFluor database found both C3 and C4 were spectrally similar to biologically derived amino acid fluorophores, the generally weak associations between these components and DKN, DON, TP, TDP, DO, chl-a, and FI did not support this characterization. The relatively low FI and BIX values further implied a low abundance of biologically derived DOM within the study lakes. Photochemical degradation of humic matter can lead to the production of smaller amino-acid like DOM within surface-water

(Olefeldt et al., 2013), which may explain the weak positive correlation between C3, $\delta^{18}O$, E:I, and temperature.

Low molecular weight PACs and PAHs can produce flurescence spectra simlar to amino acids, as such, aromatic pollution from OS sources could be responsible for C3 flourescence within ASL waters (Retelletti Brogi et al., 2019; Retelletti Brogi et al., 2022; Zito et al., 2019). Considering that OS operations are an established source of organic pollutants to regional lake sediments (Jautzy et al., 2013; Salat et al., 2021) and C3 fluorescence decreased as a function of distance from the nearest OS source, future studies should investigate the infleunce of local industry over lake CDOM throuhout the AOSR. Although C4 did not present spatial gradient relative to industrial sources, the protein like fluorophore could be assoicated with additional sources / processes not represented in the current dataset; for example, pyrogenic organic matter inputs from wildfires are capable of impacting CDOM composition within aquatic system surface-waters Song et al., 2021).

3.4.3 CDOM quality and acid-base chemistry

The low importance of pH and alkalinity as predictors of PARAFAC component variation (and insignificant correlations between pH and alkalinity with fluorophore species and aborbance metrics) indicated that acid-base chemistry had limited direct influence over CDOM in ASL surface-waters (and vice versa), including the H and L lake subpopulations, separately. Minimal differences in fluorophore emission intensity between natural pH and buffered (pH ~ 6.5) lake samples demonstrated that shifts in surface-water pH did not substantially alter CDOM optical properties. These observations were consistent with Groeneveld et al. (2021), who found that CDOM fluorescence within Swedish boreal lake waters was relatively stable when pH was adjusted at 0.5 increments between 5.5 – 7.5 (similar to the ASL pH range).

Although acid-base chemistry displayed limited influence over CDOM, factors including environmental source and degradation processes appeared consequential to organic matter quality. Considering the former, accelerating wetland degradation and permafrost thaw (linked to climate change and industrial development) may contribute to long-term shifts in CDOM quality. Continued annual monitoring of CDOM witihn ASL surface-waters (in conjunction with monitring of catchment composition and hydrology) would provide the temporal data necessary to explore the possible influence of these processes over dissolved organic matter.

3.5. Conclusions

This chapter describes the first-known study that characterized the bulk properties and primary constituents of CDOM within AOSR acid sensitive lakes (ASL) through the application of UV-Vis and fluorescence spectroscopy/ This investigation confirmed that the true colour lake subpopulations identified in Chapter 2 (Blanchard et al., 2021) presented distinct CDOM characteristics: the highly coloured “H” lakes contained relatively aromatic humic compounds that originated from the surrounding peatlands and wetlands, while and the “L” lake surface-waters contained comparatively less-conjugated terrestrial organic matter that may have undergone biological or photolytic degradation. Significantly different DOC:DON ratios between lake categories further demonstrated the corresponding surface-waters contained molecularly distinct DOM.

Multivariable analysis and comparative pH adjustment experiments demonstrated that CDOM and acid-base chemistry were not significantly linked within ASL surface-waters, and as such, the processes of lake acidification or acid recovery were not suspected to directly impact surface-water chromophoric organic matter in the AOSR. Following this line of reason, long-term shifts in CDOM quality were unlikely to influence surface-water

acid-base chemistry. It should be noted that the analysis presented in Chapter 3 is based on one period of observations and does not fully capture the temporal variability of lake CDOM throughout the AOSR. As such, broader associations between CDOM and acid-base chemistry may not have been visible within the available dataset. It is recommended that the joint Oil Sands Monitoring program incorporates EEM fluorescence spectroscopy into their routine annual monitoring of ASL surface-waters in effort to evaluate long-term CDOM variation in relation to acid-base chemistry.

4. Chapter Four: Characterization of atmospheric water-soluble brown carbon in the Athabasca Oil Sands Region, Canada[3]

4.1 Introduction

Water-soluble brown carbon (WS-BrC) represents a class of organic aerosols capable of absorbing light within the ultraviolet (UV) and visible (Vis) wavelength ranges (Fuzzi et al., 2002; Lin et al., 2012; Stone et al., 2009). Chemical species within the WS-BrC fraction are classified as chromophoric dissolved organic matter (CDOM), which generally consists of polymerized, aromatic, humic-like substances (HULIS) and lower molecular-weight protein-like substances (PRLIS). Both HULIS and PRLIS represent broad chemical groups named according to their chemical and optical similarity to humic matter and proteins found in terrestrial, aquatic, and atmospheric environments (Dey and Sarkar, 2024; Duarte et al., 2007; Graber and Rudich, 2006; Hudson et al., 2007; Laskin et al., 2015).

Owing to their light-absorbing properties and capacity as cloud condensation nuclei (CCN), WS-BrC particles can influence planetary albedo and solar radiation budgets (Facchini et al., 1999), and as such have been recognized as an influential factor in climate change research (Chakrabarty et al., 2016; Gustafsson et al., 2009). Moreover, soluble BrC has been found to play an important role in atmospheric reaction chemistry (Jiang et al., 2012) and can be detrimental to human health (Ma et al., 2019; Maulderly and Chow, 2008). Biomass and fossil fuel combustion are the dominant sources of atmospheric WS-BrC,

[3]Blanchard, D., Gordon, M., Dang, D. H., Makar, P. A., Aherne, J. (2025a). Characterization of atmospheric water-soluble brown carbon in the Athabasca Oil Sands Region, Canada*, Atmospheric Chemistry and Physics*, 25(4), 2423–2442, https://doi.org/10.5194/acp-25-2423-2025

including HULIS and PRLIS (Claeys et al., 2012; Gao et al., 2006; Wu et al, 2019); however, biogenic emissions, soil dust, and industry can all contribute to primary and secondary formation of these organic aerosols (Spranger et al., 2020; Wu et al., 2019).

Industrial operations in the Athabasca Oil Sands Region (AOSR) in north-eastern Alberta, Canada, are a substantial source of atmospheric particulate matter (PM) (Giesy et al., 2010; Landis et al., 2017; Liggio et al., 2016). Open pit mining activities, haul road dust, dry tailings, vehicle exhaust, and upgrading facilities are sources of organic–containing PM (Giesy et al., 2010; Zhang et al., 2016), while volatile precursor emissions from flue gas stacks and exposed bitumen contribute to secondary organic aerosol formation (Liggio et al., 2016). Organic PM generated from oil sands (OS) activities consists of a diverse range of chemical species, including polycyclic aromatic compounds (PAC: Bari & Kindzierski, 2018; Liggio et al., 2016; Liggio et al., 2017), oxygenated polycyclic aromatic hydrocarbons (Jariyasopit et al., 2021), naphthenic acids (Yassine and Dabek-Zlotorzynska, 2017), and organic matter linked to surface-soil and overburden dust (Wang et al., 2015). An unresolved fraction of these emissions contains relatively water-soluble species (Arp et al., 2014; Josefsson et al., 2015; Marentette et al., 2015), which can contribute to the WS-BrC fraction, partially due to their conjugated structures (Stedmon and Nelson, 2015).

Relatively little was known regarding the abundance and composition of WS-BrC in the AOSR airshed, nor was it well understood how local industry contributed to the CDOM fraction. Considering the magnitude of sources in the region, OS emissions likely contributed to WS-BrC, which in turn could influence radiative forcing on a broad scale.

The established toxicity and environmental mobility of water-soluble organic pollutants (Lemieux et al., 2008; Lundstedt et al., 2007) provide a clear incentive to monitor these species throughout the AOSR; however, the diversity of chemical formulae presents a challenge to regional monitoring efforts, due to the high operational costs of typical mass spectrometry methods (Frysinger et al., 2003).

Ultraviolet-visible (UV-vis) spectroscopy is commonly employed to characterize the bulk properties of environmental CDOM. Moreover, a sizable fraction of WS-BrC consists of fluorescent dissolved organic matter (Laskin et al., 2015) which can be evaluated through the application of excitation emission matrix (EEM) spectroscopy. Complex EEM datasets can undergo processing via Parallel Factor Analysis (PARAFAC); a multivariable model that can identify fluorescent components (fluorophores) reflective of organic compounds with shared optical properties. Fluorescence EEM spectroscopy and PARAFAC modelling has been successfully used to identify WS-BrC originating from a variety of biogenic and anthropogenic sources (Harsha et al., 2023; Wu et al., 2019; Zito et al., 2019).

In this study we evaluated WS-BrC quality in the AOSR and assessed the influence of OS activities over the organic PM fraction through the application of UV-vis and fluorescence spectroscopy techniques. During the Summer of 2021 (July 19–August 10), active filter-pack samplers were deployed at five sites throughout the study region to collect atmospheric PM for optical and chemical analysis. Fluorescent analysis of local reference materials and back-trajectory modeling were used to assist with source identification, while partial least squares regression (PLS-R) analysis was employed to characterize individual fluorophores generated by the PARAFAC model.

4.2 Methods

4.2.1 Study area and sampling sites

The AOSR is situated within a Boreal Plains ecozone, where peatlands and boreal forests are the dominant landscape features. Largely because of its northern inland geographical location, the region typically experiences warm summers and cold dry winters (ECCC, 2024). Beneath the boreal landscape lies the Athabasca oil sands deposit, the world's largest known bitumen reserve, which covers a surface area of ~ 140 200 km^2. Oil and gas companies such as Syncrude, Suncor, and Imperial Oil have established industrial facilities over these deposits to extract bitumen and upgrade it to refined material such as crude oil. The major OS facilities are located along the east and western banks of the Athabasca River (which flows North through the AOSR), as the Athabasca bitumen layer is close to the surface in these areas. The largest municipalities in the region are Fort McMurray and Fort McKay; the former is located ~50 km south of major OS operations while Fort McKay sits along the western bank of the Athabasca River, situated between several major industrial facilities (Figure 4.1).

The Wood Buffalo Environmental Association (WBEA; https://wbea.org) operates an extensive network of continuous air-quality monitoring stations and atmospheric deposition monitoring plots throughout the AOSR. Between July 19th to August 10th, 2021, active filter-pack systems for this study were co-deployed at five WBEA sites located throughout the AOSR to collect back-to-back 48 h exposures. Two of these fence-line sites (Mildred Lake deposition plot [DP2050]; Bertha Ganter station [AMS01]) were located in close proximity (DP2050 < 1 km, AMS01 < 5 km) to OS facilities (consisting of tailings

ponds, open pit mines, haul roads, upgrading facilities), a second set of stations (Patricia McInnes [AMS06]; Athabasca Valley [AMS07]) were situated in suburban/community locations > 50 km south of major OS operations, while a final background station (Stoney Mountain [AMS18]) was located ~ 150 km south of OS operations (Figure 4.1). Differences in observations between the stations thus allow us to infer sources associated with OS versus other activity, in addition to back trajectory analysis. The selected WBEA stations continuously monitor a variety of air quality and meteorological data, including sulphur dioxide (SO_2), total reduced sulphur (TRS), nitrogen oxide (NO), nitrogen dioxide (NO_2), total hydrocarbons (THC), carbon monoxide (CO), fine particulate matter ($PM_{2.5}$), wind speed, wind direction, temperature, and relative humidity.

During the year of 2021, 4.30×10^6 hectares of land across Canada were burned by wildfire compared to the 2013–2022 ten-year annual average of 2.73×10^6 hectares (source: Canadian Interagency Forest Fire Center Inc.). As a result of increased fire magnitude, substantial portions of western Canada were periodically blanketed in smoke plumes during the study period. Wildfire emissions are a substantial source of atmospheric PM and BrC (Chen and Bond, 2010; Reid et al., 2005), which can contain aromatic pollutant species with fluorescent properties (Veselovskii et al., 2020). To account for the potential influence of wildfire emissions over observed fluorescence, the temporal variability of $PM_{2.5}$ was assessed at each WBEA monitoring station to identify sampling periods of high fire smoke transport.

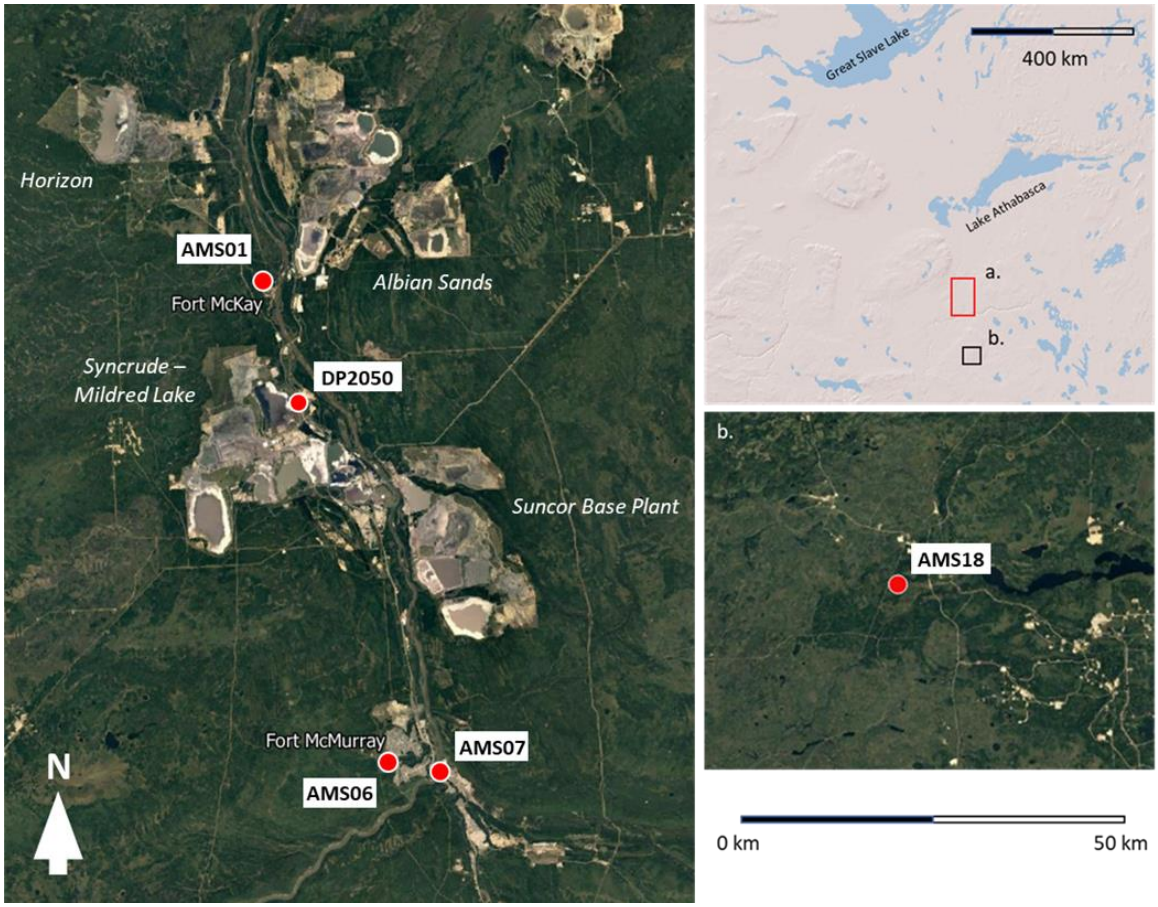

Figure 4.1 Distribution of active sampler sites (red circles) throughout near/mid-field (a) and far-field (b) study regions. Nearby communities (Fort McMurray, Fort McKay) and major active oil sands facilities are shown (Google Maps 2024). The map on the top-right displays the location of the two regions on a broader spatial scale (ESRI 1995-2024).

4.2.2 Active sampling

Active samplers consisted of a 15 liter per minute (L min^{-1}) vacuum pump connected to an in-line flowmeter and filter-pack cartridge inlet. These systems were directly powered through an AC outlet available at the WBEA monitoring stations, while a 12 V marine battery served as the power supply for a 7.5 L min^{-1} vacuum pump at the off-grid DP2050 deposition plot.

The filter-pack cartridges used in this study were obtained through the Norwegian Institute for Air Research (NILU; www.nilu.no) and consisted of two threaded compartments that housed pre-combusted quartz fiber filter (47 mm diameter, 0.3 µm aerosol retention) intended to collect total suspended particulate (TSP). After each exposure, filters were placed in a petri-dish, triple sealed in Ziploc® plastic bags and stored at – 20 °C until analysis. In total, 44 filter-pack samplers were successfully deployed (48 h exposures) during the field campaign, which broken-down by site included: 11 at AMS01 and Mildred Lake, 10 at AMS06, 8 at AMS18 and 4 at AMS07, respectively (Figure C1). During the study period, five of the forty-four samples were collected as duplicates through the deployment of two sampling units. Five additional quartz fiber filters were allocated as field blanks during the study period and were stored like exposed filters.

Prior to the field survey all components of the filter-pack cartridge were individually rinsed in reverse osmosis water and subsequently soaked in a 2 M hydrochloric acid (HCl) bath for 12 hours, after which the sampler parts were rinsed in ultrapure lab water (Milli-Q). In the field, the filter-pack cartridges were soaked in baths of Milli-Q water between exposures. To control for potential filter contamination between exposures, field blanks were loaded into (as if to collect a sample) and subsequently removed from select washed cartridges.

Following exposure, a 20 mm diameter sub-section of the filter was removed via circular punch, and subsequently extracted in conical vials containing 50 ml of Milli-Q water. Sample vials were inverted three times, placed in an ultrasonic bath for 1 hour, and filtered (nylon; 0.45 µm). Filtered samples were stored at ~ 4 °C and underwent optical analysis

within 12 hours of initial extraction. A 0.5 ml aliquot was used for determination of anionic species (Cl^-, NO_3^-, SO_4^{2-}) via ion chromatography (Dionex ICS-1100) while a separate 10 ml aliquot was acidified (2 % HNO_3) and sent to the Water Quality Center at Trent University (Peterborough, Ontario, Canada) for determination of dissolved elements (Na, Mg, P, S, K, Ca, V, Cr, Mn, Fe, Zn, Sr) using an Agilent 8800 triple quadrupole inductively coupled plasma mass spectrometer (Table C1 and C2). Additional details regarding instrument configuration and measurement parameters are available in the appendix section C1. A filtered 20 ml aliquot was used for determination of water-soluble organic carbon (WSOC), dissolved inorganic carbon (DIC), and total dissolved nitrogen (TDN) via Shimadzu TOC-V analyzer. The remaining filtered solution was adjusted to pH ~ 6.5 using 0.1 M sodium hydroxide (NaOH) or HCl to limit the influence of variable sample pH over WS-BrC optical properties (Lakowicz, 2006). Blank samples were used to determine method detection limits (MDL), which were calculated as: standard deviation (blank samples) × t-value 99.0 % confidence critical value (3.747).

Measured analytes from the filter extracts were converted to time-integrated atmospheric concentrations using the following equation:

$$C = \frac{(C_e - C_b) * V_e}{V_a} * A_f * 1000 \qquad \textbf{Eq. 4.1)}$$

Where C is the atmospheric concentration (ng m^{-3}), C_e is the analyte concentration (µg L^{-1}) within the filter extraction solution, C_b is the analyte concentration within the field blank extraction solution, V_e is the extraction solution volume (L), V_a is the volume of air sampled (m^{-3}), and A_f is the surface-area ratio (5.52) to account for the 20 mm filter cut-out.

4.2.3 UV-Vis spectroscopy

Absorbance was measured along a range of wavelengths (λ) between 200 to 800 nm (1 nm intervals) using a Cary 100 UV-vis spectrophotometer from Agilent Technologies. Filter extracts were allowed to warm to room temperature (~ 21 °C), and subsequently placed in a 1 cm (3.5 ml) Hellma® Suprasil® quartz cuvette (Hellma 101-QS) for analysis. A blank sample of Milli-Q water was first used to establish an instrument baseline. To clean, cuvettes were soaked in a 2 M HCl bath for ten minutes followed by subsequent rinses in Milli-Q water, 95% ethyl alcohol, and a final rinse in Milli-Q. The aerosol light absorption coefficient (Abs_λ, m^{-1}) at wavelength λ was calculated by the equation (Wu et al., 2019):

$$Abs_\lambda = (A_\lambda - A_{700}) \times \frac{V_w}{V \times l} \times \ln(10) \quad \textbf{Eq. 4.2)}$$

Where V_w refers to the volume (ml) of the filter extraction, V is the volume of air sampled (m^3) during the field exposure, l is the optical path length (cm), while V_λ and A_{700} are the absorbance at wavelengths λ and 700 nm, respectively. Absorbance at 700 nm is used as a reference to account for baseline drift. The light absorption coefficient at 365 nm (Abs_{365}) is frequently referenced as a proxy for BrC in the literature (Laskin et al., 2015; Wu et al., 2019), and is subsequently used to calculate the mass absorption efficiency (MAE_{365}, m^2 g C^{-1}) via the following equation (Wu et al., 2019):

$$MAE_{365} = \frac{Abs_{365}}{C_a} \quad \textbf{Eq. 4.3)}$$

Where C_a is the atmospheric concentration of WSOC (µg C m^{-3}), obtained using Eq. 1. Both Abs_{365} and MAE_{365} are frequently used in the literature to assess the radiative forcing potential of BrC aerosols (Dong et al., 2024; Yue et al., 2019).

4.2.4 Fluorescence spectroscopy and PARAFAC

Combined EEM and PARAFAC analysis is commonly used to evaluate the optical and structural characteristics of environmental CDOM since the modelling technique can identify the excitation and emission peaks of multiple distinct fluorophores (i.e., HULIS, PRLIS) within EEM scans (Harsha et al., 2023; Wu et al., 2019). Fluorescence analyses was conducted using a Cary Eclipse spectrophotometer set to the three-dimensional EEM scan and signal to reference (S/R) acquisition modes. Sample aliquots were placed in a 1 cm (3.5 ml) quartz cuvette (Hellma 101-QS) for analysis. Excitation (λ_{Ex}) and emission (λ_{Em}) scans (both measured at 5 nm intervals) ranged from 200–450 nm and 250–600 nm, respectively. A Milli-Q water blank was first measured to zero the fluorometer, then subsequent blanks were scanned every five samples. During each day of analysis, a set of quinine sulphate standards were prepared to create a calibration curve (1–100 ppb quinine sulphate in 0.5 M sulphuric acid) to convert fluorescence intensity measurements into quinine sulphate units (QSU) (Sui et al., 2017). To minimize the potential influence of the inner filter effect (IFE) over the fluorescence spectrum, all filter extracts were confirmed to have an absorbance < 0.05 at 270 nm (Trubetskoj et al., 2018).

Fluorescence data was processed via the R package "staRdom", which was used for blank and spectrum correction (Pucher et al., 2021). Inner filter effect corrections were applied to individual EEMs using the built-in IFE function and corresponding sample absorbance values (Shimadzu spectrophotometer). Rayleigh and Raman light scattering bands were removed from each sample EEM, and the empty cells infilled using the "eem_interp" function. The fluorescence intensity data was then divided by the corresponding extraction solution and air volume to convert QSU to QSU per cubic meter (QSU m^{-3}) (Deng et al.,

2022). The EEM dataset displayed limited fluorescence within the 540–600 emission and 400–450 excitation wavelength ranges, thus these regions were removed prior to PARAFAC modeling. Using the staRdom package, a PARAFAC model was employed to decompose the three-dimensional EEM data array (x_{ijk}) into a score matrix (**A**) and two loadings' matrices (**B** and **C**) with corresponding tri-linear elements a_{if}, b_{if}, and c_{kf} (Bro 1997):

$$x_{ijk} = \sum_{f=1}^{F} a_{if} b_{jf} c_{kf} + e_{ijk} \quad \textbf{Eq. 4.4)}$$

Score values in a_{if} represent the relative fluorescence intensity of fluorophore f in sample i, the elements b_{if} and c_{kf} represent the modelled emission (j) and excitation (k) loadings (i.e., wavelength coordinates) of f, while F is the total number of modelled fluorophores. Utilizing the residual element e_{ijk}, the PARAFAC model applies an alternating least-squares optimization technique to find the function that best approximates the dataset (Bro, 1997).

The appropriate number of modelled components (model rank) was selected based on four validation tools, including: 1) visual peak inspection, 2) EEM residual plots, 3) split-half analysis, and 4) core consistency (CC). These validation tools and their corresponding procedures are described in further detail in Chapter 3, section 2.4. The sample score values assigned to individual fluorescent components (a_{if}) were reported according to maximum fluorescence (F_{MAX}, QSU m^{-3}). To account for the potential influence of bulk DOM fluorescence over individual fluorophore emission intensity (due to variations in DOM concentration between samples), modelled component F_{MAX} values were divided by sample WSOC concentration (µg C m^{-3}) to normalize component fluorescence.

4.2.5 Environmental reference materials

A variety of environmental reference materials representative of dominant TSP emission sources from the OS were collected for EEM analysis, including a) dust from an unpaved road near observation site AMS01 (composite grab-sample), b) dust from a heavily trafficked unpaved road near observation site DP2050 (composite grab-sample), c) raw bitumen ore from the Athabasca Deposit and, d) dry mature fine tailings from the AOSR (MFT; composite industrial sample; Innotech Alberta). Dry road dust and MFT were sieved to < 2 mm to remove coarse material (Lanzerstorfer and Logiewa, 2019), while raw bitumen was too viscous to sieve. Each reference material was extracted in Milli-Q water and diluted to achieve a WSOC concentration of ~ 1.0 mg C L^{-1} and an absorbance < 0.05 at 270 nm (to match the filter extracts). Sample extracts were adjusted to a pH ~ 6.5 using 0.1 M NaOH or HCl (to match the pH of BrC extracts) and then stored at ~ 4 °C prior to optical analysis.

4.2.6 Data analysis

Variability in sampler observations was assessed by calculating the relative percent difference (RPD, %) from duplicate filter-pack exposures. Data displayed a non-normal distribution as determined via Shapiro-Wilk test ($\alpha < 0.05$); thus, non-parametric statistical tests were employed for subsequent analysis. Median values were used as a measure of central tendency, while data variability was evaluated using normalized median absolute deviation. Bivariate associations between measured TSP analytes and continuous pollutants were evaluated via Spearman's Rank Order correlation test, and the Kruskal-Wallis test was used to determine significant differences between sampling locations.

Partial least squares regression (PLS-R) analysis was applied to assist with fluorescent component characterization (Kothawala et al. 2014). Partial least squares analysis is a multivariable regression technique that is effective at decomposing large numbers of colinear predictor variables (X) into a smaller set of uncorrelated orthogonal components (Eriksson et al., 2013). The PLS-R model attempts to explain the maximum variability between X and response variables (Y) through a least-squares regression method. Modelled fluorescent component values (QSU m^{-3}) were assigned as Y variables while additional elements, WSOC, DIC, and TDN were designated as X. The appropriate number of components was determined via internal cross-validation, where a random subset of samples (~ 10% of dataset) was removed from the training dataset to evaluate the model. The resulting comparisons were evaluated based on model rank cumulative goodness of fit (explained variation; R^2Y) and cumulative goodness of prediction (Q^2). The relative influence of X variables over each component was interpreted via variable influence on projection scores (VIP), where values ≥ 1 signified a highly influential predictor variable (Eriksson et al., 2013). The spatial proximity of variable loadings served as a visual indicator of X and Y variable associations, while variable distance from the origin indicated the level of correlation with each component.

4.2.7 Trajectory analysis

The atmospheric transport model, HYSPLIT (Stein et al., 2015), was applied to evaluate source-receptor relationships within the study region. Meteorological data available through the Global Data Assimilation System was employed to generate bihourly backward wind trajectories (arrival height 10 m above ground level) spanning the duration (~48 h) of active sampler exposures at individual sites (i.e., 24 back-trajectories per exposure). The

resulting trajectory data were overlain onto OS facilities (polygons representing tailings, open mine pit, plant site boundaries) to explore the influence of industrial sources over observed TSP fluorescence. Using these spatial data, the relative frequency (%) of back-trajectories intersecting OS-facility boundaries (T_{OS}) during each exposure was calculated to further explore source-receptor relationships. The frequency method counts the number of times air trajectories intersect individual grid points (0.5 × 0.5 degrees) in the model domain, and then normalizes that sum value by the total number of modelled trajectories (%). It should be noted that the trajectory estimates do not account for the influence of vertical mixing and lateral diffusion over pollutant transport.

Through the Canadian National Fire Database, spatial data representing the boundaries of Canadian wildfires active during the study period (July 19–August 10) were used to evaluate the potential influence of pyrogenic sources over observed fluorescence. Using the same GDAS meteorological datasets, additional HYSPLIT backward trajectory frequency plots were modelled to evaluate atmospheric transport patterns during multi-day wildfire smoke episodes.

4.3 Results

4.3.1 Meteorology and continuous pollutant summary

Limited variation in relative humidity occurred between monitoring stations during the study period, where median values ranged from 69.8% to 71.8% (Table 4.1). The AMS01, AMS06 and AMS07 stations experienced prominent winds blowing from a range of directions (excluding NE – E) during the study period, while S – W winds were dominant in AMS18. Wind speeds were higher at AMS06, while colder temperatures were recorded

at AMS18. Moreover, the background station received a larger volume of precipitation compared with AMS01. Further, AMS01 experienced significantly higher CO, NO_2, SO_2, and TRS (Kruskal-Wallis; $\alpha < 0.05$) owing to its proximity to OS operations, while the lowest concentrations (with exception of CO) were recorded at the more distant downwind site AMS18 (Table 4.1). Ambient $PM_{2.5}$ was notably elevated at AMS18 with concentrations similar to AMS06 and AMS07.

Evaluation of WBEA station $PM_{2.5}$ timeseries data identified two periods of elevated concentrations. The first and most intense (hourly maximum $PM_{2.5} > 140$ µg m^{-3}) event occurred between July 19–22 while the second event ranged from July 31–August 6 (hourly maximum $PM_{2.5} \sim 50$ µg m^{-3}) (Figure C2). These high $PM_{2.5}$ events occurred during relatively similar periods between monitoring stations (including AMS18), suggesting a shared regional source. Trajectory frequency analysis indicated that extensive wildfires in northern Saskatchewan were the primary source of smoke ($PM_{2.5}$) in the study region (Figure C3).

The T_{OS} analysis demonstrated that the relative influence of OS emissions was expected to be strongest at the DP2050 (79.2%) and AMS01 (43.8%) sites, followed in descending order by AMS06, AMS07, and AMS18. Differences in our analysis at each of these sites thus can be used to infer source-related differences in composition (Table 4.1). Comparison of HYSPLIT trajectories against corresponding continuous station data displayed a general agreement between modelled and observed wind direction between exposure periods (Figure C4). Bivariate analysis demonstrated strong positive correlations ($R_S = 0.83 – 0.92$) between T_{OS} and continuous pollutant species reported through WBEA (exposure average

NO, NO_2, SO_2, TRS, THC; Table C3), emblematic of emission transport from OS facilities. Frequency estimates displayed weaker agreement with average $PM_{2.5}$ and CO ($R_S < 0.50$), likely because of the influence of non-OS sources, namely wildfire smoke.

Table 4.1 Summary of geographical (elevation), meteorological (wind speed, temperature, relative humidity, precipitation), air quality ($PM_{2.5}$, CO, NO, NO_2, SO_2, TRS, THC), and transport frequency (T_{OS}) variables at the co-located WBEA monitoring stations (ordered according to latitude [N to S]) during the study period (July 19–August 10, 2021). Both median and normalized median absolute deviation (%; in-parenthesis) values for each variable and station are displayed.

	AMS01	AMS06	AMS07	AMS18
Latitude	57.189428	56.751378	56.73344	55.621408
Longitude	-111.640583	-111.476694	-111.39047	-111.172686
Elevation (m)	270	362	497	673
Relative humidity (%)	70.7 (21.7)	69.8 (20.3)	71.8 (17.1)	71.3 (24.6)
Wind speed (km hr^{-1})	6.2 (46.1)	8.4 (43.1)	6.7 (44.0)	N/A
Temperature (°C)	17.5 (18.5)	17.5 (17.9)	18.3 (16.1)	16.6 (21.9)
Precipitation (mm)	45.3	N/A	N/A	48.0
$PM_{2.5}$ (µg m^{-3})	10.27 (63.8)	8.85 (61.2)	9.08 (58.6)	9.08 (55.3)
CO (ppm)	0.40 (20.0)	N/A	0.22 (22.7)	0.28 (42.9)
NO (ppb)	0.67 (25.4)	0.42 (50.0)	0.63 (68.0)	0.34 (14.7)
NO_2 (ppb)	3.28 (75.1)	1.48 (77.7)	2.23 (55.3)	0.57 (38.6)
SO_2 (ppb)	0.67 (11.9)	0.27 (37.0)	0.17 (29.4)	0.09 (77.8)
TRS (ppb)	0.54 (22.2)	0.31 (19.4)	0.13 (61.5)	0.09 (44.4)
THC (ppm)	2.11 (6.64)	1.99 (2.5)	2.09 (4.3)	1.91 (1.5)
T_{OS} (%)	43.8	22.9	12.5	0.0

4.3.2 Active sampler TSP summary

Throughout the study, the DP2050 sampler measured elevated concentrations of DIC, NO_3^-, SO_4^{2-}, Na, P, S, V, Fe, and Sr compared with the other study sites, while most variables (with exception of WSOC and TDN) were depressed at AMS18 (Table 4.2). Measured WSOC and Abs_{365} were significantly higher at the nearfield site DP2050 compared to the remaining stations (Kruskal-Wallis; $\alpha < 0.05$), while MAE_{365} values were similar across all sampling locations (Kruskal-Wallis; $\alpha > 0.05$). Dissolved V, Sr, S, and Na were strongly (positively) correlated ($R_S > 0.77$) with T_{OS} estimates, while WSOC and Abs_{365} displayed weak positive agreement ($R_S \geq 0.45$) (Table C4) with T_{OS}. Both WSOC and absorbance values were occasionally elevated during individual exposures (i.e., AMS18, August 5–7, WSOC = 7.2 µg C m^{-3}, Abs_{365} = 7.7 m^{-1}) receiving limited industrial but high wildfire atmospheric transport (Figure C5), while MAE_{365} displayed limited patterns in relation to wildfire smoke events. Moreover, WSOC and Abs_{365} were moderately correlated (Spearman $\alpha < 0.05$, $R_S = 0.30$).

Table 4.2 Summary of active sample variables (with corresponding MDL; ng m^{-3}) measured during the study period (July 19–Aug 10) at each monitoring location. Median (and normalized median absolute deviation in-parenthesis) for each variable and site are shown. Sampling locations are ordered according to latitude (N to S).

Analyte (ng m^{-3})	AMS01 (n = 9)	DP2050 (n = 11)	AMS06 (n = 8)	AMS07 (n = 3)	AMS18 (n = 7)	MDL (ng m^{-3})
WSOC	3907.4 (33.0)	6156.1 (21.6)	3329.2 (14.5)	7667.0 (63.7)	4091.6 (28.8)	6.3
DIC	469.7 (15.8)	1047.4 (17.3)	476.8 (25.7)	979.8 (58.7)	461.8 (41.5)	20.6
TDN	475.9 (75.8)	883.4 (42.7)	372.1 (50.2)	1569.9 (63.3)	732.9 (17.8)	1.9
NO_3^-	325.7 (55.1)	845.6 (67.3)	530.3 (67.0)	734.9 (94.5)	109.0 (44.6)	18.8
SO_4^{2-}	900.7 (58.0)	2931.8 (54.6)	1113.5 (73.5)	1275.2 (87.8)	301.2 (12.0)	3.3
Cl^-	9.8 (78.7)	74.9 (47.7)	81.7 (67.5)	79.3 (58.2)	20.2 (42.4)	2.4
Na	64.3 (46.1)	194.4 (44.5)	58.7 (85.4)	55.9 (21.4)	15.7 (44.6)	1.9
Mg	52.2 (53.5)	119.7 (25.7)	34.1 (22.3)	122.9 (77.3)	19.7 (48.0)	1.6
P	7.8 (41.7)	15.1 (12.6)	9.6 (14.5)	10.7 (79.4)	5.0 (30.1)	0.4
S	303.6 (32.1)	710.3 (51.2)	203.9 (31.0)	244.8 (30.9)	200.8 (12.8)	0.8
K	89.7 (19.8)	91.4 (42.4)	121.5 (39.6)	100.8 (51.2)	44.9 (25.7)	1.1
Ca	772.2 (76.8)	1938.4 (22.1)	592.9 (5.9)	1558.3 (87.9)	315.9 (45.1)	3.3
V	0.11 (57.9)	0.20 (30.6)	< 0.1 (78.7)	< 0.1 (78.7)	< 0.1 (69.1)	< 0.1
Cr	0.8 (58.8)	1.9 (9.2)	0.5 (62.8)	1.8 (93.5)	0.4 (9.4)	0.1
Mn	3.3 (48.9)	8.5 (30.9)	4.5 (42.5)	8.4 (70.8)	1.1 (34.8)	0.1
Fe	3.7 (44.6)	8.8 (28.6)	1.9 (50.9)	2.5 (36.2)	1.8 (34.9)	0.2
Zn	3.4 (30.8)	5.0 (80.4)	8.9 (27.8)	3.8 (34.3)	2.8 (14.5)	0.4
Sr	1.7 (60.4)	4.8 (22.2)	1.6 (77.5)	0.8 (32.1)	0.2 (191.0)	0.2
Abs_{365}[a]	4.1 (44.5)	7.5 (29.8)	3.1 (28.0)	4.5 (47.0)	3.2 (45.1)	0.2
MAE_{365}[b]	1.1 (40.0)	1.0 (45.6)	0.9 (25.7)	0.9 (23.8)	1.0 (29.6)	-

[a] Reported as m^{-1}
[b] Reported as m^{-2} g C^{-1}

4.3.3 Fluorescence

The EEMs produced from the TSP samples frequently displayed peak fluorescence (> 30 QSU) within the λ_{Ex} and λ_{Em} wavelength ranges of 210–350 nm and 390–430 nm,

respectively. Moreover, secondary peaks (> 20 QSU) were observed within the excitation range of 200–250 nm, and emission range of 250–400 nm. Fluorescent scans of raw bitumen and dry MFT materials produced strong peaks (> 30 QSU) in the similar region of λ_{Ex} of 200-250 nm and λ_{Em} of 250-400 nm, and limited fluorescence within the higher range (λ_{Ex} of 210-350 nm and λ_{Em} of 390-430 nm) (Figure C6). Similar scans of unpaved road dust materials displayed fluorescence in the λ_{Ex} of 200-250 nm and λ_{Em} of 250-400 nm regions; however, emission intensity was weak (≤ 8 QSU).

Comparative analysis of multiple PARAFAC models indicated that a model rank of three was most appropriate, that is, the data suggest three distinct classes of organic compounds were present. The three-component model displayed a high degree of fit (0.95), CC (96.2) and split-half validation (0.87) scores. The modelled components displayed clearly defined fluorescent peaks / regions, while no distinct and/or recuring residual peaks were observed within the model output (Figure 4.2).

The first fluorescent component (B1) presented two emission peaks generally classified as atmospheric HULIS in BrC literature (Dey and Sarkar, 2024; Laskin et al., 2015). Several water-quality studies have associated similar peaks with fluorophores of petrogenic and anthropogenic origin (Brünjes et al., 2022; Zito et al, 2019). Component two (B2) was reflective of PRLIS aerosols (Dey and Sarkar, 2024; Dong et al., 2014; Laskin et al., 2015), while component three (B3) was identified as PRLIS BrC with spectra similar to anthropogenic (Cao et al., 2023; Yan et al., 2020), and petrogenic (Whisenhant et al., 2022) fluorescent DOM.

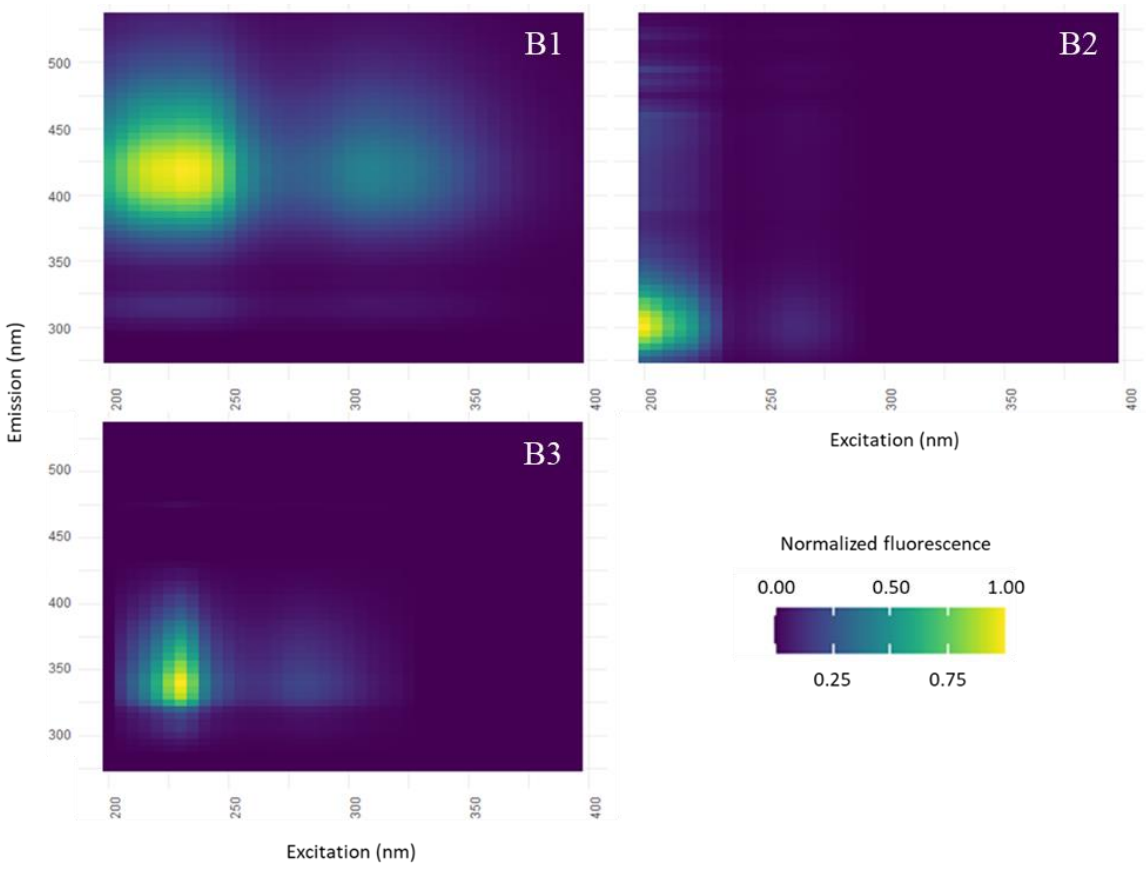

Figure 4.2 Visualization of the three PARAFAC components (B1–B3) generated from the combined TSP EEM sample set. Emission intensity values are normalized according to maximum component fluorescence.

Median normalized F_{MAX} (and normalized median absolute deviation, %) values for B1–B3 were 6.0 (100.0%), 34.6 (39.5%), and 10.4 (66.9%) QSU m^{-3}, respectively, demonstrating that the B2 amino acid-like component was the dominant fluorophore. The study average RPD calculated from duplicate exposures was 10.7, 8.5, and 9.6% for B1–B3, respectively. Both F_{MAX} and WSOC-normalized fluorescence (C_{WSOC}) values of B1 and B3 were highest at the near-field industrial sampling locations (DP2050, AMS01), followed by the mid-field urban sites (AMS06, AMS07), while the lowest values were reported at the background location (AMS18) (Figure 4.3), indicating a greater likelihood

of B1, B3 having OS-related sources. Moreover, measured fluorescence at DP2050 and AMS01 was significantly higher (Kruskal-Wallis; $\alpha < 0.05$) than AMS18, further indicating that OS operations were a dominant source of B1 and B3. The second fluorescent component (B2) displayed a distinct decay in fluorescence intensity as a function of distance from OS operations. Although B2 PRLIS fluorescence was significantly elevated in DP2050 compared to all down-field sites (excluding AMS07 due to small sample size), comparison of the remaining sampling locations (including AMS18) revealed insignificant differences in measured fluorophore intensity. High relative fluorescence at the background station suggested that a broader, regional (non-OS) source contributed to B2 in the study region.

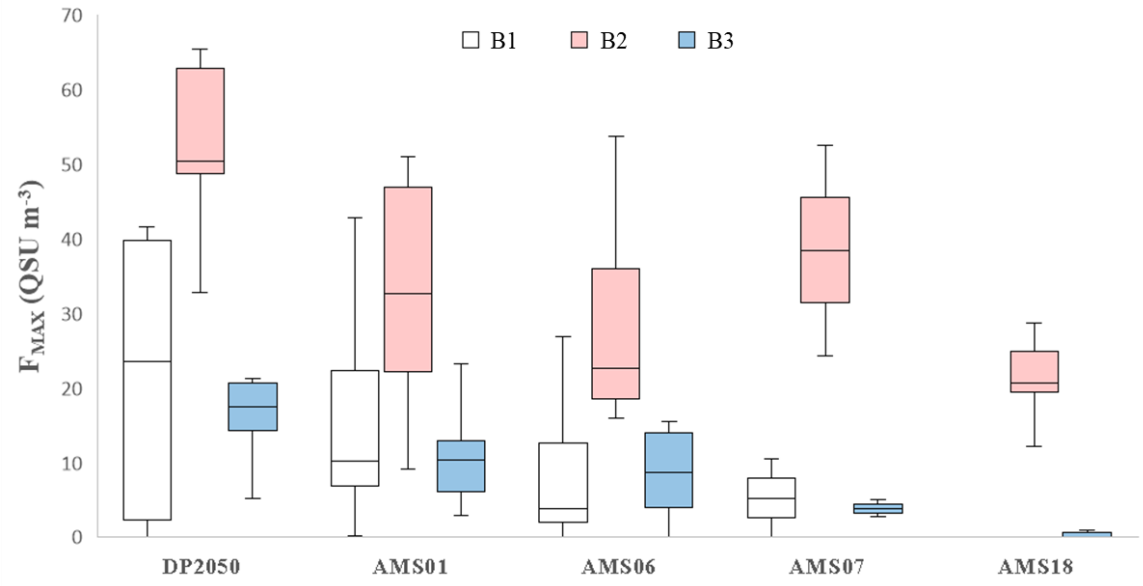

Figure 4.3 Distributions of component (B1–B3) fluorescence (QSU m^{-3}) measured at each sampling location during the study period (July 19–August 10).

Both B1 and B3 displayed strong positive correlations (R_S = 0.77 and 0.88, respectively) with T_{OS} (Figure 4.4; Table C3), suggesting fluorescence was elevated when samplers

received atmospheric transport from OS operations. As specific examples, two Mildred Lake exposures (August 6–8, 8–10) with distinctly high B1 and B3 (> 100 and > 38 QSU m^{-3}, respectively) received strong SW winds (≥ 10 km h) that passed over adjacent (~1 km from site) tailings ponds, open pit mines, and active upgrading facilities (Figure 4.5). High F_{MAX} exposures at AMS06 between August 4–6 coincided with N-E winds passing over upwind facilities (Figure C7). Conversely, when samplers received atmospheric transport from undeveloped / forested regions, B1 and B3 were markedly lower (Figure 4.5). Although generally elevated when downwind of OS facilities, B2 was occasionally heightened when sites received non-industry trajectories (Figure C5). This inconsistency is reflected by the comparatively weaker correlation between T_{OS} and B2 fluorescence (R_S < 0.62). The WSOC-normalized fluorescence ($B1_{WSOC}$–$B3_{WSOC}$) displayed spatial trends relatively similar to B1–B3 (Figure C8).

Fluorescent components B1 and B3 varied independently of wildfire transport; for example, low B1 and B3 (< 0.5 and 5.2 QSU m^{-3}, respectively) were recorded during the high-smoke event at DP2050 (July19–20; Figure C5), while some of the highest F_{MAX} values were recorded during relatively smoke-free exposures at the same site (August 8–10; B1 = 137.6 QSU m^{-3}, B3 = 20.1 QSU m^{-3}). Alternatively, high B2 concentrations frequently occurred during wildfire events, where back-trajectories displayed winds originating from fire-affected regions in BC or Saskatchewan (Figure C5).

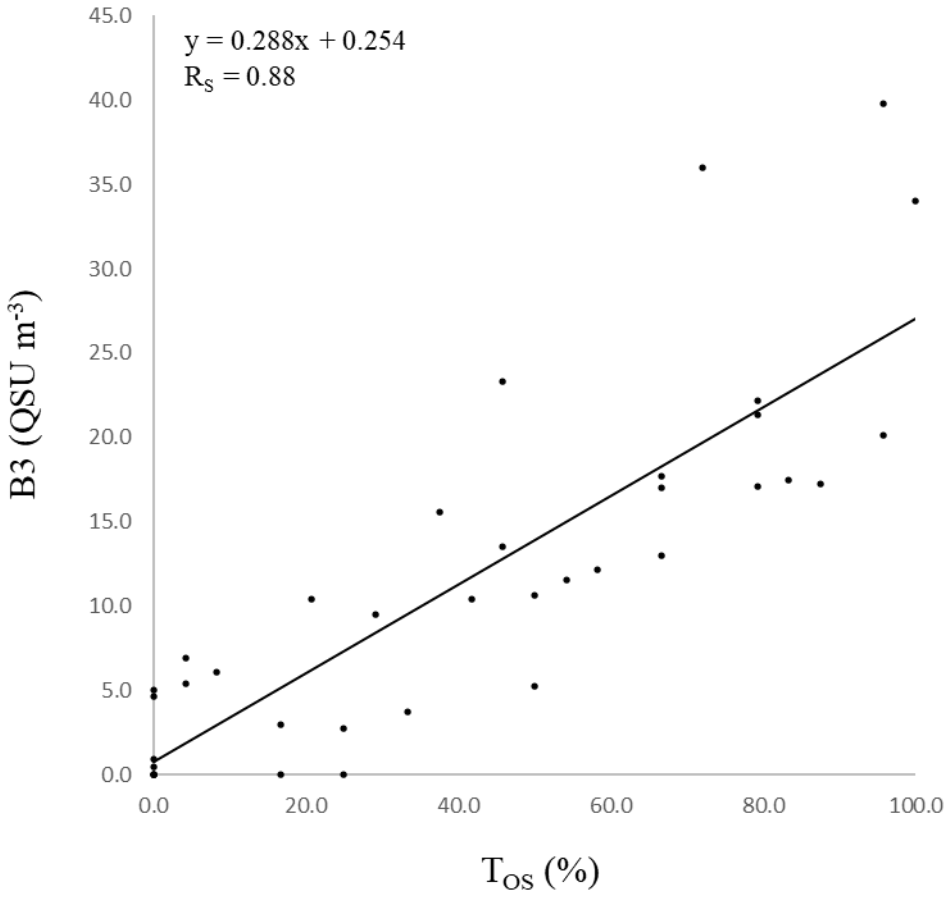

Figure 4.4 Bivariate comparison of active sampler measured B3 fluorescence (QSU m^{-3}) and corresponding OS trajectory frequency (TOS; %) estimates throughout the study period. The line of best fit and corresponding regression equations with Pearson correlation coefficient (R_S) is displayed.

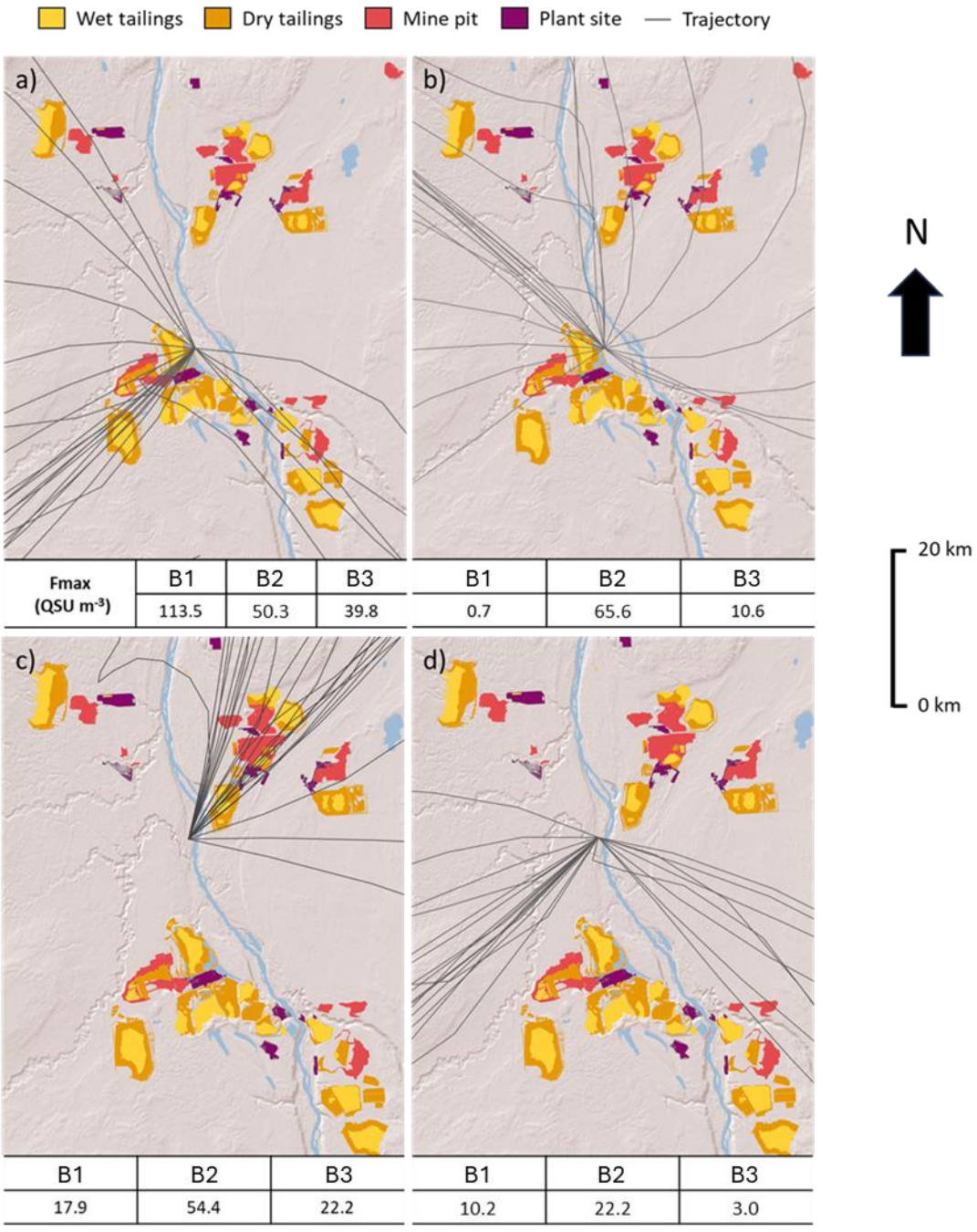

Figure 4.5 Spatial distributions of 48 h atmospheric back-trajectories (black lines) converging at sampling locations during selected exposure periods, including: a) DP2050; August 6–8, b) DP2050; July 29–31, c) AMS01; August 4–6 and, d) AMS01; July 21–23. Normalized F_{MAX} values of B1–B3 (QSU m^{-3}) measured during each exposure are shown

beneath the corresponding trajectory plots. The spatial boundaries of various OS facilities, including wet tailings (yellow), dry tailings (orange), open mine pits (red), and plant sites (purple) are shown (ESRI 1995-2024).

4.3.4 Comparison of fluorophores against supplementary TSP variables

Comparison against continuous station data found that B1 and B3 were positively correlated (Spearman; $\alpha < 0.05$) with most pollutant species (Table C3) while B2 displayed comparatively weaker correlations with continuous data. Evaluation of the complete TSP dataset found that B1 was strongly (positively) correlated ($R_s > 0.70$) with NO_3^-, SO_4^{2-}, Na, Mg, S, V, and Sr; B3 displayed similar trends, with additional correlations with Ca, P, and Mn. Moreover, B2 was moderately correlated with WSOC, DIC, Na, Mg, P, S, Ca, V, Cr, Mn, and Sr (Table C4).

Cross-validation confirmed a two-component PLS-R model that produced a relatively strong R^2Y (cumulative $R^2Y = 0.73$) and the highest cumulative Q^2Y value (0.57). The first modelled component (PLS1, $R^2Y = 0.49$) was primarily defined (VIP > 1) by NO_3^-, SO_4^{2-}, Na, Mg, P, S, Ca, V, Mn, Sr, and T_{OS}, while the second component (PLS2, $R^2Y = 0.24$) was characterized by WSOC, DIC, SO_4^{2-}, Na, P, V, and T_{OS}. Of these variables, Na and T_{OS} were the most important (VIP > 1.4) to PLS1 and PLS2. Considering certain OS fugitive emissions (e.g., tailings sand and haul road dust) are often Na enriched (Wang et al., 2015), these high VIP scores suggested both dimensions represented industrial sources. Moreover, PLS1 was positively correlated with variables previous linked to crustal (Mg, Ca, Mn) and bituminous (S, Sr, V) sources, which in the case of the AOSR could be reflective of bitumen and overburden excavation (Landis et al., 2012). Concerning PLS2,

the positive correlation with Na, SO_4^{2-}, and T_{OS}, could represent non-crustal industrial sources (Wang et al., 2015), while the negative correlation with WSOC and DIC could reflect non-OS carbonaceous PM emissions. Biplot visualization revealed that B1 and B3 fluorescence were positively correlated with both PLS-R components and plotted near Na (Figure 4.6); both fluorophores were notably distant from WSOC and Abs_{365}. Fluorescent component 2 displayed a strong positive correlation with the first PLS-R component, and was plotted in proximity to WSOC, DIC, Ca, Mn, and Abs_{365}. Score-plot visualization of individual exposures displayed a general separation between DP2050 and the remaining sites along the first PLS-R component axis (Figure C9). The PLS-R models generated using the WSOC-normalized component fluorescence ($B1_{WSOC}$–$B3_{WSOC}$) as Y variables were comparatively weak, as a two-component model displayed low cumulative R_2Y (0.48) and Q_2Y (0.18) scores.

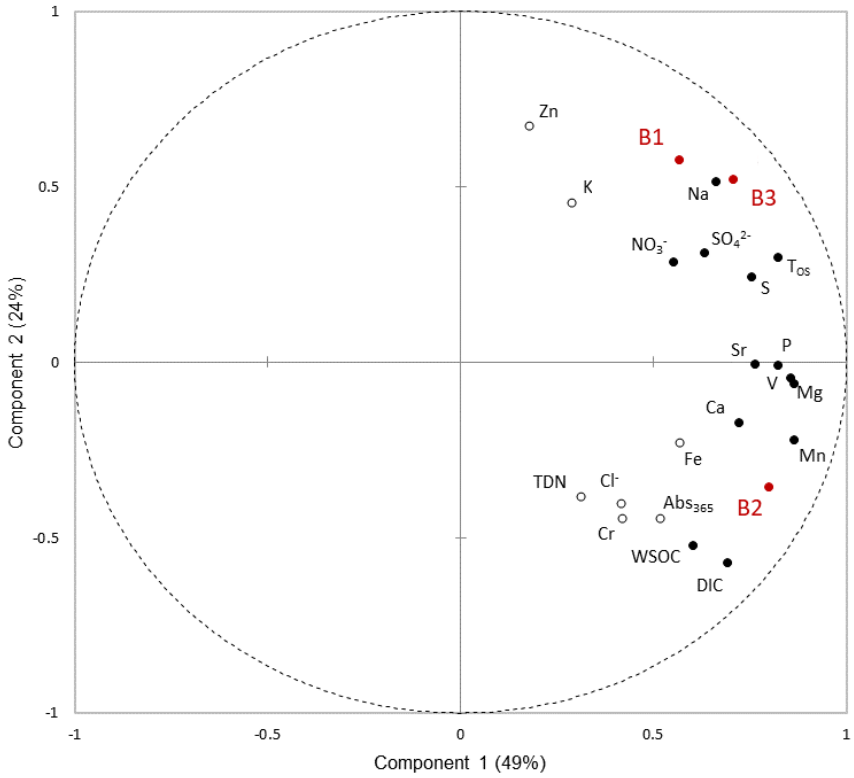

Figure 4.6 Correlation biplot displaying both X (black) and Y (red) variables in relation to the first two partial least square regression components. Filled and outlined black points indicate X variables assigned high (≥ 1) and low (< 1) VIP scores, respectively.

4.4 Discussion

4.4.1 WSOC and WS-BrC absorption

Ambient WSOC in the AOSR (including AMS18) were higher than TSP-based (summertime) measurements (WSOC < 1 μg C m^{-3}) from the remote southern Tibetan Plateau (Cong et al., 2015; Li et al., 2021) and Greenland Ice Sheet (Hagler et al., 2007), but similar to the magnitude of values (1–10 μg C m^{-3}) reported from Sinhagad, India (Kirillova et al., 2013), Bangkok, Thailand (Tang et al., 2021), Karachi, Pakistan (Chen et al., 2020), and peatland-fire affected samples from west Russia (Popovicheva et al., 2019).

Conversely, WSOC in the AOSR was generally lower than the measured concentrations (> 10 µg C m^{-3}) in New Delhi, India (Kirillova et al., 2014; Miyazaki et al., 2009).

Compared to previous studies focused on the TSP fraction, Abs_{365} in the AOSR was generally higher than summertime values reported from remote regions including the Tibetan Plateau (Abs_{365} = 0.4 m^{-1}, Zhu et al., 2018), Gobi Desert (1.9 m^{-1}, Wen et al., 2021), and the Amazon Basin (< 1.4 m^{-1}, Saturno et al., 2018), similar to observations from Bangkok (4.5 m^{-1}, Tang et al., 2021), and smaller relative to polluted urban areas in Eastern China (8.4 m^{-1}, Wen et al., 2021). Observed MAE_{365} in the AOSR was 25 – 400 % higher than the values reported across a diversity of studies (Srinivas and Sarin, 2013; Tang et al., 2021; Wu et al., 2019), demonstrating WS-BrC possessed relatively high light absorption capacity.

The moderate positive correlation between WSOC and Abs_{365} indicated that WS-BrC was an appreciable constituent of soluble organic carbon in the study region, and both TSP fractions likely shared select environmental sources. Higher WSOC and Abs_{365} values at DP2050 relative to the other study sites indicated industrial operations may contribute to regional WS-BrC; the significant positive correlation between Abs_{365} and T_{OS} further supported this assertion. However, the similarity in WSOC and Abs_{365} between the remaining stations (excluding DP2050) implied that the extent of OS influence was spatially limited, and regional sources were the primary determinant of BrC at further-field locations. Elevated WSOC and absorbance during smoke events (e.g., AMS18, August 5–7) suggested biomass combustion was a source of BrC. Regional wildfire smoke could explain why TSP-phase WSOC and Abs_{365} at the background site (AMS18) was higher

than other remote areas such as the Tibetan Plateau and Greenland ice sheet (Hagler et al., 2007; Zhu et al., 2018), but comparable to WSOC concentrations during boreal fire events in west Russia (Popovicheva et al., 2019). Insignificant differences in MAE_{365} between AOSR sites, and inconsistent MAE_{365} values during extreme fire smoke events demonstrated that aerosol light absorption capacity was not dependent upon OS or wildfire sources. Oil sands operations are large sources of

4.4.2 B1 and B3 fluorescent components

Elevated B1 and B3 fluorescence among near-field (< 5 km) industrial sites (DP2050, AMS01), and significant positive correlations with T_{OS} and continuous pollutant data indicated that OS emissions contributed to measured fluorescence. Depressed F_{MAX} values during exposures where air masses originated from non-OS (AMS01; August 21–23) and/or background regions (i.e., AMS18) further indicated that industrial operations were the primary source of B1 and B3 in the AOSR. Moreover, low emission intensity (with exception of B2) during smoke events (DP2050, July 19-20; AMS18, August 5-7; Figure C5) demonstrated that biomass combustion was not the primary source of B1 and B3 fluorescence.

Source-apportionment studies have identified bitumen excavation and hauling as a key source of PM to the AOSR; emissions that are often associated with Na, S, and V (Landis et al., 2012; 2017). Therefore, the importance of Na and SO_4^{2-} as predictors of B1 and B3 variation could further link bitumen emissions to observed fluorescence. The spectral similarity between the raw bitumen EEM and PRLIS B3 confirmed that OS material likely contributed to at least one of the observed fluorescent peaks. Resuspended oil sands

materials have been shown to significantly contribute to atmospheric loadings of total PAC species (Landis et al., 2019c), where somewhat water-soluble and low molecular weight (LMW) PACs (i.e., naphthalene, fluorene, dibenzothiophene) could fluoresce in the low excitation and emission wavelength range like B1 (Alostaz et al., 2006). Photodegradation of exposed bituminous material can produce oxygenated PACs (Yang et al., 2016), which due to their enhanced water solubility could additionally contribute to WS-BrC fluorescence.

Fugitive dust emissions from tailings ponds are an additional source of PM in the study region (Landis et al., 2012; 2019; Zhang et al., 2016). Owing to the application of NaOH to accelerate the crude extraction process (Bakhtiari et al., 2015), OS tailings contain high concentrations of Na (MacKinnon and Sethi, 1993; Wang et al., 2015). The strong association of Na with B1 and B3 (via PLS-R) provided evidence to suggest tailings dust contributed to observed fluorescence. Oil sands tailings dust has been identified as a source of 1–3 ring PACs and naphthenic acids (Landis et al., 2012; Yassine and Dabek-Zlotorzynska, 2017; Zhang et al., 2016), which can fluoresce in λ_{Ex} and λ_{Em} regions like B1 and B3 (Alostaz et al., 2006; Kaur et al., 2014). The spectral similarity between B3 and MFT reference material, and elevated B1 and B3 emission intensity during exposures downwind of tailings-sites further implied fugitive facility emissions contributed to BrC fluorescence.

Emission source profiles previously identified in the AOSR have been shown to contain loadings indicative of both crustal (Mg, Ca, Mn) and petrogenic origin (S, V, Ni) (Landis et al., 2012), largely because of the proximity and co-emission of different dust sources

associated with OS activities. The first PLS-R component, which displayed strong correlations with Mg, Ca, Mn, B1, and B3, may be broadly representative of crustal emissions (e.g., haul road dust, excavated surface-soils and overburden) from OS operations. However, separation of Mg, Ca, and Mn from B1 and B3 along the second PLS-R component (non-crustal) axis plot implied the fluorophores were co-emitted along-side these crustal sources.

Analysis of the current TSP dataset was unsuccessful in distinguishing between B1 and B3, likely indicating the co-emission of these fluorophores from industrial sources. However, unlike B3, the B1 HULIS fluorophore did not match the EEM spectra produced from the raw bitumen or MFT extracts, which suggested the two fluorophores originated from different emission sources associated with OS operations. Industrial facilities in the AOSR often contain stockpiles and beaches comprised of petroleum coke (petcoke), a carbon-rich derivative of the oil refining process that has been previously identified as a major source of particulate PAC emissions to the surrounding region (Zhang et al., 2016). Fugitive petcoke dust co-emitted from OS facilities could contribute to observed B1 fluorescence. Future BrC field studies should consider increased sampling locations near a diverse range of OS facilities, shortened exposure periods (to limit source mixing), and expanded analysis of complimentary OS indicator variables (e.g., molybdenum, nickel, PACs, [Landis et al., 2019c) to better characterize B1 and B3 source profiles in the AOSR.

4.4.3 B2 fluorescent component

Significant positive correlations between B2, WSOC and Abs_{365} suggested that the fluorophore was a key constituent of bulk WS-BrC in the AOSR, consistent with the

observed dominance of B2 over total sample fluorescence. Significantly elevated B2 at the near-field (< 1 km) Mildred Lake site, yet comparable fluorescence at AMS18 relative to the remaining stations suggested both industrial and broad regional sources contributed to BrC across the study area, consistent with what was observed for WSOC and Abs_{365}.

Occasionally elevated fluorescence during regional smoke events (e.g., July 19-20, DP2050) could indicate wildfire smoke contributed to B2 fluorescence; this is unsurprising given that biomass combustion is one of the leading sources of BrC globally (Chen and Bond, 2010). Particulate matter originating from biomass combustion can contain substantial quantities of water-soluble organic carbon (Park et al., 2013; Saarnio et al., 2010), which could explain the observed association between WSOC and B2. Future evaluations of BrC in the AOSR should additionally measure pyrogenic tracer species such as retene and levoglucosan, as these organic compounds can be used for wildfire source apportionment (Wentworth et al., 2018).

The similarity in fluorescent spectra when comparing B2 and road dust EEMs indicated the potential influence of crustal fugitive dust emissions over fluorescent PM. Haul roads throughout the AOSR are generally constructed using locally excavated limestone and bitumen, and regional road dust emission profiles often contain high loadings of DIC, Mg, Ca, and Mn (Wang et al., 2015). The observed associations (PLS-R) between these variables and B2 among the TSP samples further supported the potential influence of road dust emissions over measured fluorescence. Road dust materials can contain a diversity of chromophoric organic matter, including amino acids (Chalbot and Kavouras, 2019) and LMW PACs (in the case of hauling and industrial roads in the OS) (Landis et al., 2019c)

that can fluoresce in the low λ_{Ex} and λ_{Em} wavelength range like B2 (Christensen et al., 2005; Kim and Koh, 2020). Following initial suspension, larger diameter road dust particles are rapidly removed from the atmosphere through physical interactions with the surface environment (vegetation, man-made structures, etc.). For example, Veranth et al. (2003) found that irregular surface conditions adjacent to an unpaved road in Utah (United States) contributed to an 85% reduction of coarse particulate matter within 100 m of the emission source. In the case of the AOSR, industrial haul roads close to (< 1 km) site DP2050 contributed to elevated B2 fluorescence, while rapid removal further downwind possibly explained why B2 was relatively similar between the remaining downfield sites. In the absence of appreciable OS road dust influence, regional wildfire smoke likely became the dominant source of B2 fluorescence.

4.5 Conclusions

Optical analysis of atmospheric TSP samples collected throughout the AOSR found that OS activities were a measurable source of WS-BrC to the surrounding airshed during the summer season. Significantly higher Abs_{365} measured at the industry adjacent site (DP2050) demonstrated that OS operations likely enhanced aerosol light absorbance, which in turn could impact local solar radiation budgets and atmospheric photochemistry. However, statistically similar Abs_{365} and MAE_{365} values across the remaining stations indicated that the influence of OS emissions over WS-BrC absorbance was spatially limited and unlikely to substantially influence the regional climate during the summer. Combined EEM and PARAFAC evaluation of the TSP samples identified three distinct fluorophores (B1–B3), all of which exhibited a potential link to industrial activity. However, uniformly elevated B2 emission intensity during wildfire smoke episodes indicated biomass

combustion was also a considerable source of PRLIS aerosols to the region, while B1 and B3 were predominantly linked to OS sources.

As far as the authors are aware, this is the first study to evaluate WS-BrC in the AOSR airshed. Considering the low operational costs compared to conventional methods of mass spectrometry, UV-Vis and EEM-PARAFAC offer accessible techniques to monitor WS-BrC and initially screen for OS-sourced aerosols throughout the AOSR. Moreover, the capacity of EEM-PARAFAC to identify fluorescent species strongly linked to industry suggested that similar spectroscopic techniques could be employed to evaluate WS-BrC near other oil and gas facilities worldwide.

5. Chapter Five: Atmospheric deposition of chromophoric dissolved organic matter in the Athabasca Oil Sands Region, Canada, is strongly influenced by industrial sources during the winter months[4]

5.1 Introduction

Atmospheric deposition of water-soluble organic carbon (WSOC, also generally known as dissolved organic carbon [DOC]) serves as a ubiquitous source of labile organic carbon (C) to terrestrial and aquatic systems globally (Liptzin et al., 2022). A significant portion of atmospheric C inputs consist of chromophoric dissolved organic matter (CDOM): organic compounds capable of absorbing light within the ultraviolet and visible wavelength ranges (Laskin et al., 2015). Atmospheric CDOM primarily consists of humic-like substances (HULIS) and protein-like substances (PRLIS), which represent unresolved groups of organic species categorized according to their chemical and optical similarity to humic matter and proteins found in terrestrial and aquatic environments (Duarte et al., 2007; Graber and Rudich, 2006; Hudson et al., 2007). Note that these designations (HULIS, PRLIS) do not necessarily indicate a recent biological origin, rather, they are classifications based on chemical structure.

Although relatively understudied, dry deposition of chromophoric organic matter to lakes systems has been shown to significantly alter surface-water optical properties and light penetration (Mladenov et al., 2011; Zhang et al., 2014). Owing to its light absorbing

[4]Blanchard, D., Gordon, M., Dang., D. H., Makar, P. A., Kirk, J., Aherne, J. (2025b). Atmospheric Deposition of Chromophoric Dissolved Organic Matter in the Athabasca Oil Sands Region, Canada, is Strongly Influenced by Industrial Sources During the Winter Months. *Environmental Pollution*, 371, 125936, https://doi.org/10.1016/j.envpol.2025.125936

properties, CDOM deposition reduces snowpack albedo, which in turn can enhance snow melt rates, regional surface warming (Usha et al., 2022; Zhou et al., 2022), and ultimately impact radiative forcing processes (Jacobson, 2004). The environmental sources of atmospheric CDOM are diverse, including bioaerosols, soil erosion (Andreae et al., 1997; Deng et al., 2022; Rizzo et al., 2013), biomass burning (Ramanathan et al., 2007), fossil fuel combustion, and anthropogenic activities (Bond, 2001; Shen et al., 2023; Yan et al., 2017). The concentration and structure of CDOM in deposition often varies seasonally, largely in response to shifting emission sources, rainfall volume, photochemistry, and airmass transport (Li et al., 2020).

It has been well established that bitumen mining and processing operations in the Athabasca Oil Sands Region (AOSR) in north-eastern Alberta, Canada, are a substantial source of organic emissions to the atmosphere (Jariyasopit et al., 2021; Liggio et al., 2016). Exposed bitumen, tailings ponds, petroleum coke stockpiles, and upgrading facilities emit gaseous polycyclic aromatic compounds (PAC) (Jariyasopit et al., 2018; Qiu et al., 2018); open pit mines, mining fleet emissions, and petroleum coke generate organic-rich particulate matter containing high PAC loadings (Chibwe et al., 2021), while fugitive dust from excavated earth and haul roads can suspend soil particulates likely containing humic matter (Jariyasopit et al., 2021; Landis et al., 2019a). A substantial portion of organic emissions from OS sources inevitably renter the surface environment via wet and dry deposition (Landis et al., 2019c; Liggio et al., 2024); many of these deposited species possess light-absorbing and fluorescing properties, generally due to the presence of conjugated aromatic structures (Yamaguchi et al., 2008). Blanchard et al. (2024) found that oil sands (OS) operations were a measurable source of CDOM-containing aerosols, defined as water-

soluble brown carbon (WS-BrC). Despite the established contribution of OS activity to atmospheric CDOM, there was limited knowledge regarding the spatial and seasonal variation of CDOM deposition throughout the AOSR.

Ultraviolet – visible (UV-Vis) and excitation emission matrix (EEM) fluorescence spectroscopy are robust techniques commonly employed to characterize atmospheric CDOM (Shen et al., 2023; Zhang et al., 2014). Complex EEM datasets can undergo processing via Parallel Factor Analysis (PARAFAC; Bro, 1997); a multivariable model that can identify the excitation and emission peaks of spectrally distinct fluorescent molecules (fluorophores). Fluorescence EEM spectroscopy and PARAFAC modelling has been successfully used to identify WS-BrC originating from a variety of biogenic and anthropogenic sources (Harsha et al., 2023; Wu et al., 2019; Zito et al., 2019).

Here, we evaluate the spatial and temporal variation of CDOM deposition throughout the AOSR using absorbance and EEM fluorescence spectroscopy paired with PARAFAC modelling. Regional snowpack (2023), and weekly precipitation samples from three monitoring stations throughout the 2021 meteorological year (January 2021–December 2021) were collected for optical and elemental analysis. Regional snowpack was representative of wintertime dry and wet (bulk) atmospheric deposition, while weekly precipitation samples reflected annual wet-only deposition. The resulting datasets were further evaluated to identify the potential emission sources contributing to regional CDOM deposition.

5.2 Methods

5.2.1 Study area

The AOSR is situated within a Boreal Plains ecozone, a northern landscape predominantly comprised of peatlands and boreal forests. Within the study area lies the Athabasca oil sands deposit, an expansive bitumen reserve that covers a surface area of ~140,200 km^2. Oil and gas companies, such as Syncrude, Suncor, and Imperial Oil, have established industrial facilities over these deposits to extract and upgrade bitumen to crude oil material. The major OS facilities are located along the eastern and western banks of the Athabasca River, which flows northward through the AOSR. Industrial activity in the AOSR has steadily grown over the last decade; crude bitumen production from in-situ and surface-mining operations combined has increased from 331.4 x 10^3 cubic meters per day (m^3 d) in 2013 to 517.6 x 10^3 m^3 d and 542.1 x 10^3 m^3 d in 2021 and 2023, respectively (AER, 2024). Annual bitumen production only increased by ~ 5% between 2021 and 2023, hence interannual variation in industrial emissions were not likely responsible for any observed differences between snowpack (2023) and weekly precipitation (2021) datasets. The largest municipalities in the region are Fort McMurray (pop. ~ 70,000) and Fort McKay (pop. ~ 700); the former is located ~ 50 km south of major OS operations while Fort McKay sits along the western bank of the Athabasca River, situated between several major industrial facilities (Figure 5.1).

The study area experiences a sub-arctic climate with cold, dry winters and warm summers. According to 1981–2010 climate normal data from Fort McMurray, monthly average temperatures ranged from – 17.4°C (January) to 17.1°C (July), while annual average

temperature was 1.0 °C. The region receives 418.6 mm of precipitation annually, the majority of which (68.6%) falls between May and September.

5.2.2 Sample collection, water quality, and elemental analysis

During March 2023, snowpack samples were collected by Environment and Climate Change Canada (ECCC) from 45 sites located at varying distances from the major AOSR developments (Figure 5.1). A lichen biomonitoring study by Landis et al. (2019c) identified 17 emission sources (i.e., upgrader facilities, active mines, petroleum coke stockpiles) that can substantially contribute to pollutant deposition throughout the AOSR during the winter (Supplementary material Table D1). Approximately 90% of total PAC deposition released from major OS activities was measured at monitoring sites within 25 km of the nearest OS source; as such, snowpack sites in the current study were classified by distance from the nearest OS emission source, these included near-field (< 25 km, n = 28) and far-field (> 25 km, n = 17) locations.

Sites were accessed by helicopter, and samples were collected ~ 100 meters (m) upwind from the landing site. Using an acid washed stainless steel corer (10 cm internal diameter), snowpack cores were collected from the cleaned edge of a snow pit (excavated using acid washed stainless-steel shovels and a Teflon scraper) and transferred to a 13 L high densify polyethylene (HDPE) pail (Gopalapillai et al. 2019; Kirk et al. 2014). The standard two-person "clean hands, dirty hands" sample collection method was followed during all field operations (US EPA, 1996). The weight and depth of the 10 cores were recorded at each site to determine snow water equivalence (SWE, kg m^{-2}), which were subsequently used to

calculate deposition loadings. Three snowpack sites were sampled in duplicate, and seven field blanks were included in the sampling campaign.

Snowpack samples were melted and processed at the Canada Center for Inland Waters (CCIW) in Burlington (Ontario, Canada) and subsequently transferred to the National Laboratory for Environmental Testing (NLET; Burlington, Ontario) for nutrient, major ion, and elemental analysis. The NLET is approved by the Canadian Association for Laboratory Accreditation and is ISO 17025 certified. Following NLET standard operating practices (identified in Table D2), snow samples were analyzed for particulate organic matter (POC), particulate organic nitrogen (PON), WSOC, dissolved inorganic carbon (DIC), inorganic anions (ion chromatography) and cations (inductively coupled plasma optical emission spectrometer). Snow samples were also analyzed for 45 elements (including rare earth elements [REE]) using an inductively coupled argon plasma – collision/reaction cell mass spectrometer (Agilent 7700x ICP-MS) following the NLET TM2005/T45 and TM2005/D45W protocols (Appendix section D1). Many of the elements included in this work have been used in previous source apportionment studies in the AOSR (Gopalapillai et al., 2019; Landis et al, 2019c); for example, Vanadium (V), Molybdenum (Mo), Nickel (Ni) are enriched within raw bitumen and its associated emissions. Analyte concentrations measured across 10 filter blanks were low, with most target elements below their respective instrument reporting detection limits (RDL; Table D3). Similarly, elemental concentrations in the seven field blank samples were either below or near the RDL. Analysis of certified reference material (LKSD-3, lake sediment, Canadian Shield, n = 10) found broadly acceptable recoveries (average element recoveries ranged between 93–103%) for all target

elements (Table D4). Comparison of duplicate snow core samples revealed generally low relative percent difference (average = 8.6%) values for the target elements (Table D4).

A 50 ml aliquot from each snow melt sample was separately transferred to an acid washed HDPE bottle, shipped to Trent university, and stored at ~ 4°C prior to optical analysis for CDOM. Five HDPE bottles filled with 50 ml of ultrapure Milli-Q water were additionally shipped from the AOSR as field blanks.

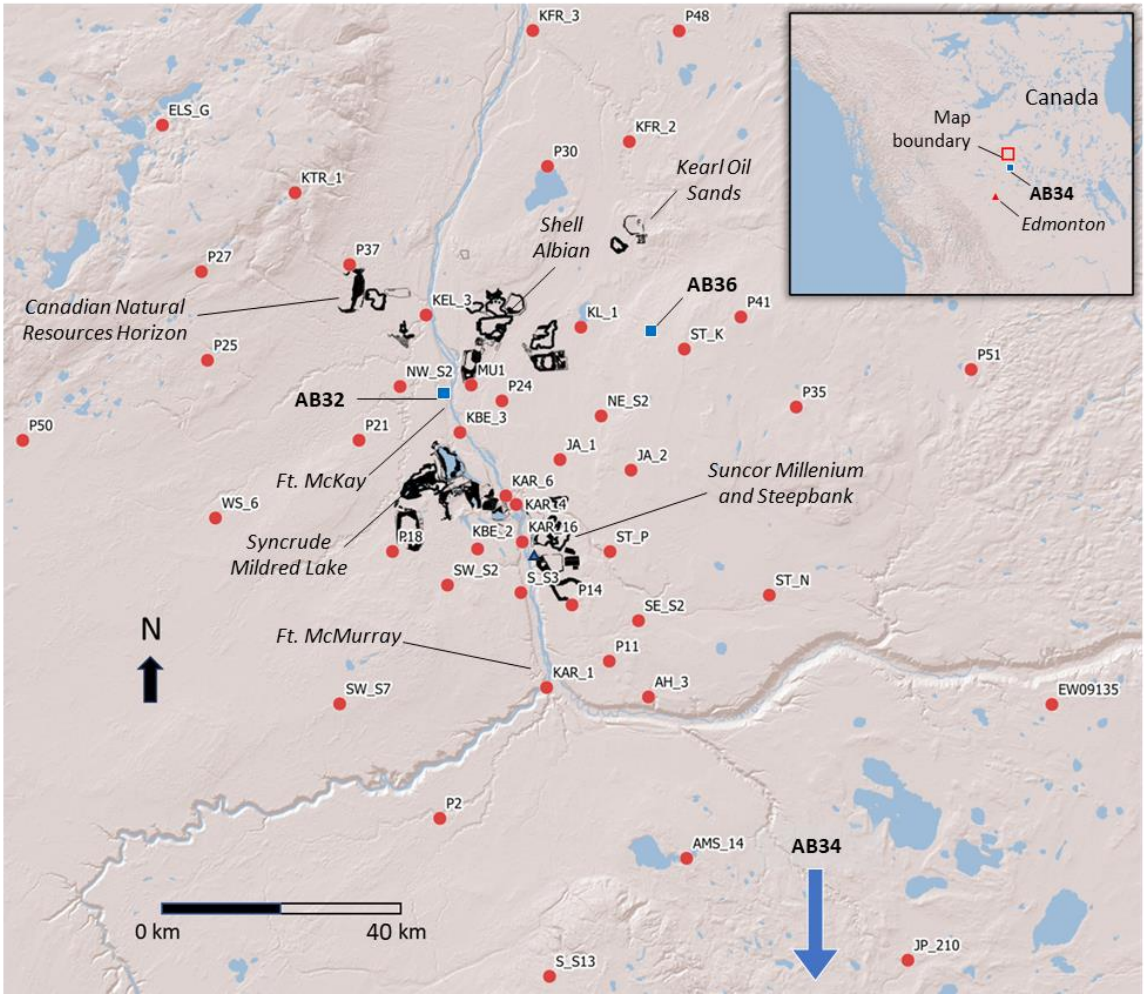

Figure 5.1 Location of the 45 snowpack sampling sites and 3 National Atmospheric Deposition Program (NADP) wet deposition monitoring stations in the Athabasca Oil Sands Region. The municipalities of Fort McMurray and Fort McKay are shown. Major oil

sands facilities and their corresponding boundaries (black) are identified. Inset map displays the location of the study area, the city of Edmonton (Alberta, Canada), and the remote NADP station (AB34), situated ~ 80 km south beyond the map boundaries.

In addition to the above samples, measurement data were collected from regional National Atmospheric Deposition Program (NADP) sites. The NADP operates a network of deposition monitoring stations distributed throughout North America, including three stations (Fort McKay, Wapasu, and Stony Mountain) located within or adjacent to the AOSR. The first of these stations (AB32), located near the community of Fort McKay, was situated < 10 km southwest and < 15 km north of the Shell Albian Sands and Syncrude Mildred Lake facilities, respectively (Figure 5.1). Wapasu station (AB36) was located < 20 km west of the major OS facilities along the Athabasca River, and approximately 10 km south of the Kearl Oil Sands facility (Imperial Oil). Stony Mountain station (AB34) was in a relatively remote region ~ 150 km south of the OS mining facilities.

From January 2021 to December 2021, weekly precipitation samples were collected from the three deposition monitoring stations and submitted to the NADP's central analytical laboratory for determination of acidity (pH), conductivity, calcium (Ca^{2+}), magnesium (Mg^{2+}), sodium (Na^{+}), potassium (K^{+}), ammonium (NH^{4+}), sulphate (SO_4^{2-}), nitrate (NO_3^{-}), and chloride (Cl^{-}). From each sample, 50 ml of water was also transferred to an acid-washed HDPE bottle and shipped to Trent University, for spectroscopy analysis. Throughout the study period, ten empty sample bottles or travel blanks were shipped to Trent University, filled with 50 ml of Milli-Q, and analyzed along with the precipitation samples. A filtered 20 ml aliquot from each precipitation and blank sample was used for

determination of WSOC, dissolved inorganic carbon (DIC), and total dissolved nitrogen (TDN) via a Shimadzu TOC-V analyzer.

The Wood Buffalo Environmental Association (WBEA; https://wbea.org) operate an extensive network of continuous air-quality monitoring stations throughout the AOSR. Three of these stations: Bertha-Ganter, Stony Mountain, and Wapasu are collocated with the NADP stations AB32, AB34, and AB36, respectively. Average air pollutant concentrations recorded at these three locations (corresponding to each weekly sampling period), including sulphur dioxide (SO_2), total reduced sulphur (TRS), nitrogen oxide (NO), nitrogen dioxide (NO_2), total hydrocarbons (THC), and fine particulate matter ($PM_{2.5}$) were compiled with the weekly precipitation dataset to assist with CDOM source characterization.

5.2.3 UV-Vis spectroscopy

Absorbance was measured along a range of wavelengths (λ) between 200 to 800 nm (1 nm intervals) using a Cary 100 UV-Vis spectrophotometer from Agilent Technologies. The snowpack and precipitation samples transferred to Trent University as noted above were warmed to room temperature (~ 21°C) and placed in a 1 cm (3.5 ml) Hellma® Suprasil® quartz cuvette (Hellma 101-QS) for analysis. A blank sample of Milli-Q water was first used to establish an instrument baseline. To clean, cuvettes were soaked in a 2 M HCl bath for ten minutes followed by subsequent rinses in Milli-Q water, 95% ethyl alcohol, and a final rinse in Milli-Q. Measured absorbance was converted to Naperian absorption coefficient units (a_λ, m^{-1}) by the following (Green and Blough, 1994):

$$a_\lambda = 2.303 \frac{A(\lambda)}{l} \quad \textbf{Eq. 5.1)}$$

where A was the absorbance (unitless) at wavelength λ, 2.303 was the conversion factor from $\log_{10}$ to $\log_e$, and l was the optical path length (m). The Naperian absorption coefficient at 254 nm (a_{254}) is frequently used as a proxy for absorbent CDOM within aqueous snowpack and precipitation samples (Vione et al., 2021; Wagner et al., 2019). The mass absorption cross section of snowpack at 365 nm (MAC_{365}; m^2 g C^{-1}) was calculated by following Bosch et al. (2014) and Yan et al. (2016):

$$MAC_{365} = 2.303 \frac{A_{365}}{(C) \times l} \quad \textbf{Eq. 5.2)}$$

Where A_{365} was the measured absorbance at 365 nm (unitless) and C was the concentration of WSOC (mg C L^{-1}). The MAC_{365} metric is frequently used to assess the radiative forcing potential of CDOM within snowpack (Zhang et al., 2020; Yan et al., 2016).

5.2.4 Fluorescence spectroscopy and PARAFAC

Fluorescence analyses was conducted using a Cary Eclipse spectrophotometer set to the three-dimensional EEM scan and signal to reference (S/R) acquisition modes. Liquid snowpack and precipitation samples were filtered (nylon; 0.45 µm, adjusted to a pH ~ 6.5 (using 0.01 M sodium hydroxide or hydrochloric acid)), and then placed in a 1 cm, 3.5 ml Hellma® Suprasil® quartz cuvette (Hellma 101-QS) for analysis. Excitation (λ_{ex}) and emission (λ_{em}) scans (5 nm intervals) ranged from 200–450 nm and 250–600 nm, respectively. A Milli-Q water blank was first measured to zero the fluorometer, then subsequent blanks were scanned every fifth sample. A set of quinine sulphate standards were prepared each day to create a calibration curve (1–100 ppb quinine sulphate in 0.5 M sulphuric acid) to convert fluorescence intensity measurements into quinine sulphate units

(QSU) (Sui et al., 2017). To minimize the potential influence of the inner filter effect (IFE) over the fluorescence spectrum, all filter extracts were confirmed to have an $a_{270} < 0.05$ (Trubetskoj et al., 2018). Triplicate EEM scans of 5 snowpack and 16 weekly precipitation samples were carried out during the study period. Following Blanchard et al. (2024), fluorescence data were processed via the R package "staRdom", which was used for blank and spectrum correction (Pucher et al., 2021).

Combined EEM and PARAFAC analysis is commonly used to evaluate the optical and structural characteristics of environmental CDOM, as the modelling technique can identify the excitation and emission peaks of multiple spectrally distinct fluorophores (i.e., HULIS, PRLIS) within EEM scans (Harsha et al., 2023; Wu et al., 2019). Here, the staRdom package was used to generate a PARAFAC model, which decomposed the three-dimensional EEM dataset into a series of tri-linear elements a_{if}, b_{if}, and c_{kf} to identify fluorescent components (i.e., fluorophores) contained within the environmental samples (Bro 1997):

$$x_{ijk} = \sum_{f=1}^{F} a_{if} b_{jf} c_{kf} + e_{ijk} \quad \textbf{Eq. 5.3)}$$

Score values in a_{if} represent the relative fluorescence intensity of fluorophore f in sample i, the elements b_{if} and c_{kf} represent the modelled emission (j) and excitation (k) loadings (i.e., wavelength coordinates) of *f*, while F is the total number of modelled fluorescent components. Utilizing the residual element e_{ijk}, the PARAFAC model applies an alternating least-squares optimization technique to find the function that best approximates the dataset (Bro, 1997) by minimizing the residuals.

The appropriate number of modelled components was selected based on four validation tools, including: 1) visual peak inspection, 2) EEM residual plots, 3) split-half analysis, and 4) core consistency (CC). These validation tools and their corresponding procedures are described in further detail in Chapter 3, section 2.4

The fluorescent components generated from the separate snowpack and weekly precipitation datasets were compared against each other and to similar fluorophores observed from WS-BrC aerosols sampled in the AOSR during the summer of 2021 (Blanchard et al., 2024). The degree of similarity between individual fluorophore spectra (including λ_{Ex} and λ_{Ex}), and hence the process by which common spectra were grouped together, was through evaluation using the Tucker Congruence Coefficient (TCC), where a score of 1 indicated identical spectra (Pucher et al., 2021). Moreover, TCC scores between 0.85–0.94 were interpreted to represent good spectral similarity between fluorophore pairs, while values > 0.95 indicated a high degree of similarity (Lorenzo-Seva and ten Berge, 2006; Murphy et al., 2014).

Individual components from the snowpack and weekly precipitation samples were reported as maximum fluorescence emission intensity (F_{MAX}; QSU) and relative emission intensity (single component F_{MAX} divided by the F_{MAX} sum of all components; %). To account for the potential influence of bulk DOM fluorescence over individual fluorophore emission intensity due to variations in DOM concentration between samples, component F_{MAX} values were divided by the corresponding sample WSOC to normalize component fluorescence (QSU mg C L^{-1}).

5.2.5 Data analysis

5.2.5.1 Calculation of deposition loads

Snowpack deposition loadings were calculated according to the methods described by Kirk et al. (2014) and Gopalapillai et al. (2019). SWE (kg m^{-2}) was determined as:

$$SWE = \frac{m_c}{\pi(r_c)^2} \quad \textbf{Eq. 5.4)}$$

where m_c was the mass (kg) of the snowpack core sample and r_c was the core radius (m). The corresponding aerial water volume (V_a, L m^{-1}) was calculated at each site according to the following:

$$V_a = \frac{SWE}{d_w} \cdot 10^3\ L\ m^{-3} \quad \textbf{Eq. 5.5)}$$

Where d_w is the density of water (kg m^{-3}). The resulting V_a estimate was multiplied by the corresponding analyte concentration (µg L^{-1} or QSU) to determine deposition loadings (µg m^{-2} or QSU m^{-2}) at each site.

Analytes measured in the weekly precipitation samples (NADP) were converted to monthly volume weighted average (VWA) concentrations by calculating the sum-product of weekly concentrations and precipitation volume, then diving the value by the total monthly precipitation volume. The wet deposition flux for each site (QSU m^{-2}, mg C m^{-2}, µg m^{-2}) was calculated by multiplying analyte concentration by the corresponding precipitation depth (mm).

5.2.5.2 Statistical analysis

The available environmental data displayed non-normal distributions (Shapiro-Wilk, $\alpha < 0.05$), therefore non-parametric tests were applied for subsequent analysis. Median values were used as a measure of central tendency and data variability was evaluated using normalized median absolute deviation (NMAD). Bivariate comparison of sample data was completed using Spearman's Rank Order correlation tests, while the Kruskal-Wallis test was used to identify significantly different sample groups. Principal component analysis (PCA) was employed for exploratory evaluation of the large multivariable data set. The resulting analysis generated linear combinations of associated variables, identified as principal components (PC), which explained a portion of the total variance within the data set.

Partial least squares regression (PLS-R) analysis was applied to assist with fluorescent component characterization, following Kothawala et al. (2014). Partial least squares analysis is a multivariable regression technique that decomposes a large set of colinear predictor (X) and response (Y) variables into a smaller series of uncorrelated orthogonal components (Eriksson et al., 2013). Modelled PARAFAC components (QSU) were assigned as Y variables while additional optical, water-quality, and elemental variables were designated as X. Details related to PLS-R model validation are described further in Chapter 3 section 2.6.

5.3.0 Results and discussion

5.3.1 Snowpack

5.3.1.1 Snowpack: Evaluation of CDOM by UV-Vis spectroscopy

Snow water equivalence measured at the 45 snowpack sites ranged from 46.8 to 117.0 kg m^{-2}, with a median value of 74.1 kg m^{-2}. Comparison of combined near and far-field sites against far-field sites found no significant difference in SWE (Kruskal-Wallis $\alpha < 0.05$; Table D3); therefore, significant differences in measured deposition loadings (between near-field and far-field sites) was not likely due to SWE. The absorbance metrics a_{254} and MAC_{365} ranged from 0.0–16.6 m^{-1}, 0 – 1.38 m^2 g C^{-1}, where the corresponding median values were 2.7 m^{-1}, 0.38 m^2 g C^{-1}, respectively. Snowpack a_{254} in the AOSR was comparable to mean values reported from the Italian Alps (2.3 ± 0.5 m^{-1}, Vione et al., 2021) and Sierra Nevada, United States (~ 2.0 m^{-1}, Beres et al., 2020). Measured MAC_{365} throughout the AOSR was relatively low compared to glacial snow from the Tibetan Plateau (mean = 1.40 ± 0.40 m^2 g C^{-1}; Yan et al., 2016), but comparable to arctic snow from across Alaska, United States (mean = 0.37 ± 0.32 m^2 g C^{-1}; Zhang et al., 2020).

Near-field sites in the AOSR displayed significantly higher a_{254} and MAC_{365} relative to far-field locations (Kruskal-Wallis, $\alpha < 0.05$; Table D3), which suggested that industrial activities contributed to CDOM deposition. Moreover, MAC_{365} displayed a visible spatial gradient relative to the nearest OS facilities (Figure D1) implying that industrial CDOM inputs could potentially influence snow radiative forcing in the AOSR. These spatial trends were consistent with the regional snowpack loadings of WSOC and numerous industry-

associated elements (e.g., Al, Mo, Ni, V), which were notably elevated near OS facilities (refer to Appendix section D2 and Figure D2 for further detail).

5.3.1.2 Snowpack: Evaluation of CDOM by fluorescence spectroscopy and PARAFAC

A three-component PARAFAC model displayed a high degree of fit (R^2 = 0.95), CC (97.7) and split-half validation (0.97) scores. The modelled components displayed clearly defined fluorescent peaks, while no distinct and/or recuring residual peaks were observed within the model output, indicating that the model effectively explained dataset variability (Figure 5.2). Snowpack fluorescent component one (S1) displayed primary and secondary peaks at λ_{ex}: 245 nm, λ_{em}: 430 nm and λ_{ex}:325 nm, λ_{em}:430 nm, respectively. Fluorescence within this spectral region has been attributed to HULIS when detected in atmospheric samples (Graber and Rudich, 2006). Modelled components two (S2) and three (S3) displayed peaks at λ_{ex}: 230 nm, λ_{em}: 340 nm, and λ_{ex}:200 nm, λ_{em}: 290 nm, respectively; the spectra of both fluorophores were consistent with PRLIS (Wu et al., 2021). The S3 spectra was notably similar (TCC > 0.98) to the B3 fluorophore previously identified within summertime BrC aerosols from the AOSR (Chapter 4). The BrC fluorophore was shown to be broadly associated with OS industrial sources, including fugitive bitumen and haul road dust, tailing sands, and vehicle emissions.

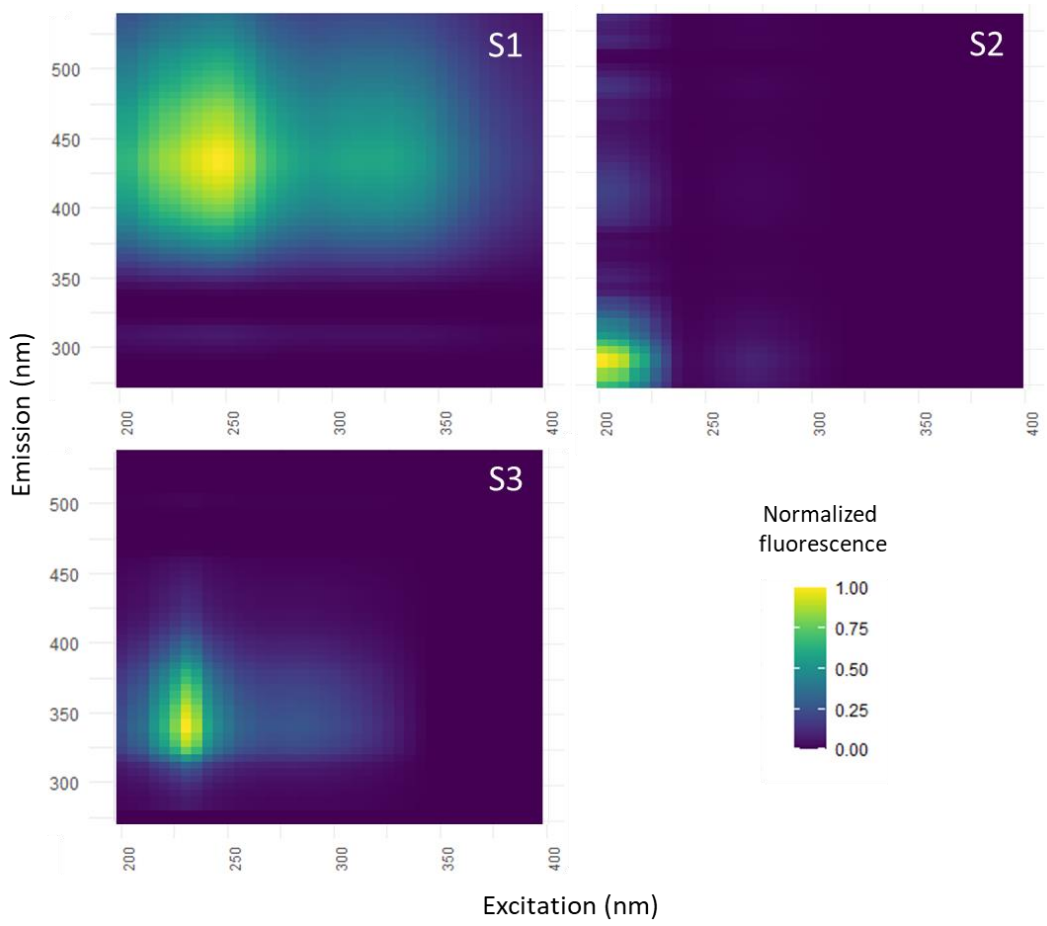

Figure 5.2 Visualization of the three PARAFAC components (S1–S3) generated from the snowpack fluorescence samples. Emission intensity values were normalized according to maximum component fluorescence.

The MDL for fluorescent components S1–S3 was 0.28, 0.74, and 0.15 QSU, respectively; the measured coefficient of variation (%) between triplicate samples remained below 6% for all three fluorophores. All available snow samples presented S1 and S2 F_{MAX} values above the MDL, while ~ 96% of S3 values were above the limit. S1 to S3 deposition loads ranged from 0.8–1989.8, 15.1–2227.8, and 0–3255.5 QSU m^{-2}, with median values of 405.8, 862.8, and 281.5 QSU m^{-2}, respectively. The median relative emission intensity of these fluorophores was 22.6, 56.2, and 18.6%. All three components and corresponding

WSOC-normalized values ($S1_{WSOC} - S3_{WSOC}$) were significantly higher (Kruskall-Wallis, $\alpha < 0.05$) among near-field sites compared to far-field locations (Table D3 and D5) and decreased as a function of distance from the nearest OS facility boundary (Figure 5.3 and D3), indicating an OS source. The highest snow loadings were consistently observed at KAR6 and KAR4, which were adjacent to major OS sources, including the Suncor upgrader, tailings facilities, and open pit mines. Both S2 and S3 were frequently elevated at sites < 5 km of mine pits and tailings facilities (Figure D3). Moreover, relative S3 emission intensity was significantly elevated among near-field sites (Table D3) and was responsible for ~ 50% of total sample fluorescence at the near-field sites KAR6 and P14, the later being located adjacent to a tailings facility.

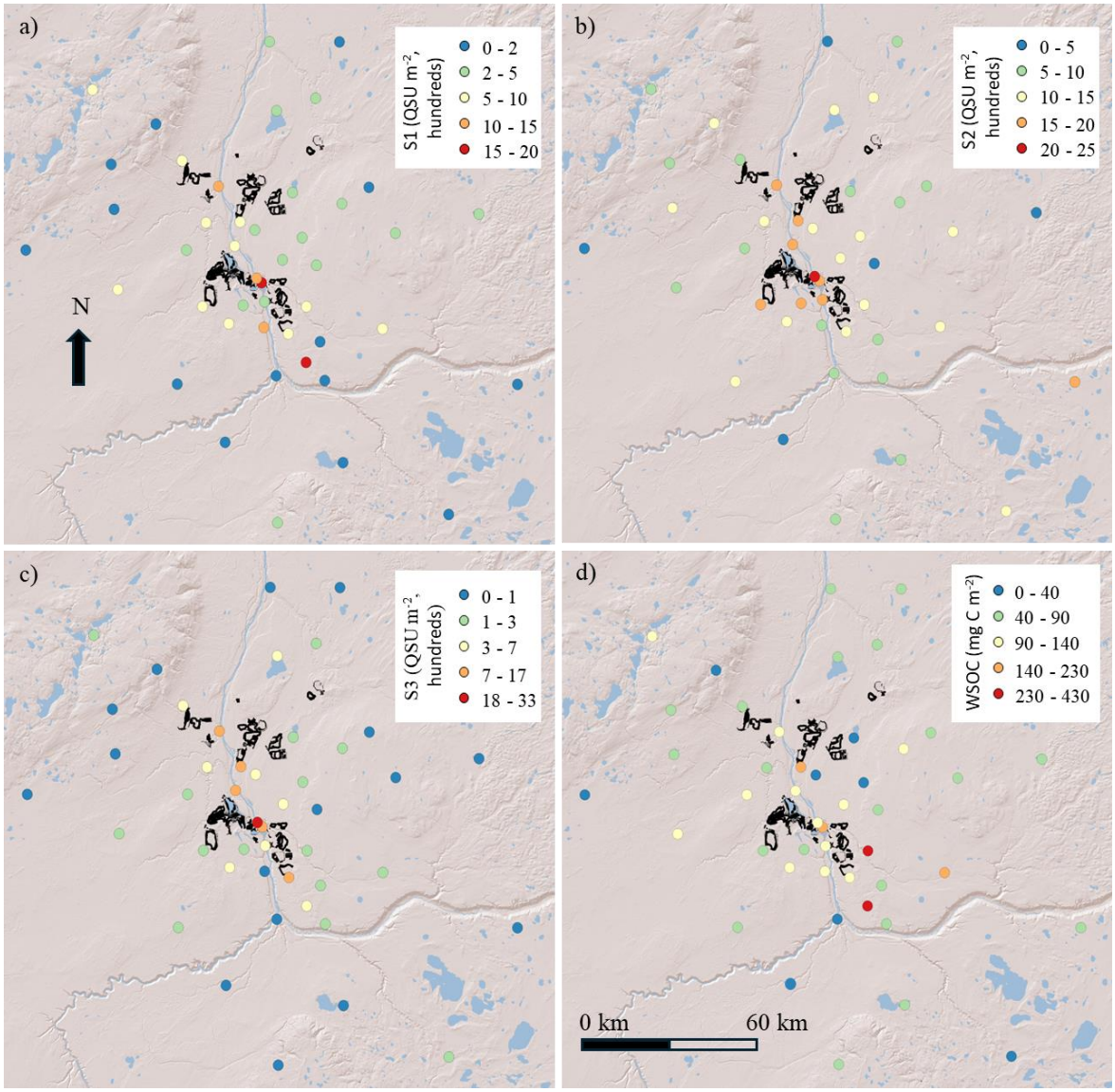

Figure 5.3 Deposition loadings of a) S1, b) S2, c) S3 (QSU m^{-2}, hundreds), and d) water soluble organic carbon (WSOC; mg C m^{-2}) throughout the Athabasca Oil Sands Region. Oil sands facility boundaries are represented by the black polygons.

5.3.1.3 Snowpack: Bivariate and multivariate analysis

Bivariate analyses of the snowpack highlighted a positive correlation (R_S = 0.89) between a_{254} and WSOC. Positive associations between S1 and both WSOC (RS = 0.81) and a_{254} (R_S = 0.65) demonstrated that S1 HULIS was an important component of snowpack

CDOM. In contrast, S2 and S3 displayed insignificant correlations with WSOC and a_{254}, which indicated that the two PRLIS components (representing the majority of fluorescent emission intensity) varied independently from bulk soluble organic matter and CDOM in the region. The third fluorescent component displayed strong positive correlations (R_S > 0.84) with numerous elements such as Ba, Cr, Fe, Mo, and REEs, many of which have been previously linked to OS industrial emissions (Gopalapillai et al. 2019; Landis et al., 2019a). Numerous variables strongly correlated with S3 displayed a high degree of collinearity, as the correlation coefficient between most variables was > 0.95. Notably, S2 displayed limited significant correlations with the available environmental variables (e.g., Ba - S2: R_S = 0.45; Cr - S2: R_S = 0.53, Fe - S2: R_S = 0.55). The corresponding WSOC-normalized fluorescent components ($S1_{WSOC}$–$S3_{WSOC}$) displayed weaker, yet statistically significant correlations with the same environmental variables.

The majority of dataset variation (75.5%) was explained by two principal components (PC), the first of which ($PC1_{snow}$ = 67.6%) displayed positive variable loadings including S1, S2, S3, PON, Ca^{2+}, Cl^-, SO_4^{2-}, Na^{2+}, WSOC, DIC, most metals, and REEs (Figure 5.4). The second principal component ($PC2_{snow}$ = 7.9%) presented positive loadings of a_{254}, S1, WSOC, Mg^{2+}, and Si. A two component PLS-R model produced a relatively strong cumulative goodness of fit (R^2Y = 0.67) value and the highest cumulative goodness of prediction (Q^2 = 0.61) score. Both component one (R^2Y = 0.57) and two (R^2Y = 0.09) displayed variable loadings similar to $PC1_{snow}$ and $PC2_{snow}$, respectively; the first component (PLS-1) presented high positive associations with OS-related variables including REEs, while the second (PLS-2) was characterized by a_{254}, WSOC, Mg^{2+}, Na^{2+} Si. Biplot visualization demonstrated that fluorescent S1 was closely associated with DIC,

Na^{2+}, and Mg; S3 fluorescence was surrounded by a cluster of elements including Ba, Cr, Fe, Mo, while S2 plotted comparatively distant from the available variables (Figure D4).

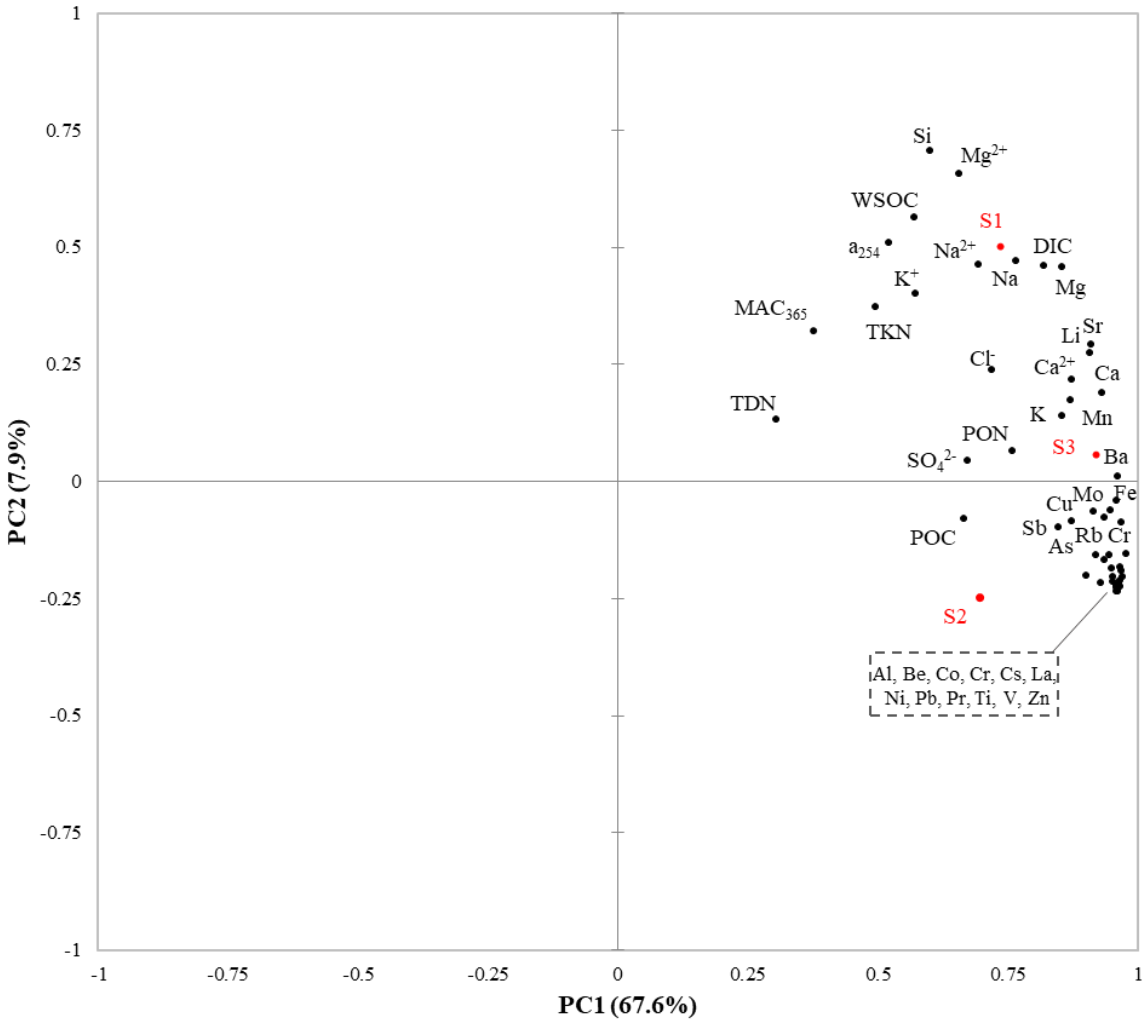

Figure 5.4 Biplot comparing $PC1_{snow}$ (67.6%) and $PC2_{snow}$ (7.9%) from the resulting principal component analysis of the complete 2023 snowpack dataset, including all geochemical and optical variables.

3.1.4 Snowpack: Identification of CDOM sources

The S3 fluorophore was positively associated with $PC1_{snow}$ and PLS-1, factors that both displayed positive element loadings (e.g., Ba, Cr, Mo, Ni, Fe, V, and REEs) frequently

linked to OS sources like raw oil sands dust, petroleum coke dust, tailings facilities, and upgrader emissions (Gopalapillai et al. 2019; Landis et al., 2019a; 2019b; 2012) Analysis of metal and PACs in AOSR snowpack samples from 2015 showed that among sites near major OS facilities, bituminous indicator metals (Mo, Ni, V) were significantly correlated with industry-sourced PACs (Chibwe et al., 2021); given their conjugated structures, these PACs could produce fluorescence in the S3 λ_{ex} and λ_{em} region. Source analysis of elemental loadings to AOSR snowpack from 2015 suggested that paved and unpaved road dust was responsible for the majority of Ca and Sr loadings to snowpack in the AOSR (Gopalapillai et al., 2019); the co-variability of these elements relative to S3 suggested that the fluorophore could also be related to road emissions (i.e., dust, vehicle exhaust) from OS facilities. Unfortunately, the high degree of collinearity between elements in the snowpack dataset made it difficult to further distinguish between specific OS emission sources.

Similar to S3, the S2 fluorophore displayed positive associations with $PC1_{snow}$ and variables previously affiliated with OS emissions, which collectively implied industrial influence. The relatively weak associations with the available snowpack variables suggested that an additional source(s) not currently represented in the dataset influenced S2 variability. Nonetheless, the source characterisation of S2 was consistent with the corresponding spatial gradients favouring elevated snowpack loadings surrounding OS facilities (Figure 5.3).

The HULIS S1 fluorophore was positively associated with $PC2_{snow}$ and PLS-2. Both of these factors were characterized by WSOC, Si, and Mg^{2+}, which have been previously linked to paved/unpaved road emissions in the AOSR (Landis et al., 2019a; Landis et al.,

2019b; Mamun et al., 2021; Wang et al., 2015); however, the low Ca and Sr loadings assigned to $PC2_{snow}$ (Figure 5.4 and D3) did not support this characterization (Gopalapillai et al., 2019). Wang et al. (2015) found that AOSR surface soils (including forest soils and excavated overburden) contained relatively high loadings of WSOC, Si, Mg^{2+}, and low Ca^{2+}. Surface soils can contain humic organic matter (Schulten and Leinweber, 2000), which possibly explained why S1 was positively associated with $PC2_{snow}$ and PLS-2. Although soil and overburden emissions are generally limited during the cold season due to frozen ground and snow cover (Landis et al., 2019a), surface disturbances through OS activities (i.e., excavation, land clearing) generate dust, which explained why S1 was also positively associated with the industrial $PC1_{snow}$ (and PLS1) and why S1 deposition loadings were highest near industrial facilities (Figure D1). Both $PC1_{snow}$ and $PC2_{snow}$ received positive a_{254} loadings which implied that dust emissions from OS activity were a primary source of bulk CDOM deposition to the AOSR during the winter.

5.3.2 Weekly precipitation

5.3.2.1 Weekly precipitation: Regional overview

Total recorded precipitation during the 2021 meteorological year was 340.5, 399.1, and 396.2 mm at AB32, AB36, and AB34, respectively. All three stations displayed increased precipitation during the spring and summer months, and a comparatively arid winter (Figure D5). Ambient air pollutant concentrations throughout the study period were generally elevated at AB32 and AB36 relative to the distant AB34 station (Table D6). Select ions (Na^{+}, Mg^{2+}, Ca^{2+}, SO_4^{2-}) displayed enhanced deposition and concentrations among near-field stations (AB32, AB36), linking these observations to anthropogenic sources (Table D6 and D7).

Annual WSOC wet deposition measured at the three NADP stations was 0.29 g C m^{-2} (AB34), 0.38 g C m^{-2}, (AB32), and 0.41 g C m^{-2} (AB46); these wet flux values were comparable to deposition reported from the remote Marshall Islands (0.63 g C m^2 yr^{-1}, Zafiriou et al., 1985), but low compared to the mean (± standard error) deposition measured in temperate regions across the globe (1.90 ± 0.13 g C m^2 yr^{-1}; Liptzin et al., 2022), and considerably lower than flux measured in a highly urbanized region in northern China (3.15 g C m^2 yr^{-1}, Xing et al., 2019). Low annual precipitation (< 400 m^{-1}) typical of northern Alberta may explain the relatively limited annual flux in the study region, as noted elsewhere (Liptzin et al., 2022).

Volume weighted average WSOC concentrations from the ASOR ranged 0.20–2.60 mg C L^{-1} (median = 0.90 mg C L^{-1}). The far-field station, AB34, displayed monthly WSOC trends consistent with other temperate regions across the globe (Liptzin et al., 2022), where the highest precipitation concentrations occur during warmer months (Figure 5.5). This seasonality is often the result of a concentration-effect due to reduced precipitation volumes during warm, dry periods; however, the study region experienced a relatively wet summer (Figure D5). Enhanced summertime biogenic productivity and biomass combustion can also enhance WSOC concentrations (Liptzin et al., 2022), and as such likely dictated seasonal WSOC concentrations at AB34. In contrast, the industry adjacent sites (AB32, AB36) displayed elevated WSOC during the colder months (Figure 5.5); this trend was unlikely due to the concentration-effect, however, given that precipitation volume and WSOC concentration were not significantly correlated.

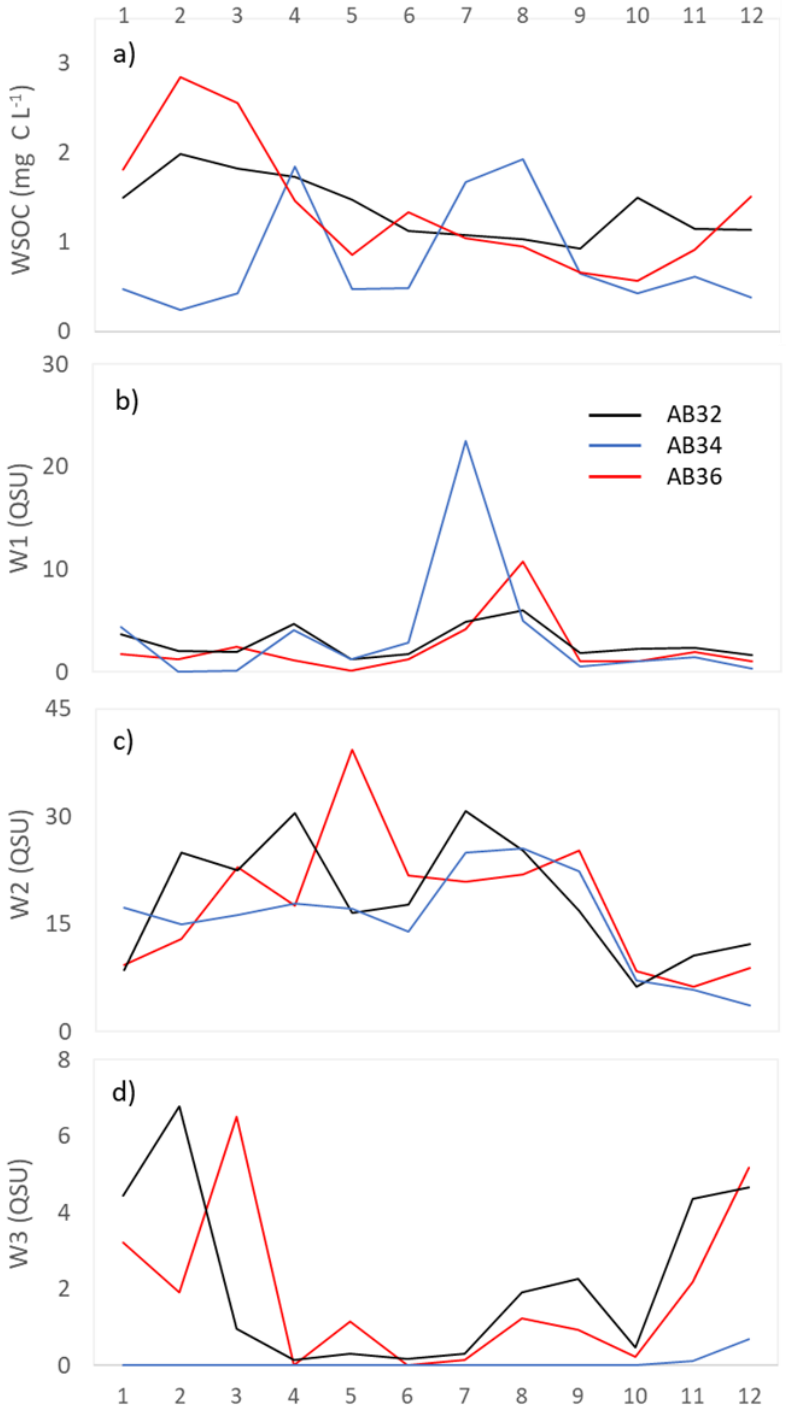

Figure 5.5 Monthly volume weighted average a) water soluble organic carbon (mg C L^{-1}), b) W1(QSU), c) W2 (QSU), and d) W3 (QSU) measured at the regional National Atmospheric Deposition Program stations (AB32, AB34, AB36) during the 2021 meteorological year (January 2021–December 2021).

5.3.2.2 Weekly precipitation: Evaluation of CDOM by UV-Vis spectroscopy

Monthly VWA a_{254} ranged from 0.5–11.8 m^{-1}, with a median of 2.0 m^{-1}. Compared to VWA values measured at the remote site (AB34), a_{254} was highest (Kruskal-Wallis, $\alpha > 0.05$) at the industry adjacent site (AB32), which suggested OS sources contributed to CDOM deposition (Table D8). Measured a_{254} was notably elevated during July and August at all stations, specifically weekly sampling periods that co-occurred with regional wildfire events (AB34, July 14 – 20: a_{254} = 20.5 m^{-1}), which implied wildfire smoke was an additional source of CDOM deposition. During the winter months when precipitation fell as snow (January – March 2021, November – December 2021) and wildfire emissions were limited, median a_{254} was 1.17 m^{-1}, and measured absorbance was considerably lower at the far-field station (Table D9). The relative abundance of CDOM within precipitation was limited; VWA a_{254} throughout the study region was low compared to the mean values (> 3 m^{-1}) reported from the northern Tibetan Plateau (Li et al., 2022), southeastern United states (Wagner et al., 2019), and Nanjing city, China (Li et al., 2020). Owing to very low absorbance values at 365 nm, MAC_{365} was not reported for the weekly precipitation sample set.

5.3.2.3 Weekly precipitation: Evaluation of CDOM by fluorescence spectroscopy and PARAFAC

A three-component PARAFAC model displayed a high degree of fit (0.94), CC (81.0), and split-half scores (0.96). Modelled component one (W1) presented primary and secondary peaks at λ_{ex}: 230 nm, λ_{em}: 430 nm and λ_{ex}: 310 nm, λ_{em}: 430 nm, spectra that were characteristic of atmospheric HULIS. The following two components (W2, W3) were

spectrally similar to PRLIS, displaying primary fluorescent peaks at λ_{ex}: 200 nm, λ_{em}: 295 nm and λ_{ex}: 225, λ_{em}: 335 nm, respectively (Figure D6). Comparison of PARAFAC spectrum loadings found that the first two modelled components (W1 and W2) were highly similar (TCC ≥ 0.95) to the corresponding S1 and S2 fluorophores identified in the 2023 AOSR snowpack samples, respectively. Comparison of the W3 and B3 fluorescent components produced a relatively weaker similarity score (TCC > 0.85). Fluorescent component 3 was spectrally comparable (TCC ≥ 0.90) to the industrial BrC fluorophore B3 observed in the AOSR by Blanchard et al. (2024), which suggested W3 was linked to OS emissions.

The MDL for fluorescent components W1 to W3 were 0.08 QSU, 0.73 QSU, and < 0.01 QSU; 94%, 81.5%, and 50.2%, of the precipitation samples were above these respective limits. The measured coefficient of variation (%) from triplicate samples remained below 7% for all three fluorophores. Monthly VWA W1–W3 fluorescence ranged from 0.0–22.6 QSU, 3.7–39.3 QSU, and 0.0–6.8 QSU, the corresponding median values were 1.7, 17.3, and 0.3 QSU, respectively.

Of the three modelled fluorophores, only W3 emission intensity was significantly different between monitoring stations (Kruskal-Wallis, $\alpha < 0.05$), where measured intensity was elevated among the AOSR sites (AB32, AB36; Table D8) during the full study period. Moreover, ~ 90% of W3 measurements at AB34 samples fell below the MDL, which implied the fluorophore did not originate from broader regional sources. Monthly VWA W1 and W2 were elevated during the summer, particularly during wildfire season (July–August) in the case of W1. During the winter months W1 was significantly higher at the

AOSR sites compared to AB34, which suggested that in the absence of major wildfire emissions, W1 deposition was measurably impacted by anthropogenic sources.

In contrast to the first two fluorophores, the highest W3 fluorescence occurred during the fall and winter (Figure 5.5). Moreover, W3 relative fluorescence shifted considerably throughout the year; low relative emission intensities (< 5%) during warmer months were contrasted by values ranging between 11.8–34.2% during the cold season (Figure D7). The AOSR typically experiences increased atmospheric stability during the wintertime, conditions that could have facilitated the accumulation of W3 within the surrounding airshed (Lukacs et al., 2007). Rapid oxidation during periods of increased photolysis (i.e, summer) have been shown to transform and deplete gas-phase organic matter within OS emission plumes (Liggio et al., 2024). Reduced photodegradation of industrial CDOM during the cold season could explain the observed W3 trends among the near-field sites.

5.3.2.4 Weekly precipitation: Bivariate and multivariate analysis

Bivariate correlation analysis found a_{254} displayed moderate positive correlations with WSOC and monthly average $PM_{2.5}$ (R_S = 0.74 and 0.59, respectively; Spearman, $\alpha < 0.5$; Table D10). Fluorescent component 1 (W1) presented a strong positive correlation with a_{254} (R_S = 0.92) and moderate agreement ($R_S > 0.64$) with WSOC, which suggested that the fluorophore was an important constituent of CDOM wet deposition in the AOSR. Component W3 displayed weak agreement with a_{254} and WSOC, but was positively correlated with Ca^{2+}, Mg^{2+}, Na^{+}, and several ambient pollutant variables (monthly average THC, NO, NO_2, SO_2, TRS; Table D10) regionally associated with vehicular and industrial influence (Davidson and Spink, 2018; Landis et al., 2017). Conversely, W2 experienced

limited significant trends with the available data, with exception of a weak positive correlation with WSOC. Only absolute fluorophore values (W1–W3) will be described from hereon, as WSOC normalized fluorescence ($W1_{WSOC}$–$W3_{WSOC}$) presented similar bivariate and multivariate trends.

Three principal components explained the majority of variation (~ 70.6%) within the complete NADP dataset. The first principal component ($PC1_{wet}$: 40.9%) displayed positive factor loadings (0.70–0.95) including W3, DIC, Ca^{2+}, Mg^{2+}, Na^{+}, Cl^{-}, NO_3^{-}, SO_4^{2-}, and NO_2 (Figure 5.6). Principal component 2 ($PC2_{wet}$; 20.2%) displayed positive loadings (0.60–0.85) of WSOC, a_{254}, W1, W2, $PM_{2.5}$, and NH_4^{+}. Principal component three ($PC3_{wet}$; 9.5%) was characterized by moderate positive loadings (0.52–0.55) of SO_4^{2-} and NH_4^{+}, but no substantial associations with CDOM variables. Biplot visualization revealed W1 was most approximate to $PM_{2.5}$, W2 was closest to NH_4^{+}, while W3 was spatially associated with Cl^{-} and NO_2. Multiple attempts at PLS-R analysis produced relatively weak models (Q^2Y < 0.20) that were ineffective at explaining fluorescent component variation ($R^2Y < 0.35$).

For temporal comparison against the snowpack dataset, PCA was conducted using weekly precipitation data from snowfall months (January – March 2021 & November – December 2021) typical in the AOSR. Three principal components explained 71.6% of total variation, where the first component ($PC1_{winter}$: 47.3%) displayed positive factor loadings (> 0.7) of a_{254}, W3, WSOC, DIC, Ca^{2+}, Mg^{2+}, Na^{+}, Cl^{-}, NO_3^{-}, SO_4^{2-}, NO, and NO_2, the second component ($PC2_{winter}$: 14.0%) displayed positive (~ 0.65) NH_4^{+} and SO_4^{2-} and negative (~ 0.5) W3, $PM_{2.5}$, NO, NO_2 factor loadings (Figure D8), and the third principal component ($PC3^{winter}$: 10.3%) presented relatively weak positive factor loadings of a_{254} and WSOC.

Compared to the PCA generated from the complete precipitation dataset, both W1 and W2 were less associated with NH_4^+ and $PM_{2.5}$.

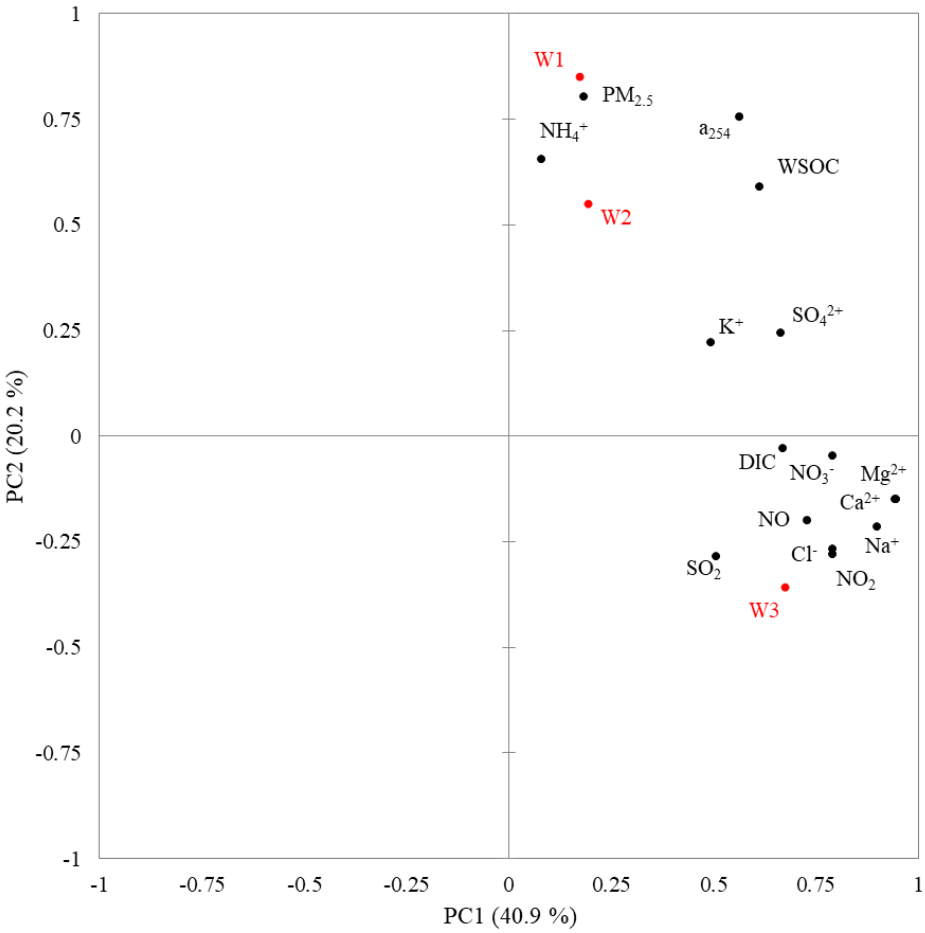

Figure 5.6 Principal component analysis biplot of 2021 weekly precipitation data displaying the factor loadings relative to principal component 1 ($PC1_{wet}$, 40.9%) and principal component 2 ($PC2_{wet}$, 20.2%).

5.3.2.5 Weekly precipitation: Identification of CDOM sources

The PRLIS W3 fluorophore was positively associated with $PC1_{wet,}$ which given its positive Ca^{2+} and Mg^{2+} factor loadings was possibly reflective of fugitive road dust (Gopalapillai et al., 2019; Wang et al., 2015). Positive Na^+, Cl^-, and NO_2 loadings further supported this

interpretation since de-icing salts (sodium chloride) and vehicle exhaust (NO_2) are frequently co-emitted with road dust (Mamun et al., 2021; Landis et al., 2017; Landis et al., 2019a). Industrial operations (i.e., haul roads, mining fleet activity) are identified as a primary sources of road dust and vehicle exhaust in the AOSR (Gopalapillai et al., 2019; Landis et al., 2019a), hence $PC1_{wet}$ and W3 were predominantly influenced by OS activity. Diesel mining fleet operations have been identified as a primary source of OS pollution in the AOSR; primary and secondary emissions from diesel vehicles contain aromatic compounds and have been shown to fluoresce in low λ_{ex} - λ_{em} regions like W3 (Cao et al., 2023; Rutherford et al., 2020).

The positive loadings of W1 and W2 assigned to $PC2_{wet}$ implied these fluorophores were both connected to biomass combustion. It has been established that wildfire emissions are substantial sources of $PM_{2.5}$, WSOC, and ammonia (NH_3) gas (Lee et al., 2022; Lindaas et al., 2021; Reid et al., 2005), the latter of which is converted to particle phase NH_4^+ via in-plume reactions with inorganic and organic acids (Seinfeld and Pandis, 2016; Tomsche et al., 2023). As such, positive $PM_{2.5}$ and NH_4^+ loadings suggested that $PC2_{wet}$ was representative of regional pyrogenic emissions. Notably elevated W1 and W2 emission intensity during the wildfire season (July-August; Figure 5.5) across all stations further demonstrated that regional smoke was a prominent source of fluorescence. Biomass burning is a substantial source of primary and secondary phenolic compounds, which owing to their aromatic properties, can contribute to the CDOM fraction (Claeys et al., 2012; Washenfelder et al., 2015). Previous studies have found that pyrogenic organic aerosols contained water soluble fluorophores with excitation-emission spectra similar to both W1 and W2 (Chen et al., 2024; Wang et al., 2020). Both $PC1_{wet}$ and $PC2_{wet}$ displayed positive

WSOC and a_{254} loadings, which suggested that industrial emissions and regional biomass combustion influenced the wet deposition of bulk soluble organic matter and CDOM.

Analysis of the truncated wintertime dataset (January – March 2021 & November – December 2021) found that both W1 and W2 were less associated with variables indicative of biomass combustion. Considering that wildfires are less frequent during the winter, these observations suggested that pyrogenic emissions were not the exclusive source of W1 and W2 fluorescence within wet deposition. Significantly higher W1 emission intensity among AOSR sites (relative to AB34) during snowfall months further suggested that the fluorophore was linked to industrial activity. However, W2 emission intensity was relatively similar between near and far-field NADP sites during the winter period, which indicated that the fluorophore was influenced by regional non-OS sources.

5.3.3 Comparison of snowpack and weekly precipitation sample optical properties

Particularly elevated TCC values (≥ 0.95) between S1–W1 and S2–W2 pairs indicated both snowpack and weekly precipitation samples contained spectrally similar HULIS and PRLIS fluorophores; however, spectral agreement in this case did not prove chemical similarity. Although a relatively sensitive and versatile technique, EEM fluorescence spectroscopy is not a particularly chemically selective analytical tool, and as such, conjugated aromatic compounds originating from distinct environmental sources could produce similar fluorescent spectra. For example, the biologically occurring amino acid tyrosine exhibits a fluorescent peak (λ_{ex}: 280 nm, λ_{em}: 348 nm, water solvent, Ghisaidoobe & Chung, 2014) like naphthalene (λ_{ex}: 280 nm, λ_{em}: 345 nm, water solvent, Jiji et al., 2000), which typically originates from pyrogenic and petrogenic sources. This analytical caveat

possibly explained why the AOSR snowpack and weekly precipitation (January – December 2021) fluorophores were affiliated with different environmental sources (Table S12). To elaborate, W1 and W2 were linked to pyrogenic emissions (i.e., wildfire smoke) while S1 and S2 were associated with soil dust and industrial sources, respectively. Fundamental differences between sample media, sampling period, and sampling frequency possibly explained this disagreement in source characterization. Regional snowpack received combined wet and dry (i.e., bulk) deposition while weekly precipitation samples represented only wet deposition, meaning that the latter could exclude industrial fluorophores removed from the atmosphere by dry flux. Additionally, regional snowpack only reflected atmospheric loadings during the colder months (November–April), hence, inputs from different CDOM sources during the remaining months could disproportionately impact fluorophore characterization within the precipitation samples. Substantially weaker associations of W1 and W2 with pyrogenic indicator variables during the snowfall months confirmed the influence of seasonal variation over fluorophore characterization. Significantly higher W1 emission intensity among AOSR monitoring stations during the wintertime suggested that OS activities contributed to fluorophore deposition during the cold season, a finding relatively consistent with S1 spatial variation.

In contrast, both S3 and W3 fluorophores were clearly associated with industrial emission sources; however, a comparatively weaker agreement (TCC > 0.85) between spectra implied PLRIS compounds within snowpack and NADP weekly precipitation were likely related, but compositionally distinct. Photochemical aging of CDOM within snowpack or the introduction of additional CDOM via dry deposition could explain this spectral difference. Moreover, significantly elevated relative S3 fluorescence among near-field sites

and relative W3 fluorescence in wintertime precipitation indicated that the industrial fluorophore was a substantial component of snowpack CDOM surrounding OS facilities.

5.4. Conclusions

This study provided the first-known spatial and temporal evaluation of CDOM deposition in the AOSR through the spectroscopic analysis of both regional snowpack (spring 2023) and weekly precipitation (January–December 2021). Elevated absorbance and fluorescence intensity measured in snowpack samples near OS facilities demonstrated that local industry was a primary source of bulk CDOM deposition during the wintertime. Combined EEM-PARAFAC analysis identified three spectrally distinct fluorophores (S1-S3), all of which appeared to originate from OS activities (Table D11). Moreover, the MAC_{365} spatial gradients relative to OS facilities implied that industrial CDOM posed the potential to reduce snowpack albedo, warming from which could accelerate snow thaw rates, reduce snowpack depth, and shorten the period of seasonal snow cover in the AOSR (Usha et al., 2022; Zhou et al., 2022). Changes to snowpack structure and coverage can further depress surface albedo, this can initiate a positive feedback mechanism that accelerates regional snowpack melt and warming (Cubasch et al., 2001). This snow albedo feedback mechanism can substantially impact the planetary radiation budget and has been identified as a major contributing factor to climate change (Groisman et al., 1994).

Although CDOM wet deposition was largely influenced by wildfire smoke during the summer, significantly elevated a_{254}, W1, and W3 within wintertime precipitation at the AOSR sites (compared to the far-field station) demonstrated that OS activities were a primary source of CDOM wet deposition during the cold season. Disproportionately elevated W3 fluorescence within AOSR precipitation during the cold months suggested

that industrial CDOM deposition was seasonally dependent, possibly due to wintertime conditions favouring the accumulation of PRLIS (i.e., the B3 identified by Blanchard et al. [2024]), or enhanced summertime photodegradation of emitted organic matter.

6. Chapter Six: Do industrial emissions influence chromophoric dissolved organic matter within lakes in the Athabasca Oil Sands Region, Canada?

6.1 Introduction

Chromophoric dissolved organic matter (CDOM) represents a broad class of water-soluble organic compounds characterized by their capacity to absorb light within the ultraviolet (UV) and visible wavelength range. The majority of CDOM originates from natural sources internal (autochthonous) or external (allochthonous) to an aquatic system; however, anthropogenic processes can serve as additional allochthonous sources (Coble, 2007; Liggio et al., 2025). Contaminated aquatic systems typically receive anthropogenic CDOM through direct discharge from waste-water treatment plants, agricultural runoff, industrial facilities, and oil / fuel spills (Shang et al., 2021; Snyder et al., 2021), but atmospheric deposition can also contribute to surface-water CDOM (Liggio et al., 2025; Mladenov et al., 2011; Zang et al., 2014).

Industrial activities conducted in the Athabasca Oil Sands Region (AOSR) in north-eastern Alberta, Canada, are a significant source of pollution to the atmosphere, as facility operations emit a wide range of polycyclic aromatic hydrocarbons (PAH), PAC, and volatile organic compounds (VOC; Bari & Kindzierski, 2018; Kirk et al., 2018; Liggio et al., 2016; Liggio et al., 2017; Yassine and Dabek-Zlotorzynska, 2017). There is substantial evidence that OS emissions contribute to atmospheric deposition of organic pollution throughout the AOSR (Kirk et al., 2018; Kurek et al., 2013). Using aircraft-based observations, Liggio et al. (2024) found that annual gas-phase organic carbon deposition from OS emissions theoretically exceeded the dissolved organic carbon (DOC) catchment

flux (excluding gas-phase DOC) of lakes within 200 km of major OS facilities. Furthermore, dissolved PAC species have been found at elevated levels along sections of the Athabasca River (and its tributaries) located near OS operations (Kelly et al., 2009). In addition to their variable toxic, carcinogenic, and mutagenic properties (CCME, 2010; IARC, 2010; Perera et al., 2009), many OS pollutants possess optical properties, generally owing to their conjugated aromatic ring structures. As such, atmospheric deposition from the OS can impact the composition of CDOM within regional surface-waters, including surrounding lake systems. As far as the authors are aware, no published studies have attempted to identify industry-sourced CDOM within AOSR lake surface-waters.

Emission and excitation matrix (EEM) fluorescence spectroscopy is an effective means of evaluating complex mixtures of natural DOM in-part due to the high detection sensitivity and broad chemical selectivity of the method. Further, processing of EEM data via multivariable parallel factor analysis (PARAFAC) can identify groups of fluorescent organic molecules (fluorophores) with chemical meaning. Owing to its versatility, the combined EEM – PARAFAC method has been successfully used to identify organic pollutants of petrogenic and pyrogenic origin (Mendoza et al., 2013; Mohamed et al., 2008). More specifically, EEM – PARAFAC analysis has been employed to detect organic pollutants linked to OS operations, including the fluorescent peaks associated with parent PAH and alkylated PAH (alkyl-PAH) species, in addition to naphthenic acids (Guha Thakurta et al., 2013; Kavanagh et al., 2009; Mahamuni et al., 2019; Martin et al., 2014).

Previous EEM – PARAFAC analysis of CDOM within the surface-waters of 50 regularly monitored acid sensitive lakes (ASL) in the AOSR identified four distinct fluorophores (fluorescent components), including two humic-like ($C1_{ASL}$ and $C2_{ASL}$) and two amino-

acid like ($C3_{ASL}$ and $C4_{ASL}$) fluorophores (refer to Chapter 3). The humic components represented terrestrial-DOM originating from the surrounding natural environment; in contrast, the amino acid-like fluorophores were similar to organic matter of anthropogenic and petrogenic origin. Moreover, fluorescent component $C3_{ASL}$ displayed increasing fluorescent intensity among lakes nearer-to OS industrial sources.

The objective of this work was to identify anthropogenic CDOM within lake surface-waters in the AOSR through the combined application of EEM fluorescence spectroscopy and PARAFAC multivariable modeling techniques. The fluorescent components of interest were evaluated in comparison to target PAC species to assist with fluorophore characterization. Lake data was further compared to modelled regional organic carbon (OC) dry deposition flux estimates (Liggio et al., 2024) to assess the lake – atmospheric connectivity. If a clear link was observed between OS emissions and ASL CDOM quality, this study would offer the first-known evidence that spectroscopy techniques (and PARAFAC modelling) could be effectively used to screen for industrial pollution within lake surface-waters in the AOSR.

6.2 Methods

6.2.1 Lake Sampling and physical characteristics

The ASL monitoring network consists of 50 lakes that are dispersed throughout the broader Wood Buffalo municipal region in north-eastern Alberta, Canada (Figure 6.1). Further description of the study region geography and hydrological characteristics are provided in Chapter 2 and 3. The majority of ASL sites are situated within a 200 km radius of the approximate center of OS operations, with numerous lakes located in relative proximity (<

50 km) to industrial facilities. A subset of remote lakes near the northern border of the province (> 200 km from OS activity) served as background sites. A detailed description of ASL biogeochemical characteristics is available in Chapter 2 and Blanchard et al. (2021).

During August 2021, the Joint Oil Sand Monitoring (OSM; https://www.alberta.ca/oil-sands-monitoring-program) program conducted a field survey of the ASL network. Lakes were accessed via float plane or helicopter, where samples were collected from the approximate center of the waterbody. The samples were subjected to a broad range of analysis, including conventional water quality metrics and dissolved and total trace metals; see Chapter 3 and Emmerton et al. (2018) for further details regarding field and laboratory analysis methods. Lake water quality data collected though the OSM is publicly available (URL: https://osmdataportal.alberta.ca/applications/public.html?publicuser=Guest#waterdata/stationoverview).

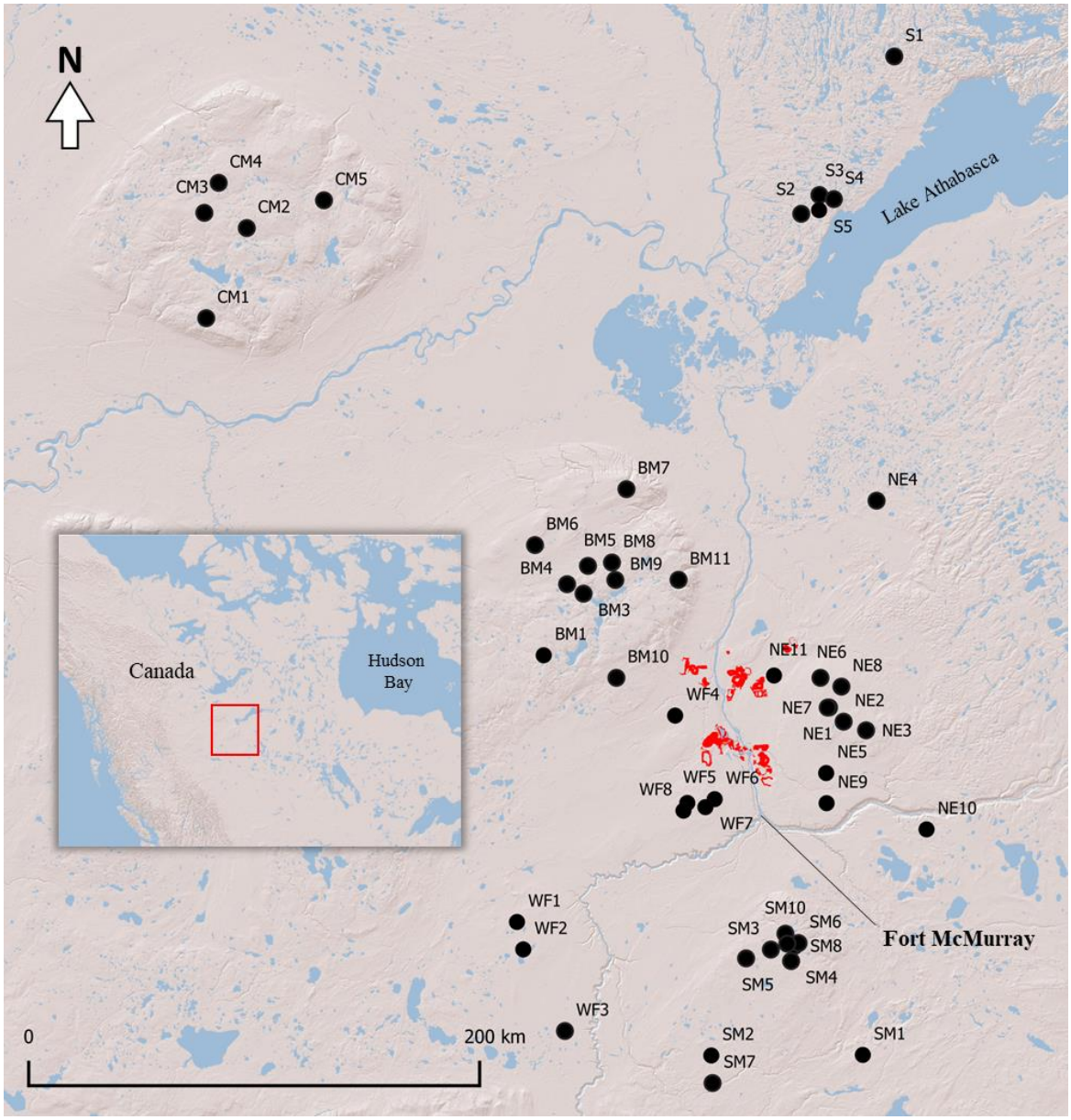

Figure 6.1 Overview of the Athabasca Oil Sands Region (ASOR) study area and Acid Sensitive Lakes network (n = 50). The inset map displays the broader geographical location of the AOSR study area while the red shapefiles indicate the boundaries of major OS operations (ESRI 1995-2024).

Surface-water samples were also transported to SGS-AXYS Analytical Services (Sidney, BC, Canada) for determination of target PAC species via gas chromatography / low

resolution spectrometry (GC/LCMS) following the EPA methods 1625C and 8270E (EPA, 1989; EPA, 2014). Prior to analysis, samples were spiked with 16 deuterated surrogate PAC standards for recovery evaluation and data correction. Twenty-seven of the PAC species reported through the OSM program were selected for the current study (Table 6.1), including a range of 2–5 ringed parent PAHs, alkyl-PAH, parent dibenzothiophenes (DBT), alkylated DBTs (alkyl-DBT), and retene (RET). Parent PAHs have been linked to both industrial and biogenic combustion processes in the AOSR, while alkyl-PAHs and BDTs are more associated with petrogenic emissions (Harner et al., 2018; Yunker et al., 2002). Owing to its natural occurrence within the resinous woods of conifers (Wakeham et al., 1980), RET has been frequently employed as indicator of biogenic combustion (Ahad et al., 2015; Simoneit et al., 2000). Unsubstituted parent homologues are denoted by the prefix "C0", while the number of alkyl substitutions are indicated by the prefixes C1 through C4.

Table 6.1 Parent and alkylated PACs measured in 2021 ASL surface-waters, including the full chemical name, associated abbreviation, and number of benzene rings.

PAC (alkyl substitution)	Abbreviation	Rings
Naphthalene (C0)	NAP	2
Alkyl-naphthalene (C1-C4)	C1-C4-NAP	2
Dibenzothiophene (C0)	DBT	3
Alkyl-dibenzothiophene (C1-C4)	C1-C4-DBT	3
Anthracene (C0)	AN	3
Phenanthrene (C0)	PHEN	3
Alkyl-phenanthrene/anthracene (C1-C4)	C1-C4-PHEN/AN	3
Retene	RET	3
Fluorene (C0)	FLE	3
Alkyl-fluorene (C1-C3)	C1-C4-FLE	3
Fluoranthene (C0)	FLA	4
Pyrene (C0)	PYR	4
Alkyl-fluoranthene/pyrene (C1-C4)	C1-C4-FLA/PYR	4
Chrysene (C0)	CHRY	4
Perylene (C0)	PER	5

In the field, additional sample aliquots were collected in acid washed (hydrochloric acid) and combusted (550°C for 6 hours) 250 ml amber glass bottles, which were then shipped to Trent University, Canada, for EEM analysis. A total of five field blank and duplicate samples (including samples intended for both OSM water quality and Trent optical analysis) were included in the field campaign.

The average recovery of the 16 labelled surrogate species was 58.8 ± 20.1% (standard deviation). Detection rates (values above reporting detection limit) of individual parent and alkyl species across ASL sites ranged from 24.5% to 100.0% (Table E1). Many of the target PAHs were measured at low concentrations, where select compounds (e.g., FLE, C4-DBT) frequently displayed surface-water concentrations ≤ MDL (Table E1). For the purpose of data analysis, PAH concentrations below the MDL were substituted by 2/3 x MDL. Individual analytes with > 30% of total observations below the MDL were excluded from subsequent statistical analysis (e.g., PLS-R). Excluding analytes with low detection frequencies, the average relative percent difference between duplicate samples was 14.2%.

6.2.2 Supplementary lake variables

Lake physical/hydrological properties, including water yield (WY; mm), lake elevation (m, ASL), lake depth (m), lake surface area (m^2), catchment surface area (m^2), catchment wetland composition (%bog, %fen; % of catchment area), and permafrost coverage (% of catchment area) were taken from of Gibson et al. (2020; 2015).

A lichen biomonitoring study by Landis et al. (2019) identified 19 emission sources (i.e., upgrader facilities, active mines, petroleum coke stockpiles) that likely contributed to pollutant deposition throughout the AOSR (source names and coordinates are listed in

Table E1). The highest PAC concentrations were observed among lichen sites within 25 km of OS facilities, and these values rapidly declined to a constant level within 25–50 km of the nearest source. Following these observations, ASL sites located within 50 km of the nearest major OS emission source were classified as near-field lakes (n = 17), and those beyond this range were classified far-field (n = 33). The linear distance between each ASL site and the nearest OS source (km) was additionally included in this work to assist with source characterization.

Using modelled (GEM-MACH; 2.5 x 2.5 km grid cells) gas-phase organic carbon deposition (g C m^{-2} yr^{-1}) from Liggio et al. (2024), the average total deposition was calculated for each ASL lake surface. The resulting estimates were used to evaluate the potential influence of OS emissions over surface-water PACs and fluorophore species.

6.2.3 Spectroscopy and PARAFAC modelling

An aliquot from each ASL sample was shipped to Trent University (Ontario, Canada) for ultraviolet-visible light (UV-Vis and fluorescence EEM spectroscopy analysis). Sample absorbance was measured between the wavelengths (λ) 200 nm and 800 nm using a Cary 100 UV-Vis spectrophotometer from Agilent Technologies. Lake samples were allowed to warm to room temperature (~ 21°C), filtered through a 0.45 µm nylon membrane, then placed in a 1 cm (3.5 ml) Hellma® Suprasil® quartz cuvette (Hellma 101-QS) for analysis. The UV-Vis scans were used to derive select absorbance metrics, including the absorbance coefficient at 254 nm (a_{254}) and specific UV absorbance at 254 nm ($SUVA_{254}$). Further details regarding instrument methodology and absorbance metrics can be found in Chapter 3, Section 2.3.

Fluorescence analyses were conducted using a Cary Eclipse spectrophotometer set to the three-dimensional EEM scan mode. The lake sample aliquots were placed in a 1 cm, 3.5 ml Hellma® Suprasil® quartz cuvette (Hellma 101-QS) for analysis. Excitation (λ_{ex}) and emission (λ_{em}) scans (5 nm intervals) ranged from 200–450 nm and 250–600 nm, respectively. During each day of analysis, a set of quinine sulphate standards were prepared to create a calibration curve (1–100 ppb quinine sulphate in 0.5 M sulphuric acid) to convert fluorescence intensity measurements into quinine sulphate units (QSU) (Sui et al., 2017); see Chapter 3 for full details on the preparation and analysis of ASL samples.

Combined EEM and PARAFAC analysis is commonly used to evaluate the optical and structural characteristics of environmental CDOM, as the modelling technique can identify numerous fluorescent components that are representative of individual or groups of fluorophores species within a sample. The appropriate number of modelled components was determined using four validation tools, including 1) visual peak inspection, 2) EEM residual plots, 3) split-half analysis, and 4) core consistency (CC). Additional details regarding model validation are described in Chapter 3, section 2.4. Individual components from the ASL samples were reported as maximum fluorescence emission intensity, which were measured as QSU. To account for the potential influence of total DOM content over observed fluorescence, component fluorescence intensity values were divided by the corresponding sample WSOC to normalize component fluorescence (QSU mg C L^{-1}).

The fluorescent components generated from the lake dataset were compared against fluorophores observed from the water-soluble brown carbon (WS-BrC) aerosols (Blanchard et al., 2025a), snowpack, and wet-deposition (Blanchard et a., 2025b) EEM samples previously collected in the AOSR. The degree of similarity between individual

fluorophore spectra (including λ_{Ex} and λ_{Ex}) was evaluated using the Tucker Congruence Coefficient (TCC; Pucher et al., 2019). TCC scores between 0.85–0.95 were interpreted to represent fair spectral similarity between fluorophore pairs, while values > 0.95 indicated a high degree of similarity (Lorenzo-Serva & ten Berge, 2006; Murphy et al., 2014). The fluorescent components generated from the lake dataset were additionally compared against PARAFAC models published in the online database, OpenFluor, to assist with fluorophore characterization.

6.2.4 PARAFAC fluorescent components

The assessment of validation metrics determined that a four component PARAFAC model was the most appropriate for further evaluation (Figure 6.2). This study will focus on the two protein-like fluorophores ($C3_{ASL}$ and $C4_{ASL}$) identified by EEM-PARAFAC analysis. Complete details regarding model validation and characterization of the first two humic components $C1_{ASL}$ and $C2_{ASL}$ are described in Chapter 3.

Comparison against the OpenFluor online database found that $C3_{ASL}$ was similar to the spectral loadings of amino acids (Retelletti Brogi et al., 2019; Yamashita et al., 2012) and anthropogenic fluorophores possibly associated with PAH and PAC species (Retelletti Brogi et al., 2022; Zito et al., 2019). Compared to the previous EEM-PARAFAC results from this thesis, $C3_{ASL}$ displayed relatively similar excitation and emission spectra to fluorophores measured in atmospheric aerosol (B3: λ_{Ex} TCC = 0.84, λ_{Em} TCC = 0.82, Chapter 4), snowpack (λ_{Ex} TCC = 0.88, λ_{Em} TCC = 0.81, Chapter 5), and wet-only deposition samples (λ_{Ex} TCC = 0.93, λ_{Em} TCC = 0.82, Chapter 5) previously collected in the AOSR (Figure 6.3). Fluorophores measured within the aerosol and deposition samples

were linked to OS industrial sources, such as raw bitumen, road dust, and mining fleet emissions (Blanchard et al., 2025a; 2025b), which suggested that $C3_{ASL}$ was linked to industry as well. Although relatively similar, the $C3_{ASL}$ absorbance and emission spectra were notably distinct from the fluorescent components observed in the AOSR aerosol and deposition samples. The λ_{Ex} peak of $C3_{ASL}$ (215 nm) was 10–15 nm lower than the peaks observed in the regional atmospheric samples, while the λ_{Em} peak (305 nm) was 15–20 nm smaller than the corresponding fluorophores; this spectral shift suggested that the ASL fluorophore group was chemically unique compared to the atmospheric samples. This difference was unsurprising however, as gradual environmental processes like microbial degradation and photochemical aging can alter the structural composition and optical characteristics of the fluorophores following their introduction to surface-waters (Hernando et al., 2015; Snyder et al., 2021).

The final component ($C4_{ASL}$) presented limited database matches, where the only model with a similarity score > 0.95 characterized the component as the amino acid phenylalanine (Wunsch et al., 2015). A second model with a similarity score of 0.94 identified the fluorescent component as photo-oxidized petroleum hydrocarbons (Whisenhant et al., 2022). Compared to the fluorophores identified in atmospheric aerosols and deposition samples (including snowpack and weekly precipitation) from the AOSR (Chapter 4 and 5), $C4_{ASL}$ displayed highly similar excitation (TCC = 0.97–0.99) and emission (TCC = 0.85–0.98) spectra compared to AOSR brown carbon aerosols (λ_{Ex} TCC = 0.97, λ_{Em} TCC = 0.85, Chapter 4), regional snowpack (λ_{Ex} TCC = 0.97, λ_{Em} TCC = 0.95, Chapter 5), and weekly precipitation (λ_{Ex} TCC = 0.99, λ_{Em} TCC = 0.98, Chapter 5) (Figure E1). The protein-like fluorophore identified within regional snowpack was linked to OS emissions; however,

similar fluorophores measured within regional aerosols and wet-only deposition did not decline with distance from industry, suggesting they were not primarily linked to OS sources.

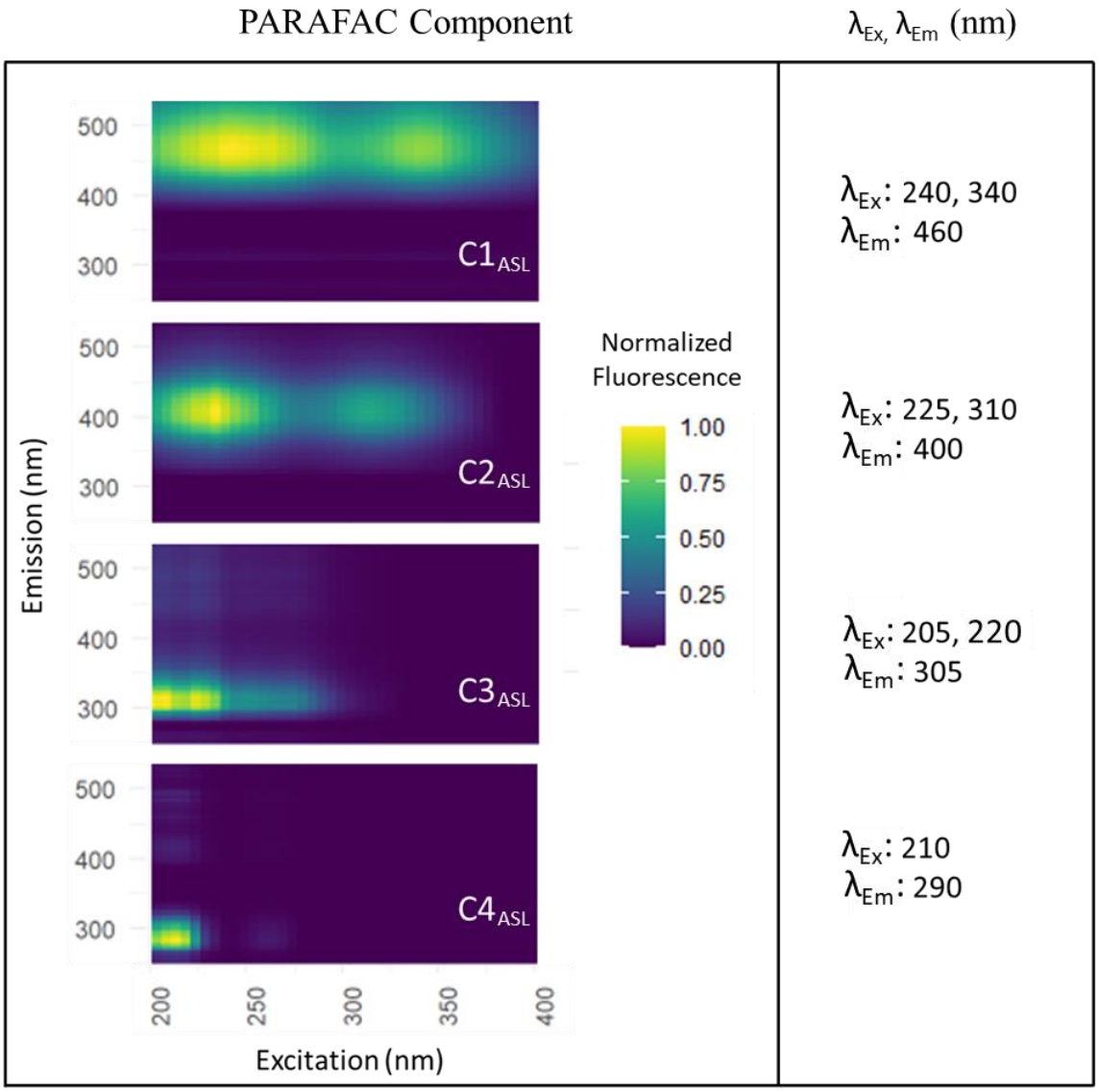

Figure 6.2 Visualization of the four PARAFAC components ($C1_{ASL}$ – $C4_{ASL}$) generated from Acid Sensitive Lake (ASL) EEM samples. Emission intensity values are normalized according to max component fluorescence. Fluorescent - peak excitation (λ_{Ex}) and emission (λ_{Ex}) coordinates (nm) are displayed for each component (source: Chapter 3).

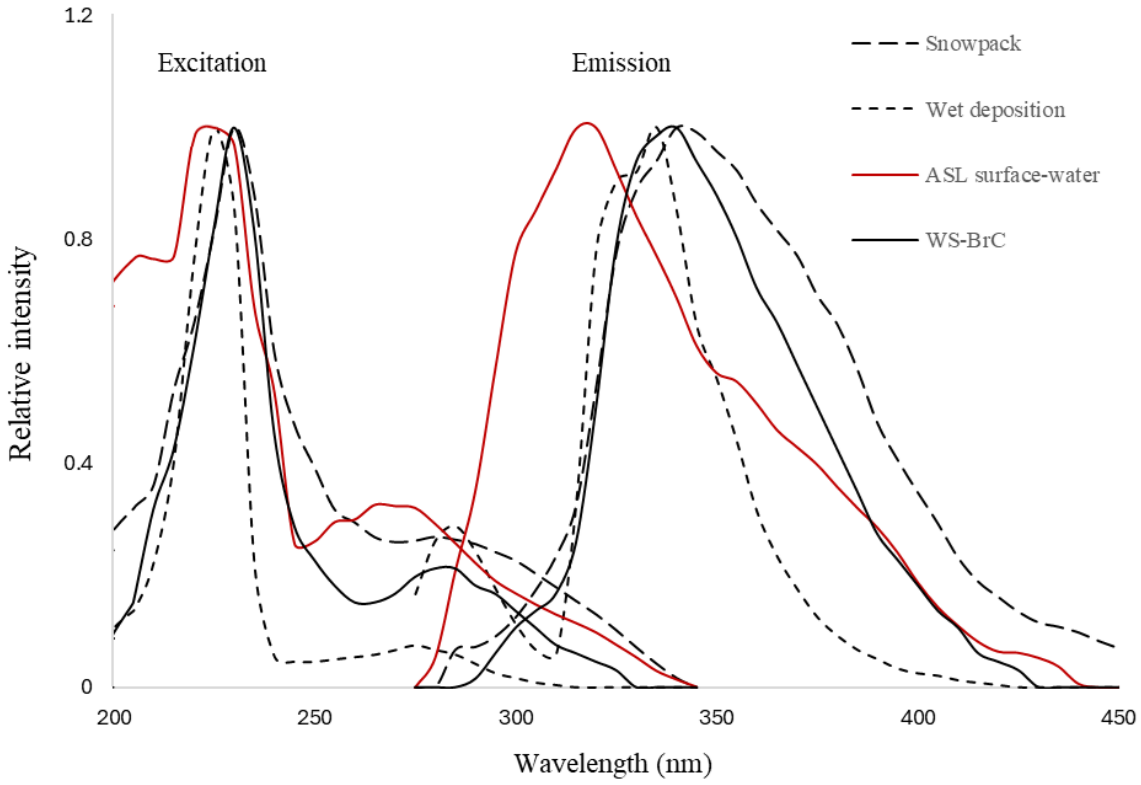

Figure 6.3 Comparison of normalized excitation (λ_{Ex}) and emission (λ_{Em}) spectra of individual fluorescent components observed in a) ASL surface-waters ($C3_{ASL}$: current study), b) atmospheric WS-BrC (B3; Chapter 4), c) snowpack (Chapter 5), and d) weekly precipitation samples (Chapter 5).

The MDL of $C3_{ASL}$ and $C4_{ASL}$ was 4.4 QSU and 5.3 QSU, while the RPD calculated from duplicate samples was 6.2% and 9.3%, respectively. Fluorescence intensity of $C3_{ASL}$ ranged from 20.8 QSU to 92.5 QSU among ASL samples with a median value of 42.6 QSU.

6.2.5 Data analysis

All water quality data were recovery (PAC analytes exclusively) and blank corrected. Blank samples were used to determine method detection limits (MDL), which were calculated as: standard deviation [n samples] × t-value 99.0% confidence critical value (3.747). Shapiro-

Wilk tests determined that the available water quality and physical variables followed a non-normal distribution, thus, non-parametric tests were employed throughout the study. Median values were used as a measure of central tendency while variability was evaluated via normalized median absolute deviation (NMAD). Spearman's Rank Order correlation tests were applied to assess bivariate associations between ASL physical and chemical variables, and the Kruskal–Wallis test was used to determine significant differences between subpopulations.

Partial least squares regression (PLS-R) modelling was applied to identify key variables influencing fluorescent component variability within the ASL dataset. Although described in detail elsewhere (Chapter 3; Eriksson et al., 2013), PLS-R is a multivariable least-squares regression model that can be used to explain the variability between predictor (X) and response (Y) variables by decomposing large datasets into a reduced set of orthogonal components. The two undefined fluorescent components ($C3_{ASL}$ or $C4_{ASL}$) identified in Chapter 3 were designated as the model Y variables, while conventional water quality chemistry variables, surface-water PACs, lake/catchment hydrology, physical properties, lake distance from the nearest OS source, and GEM-MACH total organic carbon deposition estimates were included as the X variables.

In the case of all PLS-R models, internal cross-validation was applied to generate a cumulative goodness of fit (R^2Y) and cumulative goodness of prediction (Q^2Y) value to determine the appropriate number orthogonal components. Variable influence on projection (VIP) scores indicated the relative influence of each X variable over the modelled components, where values ≥ 1 mark a highly influential variable. The spatial

proximity of variable loadings served as a visual indicator of X and Y variable associations, while distance from the origin indicated the level of correlation with each component.

6.3 Results and discussion

6.3.1 Surface water PAC

The low PAC concentrations within ASL surface-water was consistent with Birks et al. (2017). The sum of parent PAHs (ΣPAH) within ASL surface-waters ranged from 0.05 ng L^{-1} to 44.75 ng L^{-1}, where NAP was the most abundant. Total alkyl-PAH (Σalkyl-PAH) concentrations ranged from 0.72 ng/l to 364.75 ng L^{-1}, among which C1-C3-NAP, C4-PHEN/AN, and RET were the most prominent (Table 6.1). The observed dominance of C0-C4-NAP throughout the ASL network was consistent with Birks et al. (2017), who found C4-NAP was the most abundant of the few PACs detected within lake surface-waters in the AOSR. Total parent and alkylated PAHs displayed limited visible spatial trends relative to OS sources, largely owing to the disproportionate influence of parent and alkylated NAP, which also showed no visible spatial trend (Table 6.2). Although frequently linked to petrogenic sources (Akre et al., 2004), NAP is comparatively enriched within upgraded fuels (i.e., diesel) and depleted in unprocessed oil sand / bitumen (Yang et al., 2011). Mobile emissions from OS mining fleets and regional road systems could explain why NAP displayed an inconsistent spatial gradient relative to the nearest OS source, as these sources are more broadly dispersed throughout the study region.

Separately, C0-C3-DBTs, C3-FLE, C1-C3-PHEN/AN, C4-FLA/PYR and CHRY were elevated among near-field lakes (< 50 km from nearest OS source; Table E1) and displayed decreasing concentrations as a function of lake distance from OS sources (Figure 6.4).

Considering that many of these PAC species are reflective of petrogenic sources, the observed trends suggested that OS activities measurably influenced PAC loadings within ASL lakes. Conversely, RET and C4-PHEN/AN were relatively depressed among near-field lakes, compared to far-field sites (> 50 km from nearest OS source; Table 6.2), and displayed negative concentration gradients relative to industry (Figure 6.4). Retene is frequently used as pyrogenic indicator species (Simoneit et al., 2000); thus, it was interpreted that biomass combustion disproportionately impacted far-field lakes.

Table 6.2 Summary of parent and alkylated PACs measured in ASL surface-waters during 2021. Method detection limits (MDL; ng L^{-1}), detection frequency (%, values above reporting detection limit), dataset average, dataset standard deviation (Std. D; ng L^{-1}), nearfield lake (< 50 km from nearest OS source; ng L^{-1}) average, nearfield standard deviation (ng L^{-1}), and Kruskal–Wallis comparisons of near (< 50 km from nearest OS source) and far field (> 50 km from nearest OS source) lakes ($\alpha = 0.05$) are displayed.

	MDL	Detection frequency	Avg. Total (n = 50)	Std. D	Avg. Nearfield (n = 17)	Std. D.	Kruskal–Wallis
	(ng L^{-1})	(%)	(ng L^{-1})	(ng L^{-1})	(ng L^{-1})	(ng L^{-1})	($\alpha < 0.05$)
NAP	2.11	98.0	7.15	6.71	4.75	3.07	Y
C1-NAP	*5.54*	93.9	5.19	7.70	3.60	2.28	
C2-NAP	*2.67*	100.0	7.80	12.87	7.26	6.14	
C3-NAP	*0.91*	95.9	5.26	5.74	5.45	2.55	
C4-NAP	1.30	36.7	5.24	6.12	5.54	3.73	
DBT	*0.13*	100.0	0.25	0.32	0.39	0.21	Y
C1-DBT	0.26	40.8	0.93	0.69	1.15	0.78	
C2-DBT	*0.61*	70.0	1.84	1.89	2.85	2.23	Y
C3-DBT	0.16	38.8	1.16	1.70	3.00	2.12	Y
C4-DBT	0.72	40.8	1.11	1.54	1.77	2.88	
AN	0.17	24.5	< MDL	-	< MDL	-	
PHEN	*1.32*	100.0	1.62	1.52	1.75	0.62	
C1-PHEN/AN	*0.38*	100.0	1.57	2.06	2.19	0.96	Y
C2-PHEN/AN	*0.49*	100.0	1.08	1.68	1.52	0.67	Y
C3-PHEN/AN	*0.26*	75.5	0.88	1.08	1.32	0.76	Y
C4-PHEN/AN	*0.82*	100.0	6.75	15.74	2.42	2.94	Y
RET	0.49	100.0	5.23	13.34	0.94	2.60	
FLE	0.37	100.0	0.47	0.74	0.40	0.28	
C1-FLE	0.84	98.0	0.93	1.22	0.74	0.50	Y
C2-FLE	1.83	95.9	2.35	4.08	1.05	0.80	
C3-FLE	3.64	77.6	4.01	3.58	6.01	5.16	Y
FLA	0.93	100.0	< MDL	0.47	< MDL	0.36	
PYR	0.45	100.0	< MDL	0.23	< MDL	0.21	Y
C1-FLA/PYR	0.30	73.5	0.57	0.95	0.46	0.20	
C2-FLA/PYR	0.66	46.9	0.73	1.24	0.57	0.20	Y
C3-FLA/PYR	0.83	20.0	< MDL	-	< MDL	-	
C4-FLA/PYR	0.31	85.7	3.33	4.64	5.16	8.16	Y
CHRY	0.24	100.0	0.31	0.38	0.37	0.18	Y
PER	0.23	34.8	1.01	1.28	0.58	0.8	

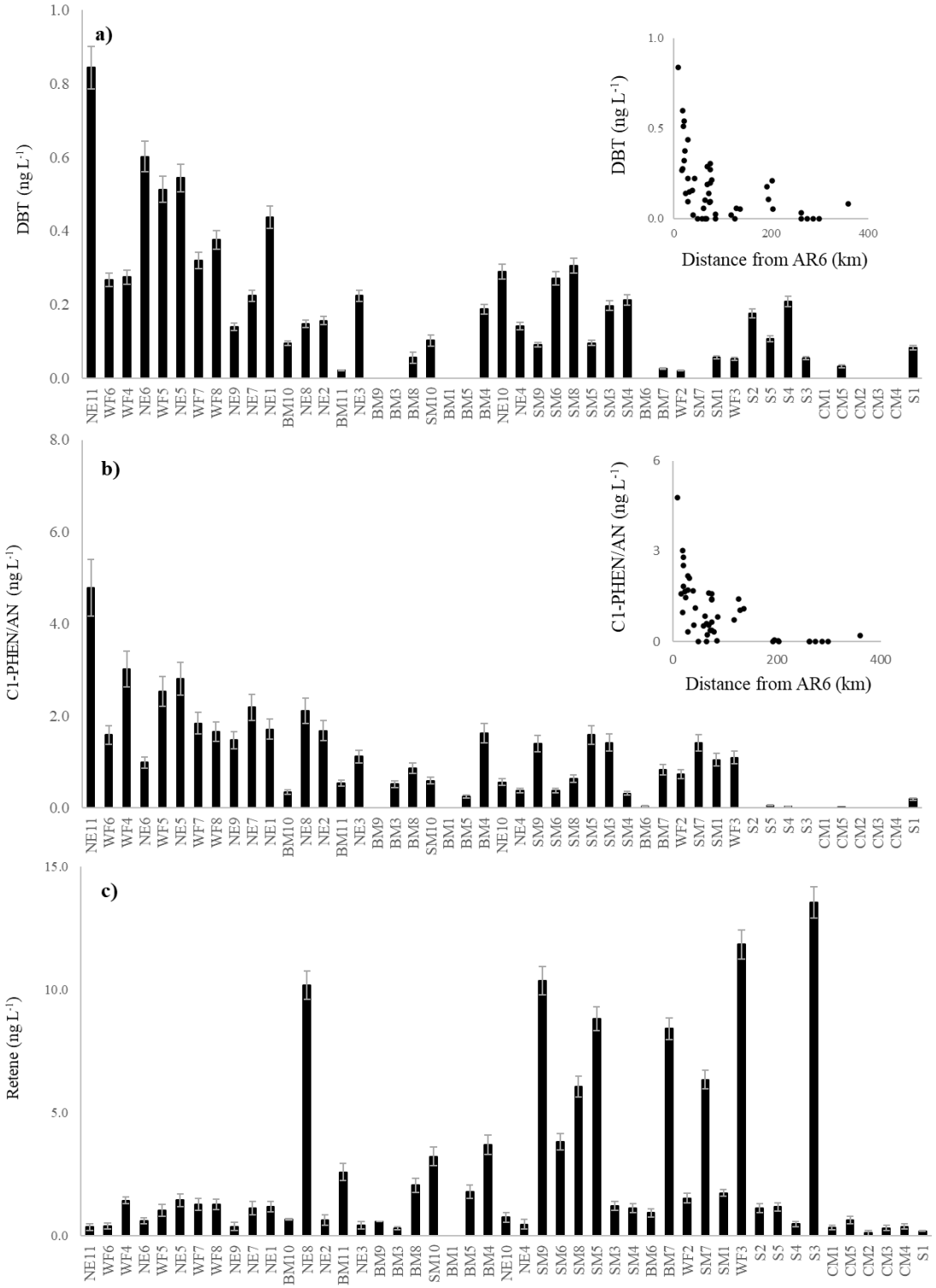

Figure 6.4 Distribution of a) DBT (ng L^{-1}), C1-PHEN-AN, and b) retene (ng L^{-1}) measured within Acid Sensitive Lake (ASL; n = 50) surface-waters during the 2021 Oil Sands Monitoring Program survey. Lakes are ordered (left to right) according to distance from

the nearest oil sands operations (WF6 < 20 km, CM4 > 300km). Error bars represent the analytical precision determined via duplicate samples. The inset plot in Figure 6.4a and 6.4b display DBT and C1-PHEN-AN concentrations (respectively) a function of lake distance (km) from the nearest OS source.

6.3.2 Fluorescent component spatial variability

Generally, surface-water $C3_{ASL}$ fluorescence gradually declined relative to lake distance from OS operations (Figure 6.5). In exception to this trend, the mid-field lakes WF1 and SM2 experienced some of the highest $C3_{ASL}$ fluorescence out of the entire ASL network. The explanation for these outliers is uncertain, however, notably elevated retene concentrations at WF1 and SM2 suggested a potential pyrogenic influence. Although fluorescence decreased as a function of distance from OS sources, the comparatively low $C3_{ASL}$ values at far-field lakes were still well above MDL. This observation suggested that either: a) OS emissions exerted a substantial influence over lake CDOM at great distances (> 300 km), or b) non-petrogenic (e.g., biological, pyrogenic) aromatic compounds contributed to background $C3_{ASL}$ fluorescence within lakes throughout the study region. Surface-water $C4_{ASL}$ fluorescence ranged between 20.4 QSU to 272.4 QSU, with a median of 70.9 QSU. Unlike the former component, $C4_{ASL}$ variation presented limited spatial trends throughout the study region.

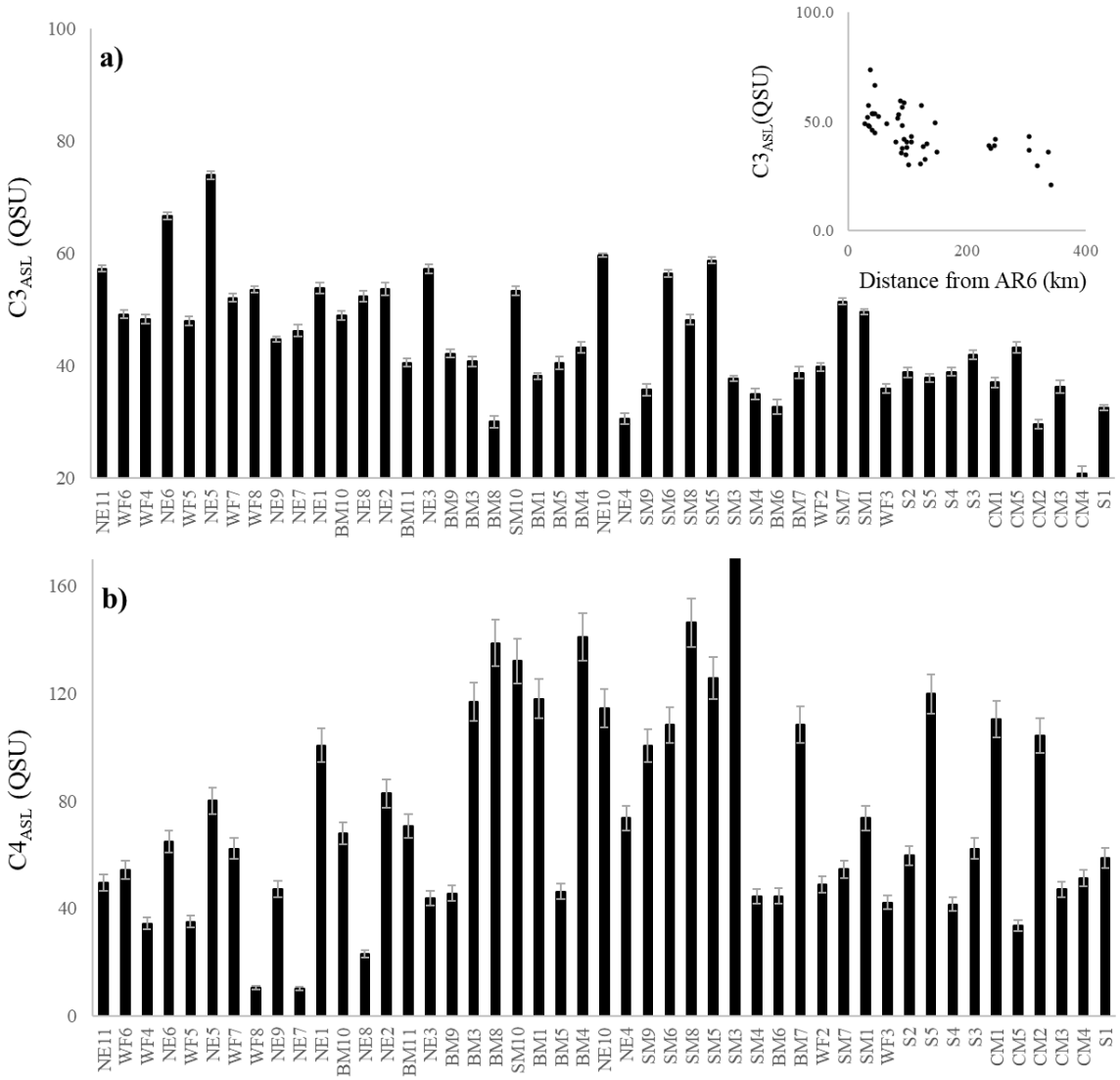

Figure 6.5 Distribution of a) $C3_{ASL}$ and b) $C4_{ASL}$ fluorescence (QSU) within acid sensitive lake (ASL) surface-waters during the 2021 survey. Lakes are ordered (left to right) according to distance from the nearest OS source (WF6 < 20 km, CM4 > 300 km). The inset plot in Figure 6.5a displays $C3_{ASL}$ intensity (QSU) as a function of lake distance (km) from nearest OS source.

6.3.3 Bivariate and multivariate analysis of ASL data

The third fluorescent component ($C3_{ASL}$) displayed significant positive correlations (Spearman: $\alpha > 0.05$, $R_S > 0.50$) with lake temperature, and a selection of PACs, namely DBT, and C0–C2-PHEN/AN. Parent DBT displayed the strongest monotonic agreement with the fluorescent component, with an R_S value of 0.66 (Figure E2). Heterocyclic compounds such as DBT are relatively water-soluble compared to homocyclic molecules (Feldmannová et al., 2006); this possibly contributed to the strong association between $C3_{ASL}$ and DBT, as lake sample filtration would have removed less-soluble aromatics prior to EEM analysis. Analysis by Sun et al. (2018) established that OS-influenced surface-waters in the AOSR contain a broad variety of 2–3 ring heterocyclic compounds, which given their higher relative water-solubility could contribute to $C3_{ASL}$ fluorescence. Moreover, $C3_{ASL}$ fluorescence was significantly correlated (Spearman: $\alpha > 0.05$, $R_S = 0.56$) with modelled total carbon deposition estimates, which suggested that the fluorophore was linked to OS emissions. Unlike $C3_{ASL}$, the $C4_{ASL}$ fluorophore displayed limited significant correlations with the available variables, including PACs and modelled deposition estimates.

Cross-validation of a PLS-R model determined that two orthogonal components were most appropriate, producing a R^2Y and Q^2 score of 0.78 and 0.61, respectively. The primary orthogonal component displayed moderate positive correlations with the C3 fluorophore, FLE, DBT, C0-C2 -PHEN/AN, CHRY, PYR, GEM-MACH, and a negative correlation with lake distance from the nearest OS source; these associations suggested that the PLS-R component represented industrial-sourced PAC lake inputs. The second orthogonal component displayed strong-positive correlations with C0-C3-NAP, C4-PHEN/AN, and

RET, possibly indicative of pyrogenic PAC inputs. Given their high VIP scores (> 1) and proximity to $C3_{ASL}$ in the correlation plot (Figure 6.6), the petrogenic-associated DBT and C1-PHEN/AN were the strongest predictors of $C3_{ASL}$ variation; moreover, the Y variable's associations with distance from OS sources and organic carbon deposition estimates provided considerable evidence that $C3_{ASL}$ fluorescence was linked to local industry. However, the background level of $C3_{ASL}$ emission intensity among far-field ASL waters suggested that organic matter originating from non-OS sources additionally contributed to measured fluorescence.

Fluorescence EEM spectroscopy is capable of broad chemical selectivity; hence, the $C3_{ASL}$ fluorescent peak observed within ASL surface-waters likely reflected a mixture of 2–3 ring aromatic compounds extending beyond the PACs measured in the current study. Considering that the $C3_{ASL}$ fluorophore was measured within the dissolved organic matter fraction, these fluorescent aromatic species were expected to largely consist of polar and semi-polar compounds such as oxygenated and nitrated PACs. Although not as well studied as their non-polar counterparts, polar PACs are uniquely potent environmental pollutants owing to their enhanced genotoxic, mutagenic and carcinogenic effects (Idowu et al., 2019).

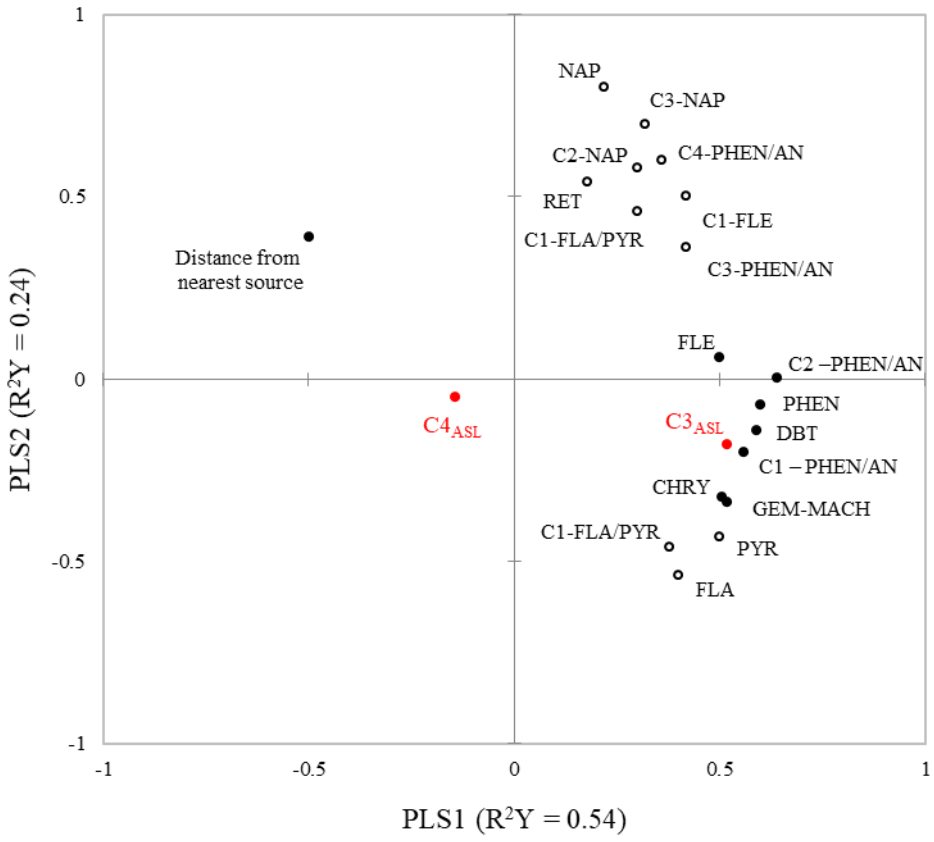

Figure 6.6 Correlation biplot displaying both X (black) and Y variables (red) in relation to PLS components one and two. The solid black and outlined black points indicate X variables with high (≥ 1) and low (< 1) VIP scores, respectively.

As was demonstrated by bivariate and PLS-R analysis, $C4_{ASL}$ displayed weak/limited associations with the available variables, which made it difficult to further characterize the fluorophore. The spectral similarity between $C4_{ASL}$ and the OS-associated fluorophores measured in AOSR aerosol and deposition samples suggested that industrial deposition could result in the observed fluorescence in ASL surface-waters. However, the absence of a clear spatial gradient relative to OS sources and weak associations with available PACs implied $C4_{ASL}$ was not related to OS emissions. It is possible that the fluorophore was

reflective of biologically derived proteins and amino acids, which present fluorescent peaks similar to $C4_{ASL}$ (Kothawala et al. 2014).

6.4 Conclusions

Oil sands operations are a substantial source of CDOM emissions to the surrounding atmosphere. Their subsequent deposition may impact organic matter composition within regional lakes. Combined EEM-PARAFAC analysis of water samples from 50 AOSR lakes surface-water identified two spectrally distinct fluorophores ($C3_{ASL}$ and $C4_{ASL}$) that were not clearly affiliated with natural / biological sources and presented spectra similar to industry-sourced CDOM previously measured in atmospheric samples from the AOSR. Fluorescent component 3 ($C3_{ASL}$) emission intensity was significantly elevated among lakes located near OS facilities and declined as a function of distance from industrial sources. Moreover, $C3_{ASL}$ displayed positive associations with surface-water PACs, specifically petrogenic species like DBT. The fourth fluorescent component ($C4_{ASL}$) displayed generally weak or insignificant association with the available environmental variables, including variables representative of industrial contamination.

Given the observed positive associations with modelled organic carbon deposition estimates and petrogenic PAC species, there was evidence to suggest that the $C3_{ASL}$ fluorophore was representative of a broad range of aromatic compounds originating from OS emissions. Although the chemical composition of the C3 fluorophore was undefined, the many petrogenic aromatic compounds likely contributing to observed fluorescence (e.g., DBT) are hazardous pollutants (Shemer & Linden, 2007) that should be of environmental concern. Compared to conventional analytical methodologies, such as mass

spectrometry, combined EEM – PARAFAC analysis is a cost-effective technique; as such, fluorescence spectroscopy may offer accessible means of detecting industrial pollution within lake systems in the AOSR.

7. Chapter Seven: Conclusion

7.1 Study overview

7.1.1 Review: Chromophoric dissolved organic matter in the environment

Chromophoric dissolved organic matter (CDOM) represents a broad class of dissolved organic matter (DOM) characterized by its capacity to absorb light across the ultraviolet (UV) and visible wavelength ranges (100–800 nm). Chromophoric organic matter plays numerous roles in aquatic system function; for example, CDOM can directly influence ecosystem solar radiation budgets and primary productivity, assist in nutrient and metal transport, and serve as a medium for biological activity (Dodds & Whiles, 2010; Fisher & Likens, 1973). The CDOM of an aquatic system either originates from internal biological processes (autochthonous) or external (allochthonous) sources, while numerous environmental processes and characteristics (e.g., photochemistry, biological metabolism, hydrology) can subsequently impact organic matter composition and fate (Huang et al., 2022; Kothawala et al., 2013; Olefeldt et al., 2013). It is well established that acid-base chemistry can directly and indirectly influence the abundance and structure of CDOM within aquatic systems (Anesio & Granéli, 2003; Gu et al., 2017), while chromophoric organic molecules containing acidic functional groups (e.g., humic and fulvic acids) can increase or decrease surface-water pH and acid neutralization capacity (Castrillon-Munoz et al., 2022; Munson & Gherini, 1993; Oliver et al., 1983).

Although commonly studied in aquatic systems, CDOM persists throughout the atmospheric environment in both gaseous and particle phases (Chen et al., 2021). This organic matter fraction can originate from several environmental sources, the most

prominent of which include bioaerosols (Rizzo et al., 2013), biomass combustion (Ramanathan et al., 2007), and fossil fuel combustion (Shen et al., 2023; Yan et al., 2017). Particle-phase CDOM, also known as water-soluble brown carbon (WS-BrC), has been recognized as an important factor contributing to regional and global climate change owing to its capacity to directly and indirectly absorb solar radiation (Chakrabarty et al., 2016). Following initial emission, atmospheric CDOM (including WS-BrC) re-enters the surface environment (including aquatic systems) through wet and dry deposition (Mladenov et al., 2011; Zang et al., 2014).

7.1.2 Athabasca Oil Sands Region

The Athabasca Oil Sand Region (AOSR), located in northern Alberta, Canada, is home to the world's largest known bitumen deposit, which encompasses an area of ~140,200 km^2. Intensive industrial operations in the AOSR are a major source of inorganic acidic species (sulphur and nitrogen) and organic pollutant emission to the surrounding region (Bennet et al., 2008; Cathcart et al., 2016; Jariyasopit et al., 2018). Altered acid-base chemistry and organic pollutant inputs following the deposition of industrial emissions posed the potential to alter the composition of CDOM within lake surface-waters throughout the AOSR. The primary objectives of this thesis were to determine **a)** if CDOM and acid-base chemistry were related within AOSR lakes, and **b)** if OS organic emissions influenced the composition of lake surface-water CDOM. The null hypotheses corresponding to these objectives were H_0: a) CDOM and acid-base variables were not significantly associated, and H_0: b) industrial emissions do not measurably contribute to CDOM within regional lake surface-waters.

7.2 Summary of key findings

This investigation consisted of five independent research chapters, the contents and major findings of which are summarized below:

a) Chapter 2 involved the reanalysis of the historical (1999–2017) Acid Sensitive Lakes (ASL; n = 50) dataset to evaluate the spatiotemporal variability of DOM among AOSR lakes. Multivariable analysis found that the ASL dataset consisted of two distinct subpopulations, including a large cohort of lakes (titled "High" or "H") characterized by relatively high surface-water colour, dissolved metals (specifically Fe), and low DOC, alkalinity, and pH, while the remaining lakes (titled "Low" or "L") displayed the inverse characteristics. Given the strong positive correlation between surface water colour and DOC, it was assumed that the coloured H lakes were rich in CDOM. Monotonic trend analysis showed limited evidence of long-term acidification throughout the region; conversely, many lakes displayed increasing pH and alkalinity. However, regional back-trajectory analysis indicated that H-classified lakes more likely to receive atmospheric transport from OS sources displayed significantly lower pH and alkalinity. These findings suggested that the acid-base chemistry of H lakes could be influenced by acid inputs from OS sources, this in turn could alter the composition of surface-water CDOM.

b) Building on the initial findings of the previous study, Chapter 3 directly evaluated the structure of lake CDOM throughout the AOSR by analyzing ASL surface-waters (sampled during the summer of 2021) with ultraviolet-visible (UV-Vis) and excitation – emission matrix (EEM) fluorescence spectroscopy. Regional lakes contained four spectrally distinct fluorescent compounds (i.e., fluorophores), including two humic acid like fluorophores (C1

and C2) and two amino-acid like compounds (C3 and C4). Multivariate analysis indicated that C1 and C2 likely originated from surrounding peatlands and were associated with surface-water colour and dissolved organic carbon, respectively. Strong associations with select metals and variables reflective of irradiation suggested that the comparatively aromatic C1 formed CDOM–metal complexes that were vulnerable to photodegradation. Both C3 and C4 remained largely unresolved due to limited associations with the available data; however, C3 spectra were similar to anthropogenic fluorescent species reported in the literature. Weak associations were observed between CDOM variables and surface-water pH and alkalinity, providing limited evidence to suggest CDOM and acid-base chemistry shared a direct relationship within AOSR lakes. As such, the first null hypothesis (H_0: a) could not be rejected. Potential acid inputs from OS sources were unlikely to influence the composition of CDOM within regional lakes, including the potentially acid sensitive H-classified lakes.

c) Chapter 4 set out to measure and characterize WS-BrC throughout the AOSR through the deployment of active sampler systems during the summer of 2021. Combined UV-Vis and EEM fluorescence analysis, paired with complimentary particle-phase metals and air-quality data found that the OS industry was a measurable source of CDOM aerosols to the surrounding airshed. Three spectrally distinct fluorophores (B1–B3) were observed within the WS-BrC samples, two of which (B1, B3) were associated with industrial emissions, while the last component (B2) was likely influenced by both industrial and pyrogenic (wildfire) sources.

d) Chapter 5 investigated the spatial and temporal variability of CDOM deposition throughout the AOSR through the spectroscopic analysis of regional snowpack (collected spring 2023) and weekly precipitation (January 2021–December 2021) samples. Fluorescence EEM analysis identified three fluorophore species; interestingly, the fluorescence spectra measured within the snowpack and weekly precipitation samples were very similar. Moreover, the third fluorescent component detected within the snow (S3) and precipitation (W3) samples were spectrally similar to the industrial fluorescent component observed from the WS-BrC samples (C3). Measured absorbance and fluorescence were significantly elevated within near-field snowpack samples, which demonstrated that OS operations were a key source of CDOM deposition to the region. Two fluorophore species from the precipitation samples (W1 and W2) displayed an association with pyrogenic sources (i.e., wildfires), while the third fluorophore (W3) was significantly elevated among near-field stations and positively correlated with industrial indicator variables. These observations suggested that at least one industrially sourced fluorophore (C3, S3, W3) was ubiquitous throughout the AOSR airshed.

e) The final research chapter revisited the ASL surface-water dataset (2023) from chapter 2; notably, this work focused on characterizing the third and fourth fluorescent components (C3 and C4), primarily by comparison to corresponding measurements of PACs. Measured C3 displayed a spatial gradient of decreasing fluorescence intensity as a function of distance from OS facilities and additionally presented positive correlations with PACs. Moreover, C3 was spectrally similar to the industrial fluorophores measured within WS-BrC (B3), snowpack (S3), and weekly precipitation (W3) samples, which further suggested that atmospheric inputs could contribute to observed fluorescence within regional lakes. These

observations offer considerable evidence that OS emissions and deposition measurably alter the composition of CDOM within regional lakes; as such, the second null hypothesis (H_0: b) was rejected.

7.3. Implications and future recommendations

7.3.1 Regional lake surface-waters

The classification of H and L lake subpopulations (initially identified in Chapter 2) provided a useful context to evaluate CDOM dynamics throughout the AOSR. The two cohorts displayed distinct chemical, geological, and hydrological characteristics that likely contributed to the divergent CDOM composition observed between H and L sites. Future studies investigating the influence of acid deposition on lake chemistry in the AOSR should take particular interest in H-classified lakes, considering that the CDOM-rich (and low acid neutralizing capacity) lakes are potentially vulnerable to acid inputs from OS sources.

According to the findings of Chapter 3, the weak association between CDOM and acid-base chemistry demonstrated that lake acidification (or acid recovery) would not likely impact surface-water chromophoric organic matter in the AOSR. It should be noted that the analysis presented in Chapter 3 was based on one period of observations and did not fully capture the temporal variability of lake CDOM throughout the AOSR. As such, broader associations between CDOM and acid-base chemistry may not have been visible within the available dataset. It is recommended that EEM fluorescence spectroscopy is incorporated into the routine annual monitoring of ASL surface-waters in effort to evaluate long-term CDOM variation in relation to acid-base chemistry.

The investigation in Chapter 3 did find, however, that CDOM appeared to be primarily influenced by catchment characteristics, which themselves are currently experiencing dynamic shifts due to external factors. Continued industrial land-development and climate change are contributing to ongoing peatland degradation and permafrost thaw in northern Alberta (Daniel et al., 2021; Gibson et al., 2019; Price et al., 2013), and these processes may lead to conflicting CDOM shifts. For example, a reduction in organic-rich peatlands within catchments would limit allochthonous humic and fulvic acid inputs to lakes, which in turn could impact surface-water colour and primary productivity. On the other hand, meltwater drainage from humic-rich peatland permafrost could temporality accelerate allochthonous flux to adjacent lakes, consequently enhancing CDOM abundance and light absorbing capacity. Again, it is recommended that spectroscopy analysis is incorporated into routine ASL monitoring to assess long-term variation in CDOM quality.

It is well established that industry is a notable source of organic pollutants (e.g., PACs) to aquatic systems throughout the AOSR; nonetheless, this thesis offered the first-known evidence that OS emissions and deposition measurably influenced the chromophoric properties of lake surface-waters in the region. The industrial fluorophore (C3) displayed the lowest emission intensity out of the four measured fluorophores and was weakly associated with a_{254} and $SUVA_{254}$, and as such did not likely impact lake energy budgets and primary productivity. However, the clear industrial CDOM signal measured within ASL waters demonstrated that combined EEM-PARAFAC analysis could serve as a valuable tool to screen for organic pollution within aquatic systems throughout the AOSR. Owing to the low operational costs associated with the method, EEM-PARAFAC would be easily accessible to smaller organizations or individuals (community groups, concerned

citizens) interested in monitoring surface-water quality throughout the AOSR. Given the potential utility of this technique, future studies in the region should further characterize the C3 fluorophore within lake surface-waters and attempt to identify the key chemical species responsible for fluorescence.

7.3.2 Atmospheric environment

This thesis provided the first-known analysis of CDOM within aerosols and atmospheric deposition in the AOSR. Given that OS operations significantly contributed to light-absorbing CDOM within atmospheric aerosols and deposition, future studies should consider quantifying the radiative forcing potential of industrial CDOM. Decreased atmospheric and surface albedo due to industrial CDOM emissions could measurably contribute to regional warming and compound the ongoing processes related to global climate change. Given the established reactive potential of chromophoric aerosols (Jiang et al., 2012), subsequent studies should investigate how industrial BrC impact atmospheric chemical processes throughout the AOSR airshed.

Combined analysis of atmospheric aerosol and deposition samples by EEM-PARAFAC (Chapters 4 and 5) identified spectrally distinct fluorophores (e.g., C3, S3, W3) clearly linked to OS sources, these observations confirmed that EEM-PARAFAC was an effective tool to measure atmospheric CDOM in the AOSR. A substantial portion of organic pollutants emitted by the OS industry (e.g., PACs) possess conjugated ring structures capable of fluorescence, and as such, EEM-PARAFAC sampling techniques could be used as an alternative method to screen for industrial pollutants in the AOSR. Owing to the low operational costs and relative simplicity of fluorescence spectrometers, EEM-PARAFAC

can be used to efficiently analyze high volumes of environmental samples collected across broad spatial and temporal ranges.

The vast majority of atmospheric BrC research has been limited to the particle phase (BrC-PP). However, certain BrC-PP chemical species including oxygenated and nitrated PACs and quinones possess semi-volatile properties that likely contribute to light absorption in the gas-phase (Laskin et al., 2015). A preliminary study by Chen et al. (2021) in Taiyuan, China confirmed that gas-phase BrC (BrC-GP) was responsible for a measurable portion (30–50 %) of total BrC (BrC-PP + BrC-GP) absorbance and up to 80% of total fluorescence in the atmosphere. Given the established link between OS operations and regional BrC aerosols and CDOM deposition, there is reasonable evidence to suggest that local industry contributes to BrC-GP in the AOSR. Additional light-absorbance by these gas-phase chromophores could further enhance radiative forcing within atmospheric and surface environments, which could contribute to regional warming. It is recommended that future studies in the AOSR measure the BrC-GP fraction in effort to evaluate the composition, sources, and light-absorbing potential of the gas-phase chromophores in the region.

References

Agriculture and Agri-Food Canada. (2005). Soil Landscapes of Canada Working Group. Soil Landscapes of Canada, version 3.0, digital map and database at 1:1 million scale.

Alberta Environment and Sustainable Resource Development (ESRD). (2015). Alberta wetland classification system. Water Policy Branch, Policy and Planning Division, Edmonton, AB.

Alberta Environment and Parks (AEP). (2018). Alberta merged wetland inventory. Available from https://maps.alberta.ca/genesis/rest/services/Alberta_Merged_Wetland_Inventory/Latest/ MapServer/

Alostaz, M., Biggar, K., Donhue, R., Hall, G. (2006). Using fluorescence emission-excitation matrices (EEMs) and Parallel Factor Analysis (PARAFAC) for characterizing petroleum fractions. *Journal of Environmental Engineering and Science*, 7, 183-197

Akash, M.S.H., Rehman, K. (2020). Ultraviolet-Visible (UV-VIS) Spectroscopy. In: Essentials of Pharmaceutical Analysis. Springer, Singapore. https://doi.org/10.1007/978-981-15-1547-7_3

Akre, C.J., Headley, J.V., Conly, F.M., Peru, K.M., Dickson, L.C. (2004). Spatial Patterns of Natural Polycyclic Aromatic Hydrocarbons in Sediment in the Lower Athabasca River. *Journal of Environmental Science and Health, Part A. Toxic/hazardous substances and environmental engineering*., 39 (5), 1163–1176.

Anesio, A. M., Granéli, W. (2003). Increased photoreactivity of DOC by acidification: Implications for the carbon cycle in humic lakes, *Limnology and Oceanography*, 2.

Arp, H. P. H., Lundstedt, S., Josefsson, S., Cornelissen, G., Enell, A., Allard A.-S., Kleja, D. B. (2014). Native Oxy-PAHs, N-PACs, and PAHs in Historically Contaminated Soils from Sweden, Belgium, and France: Their Soil-Porewater Partitioning Behavior, Bioaccumulation in Enchytraeus crypticus, and Bioavailability, *Environmental Science and Technology*, 48, 19, 11187–11195

Aryal, R., Lee, BK., Beecham, S. et al. (2015). Characterisation of Road Dust Organic Matter as a Function of Particle Size: A PARAFAC Approach. *Water Air Soil Pollution* 226, 24.

Asa-Awuka (2009). Relating CCN activity, volatility, and droplet growth kinetics of β-caryophyllene secondary organic aerosol. *Atmospheric Chemistry and Physics*

Bacosa, H. P., Erdner, D. L., Liu, Z. (2015). Differentiating the roles of photooxidation and biodegradation in the weathering of Light Louisiana Sweet crude oil in surface water from the Deepwater Horizon site. *Marine Pollution Bulletin*, 95(1), 265-272

Bakhtiari, T. M., Harbottle, D., Curran, M., Ng, S., Spence, J., Siy, R., Liu, Q., Masliyah, J., Xu. Z. (2015). Role of caustic addition in bitumen-clay interactions. *Energy Fuels* 29,1, 58–69

Bari, A., Kindzierski, W. B. (2017). Ambient fine particulate matter (PM2.5) in Canadian oil sands communities: Levels, sources, and potential human health risk. *Science of the Total Environment*, 595, 828-838.

Bari, M., Kindzierski, W. (2018). Ambient volatile organic compounds (VOCs) in communities of the Athabasca oil sands region: Sources and screening health risk assessment. *Environmental Pollution*, 235, 602-614.

Battin, T. J., Luyssaert, S., Kaplan, L. A., Aufdenkampe, A. K., Richter, A. K., Tranvik, L. J. (2009) The boundless carbon cycle. *Nature Geosciences* 2, 598-600.

Bennett, K., Gibson, J., McEachern, P. (2008). Water-yield estimates for critical loadings assessment: comparisons of gauging methods versus an isotopic approach. *Canadian Journal of Fisheries and Aquatic Sciences*, 65(1), 83-99.

Beres, N. D., Sengupta, D., Samburova, V., Khlystov, A. Y., Moosnüller, H. (2020). Deposition of brown carbon onto snow: changes in snow optical and radiative properties. *Atmospheric Chemistry and Physics.* 20(10), 6095-6114.

Birks, S. J., Cho, S., Taylor, E., Yi, Y., Gibson, J. J. (2017). Characterizing the PAHs in Surface Waters and Snow in the Athabasca Region: Implications for Identifying Hydrological Pathways of Atmospheric Deposition. *Science of the Total Environment*. 603-604, 570-583.

Blanchard, D., Aherne, J., Makar, P. (2021). Dissolved Organic Carbon in Lakes of the Athabasca Oil Sands Region: Is Color an Indicator of Acid Sensitivity?. *Environmental Science and Technology*, 55(10), 6791-6803.

Blanchard, D., Gordon, M., Dang, D. H., Makar, P. A., Aherne, J. (2025a). Characterization of atmospheric water-soluble brown carbon in the Athabasca Oil Sands Region, Canada, *Atmospheric Chemistry and Physics*, 25(4), 2423–2442

Blanchard, D., Gordon, M., Dang., D. H., Makar, P. A., Kirk, J., Aherne, J. (2025b). Atmospheric Deposition of Chromophoric Dissolved Organic Matter in the Athabasca Oil Sands Region, Canada, is Strongly Influenced by Industrial Sources During the Winter Months. *Environmental Pollution*, 371, 125936

Bond, T. C. (2001). Spectral dependence of visible light absorption by carbonaceous particles emitted from coal combustion. *Geophysical Research Letters*, 28(21), 4075-4078

Bosch, C., Andersson, A., Kirillova, E., Budhavant, K., Tiwari, S., Praveen, P.S., Russell, L.M., Beres, N.D., Ramanathan, V., Gustafsson, O. (2014). Source-diagnostic dual-isotope composition and optical properties of water-soluble organic carbon and elemental carbon in the South Asian outflow intercepted over the Indian Ocean. *Journal of Geophysical Research*. 119, 11743–11759.

Brandstetter, A., Sletten, R. S., Mentler, A., Wenzel, W. W. (1996). Estimating dissolved organic carbon in natural waters by UV absorbance (254 nm). *Journal of Plant Nutrition and Soil Science*, 159, 605–607.

Brezonik, P. L., Finlay JC, Griffin CG, Arnold WA, Boardman EH, Germolus N, Hozalski, R. M., Olmanson, L. G. (2019). Iron influence on dissolved color in lakes of the Upper Great Lakes States. *PLoS ONE*, 14(2): e0211979

Bro, R. (1997). PARAFAC. Tutorial and applications. *Chemometrics and Intelligent Laboratory Systems*, 38(2), 149-171.

Bro, R., Kiers, H.A. (2003). A new efficient method for determining the number of components in PARAFAC models. *Journal of Chemometrics* 17.

Brünjes, J., Seidel, M., Dittmar, T., Niggemann, J., Schubotz, F. (2022). Natural Asphalt Seeps Are Potential Sources for Recalcitrant Oceanic Dissolved Organic Sulfur and

Dissolved Black Carbon. *Environmental Science and Technology*, 56,12, 9092-9102

Buffam, I., McGlathery, K. J. (2003) Effect of ultraviolet light on dissolved nitrogen transformations in coastal lagoon water. *Limnology & Oceanography*, 48:723-734

Canadian Association of Petroleum Producers (CAPP). Statistical Handbook 2020. Retrieved 19 July 2020, from https://www.capp.ca/publications-and-statistics/statistics/statistical-handbook

Canadian Council of Ministers of the Environment (CCME). (2010). Canadian Soil Quality Guidelines for Carcinogenic and Other Polycyclic Aromatic Hydrocarbons (Environmental and Human Health Effects). Scientific Criteria Document, Environment and Climate Change Canada, Gatineau, Québec, Canada, 218

Cao, T., Li, M., Xu, C., Song, J., Fan, X., Li, J., Jia, W., Peng, P. (2023). Technical note: Chemical composition and source identification of fluorescent components in atmospheric water-soluble brown carbon by excitation–emission matrix spectroscopy with parallel factor analysis – potential limitations and applications, *Atmospheric Chemistry and Physics*, 23, 2613–2625

Carou, S., Dennis, I., Aherne, J., Ouimet, R., Arp, P. A., Watmough, S. A., Demerchant, I., Shaw, M., Vet, R., Bouchet, V., Moran, M. (2008). A national picture of acid deposition critical loads for forest soils in Canada. Canadian Council of Ministers of the Environment, PN 1412.

Castrillon-Munoz, F. J., Gibson, J. J., Birks, S. J. (2022). Carbon dissolution effects on pH changes of RAMP lakes in northeastern Alberta, Canada, *Journal of Hydrology: Regional Studie*s, 40, 101045, 2214-5818

Cathcart, H., Aherne, J., Jeffries, D., Scott, K. (2016). Critical loads of acidity for 90,000 lakes in northern Saskatchewan: A novel approach for mapping regional sensitivity to acidic deposition. *Atmospheric Environment 146*, 290-299.

Chakrabarty, R. K., Gyawali, M., Yatavelli, R. L., Pandey, A., Watts, A. C., Knue, J., Moosmüller, H. (2016). Brown carbon aerosols from burning of boreal peatlands: microphysical properties, emission factors, and implications for direct radiative forcing. Atmos. Chem. Phys., 16 (5), 3033-3040

Chalbot, M-C. G., Kavouras, I. G. (2019). Nuclear Magnetic Resonance characterization of water-soluble organic carbon of atmospheric aerosol types. *Natural Product Communications*, 14,5

Chen, Y., Bond, T. C. (2010). Light absorption by organic carbon from wood combustion. *Atmospheric Chemistry and Physics*, 10,4, 1773– 1787,

Chen B, Huang W, Ma S, Feng M, Liu C, Gu X, Chen K. (2018). Characterization of Chromophoric Dissolved Organic Matter in the Littoral Zones of Eutrophic Lakes Taihu and Hongze during the Algal Bloom Season. *Water*, 10(7):861.

Chen, Q., Mu, Z., Song, W., Wang, Y., Yang, Z., Zhang, L., Zhang, Y.-L. (2019). Size-resolved characterization of the chromophores in atmospheric particulate matter from a typical coal-burning city in China. *Journal of Geophysical Research: Atmospheres*, 124, 10546– 10563

Chen, P., Kang, S., Gul, C., Tripathee, L., Wang, X., Hu, Z., Li, C., Pu, T. (2020). Seasonality of carbonaceous aerosol composition and light absorption properties in Karachi, Pakistan. *Journal of Environmental Science*, 90, 286-296

Chen, Q., Chen, Q., Hua, X., Guan, D., Chang, T. (2021). Gas-phase brown carbon: Absorbance and chromophore types. Atmospheric Environment, 264(1), 118646

Chibwe, L., Muir, D. C. G., Gopalapillai, Y., Shang, D., Kirk, J. L., Manzano, C. A., Atkinson, B., Wang, X., Teixeira, C. (2021). Long-term spatial and temporal trends, and source apportionment of polycyclic aromatic compounds in the Athabasca Oil Sands Region, *Environmental Pollution*, 268, Part A, 115351, 0269-7491

Christensen, J. H., Hansen, A. B., Mortensen, J., Anderson, O. (2005). Characterization and matching of oil samples using fluorescence spectroscopy and parallel factor analysis. *Analytical Chemistry*, 77, 2210 – 2217

Cho, S., Sharma, K., Brassard, B., Hazewinkel, R. (2014). Polycyclic aromatic hydrocarbon deposition in the snowpack of the Athabasca Oil Sands Region of Alberta, Canada. *Water, Air, and Soil Pollution*, 225, 1910.

Claeys, M., Vermeylen, R., Yasmeen, F., Gómez-González, Y., Chi, X., Maenhaut, W., Mészáros, T., Salma, I. (2012). Chemical characterisation of humic-like substances from urban, rural and tropical biomass burning environments using liquid chromatography with UV/vis photodiode array detection and electrospray ionisation mass spectrometry. *Environmental Chemistry*, 9, 273-284.

Coble, P. (1996). Characterization of marine and terrestrial DOM in seawater using excitation-emission matrix spectroscopy. *Marine Chemistry* 51(4), 325-346

Coble, P. G., Del Castillo, C. E., Avril, B. (1998), Distribution and optical properties of CDOM in the Arabian Sea during the 1995 southwest monsoon. *Deep Sea Research, Part II,* 45(10–11), 2195–2223,

Coble, P. (2007). Marine optical biogeochemistry: the chemistry of ocean color. *Chemical Rev*iews, 107(2):402–418

Cong, Z., Kang, S., Kawamura, K., Liu, B., Wan, X., Wang, Z., Gao, S., Fu. P. (2015). Carbonaceous aerosols on the south edge of the Tibetan Plateau: concentrations, seasonality and sources. *Atmospheric Chemistry and Physics*, 15 (3),1573-158

Cooke, C., Kirk, J., Muir, D., Wiklund, J., Wang, X., Gleason, A., Evans, M. (2017). Spatial and temporal patterns in trace element deposition to lakes in the Athabasca oil sands region (Alberta, Canada). *Environmental Research Letters*, 12(12), 124001.

Cory, R. M., McKnight, D. M. (2005). Fluorescence Spectroscopy Reveals Ubiquitous Presence of Oxidized and Reduced Quinones in Dissolved Organic Matter. *Environmental Science & Technology* 39(21), 8142–8149.

Cowie, B., James, B., Mayer, B. (2015). Distribution of total dissolved solids in McMurray Formation water in the Athabasca oil sands region, Alberta, Canada: Implications for regional hydrogeology and resource development. *AAPG Bulletin,* 99(01), 77-90. doi: 10.1306/07081413202

Cubasch, U., Meehl, G. A., Boer, G. J., Stouffer, R. J., Dix, M., Noda, A., Senior, C. A., Raper, S. U. Yap, K. S. (2001). Projections of future climate change. In *Climate Change 2001: The scientific basis. Contribution of WG1 to the Third Assessment Report of the IPCC (TAR)* (pp. 525-582). Cambridge University Press

Curtis, C., Flower, R., Rose, N., Shilland, J., Simpson, G., Turner, S., Yang, H., Pla, S. (2010). Palaeolimnological assessment of lake acidification and environmental change in the Athabasca Oil Sands Region, Alberta. *Journal of Limnology*, 69 (1s), 92.

Dabros, A., Pyper, M., Castilla, G. (2018). Seismic lines in the boreal and arctic ecosystems of North America: environmental impacts, challenges, and opportunities. *Environmental Reviews*, 26(2): 214-229.

Dalmagro, H., Lathuillière, M., Sallo, F., Guerreiro, M., Pinto, O., de Arruda, P. et al. (2019). Streams with Riparian Forest Buffers versus Impoundments Differ in Discharge and DOM Characteristics for Pasture Catchments in Southern Amazonia. *Water*, 11(2), 390.

Daniel, J., Rooney, R. C., Robinson, D. T. (2022). Climate, land cover and topography: essential ingredients in predicting wetland permanence. *Biogeosciences, 19(5), 1547–1570.*

Davidson, C., Spink, D. (2018). Alternate approaches for assessing impacts of oil sands development on air quality: A case study using the First Nation Community of Fort McKay. *Journal of the Air & Waste Management Association*, *68*(4), 308–328.

Del Vecchio, R., N. V. (2004). Blough. On the origin of the optical properties of humic substances, *Environmental Science and Technology* 38(14), 3885–3891.

Deng, J., Ma, H., Wang, X., Zhong, S., Zhang, Z., Zhu, J., Fan, Y., Hu, W., Wu, L., Li, X., Ren, L., Pavuluri, C. M., Pan, X., Sun, Y., Wang, Z., Kawamura, K., Fu, P. (2022). Measurement report: Optical properties and sources of water-soluble brown carbon in Tianjin, North China – insights from organic molecular compositions, *Atmospheric Chemistry and Physics*, 22, 6449–6470

Dey, S., Sarkar, S. (2024). Compositional and optical characteristics of aqueous brown carbon and HULIS in the eastern Indo-Gangetic Plain using a coupled EEM PARAFAC, FT-IR and 1H NMR approach. *Science of the Total Environment*, 921, 171084

Dillon, P. J., Molot, L. A. (1997). Effect of landscape form on export of dissolved organic carbon, iron, and phosphorus from forested stream catchments, *Water Resources Research* 33(11), 2591– 2600

Dodds, W., Whiles, M. (2010). Freshwater Ecology: Concepts and Environmental Applications of Limnology. 2nd Edition, Elsevier, Amsterdam, 330-333.

Dong, Z., Pavuluri, C. M., Li, P., Xu, Z., Deng, J., Zhao, X., Zhao, X., Fu, P., Liu, C.-Q. (2024). Measurement report: Optical characterization, seasonality, and sources of brown carbon in fine aerosols from Tianjin, North China: year-round observations, *Atmospheric Chemistry and Physics*, 24, 5887–5905

Driscoll, C., Fuller, R., Schecher, W. (1989). The role of organic acids in the acidification of surface waters in the Eastern U.S. *Water, Air, And Soil Pollution*, 43 (1-2), 21-40.

Driscoll, C. T., Lehtinen, M. D., Sullivan, T. J. (1994). Modeling the acid-base chemistry of organic solutes in Adirondack, New York, lakes, *Water Resources Research* 30(2), 297– 306

Driskill, A. K., Alvey, A., Dotson, A. D., Tomco, P. L. (2018). Monitoring polycyclic aromatic hydrocarbon (PAH) attenuation in Arctic waters using fluorescence spectroscopy, *Cold Regions Science and Technology*, 145, 76-85

Duarte, R. M. B. O., Santos, E. B. H., Pio, C. A., Duarte, A. D-C. (2007). Comparison of structural features of water-soluble organic matter from atmospheric aerosols with those of aquatic humic substances. *Atmospheric Environment*, 41, 8100-8113

Dufresne, M. B., Eccles, D. R., Leckie, D. A. (2001). The Geological and Geochemical Setting of the Mid-Cretaceous Shaftesbury Formation and Other Colorado Group Sedimentary Unities in Northern Alberta; Alberta Geological Survey.

Edgerton, E., Hsu, Y., White, E., Fenn, M., Landis, M. (2020). Ambient concentrations and total deposition of inorganic sulfur, inorganic nitrogen and base cations in the Athabasca Oil Sands Region. *Science of the Total Environment*, 706, 134864.

Emmerton, C. A., Cooke, C. A., Wentworth, G. R., Graydon, J. A., Ryjkov, A., Dastoor, A. (2018). Total Mercury and Methylmercury in Lake Water of Canada's Oil Sands Region. *Environmental Science and Technology*, 52(19):10946-10955.

Environment and Climate Change Canada (ECCC), Air Quality Research Division., Alberta Environment and Parks (AEP), Air Policy Branch. (2016). Joint Oil Sands Monitoring Program Emissions Inventory Compilation Report, *Joint Canada-Alberta Implementation Plan for Oil Sands Monitoring – Air Emissions Inventory Working Group*.

Environment and Climate Change Canada (ECCC). (2020). Historical Data. Government of Canada 2020, Retrieved September 16, 2016, from http://climate.weather.gc.ca/climate_normals /results_1981 _2010_e.html?stnID=402 &dCode=&dispBack=1

Environment and Climate Change Canada (ECCC) (2024). Historical Data; Government of Canada.http://climate.weather.gc.ca/climate_normals/results_1981_2010_e.html?stnID=402&dode=&dispBack=1

Eriksson, L., Byrne, T., Johansson, E., Trygg, J., Vikström, C. (2013). Multi- and Megavariate Data Analysis Basic Principles and Applications, 3rd ed, Vol. 1. Umetrics Academy.

Erlandsson, M., Cory, N., Köhler, S., Bishop, K. (2010). Direct and indirect effects of increasing dissolved organic carbon levels on pH in lakes recovering from acidification. *Journal of Geophysical Research*, 115, G03004.

Erlandsson, M., Futter, M. N., Kothawala, D. N., Köhler, S. J. (2012). Variabiltiy in spectral absorbance metrics across boreal lake waters. Journal of Environmental Monitoring, 14, 2643-2652.

Evans, C.D., Jutterström, S., Stadmark, J. *et al.* (2024). Four decades of changing dissolved organic matter quality and stoichiometry in a Swedish forest stream. *Biogeochemistry* 167, 1139–115.

Facchini, M. C., Mircea, M., Fuzzi, S., Charlson, R. (1999). Cloud albedo enhancement by surface-active organic solutes in growing droplets, *Nature*, 401, 257-259.

Feldmannová M., Hilscherová K., Maršálek B., and Bláha L. (2006). Effects of N-heterocyclic polyaromatic hydrocarbons on survival, reproduction, and biochemical parameters in Daphnia magna. *Environmental Toxicology*, 21(4): 425–431.

Ferretto, N., Tedetti, M., Guigue, C., Mounier, S., Redon, R., Goutx, M. (2014). Identification and quantification of known polycyclic aromatic hydrocarbons and pesticides in complex mixtures using fluorescence excitation–emission matrices and parallel factor analysis. *Chemosphere*, 107, 344-353.

Fisher, S.G., Likens, G.E. (1973). Energy Flow in Bear Brook, New Hampshire: An Integrative Approach to Stream Ecosystem Metabolism. *Ecological Monographs* 43, 421-439.

Frysinger, G. S., Gaines, R. B., Xu, L., Reddy, C. M. (2003). Resolving the Unresolved Complex Mixture in Petroleum-Contaminated Sediments. Environ. Sci. Technol., 37(8), 1653-1662,

Fu, P. Q., Kawamura, K., Chen, J., Qin, M. Y., Ren, L. J., Sun, Y. L., Wang, Z. F., Barrie, L. A., Tachibana, E., Ding, A. J., and Yamashita, Y. (2015). Fluorescent water-soluble organic aerosols in the High Arctic atmosphere. *Scientific Reports - UK*, 5, 9845

Fu, X., Du, H., Xu, H. (2021). Comparison in UV-induced photodegradation properties of dissolved organic matters with different origins. Chemosphere, 280, 130633.

Fulton, R.J. (1996). Surficial material map of Canada – Map 1880A, scale 1:5 000 000. Natural Resources Canada, Terrain Sciences Division, Ottawa, Ontario

Fuzzi, S., Facchini, M. C., Decesari, S., Matta, E., Mircea, M. (2002). Soluble organic compounds in fog and cloud droplets: what we have learned over the past few years?, *Atmospheric Research* 64, 89.

Gao, S., Surratt, J. D., Knipping, E. M., Edgerton, E. S., Shahgholi, M., Seinfeld, J. H. (2006). Characterization of polar organic components in fine aerosols in the southeastern United States: Identity, origin, and evolution, *Journal of Geophysical Research*, 111, D14314

Garcia, R., Diéguez, M., Gerea, M., Garcia, P., Reissig, M. (2018). Characterization and reactivity continuum of dissolved organic matter in forested headwater catchments of Andean Patagonia. *Freshwater Biology*, 63(9), 1049-1062.

Ghio A. J., Quigley D. R. (1994). Complexation of iron by humic-like substances in lung tissue: Role in coal workers' pneumoconiosis. American Journal of Physiology 267, 173–179

Gibson, J. J., Birks, S. J., Yi, Y., Vitt, D. H. (2015). Runoff to boreal lakes linked to land cover, watershed morphology and permafrost thaw: a 9-year isotope mass balance assessment. *Hydrological Processes*, 29, 3848– 3861.

Gibson, J. J., Yi, Y., Birks. S. J. (2019). Isotopic tracing of hydrologic drivers including permafrost thaw status for lakes across Northeastern Alberta, Canada: A 16-year, 50-lake assessment. *Journal of Hydrology: Regional Studies*, 26, 100643, ISSN 2214-5818,

Gibson, J., Yi, Y., Birks, S. (2020). Watershed, climate, and stable isotope data (oxygen-18 and deuterium) for 50 boreal lakes in the oil sands region, northeastern Alberta, Canada, 2002–2017. Data in Brief, 29, 105308.

Gibson, J. J., Birks, S. J., Moncur, M. C., Vallarino, A., Kusel, C., Cherry, M. (2021). Hydro geochemistry Studies in the Oil Sands Region to Investigate the Role of Terrain Connectivity in Nitrogen Critical Loads. *Water*, 13, 2204.

Giesy, J. P., Ansderson, J. C., Wiseman, S. B. (2010). Alberta oil sands development. *PNAS: Commentary*, 107,3, 951-952

Gopalapillai, Y., Kirk, J. L., Landis, M. S., Muir, D. C. G., Cooke, C. A., Gleason, A. Ho, A., Kelly, E., Schindler, D., Wang, X., Lawson, G. (2019). Source Analysis of Pollutant Elements in Winter Air Deposition in the Athabasca Oil Sands Region: A Temporal and Spatial Study. *ACS Earth and Space Chemistry*, 3, 1656 – 1668

Graber, E. R., Rudich, Y. (2006). Atmospheric HULIS: How humic-like are they? A comprehensive and critical review. *Atmospheric Chemistry and Physics*, 6, 729–753

Green, S. A., Blough, N. V. (1994). Optical absorption and fluorescence properties of chromophoric dissolved organic matter in natural waters, *Limnology and Oceanography*, 39(8), 1903–1916.

Groisman, P. Y., Karl, T. R., Knight, R. W. (1994). Observed impact of snow cover on the heat balance and the rise of continental spring temperatures. *Science*, 263, 198–200.

Gu, Y., Lensu, A., Ki, S., Ojala, A., Talo, A. (2017). Iron and pH Regulating the Photochemical Mineralization of Dissolved Organic Carbon. *ACS Omega* 2.

Guéguen, C., Clarisse, O., Perroud, A., McDonald, A. (2011). Chemical speciation and partitioning of trace metals (Cd, Co, Cu, Ni, Pb) in the lower Athabasca River and its tributaries (Alberta, Canada). *Journal of Environmental Monitoring*, 13(10), 2865–2872.

Guha Thakurta, S., Maiti, A., Pernitsky, D., Bhattacharjee, S. (2013). Dissolved Organic Matter in Steam Assisted Gravity Drainage Boiler Blow-Down Water. *Energy & Fuels*, 27(7), 3883-3890.

Gustafsson, Ö., Kruså, M., Zencak, Z., Sheesley, R. J., Granat, L., Engström, E., Rodhe. H. (2009). Brown clouds over South Asia: biomass or fossil fuel combustion? *Science*, 323 (5913), 495-49833

Hagler, G., Bergin, M., Smith, E., Dibb, J. (2007). A summer time series of particulate carbon in the air and snow at Summit, Greenland. *Journal of Geophysical Research*, 112.

Hansell, D., Carlson, C., Repeta, D., Schlitzer, R. (2009). Dissolved organic matter in the ocean: A controversy stimulates new insights. *Oceanography*, 22 (4), 202-211.

Hansen, A.M., Kraus, T.E.C., Pellerin, B.A., Fleck, J.A., Downing, B.D., Bergamaschi, B.A. (2016). Optical properties of dissolved organic matter (DOM): Effects of biological and photolytic degradation. *Limnology and Oceanography*, 61, 1015-1032

Harner, T., Rauert, C., Muir, D., Schuster, J. K., Hsu, Y., Zhang, L., Marson, G., Watson, J. G., Ahad, J., Cho, S., Jariyasopit, N., Kirk, J., Korosi, J., Landis, M. S., Martin, J. W., Zhang, Y., Fernie, K., Wentworth, G. R., Wnorowski, A., Dabek, E., Charland, J., Pauli, B., Wania, F., Galarneau, E., Cheng, I., Makar, P., Whaley, C., Chow, J. C., Wang, X. (2018). Air synthesis review: polycyclic aromatic compounds in the oil sands region. *Environmental Reviews*. 26(4): 430-468.

Harsha, M. L., Redman, Z. C., Wesolowski, J., Podgorski, D. C., Tomco, P. L. (2023). Photochemical formation of water soluble oxyPAHs, naphthenic acids, and other hydrocarbon oxidation products from Cook Inlet, Alaska crude oil and diesel in simulated seawater spills. *Environmental Science Advances*, 2, 447-461

Hazewinkel, R., Wolfe, A., Pla, S., Curtis, C., Hadley, K. (2008). Have atmospheric emissions from the Athabasca Oil Sands impacted lakes in northeastern Alberta, Canada?. Canadian *Journal of Fisheries and Aquatic Sciences*, 65 (8), 1554-1567.

Headley, J.V., Akre, C., Conly, F.M., Peru, K.M., Dickson, L.C. (2001). Preliminary characterization and source assessment of PAHs in tributary sediments of the Athabasca River, Canada. *Environmental Forensics* 2, 335–345

Heikkinen, K. (1990). Seasonal changes in iron transport and nature of dissolved organic matter in a humic river in northern Finland. *Earth Surface Processes and Landforms*, 15 (7), 583-596.

Holt, C., Yan, N., Somers, K. (2003). pH 6 as the threshold to use in critical load modeling for zooplankton community change with acidification in lakes of south-central Ontario: accounting for morphometry and geography. *Canadian Journal of Fisheries and Aquatic Sciences*, 60(2), 151-158. doi: 10.1139/f03-008

Hosen, J. D., Armstrong, A. W., Palmer, M. A. (2018). Dissolved organic matter variations in coastal plain wetland watersheds: The integrated role of hydrological connectivity, land use, and seasonality. *Hydrological Processes*, 32, 1664–1681

Hruška, J., Laudon, H., Johnson, C., Köhler, S., Bishop, K. (2001). Acid/base character of organic acids in a boreal stream during snowmelt. *Water Resources Research*, 37(4), 1043-1056.

Huang, Q., Liu, L., Huang, J., Chi, D., Devlin, A. T., Wu, H. (2022). Seasonal dynamics of chromophoric dissolved organic matter in Poyang Lake, the largest freshwater lake in China, *Journal of Hydrology* 605, 127298

Hudson, N., Baker, A. Reynolds, D. (2007). Fluorescence analysis of dissolved organic matter in natural, waste and polluted waters — a review. *River Research and Applications*. 23: 631-649

Huguet, A., L. Vacher, S. Relexans, S. Saubusse, J. M.Froidefond, E. Parlanti. (2009). Properties of fluorescent dissolved organic matter in the Gironde Estuary. *Organic Geo-chemistry* 40, 706–719.

Huser, B., Futter, M., Wang, R., Fölster, J. (2018). Persistent and widespread long-term phosphorus declines in Boreal lakes in Sweden. *Science of the Total Environment*, 613-614, 240-249.

Iavorivska, L., Boyer, E. W., Grimm. J. W. (2017). Wet atmospheric deposition of organic carbon: An underreported source of carbon to watersheds in the northeastern United States. *Journal of Geophysical Research: Atmospheres*, 122, 3104–3115.

Idowu, O., Semple, K. T., Ramadass, K., O'Connor, W., Hansbro, P., Thavamani, P. (2019). Beyond the obvious: Environmental health implications of polar polycyclic aromatic hydrocarbons. *Environment international*, 123, 543–557. https://doi.org/10.1016/j.envint.2018.12.051

Ilbert, M., Bonnefoy, V. (2013). Insight into the evolution of the iron oxidation pathways. *Biochimica Et Biophysica Acta (BBA) – Bioenergetics*, 1827 (2), 161-175.

Ingersoll, George P., Turk, J. T., Mast, A., Clow, D. W., Campbell, D. H., Bailey, Z. C. (2002). Rocky Mountain snowpack chemistry network: History, methods, and the importance of monitoring mountain ecosystems. *United States Geological Survey*, Open-File Report, 2001-466.

International Agency for Research on Cancer (IARC). (2010). Some non-heterocyclic polycyclic aromatic hydrocarbons and some related exposures. IARC monographs on the evaluation of carcinogenic risks to humans. International Agency for Research on Cancer, World Health Organization, Lyon, France. Vol. 92.

Jacobson, M.C., Hansson, H.C., Noone, K.J., Charlson, R.J. (2000). Organic atmospheric aerosols: review and state of the science. *Reviews in Geophysics* 38, 267–294

Jacobson, M. Z. (2004). Climate response of fossil fuel and biofuel soot, accounting for soot's feedback to snow and sea ice albedo and emissivity, *Journal of Geophysical Research*, 109, D21201,

Jariyasopit, N., Harner, T., Wu, D., Williams, A., Halappanavar, S., Su, K. (2016). Mapping indicators of toxicity for polycyclic aromatic compounds in the atmosphere of the

Athabasca oil sands region, *Environmental Science and Technology*, 50, 11282–11291

Jariyasopit, N., Zhang, Y., Martin, J. W., Harner, T. (2018). Comparison of polycyclic aromatic compounds in air measured by conventional passive air samplers and passive dry deposition samplers and contributions from petcoke and oil sands ore. *Atmospheric Chemistry and Physics*, 18, 9161–9171

Jariyasopit, N., Harner, T., Shin, C., Park, R. (2021). The effects of plume episodes on PAC profiles in the Athabasca Oil Sands Region. *Environmental Pollution*, 282, 117014

Jason M.E. Ahad, J. M. E., Jautzy, J. J., Cumming, B. F., Das, B., Laird, K. R., Sanei, H. (2015). Sources of polycyclic aromatic hydrocarbons (PAHs) to northwestern Saskatchewan lakes east of the Athabasca oil sands, *Organic Geochemistry*, 80, 35-45.

Jautzy, J., Ahad, J. M. E., Gobeil, C., Savard, M. M. (2013). Century-long source apportionment of PAHs in Athabasca Oil Sands Region lakes using diagnostic ratios and compound specific carbon isotope signatures, *Environmental Science and Technology*, 47(12), 615-6163.

Jiang, X., Wiedinmyer, C., Carlton, A. G. (2012). Aerosols from Fires: An Examination of the Effects on Ozone Photochemistry in the Western United States. *Environmental Science and Technology* 46, 11878.

Jiji, R.D., Andersson, G.G., Booksh, K.S. (2000). Application of PARAFAC for calibration with excitation-emission matrix fluorescence spectra of three classes of environmental pollutants. *Journal of Chemometrics* 14, 171,

Jones, R. (1998). Phytoplankton, primary production and nutrient cycling. *Ecological Studies*, 145-175.

Josefsson, S., Arp, H. P. H., Kleja, D. B., Enell, A., Lundstedt, S. (2015). Determination of polyoxymethylene (POM) – water partition coefficients for oxy-PAHs and PAHs, *Chemosphere*, 119, 1268–1274

Jiang, X., Wiedinmyer, C., Carlton, A. G. (2012). Aerosols from Fires: An Examination of the Effects on Ozone Photochemistry in the Western United States. *Environmental Science and Technology*, 46, 11878,

Kakumanu, M.L., Ma, L. Williams, M.A (2019). Drought-induced soil microbial amino acid and polysaccharide change and their implications for C-N cycles in a climate change world. *Scientific Reports*, 9, 10968

Kaur, K., Bhattacharjee, S., Pillai, R. G., Ahmed, S., Azmi, S. (2014). Peptide arrays for detecting naphthenic acids in oil sands process affected waters. *RSC Advances* 105, 60694-60701.

Kavanagh, R. J., Burnison, K., Frank, R. A., Solomon, K. R., Van Der Kraak, G. (2009). Detecting oil sands process-affected waters in the Alberta oil sands region using synchronous fluorescence spectroscopy. *Chemosphere* 76(1), 120-126,

Kellerman, A., Dittmar, T., Kothawala, D., Tranvik., L. J. (2014). Chemodiversity of dissolved organic matter in lakes driven by climate and hydrology. *Nature Communications* 5, 3804.

Kelly, E.N., Short, J.W., Schindler, D.W., Hodson, P.V., Ma, M., Kwan, A. K., Fortin, B.L. (2009). Oil sands development contributes polycyclic aromatic compounds to the Athabasca River and its tributaries. *Proceedings of the National Academy of Sciences of the United States of America*. 106 (52) 22346-22351,

Kim, K. H., Jahan, S. A., Kabir, E., Brown, R. J. (2013). A review of airborne polycyclic aromatic hydrocarbons (PAHs) and their human health effects, *Environment International*, 60, 71–80

Kim, H., Kim, J. Y., Jin, H. C., Lee, J. Y., Lee, S. P. (2016). Seasonal variations in the light-absorbing properties of water-soluble and insoluble organic aerosols in Seoul, Korea. Atmospheric Environment 129, 234–242

Kim, E. A., Koh, B. (2020). Utilization of road dust chemical profiles for source identification and human health impact assessment. *Scientific Reports*, 10,1, 14259

Kirillova E. N., Andersson, A., Sheesley, R. J., Krusa, M., Praveen, P. S., Budhavant, K., Safai, P. D., Rao, P. S. P., Gustafsson, Ö. (2013). 13C- and 14C-based study of sources and atmospheric processing of water-soluble organic carbon (WSOC) in South Asian aerosols. *Journal of Geophysical Research: Atmosphere*, 118, 614 – 626

Kirillova, E. N., Andersson, A., Tiwari, A. S., Srivastava, A. K., Bisht, D. S., Gustafsson, Ö. (2014). Water-soluble organic carbon aerosols during a full New Delhi winter: Isotope-based source apportionment and optical properties, Journal Geophysical Research: Atmosphere, 119, 3476–3485

Kirillova, E. N., Marinoni, A., Bonasoni, P., Vuillermoz, E., Facchini, M. C., Fuzzi, S., Decesari, S. (2016) Light absorption properties of brown carbon in the high Himalayas. *Journal of Geophysical Research: Atmospheres* 121(16), 9621-9639

Kirk. J. L., Muir. D. C. G., Gleason. A., Wang. X., Lawson. G., Frank. R. A., Lehnherr. I., Wrona. F. (2014). Atmospheric Deposition of Mercury and Methylmercury to Landscapes and Waterbodies of the Athabasca Oil Sands Region. *Environmental Science and Technology*, 48 (13), 7374-7383

Kirk, J., Muir, D., Manzano, C., Cooke, C., Wiklund, J., Gleason, A., Summers, J., Smol, J., J. Kurek. (2018). Atmospheric deposition to the Athabasca Oil Sands region using snowpack measurements and dated lake sediment cores. Oil Sands Monitoring Program Technical Report Series No. 1.2. 43 p.

Koehler B, Von Wachenfeldt E, Kothawala DN, Tranvik LJ. Reactivity continuum of dissolved organic carbon decomposition in lake water. J Geophys Res Biogeosciences. 2012;117: 1–14. doi: 10.1029/2011JG001793

Köhler, S., Hruška, J., Bishop, K. (1999). Influence of organic acid site density on pH modeling of Swedish lakes. *Canadian Journal of Fisheries and Aquatic Sciences*, 56 (8), 1461-1470.

Koptsik, S., Berezina, N., Livantsova, S. (2001). Effects of natural soil acidification on biodiversity in boreal forest ecosystems. *Water, Air, and Soil Pollution*, 130(1/4), 1025-1030. doi: 10.1023/a:1013904211461

Kothawala, D., Murphy, K. R., Stedmon, C. A., Weyhenmeyer, G. A., Tranvik, L. J. (2013). Inner filter correction of dissolved organic matter fluorescence. *Limnology and Oceanography: Methods* 11, 616-630.

Kothawala, D., Stedmon, C., Müller, R., Weyhenmeyer, G., Köhler, S., Tranvik, L. (2014). Controls of dissolved organic matter quality: evidence from a large-scale boreal lake survey. *Global Change Biology*, 20(4), 1101-1114.

Kritzberg, E., Hasselquist, E., Škerlep, M., Löfgren, S., Olsson, O., Stadmark, J., Valinia, S., Hansson, L, E., Laudon, H. (2020). Browning of freshwaters: Consequences to

ecosystem services, underlying drivers, and potential mitigation measures. *Ambio*, 49 (2), 375-390.

Kritzberg, E. (2017). Centennial-long trends of lake browning show major effect of afforestation. *Limnology and Oceanography Letters*, 2 (4), 105-112.

Kurek, J., Kirk, J., Muir, D., Wang, X., Evans, M., Smol, J. (2013). Legacy of a half century of Athabasca Oil Sands development recorded by lake ecosystems. *Proceedings of The National Academy of Sciences*, 110 (5), 1761-1766.

Kutser, T., Alikas, K., Kothawala, D., Köhler, S. (2015). Impact of iron associated to organic matter on remote sensing estimates of lake carbon content. *Remote Sensing of Environment*, 156, 109-116.

Laird, K., Das, B., Kingsbury, M., Moos, M., Pla-Rabes, S., Ahad, J., Wiltse, B., Cumming, F, B. (2013). Paleolimnological assessment of limnological change in 10 lakes from northwest Saskatchewan downwind of the Athabasca oils sands based on analysis of siliceous algae and trace metals in sediment cores. *Hydrobiologia*, 720 (1), 55-73.

Lakowicz, R. R. (2006). Principles of Fluorescence Spectroscopy, Springer-Verlag, New York, USA, 3rd edn

Lan, T., Wu, P., Liu, Z., Stroet, M., Liao, J., Chai, Z., Mark, A. E., Liu, N., Wang, D. (2022). Understanding the Effect of pH on the Solubility and Aggregation Extent of Humic Acid in Solution by Combining Simulation and the Experiment. *Environmental Science & Technology 56* (2), 917-927

Landis, M. S., Pancras, J. P., Graney, J. R., Stevens, R. K., Percy, K. E., Krupa, S. (2012). Receptor Modeling of Epiphytic Lichens to Elucidate the Sources and Spatial Distribution of Inorganic Air Pollution in the Athabasca Oil Sands Region. Develop. *Environmental Science*, 427–467

Landis, M. S., Pancras, J. P., Graney, J. R., White, E. M., Edgerton, E. S., Legge, A., Percy., K. E. (2017). Source apportionment of ambient fine and coarse particulate matter at the Fort McKay community site, in the Athabasca Oil Sands Region, Alberta, Canada. *Science of the Total Environment*, 584–585, 105-117

Landis. M. S., Studabaker. W. B., Pancras. J. P., Graney. J. R., White. E. M., Edgerton. E. S. (2019a). Source apportionment of ambient fine and coarse particulate matter polycyclic aromatic hydrocarbons at the Bertha Ganter-Fort McKay community site in the Oil Sands Region of Alberta, Canada, *Science of The Total Environment*, 666, 540-558, ISSN 0048-9697

Landis, M. S., Pancras, J. P., Graney, J. R., White, E. M., Edgerton, E. S., Legge, A., Percy., K. E. (2019b). Source apportionment of ambient fine and coarse particulate matter at the Fort McKay community site, in the Athabasca Oil Sands Region, Alberta, Canada. *Science of The Total Environment*, 584–585, 105-117.

Landis, M., Studabaker, W., Patrick Pancras, J., Graney, J., Puckett, K., White, E., Edgerton, E. (2019c). Source apportionment of an epiphytic lichen biomonitor to elucidate the sources and spatial distribution of polycyclic aromatic hydrocarbons in the Athabasca Oil Sands Region, Alberta, Canada. *Science of The Total Environment*, 654, 1241-1257.

Lanzerstorfer C, Logiewa A. (2019). The upper size limit of the dust samples in road dust heavy metal studies: Benefits of a combined sieving and air classification sample preparation procedure. *Environmental Pollution*, 245:1079-1085

Laskin, A., Laskin, J., Nizkorodov. S. A. (2015). Chemistry of atmospheric brown carbon. Chem. Rev., 115,10, 4335-4382

Lee, J. Y., Peterson, P. K., Vear, L. R., Cook, R. D., Sullivan, A. P., Smith, E., Hawkins, L. N., Olson, N. E., Hems, R., Snyder, P. K., & Pratt, K. A. (2022). Wildfire Smoke Influence on Cloud Water Chemical Composition at Whiteface Mountain, New York. *Journal of geophysical research. Atmospheres : JGR*, 127(19), e2022JD037177.

Lemieux, C. L., Lambert, I. B., Lundstedt, S., Tysklind, M., White, P. A. (2008). Mutagenic hazards of complex polycyclic aromatic hydrocarbon mixtures in contaminated soil, *Environmental Toxicology and Chemistry*, 27, 978–990

Li, S., Fan, R., Luo, D., Xue, D., Li, L., Yu, X., Huang, T., Yang, H., Huang, C. (2020). Variation in quantity and quality of rainwater dissolved organic matter (DOM) in a peri-urban region: Implications for the effect of seasonal patterns on DOM fates. *Atmospheric Environment*. 239, 117769.

Li, Y., Yan, F., Kang, S., Zhang, C., Chen, P., Hu, Z., Li, C. (2021). Sources and light absorption characteristics of water-soluble organic carbon (WSOC) of atmospheric particles at a remote area in inner Himalayas and Tibetan Plateau, *Atmospheric Research*, 253, 105472

Li, X., Yu, F., Tripathee, L., Yan, F., Hu, Z., Gao, S., Xiaobo, H., Li, C., Kang, S. (2022). Concentrations, sources, fluxes, and absorption properties of carbonaceous matter in a central Tibetan Plateau river basin. *Environmental Research.* 216. 114680

Libiseller, C., Grimvall, A. (2002). Performance of partial Mann-Kendall tests for trend detection in the presence of covariates. *Environmetrics*, 13 (1), 71-84.

Liggio, J., Li, S., Hayden, K., Taha, Y., Stroud, C., Darlington, A., Drollette, B., Gordon, M., Lee, P., Liu, P., Leithead, A., Moussa, S., Wang, D., O'Brien, J., Mittermeier, R., Brook, J., Lu, G., Staebler, R., Han, Y., Tokarek, T., Osthoff, H., Makar, P., Zhang, J., Plata, D., Gentner, D. (2016). Oil sands operations as a large source of secondary organic aerosols. *Nature*, 534 (7605), 91-94.

Liggio, J., Moussa, S., Wentzell, J., Darlington, A., Liu, P., Leithead, A., Hayden, K., O'Brien, J., Mittermeier, R., Staebler, R., Wolde, M., Li, S. (2017). Understanding the primary emissions and secondary formation of gaseous organic acids in the oil sands region of Alberta, Canada. *Atmospheric Chemistry and Physics*, 17 (13), 8411-8427.

Liggio, J., Makar, P., Li, S. M., Hayden, K., Darlington, A., Moussa, S., Wren, S., Staebler, R., Wentzell, J., Wheeler, M., Leithead, A., Mittermeier, R., Narayan, J., Wolde, M., Blanchard, D., Aherne, J., Kirk, J., Lee, C., Stroud, C., Zhang, J., Akingunola, A., Katal, A., Cheung, P., Ghahreman, R., Majdzadeh, M., He, M., Ditto, J., Gentner, D. (2024). Organic carbon dry deposition outpaces atmospheric processing with unaccounted implications for air quality and freshwater ecosystems. *Science Advances*.

Likens, G., Driscoll, C., Buso, D., Siccama, T., Johnson, C., Lovett, G., Fahey, T., Reiners, W., Ryan, C., Martin, C., Bailey, S. (1998). The biogeochemistry of calcium at Hubbard Brook. *Biogeochemistry*, 41(2), 89-173. doi: 10.1023/a:1005984620681

Lin, P., Rincon, A. G., Kalberer, M., Yu, J. Z. (2012). Elemental Composition of HULIS in the Pearl River Delta Region, China: Results Inferred from Positive and Negative

Electrospray High Resolution Mass Spectrometric Data. *Environmental Science and Technology* 46, 7454.

Lindaas, J., Pollack, I. B., Calahorrano, J J., O'Dell, K., Garofalo, L. A., Pothier, M. A., Farmer, D. K., Kreidenweis, S. M., Campos, T., Flocke, F., Weinheimer, A. J., Montzka, D. D., Tyndall, G. S., Apel, E. C., Hills, A. J., Hornbrook, R. S., Palm, B. B., Peng, Q., Thornton, J. A., Permar, W., Wielgasz, C., Hu, L., Pierce, J. R., Collett, J. L., Sullivan, A. P., Fischer, E. V. (2021). Empirical insights into the fate of ammonia in western U.S. wildfire smoke plumes. *Journal of Geophysical Research: Atmospheres*. 126(11): e2020JD033730

Liptzin, D., Boy, J., Campbell, J. L., Clarke, N., Laclau, J.-P., Godoy, R., Johnson, S. L., Kaiser, K., Likens, G. E., Karlsson, G. P., Markewitz, D., Rogora., M., Sebestyen, S. D., Shanley, J. B., Vanguelova, E., Verstraeten, A., Wilcke, W., Worrall, F., McDowell, W. H. (2022). Spatial and temporal patterns in atmospheric deposition of dissolved organic carbon. *Global Biogeochemical Cycles*, 36, e2022GB007393

Lorenzo-Seva, U., ten Berge, J. M. F. (2006). Tucker's congruence coefficient as a meaningful index of factor similarity. Methodology: European Journal of Research Methods for the Behavioral and Social Sciences, 2(2), 57–64

Luider, C., Petticrew, E. Curtis, P.J. (2003). Scavenging of dissolved organic matter (DOM) by amorphous iron hydroxide particles Fe(OH)3(s). *Hydrobiologia*, 494, 37–41.

Lukacs, H., Gelencsér, A., Hammer, S., Puxbaum, H., Pio, C., Legrand, M., Kasper-Giebl, A., Handler, M., Limbeck, A., Simpson, D., Preunkert, S. (2007). Seasonal trends and possible sources of brown carbon based on 2-year aerosol measurements at six sites in Europe. Journal of Geophysical Research, 112, D23S18.

Lundstedt, S., White, P. A., Lemieux, C. L., Lynes, K. D., Lambert, I. B., Öberg, L., Haglund, P., Tysklind, M. (2007). Sources, Fate, and Toxic Hazards of Oxygenated Polycyclic Aromatic Hydrocarbons (PAHs) at PAH- contaminated Sites, *Ambio*, 36, 475–485

Ma, H., Li, J.,Wan, C., Liang, Y., Zhang, X., Dong, G., Hu, L., Yang, B., Zeng, X., Su, T., Lu, S., Chen, S., Khorram, M. S., Sheng, G., Wang, X., Mai, B., Yu, Z., Zhang, G. (2019). Inflammation Response of Water-Soluble Fractions in Atmospheric Fine Particulates: A Seasonal Observation in 10 Large Chinese Cities. *Environmental Science and Technology* 53, 3782−3790.

MacKinnon, M., and Sethi, A. (1993). A comparison of the physical and chemical properties of the Tailings ponds at the Syncrude and Suncor oil sands plants, Proceedings of Fine Tailings Symposium, Oil Sands- Our Petroleum Future Conference, April 4-7, Edmonton, Alberta, Canada

Makar, P., Akingunola, A., Aherne, J., Cole, A., Aklilu, Y., Zhang, J., Wong, I., Hayden, K., Li, S, M., Kirk, J., Scott, K., Moran, M. D., Robichaud, A., Cathcart, H., Baratzedah, P., Pabla, B., Cheung, P., Zheng, Q., Jeffries, D, S. (2018). Estimates of exceedances of critical loads for acidifying deposition in Alberta and Saskatchewan. *Atmospheric Chemistry and Physics*, 18 (13), 9897-9927.

Mahadevan, S., Shah, S. L., Marrie, T. J., Slupsky, C. M. (2008). Analysis of metabolomic data using support vector machines. *Analytical Chemistry*, 80:7562-70.

Mahamuni G, He J, Rutherford J, Ockerman B, Majumdar A, Seto E, Korshin, G., Novosselov, I. (2021) Solid-phase excitation-emission matrix spectroscopy for chemical analysis of combustion aerosols. PLoS ONE 16(5): e0251664.

Maloney, K., Morris, D., Moses, C., Osburn, C. (2005). The role of iron and dissolved organic carbon in the absorption of ultraviolet radiation in humic lake water. *Biogeochemistry* 75 (3), 393-407.

Mamun, A. A, Celo, V., Dabek-Zlotorzynska, E., Charland, J-P., Cheng, I., Zhang, L. (2021). Characterization and source apportionment of airborne particulate elements in the Athabasca oil sands region, *Science of the Total Environment*, 788,147748

Mantoura, R. F. C., Dickson, A., Riley, J. P. (1978). The complexation of metals with humic materials in natural waters. *Estuarine and Coastal Marine Science,* 6 (4), 387-408.

Maranger, R., Pullin, M. Elemental complexation by dissolved organic matter in lakes. Aquatic Ecosystems 2003, 185-214.

Marentette, J. R., Frank, R. A., Bartlett, A. J., Gillis, P. L., Hewitt, L. M., Peru, K. M., Headley, J. M., Brunswick, P., Shang, D., Parrott, J. L. (2015). Toxicity of naphthenic acid fraction components extracted from fresh and aged oil sands process-affected waters, and commercial naphthenic acid mixtures, to fathead minnow (Pimephales promelas) embryos, *Aquatic Toxicology*, 164, 108–117

Martin, N., Burkus, Z., McEachern, P., Yu, T. (2013). Naphthenic acids quantification in organic solvents using fluorescence spectroscopy. *Journal of Environmental Science and Health, Part A,* 49(3), 294-306.

Mattsson, T., Kortelainen, P., David, M. (1995). Acid neutralizing capacity of solutions containing organic acids isolated from Finnish lakes. *Water, Air, and Soil Pollution*, 85 (2), 505-510.

Mauderly, J. L., Chow, J. C. (2008). Health effects of organic aerosols. *Inhalation Toxicol*ogy, 20, 257−288.

McCoy, D. T., Burrows, S. M., Wood, R., Grosvenor, D. P., Elliot, S. M., Ma, P-L., Rasch, P. J., Hartmann, D. L. (2015). Natural aerosols explain seasonal and spatial patterns of Southern Ocean cloud albedo. Science Advances 1, e1500157

McDowell, W. H, Zsolnay, A., Aitkenhead-Peterson, J., Gregorich, E. G., Jones, D. L., Jödemann, D., et al (2006). A comparison of methods to determine the biodegradable dissolved organic carbon from different terrestrial sources. *Soil Biology and Biochemistry* 38: 1933–1942.

Mendoza, W. G., Riemer, D. D., Zika, R. G. (2013). Application of fluorescence and PARAFAC to assess vertical distribution of subsurface hydrocarbons and dispersant during the Deepwater Horizon oil spill. *Environmental Science: Processes & Impacts* 15, 1017-1030.

Meyer-Jacob, C., Michelutti, N., Paterson, A., Cumming, B., Keller, W., Smol, J. (2019). The browning and re-browning of lakes: Divergent lake-water organic carbon trends linked to acid deposition and climate change. *Scientific Reports,* 9, 16676.

Miyazaki, Y., Aggarwal, S. G., Singh, K., Gupta, P. K., Kawamura, K. (2009). Dicarboxylic acids and water-soluble organic carbon in aerosols in New Delhi, India, in winter: Characteristics and formation processes, *Journal of Geophysical Research*, 114, D19206

Mierle, G., Ingram, R. (1991). The role of humic substances in the mobilization of mercury from watersheds. *Water Air and Soil Pollution*, 56 (1), 349-357.

Miller, J. N., Miller, J. C. (2002). Estadística y quimiometría para química analítica (No. 543.062: 519.23 MIL).

Mladenov. N., Lopez-Ramos. J., McKnight. D. M., Reche. I. (2009). Alpine lake optical properties as sentinels of dust deposition and global change. Limnology and Oceanography, 52(6), part 2, 2386-2400

Mohamed, M., Wilson, L., Headley, J., Peru, K. (2008). Screening of oil sands naphthenic acids by UV-Vis absorption and fluorescence emission spectrophotometry. *Journal of Environmental Science and Health, Part A*, 43(14), 1700-1705.

Molot, L. (2009). Color of Aquatic Ecosystems. *Encyclopedia of Inland Waters*, 657-663.

Molot, L., Dillon, P. (1997). Colour - mass balances and colour - dissolved organic carbon relationships in lakes and streams in central Ontario. *Canadian Journal of Fisheries and Aquatic Sciences*, 54 (12), 2789-2795.

Monteith, D., Stoddard, J., Evans, C., de Wit, H., Forsius, M., Høgåsen, T., Wilander, A., Skjelkvåle, B. R., Jeffries, D.S., Vuorenmaa, J., Keller, B., Kopácek, J., Vesely, J. (2007). Dissolved organic carbon trends resulting from changes in atmospheric deposition chemistry. *Nature*, 450 (7169), 537-540.

Munson, R. K., Gherini, S. A. (1993), Influence of organic acids on the pH and acid-neutralizing capacity of Adirondack Lakes. *Water Resources Research* 29(4), 891– 899

Murphy, K., Stedmon, C., Wenig, P., Bro, R. (2014). OpenFluor—A spectral database of auto-fluorescence by organic compounds in the environment. *Analytical Methods* 6, 658.

Murphy, K. R., Stedmon, C. A, Graeber, D., Bro, R. (2013). Fluorescence spectroscopy and multi-way techniques. PARAFAC. *Analytical Methods* 5, 6557-6566.

Natural Resources Canada. Crude oil facts 2020, Retrieved 19 July 2020, from https://www.nrcan.gc.ca/science-data/data-analysis/energy-data-analysis/energy-facts/crude-oil-facts/20064

Nierop, K., Jansen, B., Verstraten, J. (2002). Dissolved organic matter, aluminium and iron interactions: precipitation induced by metal/carbon ratio, pH and competition. *Science of the Total Environment*, 300 (1-3), 201-211.

Nowak, A., Hodson, A., Turchyn, A. V. (2018). Spatial and Temporal Dynamics of Dissolved Organic Carbon, Chlorophyll, Nutrients, and Trace Metals in Maritime Antarctic Snow and Snowmelt. *Frontiers in Earth Science*, 6.

Ohno, T. (2002). Fluorescence inner-filtering correction for determining the humification index of dissolved organic matter. *Environmental Science and Technology* 36: 742–746.

Olefeldt, D., Devito, K. J., Turetsky, M. R. (2013). Sources and fate of terrestrial dissolved organic carbon in lakes of a Boreal Plains region recently affected by wildfire. *Biogeosciences* 10, 6247–6265

Oliver, B., Thurman, E., Malcolm, R. (1983). The contribution of humic substances to the acidity of colored natural waters. *Geochimica et Cosmochimica Acta 47* (11), 2031-2035.

Oni, S., Futter, M., Bishop, K., Köhler, S., Ottosson-Löfvenius, M., Laudon, H. (2013). Long-term patterns in dissolved organic carbon, major elements and trace metals in boreal headwater catchments: trends, mechanisms and heterogeneity. *Biogeosciences*, 10 (4), 2315-2330.

Osburn, C., Boyd, T., Montgomery, M., Bianchi, T., Coffin, R., Paerl, H. (2016). Optical Proxies for Terrestrial Dissolved Organic Matter in Estuaries and Coastal Waters. *Frontiers in Marine Science*, 2.

Palmer, J., Trew, O. (1987). The sensitivity of Alberta lakes and soils to acidic deposition. Overview report, Environmental Protection Services, Alberta Environment, Edmonton, 44p.

Park, S-S., Sim, S. Y., Bae, M-S., Schauer. J. J. (2013). Size distribution of water-soluble components in particulate matter emitted from biomass burning, *Atmospheric Environment*, 73, 62-72

Paul, D., Skrzypek, G. (2006). Flushing time and storage effects on the accuracy and precision of carbon and oxygen isotope ratios of sample using the Gasbench II technique. *Rapid Communications in Mass Spectrometry*. 20, 2033-2040.

Pemberton, J., Lloyd, C., Arthur, C., Johnes, P., Dickinson, M., Charlton, A., Evershed, R. (2019). Untargeted characterisation of dissolved organic matter contributions to rivers from anthropogenic point sources using direct-infusion and high-performance liquid chromatography/Orbitrap mass spectrometry. *Rapid communications in mass spectrometry*, 34 (S4), e8618.

Perera, F. P., Li, Z., Whyatt, R., Hoepner, L., Wang, S., Camann, D., Rauh, V. (2009). Prenatal airborne polycyclic aromatic hydrocarbon exposure and child IQ at age 5 years, *Pediatrics*, 124, 195–202.

Polissar, A., Hopke, P., Poirot, R. (2001). Atmospheric Aerosol over Vermont: Chemical Composition and Sources. *Environmental Science and Technology*, 35 (23), 4604-4621.

Popovicheva, O. B., Engling, G., Ku, I-T., Timofeev, M. A., Shonija, N. K. (2019). Aerosol emissions from long-lasting smoldering of boreal peatlands: chemical composition, markers, and microstructure. *Aerosol Air Quality Research*, 19, 484-503

Price, D.T., Alfaro, R., Brown, K., Fleming, R., Hogg, E., Girardin, M., Lakusta, T., Johnston, M., McKenney, D., Pedlar, J., Stratton, T., Sturrock, R., Thompson, I., Trofymow, J., Venier, L. (2013). Anticipating the consequences of climate change for Canada's boreal forest ecosystems. *Environmental Reviews*, 21, 322–365

Prior, J., Hathway, B., Glombick, M., Pana, I., Banks, J., Hay, C., Schneider, L., Grobe, M., Elgr, R., Weiss, A. (2013). Bedrock geology of Alberta. AER/AGS Map 600. Alberta Energy Regulator.

Pucher, M., Wünsch, U., Weigelhofer, G., Murphy, K., Hein, T., Graeber, D. (2019). staRdom: Versatile Software for Analyzing Spectroscopic Data of Dissolved Organic Matter in R, Water, 11, 2366

Pucher, M., Flödl, P., Graeber, D., Felsenstein, K., Hein, T., Weigelhofer, G. (2021). Complex interactions of in-stream dissolved organic matter and nutrient spiralling unravelled by Bayesian regression analysis. *Biogeosciences* 18(10), 3103-3122.

Qiu, X., Cheng, I., Yang, F., Horb, E., Zhang, L., Harner, T. (2018). Emissions databases for polycyclic aromatic compounds in the Canadian Athabasca oil sands region – development using current knowledge and evaluation with passive sampling and air dispersion modelling data. *Atmospheric Chemistry and Physics*, 18, 3457–3467

Ramanathan, V., Li. F., Ramana. M. V., Praveen. P. S., Kim. D., Corrigan. C. E., Nguyen. H., Stone. E. A., Schauer. J. J., Carmichael. G. R., Adhikary. B., Yoon. S. C. (2007). Atmospheric brown clouds: Hemispherical and regional variations in long-range

transport, absorption, and radiative forcing. *Journal of Geophysical Research*, 112, D22S21

Rautio, M., Dufresne, F., Laurion, I., Bonilla, S., Vincent, W. F., Christoffersen, K. (2011). Shallow freshwater ecosystems of the circumpolar Arctic. *Ecoscience*, 18, 204–222

Reid, J. S., Koppmann, R., Eck, T. F., Eleuterio, D. P. (2005). A review of biomass burning emissions Part II: intensive physical properties of biomass burning particles. *Atmospheric Chemistry and Physics*, 5, 799–825

Reid, C. E., Brauer, M., Johnston, F. H., Jerrett, M., Balmes, J. R., Elliott, C. T. (2016). Critical review of health impacts of wildfire smoke exposure. Environ. Health Perspect., 124,9

Retelletti Brogi, S., Kim, J., Ryu, J., Jin, Y., Lee, Y., Hur, J. (2019). Exploring sediment porewater dissolved organic matter (DOM) in a mud volcano: Clues of a thermogenic DOM source from fluorescence spectroscopy. *Marine Chemistry*, 211, 15-24.

Retelletti Brogi, S., Cossarini, G., Bachi, G., Balestra, C., Camatti, E., Casotti, R., Checcucci, G., Colella, S., Evangelista, V., Falcini, F., Francocci, F., Giorgino, T., Margiotta, F., Ribera d'Alcalà, M., Sprovieri, M., Vestri, S., Santinelli, C. (2022). Evidence of Covid-19 lockdown effects on riverine dissolved organic matter dynamics provides a proof-of-concept for needed regulations of anthropogenic emissions. *Science Of the Total Environment*, 812, 152412.

Rizzo, L. V., Artaxo, P., Müller, T., Wiedensohler, A., Paixão, M., Cirino, G. G., Arana, A., Swietlicki, E., Roldin, P., Fors, E.O., Wiedemann, K.T. (2013). Long term measurements of aerosol optical properties at a primary forest site in Amazonia. *Atmospheric Chemistry and Physics*, 13(5), 2391-2413

Rochelle-Newall., E. J., Fisher, T.R. (2002). Chromophoric dissolved organic matter and dissolved organic carbon in Chesapeak Bay. *Marine Chemistry* 77 (1). 23-41.

Rutherford, J. W., Dawson-Elli, N., Manicone, A. M., Korshin, G. V., Novosselov, I. V., Seto, E., Posner, J. D. (2020). Excitation emission matrix fluorescence spectroscopy for combustion generated particulate matter source identification. *Atmospheric Environment*, 220,117065, ISSN 1352-2310,

Saarnio, K., Aurela, M., Timonen, H., Saarikoski, S., Teinilä, K., Mäkelä, T., Sofiev, M., Koskinen, J., Aalto, P., Kulmala, M., Kukkonen, J., Hillamo, R. (2010). Chemical composition of fine particles in fresh smoke plumes from boreal wild-land fires in Europe. *Science of the Total Environment*, 408. 2527-42

Salat, A. P. L., Eickmeyer, D. C., Kimpe, L. E., Hall, R. I., Wolfe, B. B., Mundy, L. J, Trudeau, V. L., Blais, J. M. (2021). Integrated analysis of petroleum biomarkers and polycyclic aromatic compounds in lake sediment cores from an oil sands region. *Environmental Pollution*, 270, 116060.

Santana-Casiano, J., González-Santana, D., Devresse, Q., Hepach, H., Santana-González, C., Quack, B., Engel, A., González-Dávila, M. (2022). Exploring the Effects of Organic Matter Characteristics on Fe(II) Oxidation Kinetics in Coastal Seawater. *Environmental Science and Technology*, 56(4), 2718-2728.

Saturno, J., Holanda, B., Pöhlker, C., Ditas, F., Wang, Q., Moran Z. D., F. de Brito, J., Carbone, S., Cheng, Y., Chi, X., Ditas (née Katzwinkel), J., Hoffmann, T., Hrabe de Angelis, I., Könemann, T., Lavrič, J., Ma, N., Ming, J., Paulsen, H., Pöhlker, M., Andreae, M. (2018). Black and brown carbon over central Amazonia: Long-term

aerosol measurements at the ATTO site. *Atmospheric Chemistry and Physics*, 18, 17, 12817-1284

Schulman, S. G., Di, Q. Q., Juchum, J. (2017). Fluorescence Spectroscopy, Organic Chemistry Applications, Editor(s): John C. Lindon, George E. Tranter, David W. Koppenaal, Encyclopedia of Spectroscopy and Spectrometry (Third Edition), Academic Press, 641-646, ISBN 9780128032244

Schulten, H.R., Leinweber, P. (2000). New insights into organic-mineral particles: Composition, properties and models of molecular structure. *Biol. Fertil. Soils* 30(5–6), 399–432.

Schindler, D., Bayley, S., Curtis, P., Parker, B., Stainton, M., Kelly, C. (1992). Natural and man-caused factors affecting the abundance and cycling of dissolved organic substances in precambrian shield lakes. *Hydrobiologia*, 229(1), 1-21.

Schindler, D. (1998). A dim future for boreal waters and landscapes: Cumulative effects of climatic warming, stratospheric ozone depletion, acid precipitation, and other human activities. *Bioscience*, 48(3), 157-164.

Seinfeld, J. H., Pandis, S. N. (2016). Atmospheric Chemistry and Physics: From Air Pollution to Climate Change, *John Wiley & Sons*, ISBN 978-1-118-94740-1,

Sgroi, M., Roccaro, P., Korshin, G. V., Vagliasindi, F. G. A. (2017). Monitoring the behaviour of emerging contaminants in wastewater-impacted rivers based on the use of fluorescence excitation matrixes (EEM). *Environmental Science & Technology* 51 (8), 4306-4316

Shang, Y., Song, K., Jacinthe, P-A., Wen, Z., Zhao, Y., Lyu, L., Fang, C., Li, S., Liu, G., Hou, J., Zhang, N. (2021). Fluorescence spectroscopy of CDOM in urbanized waters across gradients of development/industrialization of China. *Journal of Hazardous Materials*, 415, 125630.

Shemer H, Linden K.G. (2007). Aqueous photodegradation and toxicity of the polycyclic aromatic hydrocarbons fluorene, dibenzofuran, and dibenzothiophene. Water Research. 2007 Feb;41(4):853-61.

Shen, J., Song, Y., Cheng, C., Duan, F., Liu, C., Chai, Y., Wang, S., Xiong, Q., Wu, J. (2023). Spectroscopic and compositional profiles of dissolved organic matters in urban snow from 2019 to 2021: Focusing on pollution features identification. *Water Research*, 229, 119408, ISSN 0043-1354

Shutova, Y., Baker, A., Bridgeman, J., Henderson, R. (2014). Spectroscopic characterisation of dissolved organic matter changes in drinking water treatment: From PARAFAC analysis to online monitoring wavelengths. *Water Research*, 54, 159-169.

Simoneit, B. R. T., Rogge, W. F., Lang, Q., Jaffé. R., (2000). Molecular characterization of smoke from campfire burning of pine wood (Pinus elliottii). *Chemosphere - Global Change Science*, 2(1), 107-122.

Siudek, P., Frankowski, M., Siepak, J. (2015). Seasonal variations of dissolved organic carbon in precipitation over urban and forest sites in central Poland. *Environmental Science and Pollution Research*, 22 (14), 11087-11096.

Small, C. C., Cho, S., Hashisho, Z., Ulrich, A. C. (2015). Emissions from oil sands tailings ponds: Review of tailings pond parameters and emission estimates, *Journal of Petroleum Science and Engineering*, 127, 490–501

Snucins, E., Gunn, J. (2000). Interannual variation in the thermal structure of clear and colored lakes. Limnology and Oceanography, 45 (7), 1639-1646.

Snyder, K., Mladenov, N., Richardot, W., Dodder, N., Nour, A., Campbell, C., Hoh, E. (2021). Persistence and photochemical transformation of water-soluble constituents from industrial crude oil and natural seep oil in seawater. *Marine Pollution Bulletin*, 165, 112049.

Sobek, S., Tranvik, L., Prairie, Y., Kortelainen, P., Cole, J. (2007). Patterns and Regulation of Dissolved Organic Carbon: An Analysis of 7,500 Widely Distributed Lakes. *Limnology and Oceanography*. 52. 1208-1219.

Soil landscapes of Canada working group. (2005). Soil landscapes of Canada. Version 3.0. Agriculture and agri-food Canada, digital map and database at 1:1 million scale.

Song, F., Li, T., Shi, Q., Guo, F., Bai, Y., Wu, F., Xing, B. (2021). Novel insights into the molecular-level mechanism linking the chemical diversity and copper binding heterogeneity of biochar-derived dissolved black carbon and dissolved organic matter. Environmental Science and Technology, 55 (17), 11624– 11636,

Soto Cárdenas, C., Gerea, M., Garcia, P., Pérez, G., Diéguez, M., Rapacioli, R., Reissig, M., Queimaliños, C. (2017). Interplay between climate and hydrogeomorphic features and their effect on the seasonal variation of dissolved organic matter in shallow temperate lakes of the Southern Andes (Patagonia, Argentina): a field study based on optical properties. *Ecohydrology*, 10(7).

Spranger, T., Pinxteren, D. V., Herrmann, H. (2020). Atmospheric "HULIS" in Different Environments: Polarities, Molecular Sizes, and Sources Suggest More Than 50% Are Not "Humic-like". *ACS Earth Space Chemistry*, 4,2, 272-282

Srinivas, B., Sarin. M. M. (2013). Light-absorbing organic aerosols (brown carbon) over the tropical Indian Ocean: impact of biomass burning emissions, *Environmental Research Letters*, 8

St. Louis, V. L., Rudd, J. W. M., Kelly, C. A., Beaty, K. G., Bloom, N. S., Flett, R. J. (1994). Importance of wetlands as sources of methyl mercury to boreal forest ecosystems. *Canadian Journal of Fisheries and Aquatic Science.* 543, 51, 1065-1076.

Stedmon, C. A., Markager, S., Bro, R. (2003). Tracing Dissolved Organic Matter in Aquatic Environments Using a New Approach to Fluorescence Spectroscopy. *Marine Chemistry*, 82, 239-254

Stedmon, C.A., Nelson, N.B. (2015). The optical properties of DOM in the ocean. In Biogeochemistry of Marine Dissolved Organic Matter, 2nd ed.; Hansell, D., Carlson, C., Eds.; Academic Press: San Diego, CA, USA; 481–508

Stein, A.F., Draxler, R.R, Rolph, G.D., Stunder, B.J.B., Cohen, M.D., Ngan, F. (2015). NOAA's HYSPLIT atmospheric transport and dispersion modeling system, *Bulletin American Meteorological Society*, 96, 2059-2077

Stone, E. A., Hedman, C. J., Sheesley, R. J., Shafer, M. M., Schauer, J. J. (2009). Investigating the chemical nature of humic-like substances (HULIS) in North American atmospheric aerosols by liquid chromatography tandem mass spectrometry. *Atmospheric Environment* 43, 4205.

Strack, M., Hayne, S., Lovitt, J., Mcdermid, G., Rahman, M, M., Belwase, S., Xu, B. (2019). Petroleum exploration increases methane emissions from northern peatlands. *Nature Communications*, 10. 2804.

Subhayan Guha Thakurta, S., Maiti, A., Pernitsky, D. J., Bhattacharjee, S. (2013). Dissolved organic matter in steam assisted gravity drainage boil blow down water. *Energy & Fuels* 27 (7), 3883-3890

Sui, X., Wu, Z., Lin, C., Zhou, S. (2017). Terrestrially derived glomalin-related soil protein quality as a potential ecological indicator in a peri-urban watershed. *Environmental Monitoring and Assessment*, *189*(7).

Sun, C., Shotyk, W., Cuss, C. W., Donner, M. W., Fennell, J., Javed, M., Noernberg, T., Poesch, M., Pelletier, R., Sinnatamby, N., Siddique, T., Marti. J. J. (2017). *Environmental Science & Technology*, 51 (17), 9524-9532

Sweetman, J. N., K. M. Ruhland., J. P. Smol. (2010). Environmental and spatial factors influencing the distribution of cladocerans in lakes across the central Canadian Arctic treeline region, *Journal of Limnology***,** 69, 76–87.

Tang, J., Wang, J., Zhong, G., Jiang, H., Mo, Y., Zhang, B., Geng, X., Chen, Y., Tang, J., Tian, C., Bualert, S., Li, J., Zhang, G. (2021). Measurement report: Long-emission-wavelength chromophores dominate the light absorption of brown carbon in aerosols over Bangkok: impact from biomass burning, *Atmospheric Chemistry and Physics*, 21, 11337–11352

Tarnocai, C. (2006). The effect of climate change on carbon in Canadian peatlands. Global Planet Change, 53, 222–232

Thurman, E. M. (1985). Organic Geochemistry of Natural Waters; Martinus Nijhoff/Junk: Netherlands.

Toming, K., Kotta, J., Uuemaa, E., Sobek, S., Kutser, T., Tranvik, L. (2020). Predicting lake dissolved organic carbon at a global scale. *Scientific Reports*, 10, 8471.

Tomsche, L., Piel, F., Mikoviny, T., Nielsen, C. J., Guo, H., Campuzano-Jost, P., Nault, B. A., Schueneman, M. K., Jimenez, J. L., Halliday, H., Diskin, G., DiGangi, J. P., Nowak, J. B., Wiggins, E. B., Gargulinski, E., Soja, A. J., and Wisthaler, A. (2023). Measurement report: Emission factors of NH3 and NHx for wildfires and agricultural fires in the United States, *Atmospheric Chemistry and Physics*, 23, 2331–2343

Tranvik, L.J. (1998). Degradation of Dissolved Organic Matter in Humic Waters by Bacteria. In: Hessen, D.O., Tranvik, L.J. (eds) Aquatic Humic Substances. *Ecological Studies*, 133. Springer, Berlin, Heidelberg.

Trubetskoj, O. A, Richard, C., Voyard, G., Marchenkov V.V., Trubetskaya, O. E. (2018). Molecular size distribution of fluorophores in aquatic natural organic matter: application of HPSEC with multi-wavelength absorption and fluorescence detection following LPSEC-PAGE fractionation. *Environmental Science and Technology*, 52,9, 5287–5295

United States Environmental Protection Agency (EPA). (1989). Method 1625C: Semivolatile Organic Compounds by Isotope Dilution GCMS.

United States Environmental Protection Agency (EPA). (1994). Method 200.8. Determination of Trace Elements in Waters and Wastes by Inductively Coupled Plasma-Mass Spectrometry; U.S. EPA.

United States Environmental Protection Agency (EPA). (1996). Method 1669. Sampling Ambient Water for Trace Metals at EPA Water Quality Criteria Levels; US Environmental Protection Agency, Office of Water: Washington, DC, 39.

United States Environmental Protection Agency (EPA). (2014). Method 8270E (SW-846): Semivolatile Organic Compounds by Gas Chromatography/ Mass Spectrometry (GC/MS).

Usha, K. H., Nair, V. S., Babu, S. S. (2022). Effects of Aerosol–Induced Snow Albedo Feedback on the Seasonal Snowmelt Over the Himalayan Region. Water Resources Research, 58(2), e2021WR030140

Valeur, B. (2002). Molecular fluorescence. Principles and applications. Wiley-VCH, Weinheim

Valeur, B., Berberan-Santos, M. N. (2013). Molecular fluorescence. Principles and applications. Wiley-VCH

Veranth, J. M., Pardyjak, E. R., Seshardi. (2003). Vehicle-generated fugitive dust transport: analytic models and field study, *Atmospheric Environment*, 37, 16, 2295-2303

Veselovskii, I., Hu, Q., Goloub, P., Podvin, T., Korenskiy, M., Pujol, O., Dubovik, O., Lopatin, A. (2020). Combined use of Mie–Raman and fluorescence lidar observations for improving aerosol characterization: feasibility experiment, *Atmospheric Measurement Technology*., 13, 6691–6701

Vione, D., Colombo, N., Said-Pullicino, D., Bocchiola, D., Confortola, G., Salerno, F., Viviano, G., Fratianni, S., Martin, M., Godone, D., Freppaz. M. (2021). Seasonal variations in the optical characteristics of dissolved organic matter in glacial pond water. *Science of The Total Environment*, 759, 143464, ISSN 0048-9697,

von Wachenfeldt E, Sobek S, Bastviken D, Tranvik LJ. (2008). Linking allochthonous dissolved organic matter and boreal lake sediment carbon sequestration: the role of light-mediated flocculation. *Limnology and Oceanography*, 53, 2416–26.

Wagner, S., Brantley, S., Stuber, S., Van Stan, J., Whitetree, A., Stubbins, A. (2019). Dissolved black carbon in throughfall and stemflow in a fire-managed longleaf pine woodland. *Biogeochemistry*, 146(2), 191-207.

Wakeham, S.G., Schaffner, C., Giger, W. (1980). Polycyclic Aromatic Hydrocarbons in Recent Lake Sediments. II. Compounds Derived from Biogenic Precursors During Early Diagenesis. *Geochimica et Cosmochimica Acta* 44, 415–429.

Walker, S. A., Amon, R. M. W., Stedmon, C. A. (2013), Variations in high-latitude riverine fluorescent dissolved organic matter: A comparison of large Arctic rivers. *Journal of Geophysical Research: Biogeosciences*, 118, 1689–1702,

Wang, Y., Zhang, X., Draxler, R. (2009). TrajStat: GIS-based software that uses various trajectory statistical analysis methods to identify potential sources from long-term air pollution measurement data. *Environmental Modelling and Software,* 24 (8), 938-939.

Wang, X., Chow, J. C., Kohl, D. D., Percy, K. E., Legge, A. H., Watson, J. G. (2015). Characterization of PM2.5 and PM10 fugitive dust source profiles in the Athabasca Oil Sands Region, *Journal of Air Waste Management Association*, 65, 12, 1421-1433

Wang, X., Chow, J. C., Kohl, S. D., Percy, K. E., Legge, A. H., Watson, J. G. (2016). Real-world emission factors for Caterpillar 797B heavy haulers during mining operations. *Particuology*, 28, 22–30

Washenfelder, R.A., Attwood, A.R., Brock, C.A., Guo, H., Xu, L., Weber, R.J., Ng, N.L., Allen, H.M., Ayres, B.R., Baumann, K., Cohen, R.C. (2015). Biomass burning

dominates brown carbon absorption in the rural southeastern United States. *Geophysical Research Letters*, 42(2), 653-664.

Watmough, S., Whitfield, C., Fenn, M. (2014). The importance of atmospheric base cation deposition for preventing soil acidification in the Athabasca Oil Sands Region of Canada. *Science of The Total Environment*, 493, 1-11.

Wauthy, M., Rautio, M., Christoffersen, K.S., Forsström, L., Laurion, I., Mariash, H.L., Peura, S., Vincent, W.F. (2018). Increasing dominance of terrigenous organic matter in circumpolar freshwaters due to permafrost thaw. *Limnology and Oceanography Letters*, 3: 186-198.

Weishaar, J. L., Aiken, G. R., Bergamaschi, B. A., Fram, M. S., Fujii, R., Mopper, K. (2003). Evaluation of specific ultra-violet absorbance as an indicator of the chemical composition and reactivity of dissolved organic carbon. *Environmental Science and Technology* 37, 4702–4708.

Wen, H., Zhou, Y., Xu, X., Wang, T., Chen, Q., Chen, Q., Li, W., Wang, Z., Huang, Z., Zhou, T., Shi, J., Bi, J., Ji, M., Wang. X. (2021). Water-soluble brown carbon in atmospheric aerosols along the transport pathway of Asian dust: Optical properties, chemical compositions, and potential sources. *Science of the Total Environment*, 789,147971

Wentworth, G. R., Aklilu, Y. A., Landis, M. S., Hsu, Y. M. (2018). Impacts of a large boreal wildfire on ground level atmospheric concentrations of PAHs, VOCs and ozone, *Atmospheric Environment*, 178, 19-30

Weyhenmeyer, G., Prairie, Y., Tranvik, L. (2014). Browning of Boreal Freshwaters Coupled to Carbon-Iron Interactions along the Aquatic Continuum. *Plos ONE*, 9 (2), e88104.

Whisenhant, E. A., Zito, P., Podgorski, D. C., McKenna, A. M., Redman, Z. C., Tomco P. L. (2022). Unique Molecular Features of Water-Soluble Photo-Oxidation Products among Refined Fuels, Crude Oil, and Herded Burnt Residue under High Latitude Conditions, *ACS Environmental Science and Technology: Water*, 2, 6, 994-1002

Whittington P.N., Price J.S. (2012). Impact of mine dewatering on peatlands of the James Bay lowlands: the role of bioherms. *Hydrolological Processes*, 26: 1818–1826.

Wilson, H. F., Xenopoulos, M. A. (2009). Effects of agri-cultural land use on the composition of fluvial dissolved organic matter. *Nature Geoscience* 2, 37–41

Wold, S., Sjöström, M., Eriksson, L. (2001). PLS-regression: a basic tool of chemometrics. *Chemometrics and Intelligent Laboratory Systems*, 58(2), 109-130.

Wolfbeis, O.S. (1985). The fluorescence of organic natural products. In: Schulman SG (ed) Molecular Luminescence Spectroscopy: Methods and Applications, Part I, Chapter 3, pp 167-370. New York: Wiley.

Wu, G., Ram, K., Fu, P., Wang, W., Zhang, Y., Liu, X., Stone, E. A., Pradhan, B. B., Dangol, P. M., Panday, A. K., Wan, X., Bai, Z., Kang, S., Zhang, Q., Cong, Z. (2019). Water-Soluble Brown Carbon in Atmospheric Aerosols from Godavari (Nepal), a Regional Representative of South Asia. *Environmental Science and Technology*, 53, 7, 3471-3479

Wu, G., Fu, P., Ram, K., Song, J., Chen, Q., Kawamura, K., Wan, X., Kang, S., Wang, X., Laskin, A., Cong, Z. (2021). Fluorescence characteristics of water-soluble organic carbon in atmospheric aerosol. *Environmental Pollution*, 268, Part A, 115906

Wünsch, U., Murphy, K., Stedmon, C. (2015). Fluorescence Quantum Yields of Natural Organic Matter and Organic Compounds: Implications for the Fluorescence-based Interpretation of Organic Matter Composition. *Frontiers in Marine Science,* 2.

Xiao, Y., Sara-Aho, T., Hartikainen, H., Vähätalo, A. (2013). Contribution of ferric iron to light absorption by chromophoric dissolved organic matter. *Limnology and Oceanography*, 58 (2), 653-662.

Xiaowei Fu, X., Haiyan Du, H., Huacheng Xu, H. (2021). Comparison in UV-induced photodegradation properties of dissolved organic matters with different origins. Chemosphere, 280, 130633

Xie, M. J., Mladenov, N., Williams, M. W., Neff, J. C., Wasswa, J., Hannigan, M. P. (2016). Water soluble organic aerosols in the Colorado Rocky Mountains, USA: composition, sources and optical properties, Sci. Rep.-UK, 6, 39336,

Xing, Z., Xiong, Y., Du, K. (2020). Source apportionment of airborne particulate matters over the Athabasca oil sands region: Inter-comparison between PMF modeling and ground-based remote sensing. *Atmospheric Environment*, 221, 117103,

Yamaguchi. Y., Matsubara. Y., Ochi. T., Zen-ichi. Y. (2008). How the π Conjugation Length Affects the Fluorescence Emission Efficiency. *Journal of the American Chemical Society*, 130(42), 13867-13869

Yamashita, Y., Kloeppel, B., Knoepp, J., Zausen, G., Jaffé, R. (2011). Effects of Watershed History on Dissolved Organic Matter Characteristics in Headwater Streams. *Ecosystems*, 14(7), 1110-1122.

Yan, F., Kang, S., Li, C., Zhang, Y., Qin, X., Li, Y., Zhang, Y., Qin, X., Li, Y., Zhang, X., Hu, Z., Chen, P., Li, X., Qu, B., Sillanpää, M. (2016). Concentration, sources and light absorption characteristics of dissolved organic carbon on a medium-sized valley glacier, northern Tibetan Plateau. *Cryosphere* 10, 2611–2621.

Yan. C., Zheng. M., Bosch. C., Andersson. A., Desyaterik. Y., Sullivan. A. P., Collett. J. L., Zhao. B., Wang. S., He. K., Gustafsson. Ö. (2017). Important fossil source contribution to brown carbon in Beijing during winter. *Scientific Reports*, 7, 43182

Yan, C., Zheng, M., Desyaterik, Y., Sullivan, A. P., Wu, Y., Collett, J. L. (2020). Molecular characterization of water-soluble brown carbon chromophores in Beijing, China. *Journal of Geophysical Research: Atmosphere*, 125, e2019JD032018

Yates, C. A., Johnes, P. J., Owen, A. T., Brailsford, F. L., Glanville, H. C., Evans, C. D., Marshall, M. R., Jones, D. L., Lloyd, C. E., Jickells, T., Evershed, R. P. (2019). Variation in Dissolved Organic Matter (DOM) stoichiometry in UK freshwaters: assessing the influence of land cover and soil C: N ratio on DOM composition. Limnology and Oceanography 64:2328–2340

Yang, Z., Hollebone, B.P., Brown, C.E., Yang, C., Wang, Z., Zhang, G., Lambert, P., Landriault, M., Shah, K. (2016). The photolytic behavior of diluted bitumen in simulated seawater by exposed to the natural sunlight. *Fuel*, 186, 128–139

Yassine, M. M., and Dabek-Zlotorzynska. E. (2017). Application of ultrahigh-performance liquid chromatography–quadrupole time-of-flight mass spectrometry for the characterization of organic aerosol: Searching for naphthenic acids. *Journal of Chromatography A*, 1512, 22-33

Yue, S., Bikkina, S., Gao, M., Barrie, L. A., Kawamura, K., Fu, P. (2019). Sources and radiative absorption of water-soluble brown carbon in the high Arctic atmosphere. *Geophysical Research Letters*, 46, 14881–14891.

Yunker, M.B., Macdonald, R.W., Vingarzan, R., Mitchell, R.H., Goyette, D., Sylvestre, S. (2002). PAHs in the Fraser River basin: a critical appraisal of PAH ratios as indicators of PAH source and composition. *Organic Geochem*istry, 33, 489–515.

Zafiriou, O.C., Gagosian, R.B., Peltzer, E.T. (1985). Air-to-sea fluxes of lipids at Enewetak Atoll. *Journal of Geophysical Research: Atmosphere*. 90(ND1), 2409–2423

Zhang, Y. L., Yin, Y., Feng, L. Q., Zhu, G. W., Shi, Z. Q., Liu, X. H., Zhang, Y. (2011). Characterizing chromophoric dissolved organic matter in Lake Tianmuhu and its catchment basin using excitation-emission matrix fluorescence and parallel factor analysis. *Water Resources* 45(16), 5110–5122.

Zhang, X. L, Lin, Y. H., Surratt, J. D., Weber, R. J. (2013). Sources, Composition and absorption Angstrom exponent of light-absorbing organic components in aerosol extracts from the Los Angeles Basin. *Environmental Science & Technology* 47:3685–3693

Zhang. Y., Gao. G., Shi. K., Niu. C., Zhou. Y., Qin. B., Liu. X. (2014). Absorption and fluorescence characteristics of rainwater CDOM and contribution to Lake Taihu, China. *Atmospheric Environment*, 98, 483-491

Zhang, Y., Shotyk, W., Zaccone, C., Noernberg, T., Pelletier, R., Bicalho, B., Froese, D. G., Davies, L., Martin J. W. (2016). Airborne Petcoke Dust is a Major Source of Polycyclic Aromatic Hydrocarbons in the Athabasca Oil Sands Region. *Environmental Science and Technology*, 50, 4, 1711-1720

Zhang, Y., Kang, S., Gao, T., Schmale, J., Liu, Y., Zhang, W., Guo, J., Du, W., Hu, Z., Cui, X., and Sillanpaa, M. (2019). Dissolved organic carbon in snow cover of the Chinese Altai Mountains, Central Asia: Concentrations, sources and light absorption properties, *Science of the Total Environment*, 647, 1385–1397.

Zhang, Y., Kang, S., Gao, T., Sprenger, M., Dou, T., Han, W., Zhang, Q., Sun, S., Du, W., Chen, P., Guo, J., Cui, X., Sillanpää, M. (2020) Dissolved organic carbon in Alaskan Arctic snow: concentrations, light-absorption properties, and bioavailability, *Tellus B: Chemical and Physical Meteorology*, 72:1, 1-19,

Zhou, Y., West, C. P., Hettiyadura, A. P. S., Niu, X., Wen, H., Cui, J., Shi, T., Pu, W., Wang, X., and Laskin, A. (2021). Measurement report: Molecular composition, optical properties, and radiative effects of water-soluble organic carbon in snowpack samples from northern Xinjiang, China, *Atmospheric Chemistry and Physics*, 21, 8531–8555

Zhou Y, West CP, Hettiyadura APS, Pu W, Shi T, Niu X, Wen H, Cui J, Wang X, Laskin A. (2022). Molecular Characterization of Water-Soluble Brown Carbon Chromophores in Snowpack from Northern Xinjiang, China. *Environmental Science and Technology*, 56(7), 4173-4186.

Zhu, C. S., Cao, J. J., Huang, R. J., Shen, Z. X.,Wang, Q. Y., Zhang, N. N. (2018). Light absorption properties of brown carbon over the southeastern Tibetan Plateau. *Science of the Total Environment*, 625, 246-251

Zito, P., Podgorski, D., Johnson, J., Chen, H., Rodgers, R.., Guillemette, F., Kellerman, A., Spencer, R., Tarr, M. (2019). Molecular-Level Composition and Acute Toxicity of Photosolubilized Petrogenic Carbon. *Environmental Science and Technology*, 53(14), 8235-8243

Appendix A

Chapter 2: Dissolved Organic Carbon in lakes of the Athabasca Oil Sands Region: Are coloured lakes more sensitive to atmospheric deposition?

Appendix A: Figures

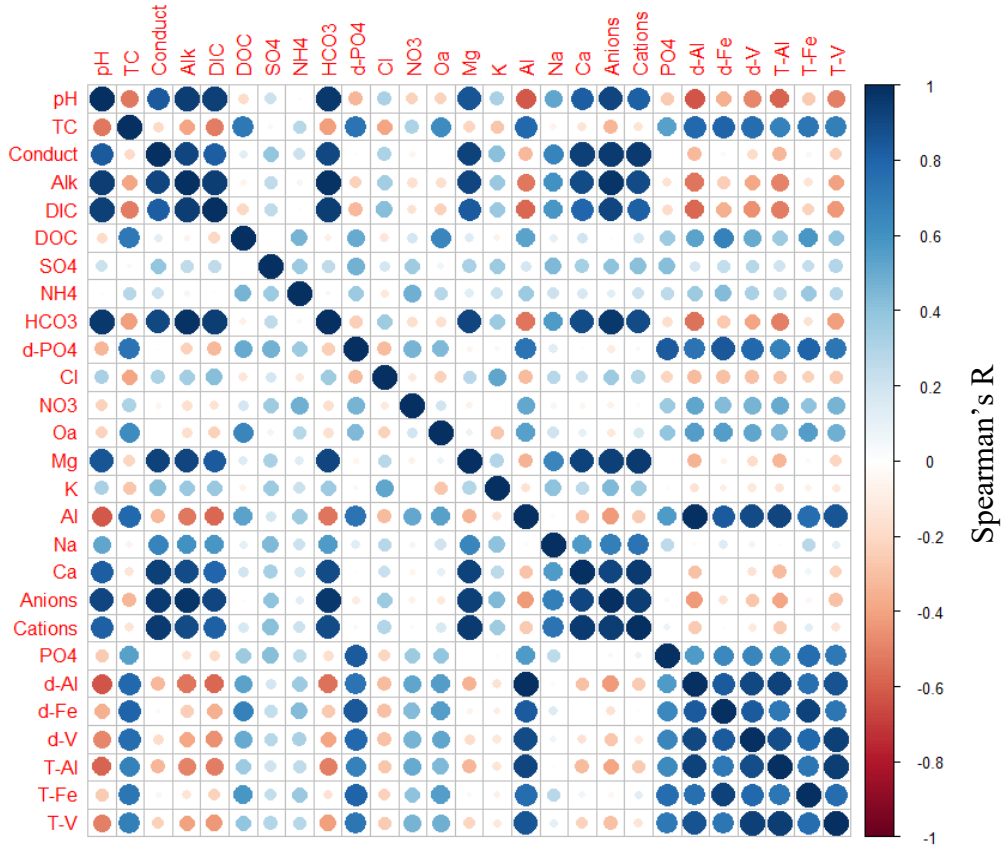

Figure A1. Spearman correlation matrix comparing water-quality parameters among H ASL sites, correlation coefficient strength is represented by cell colour intensity (red = negative; blue = positive) and diameter.

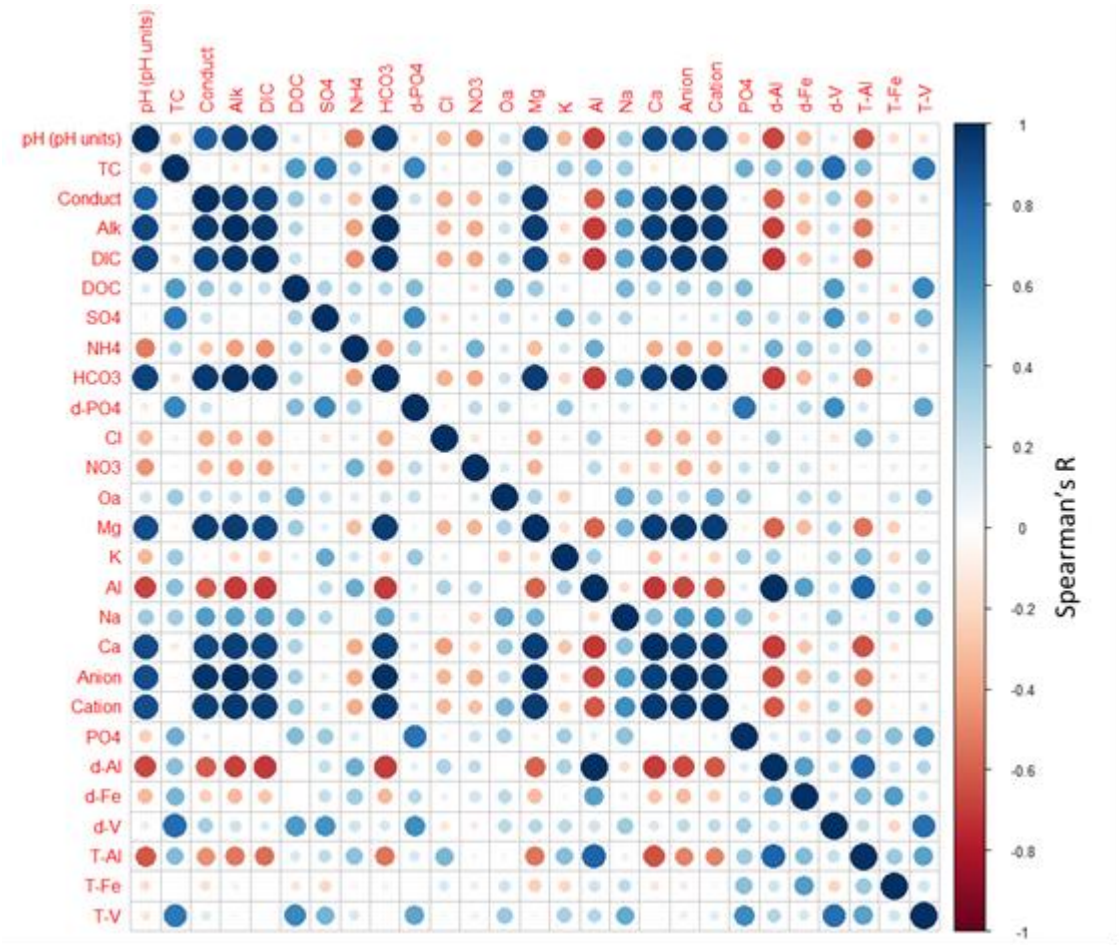

Figure A2. Spearman correlation matrix comparing water-quality parameters among L ASL sites, correlation coefficient strength is represented by cell colour intensity (red = negative; blue = positive) and diameter.

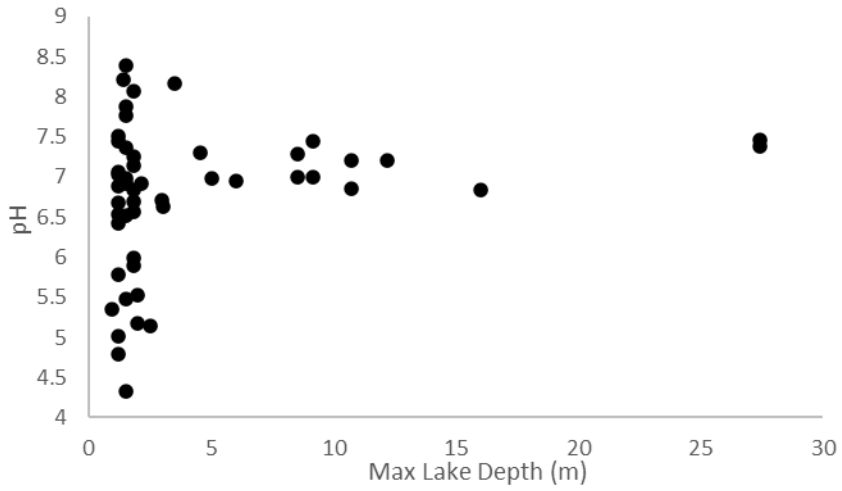

Figure A3. Comparison of maximum lake depth (m) and surface-water pH among ASL sites.

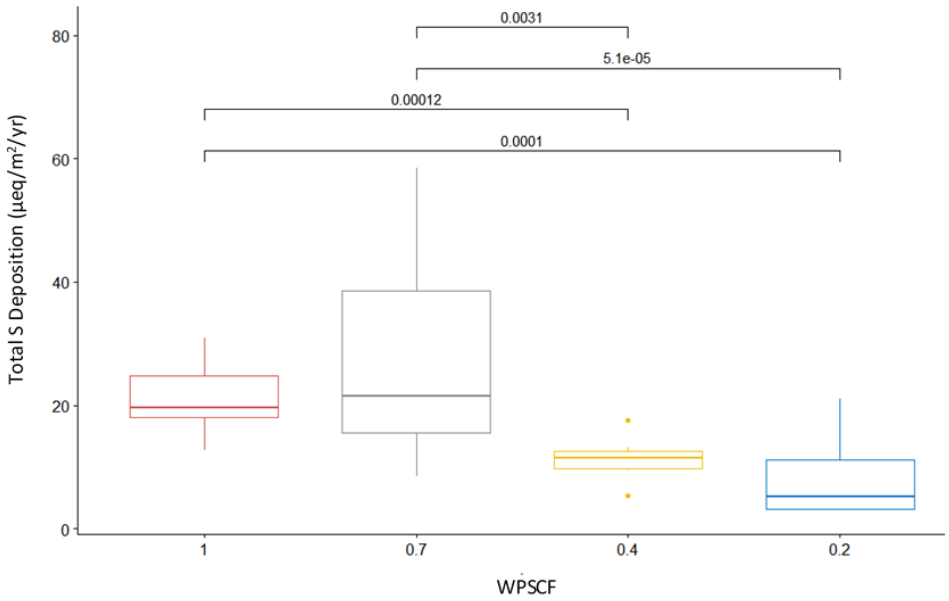

Figure A4. Boxplot comparing the distribution of GEM-MACH modelled total S deposition (µeq/m^{-2}/yr) in relation to lake WPSCF categories (1.0, 0.7, 0.4, and 0.2) among ASL sites. Mann-Whitney U test p-values are presented for significantly different samples.

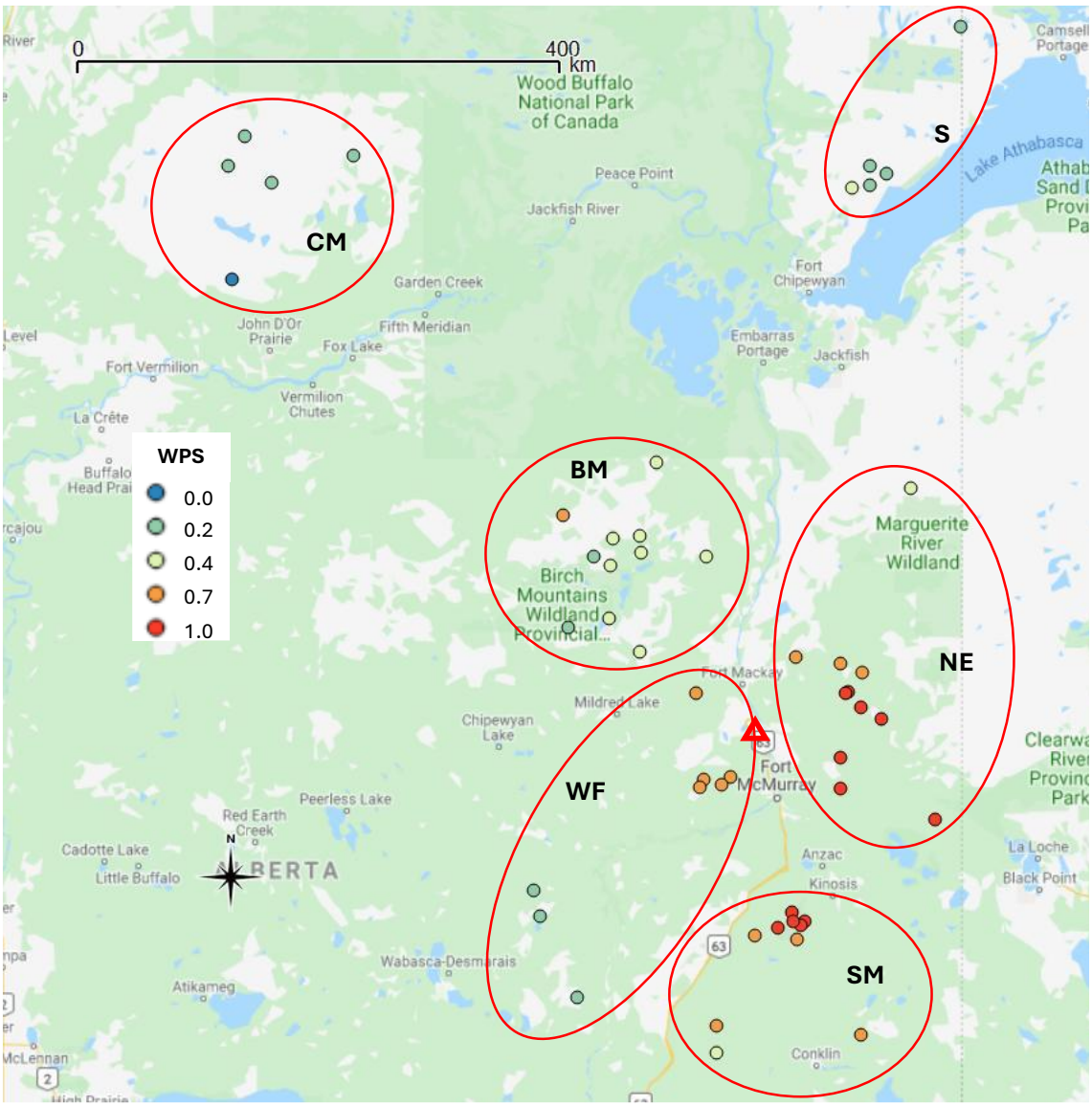

Figure A5. Distribution of WPSCF values among ASL sites, as indicated by colour; lake subregions are highlighted within each red-encircled area. The red-outlined triangle indicates the location of AR6 (source: Google Maps).

Appendix A: Tables

Table A1. Spearman correlation analysis comparing lake pH and select ion ratios; correlation coefficient and significance are presented.

RATIO	SO_4^{2-}	Cl^-	PO_4^{3-}	NO_3^-	O_a	Na^{2+}	Ca^{2+}	Mg^{2+}	K^+	Al^{3+}	HCO_3^-
R	-0.54	-0.42	-0.79	-0.71	-0.86	-0.47	-0.28	-0.28	-0.42	-0.88	0.76
RHO ≠ 0	Yes	Yes	Yes	Yes	Yes	Yes	Yes	Yes	Yes	Yes	Yes

Table A2. Summary of Mann-Kendal monotonic trend analysis (1999 – 2017) for individual according to PCSF category (0.0 – 1.0, 0.0 – 0.4, and 0.7 – 1.0), which are further separated into H and L subpopulations. The relative fraction (%) of lakes which displayed significant positive (no parenthesis) or negative (in parentheses) Z test statistic values are presented for each parameter and category. The number of lakes within each defined category is shown.

WPCSF	**0.0 – 1.0**		**0.0 – 0.4**		**0.7 – 1.0**	
ASL subpopulation	**High**	**Low**	**High**	**Low**	**High**	**Low**
# of lakes	35	15	21	4	14	11
TC (mg/l Pt)	5.6 (2.8)	(7.1)	9.5 (4.8)			(9.1)
DOC (mg/l)	2.8 (11.1)	(28.5)	4.8 (14.3)	(25.0)	(7.1)	(27.3)
DIC (µeq/l)	19.4	14.3 (21.4)	28.6		7.1	18.2 (27.3)
O_a (µeq/l)	2.8 (2.8)		4.8		(7.1)	
O_aR	(27.8)		(28.6)		(28.6)	
SO_4^{2-} (µeq/l)	5.6 (11.1)	14.3 (50.0)	9.5 (9.5)	(25.0)	(14.3)	18.2 (54.5)
PO_4^{3-} (µeq/l)	(19.4)	(78.6)	(18.2)		(21.4)	(90.9)
NO_3^- (µeq/l)	(22.2)		(23.8)		(21.4)	
Cl^- (µeq/l)	(36.1)	7.1 (35.7)	(23.8)	(25.0)	(57.1)	9.1 (36.4)
Ca^{2+} (µeq/l)	16.7 (2.8)	7.1 (7.1)	23.8		7.1 (7.1)	9.1 (9.1)
Na^+ (µeq/l)	11.1	14.3 (21.4)	18.2			18.2 (27.3)
K^+ (µeq/l)	13.9 (2.8)	14.3 (14.3)	18.2		7.1 (7.1)	18.2 (18.2)
Mg^{2+} (µeq/l)	16.7	14.3 (14.3)	23.8		7.1	18.2 (18.2)
Al^{3+} (µeq/l)	2.8	7.1 (7.1)		(25.0)	7.1	9.1
Anion sum (µeq/l)	44.4 (2.8)	21.4 (21.4)	52.4		35.7 (7.1)	27.3 (27.3)
Cation sum (µeq/l)	22.2 (2.8)	14.3 (14.3)	28.6 (4.8)		14.3	18.2 (18.2)
d-Fe (µg/l)	11.1	7.1	9.5		14.3	9.1
Alkalinity (µeq/L)	58.3	14.3 (14.3)	57.1		64.3	18.2 (18.2)
pH (pH units)	69.4	35.7 (7.1)	81.0	50.0	57.1	27.3 (9.1)
Conductivity (µs/cm)	13.9 (8.3)	21.4 (21.4)	18.2 (4.8)		7.1 (14.3)	27.3 (27.3)

Appendix B

Chapter 3: Characterization of chromophoric dissolved organic matter in the Athabasca Oil Sands Region, Canada, and its association to lake acid sensitivity

Appendix B1: Elemental analysis QA/QC

Elemental (total recoverable and dissolved) concentrations measured across 5 field blanks (one per sampling day) were considerably low, as most target analytes fell below their respective instrument reporting detection limits. Comparison of 5 duplicate sample sets revealed generally low relative percent difference (RPD; average = 7.5%, standard deviation = 7.4%) values for the target elements. Routine analysis of certified reference waters (Water-Trace elements TM-27.4; National Research Council, Canada) by InnoTech Alberta found broadly acceptable recoveries for the target analytes. For example, the average elemental recoveries measured from 27 reference water samples (analyzed during the January 2023 to March 2024 period) ranged between 96.1 - 111.6%.

Appendix B: Figures

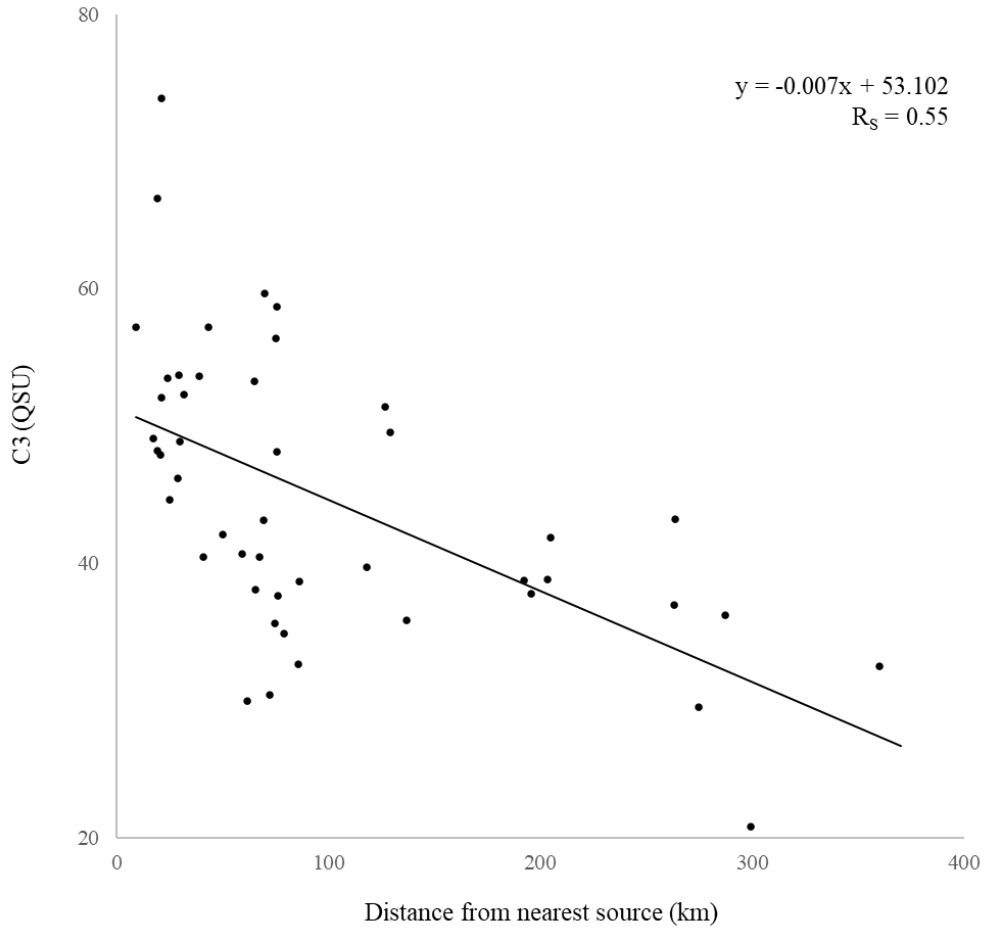

Figure B1. Comparison of lake distance from nearest industrial source (km) and C3 fluorescence intensity (QSU) measured at individual Acid Sensitive Lakes (ASL; 2021 sample data). The line of best fit and corresponding regression equations with Pearson correlation coefficient are displayed.

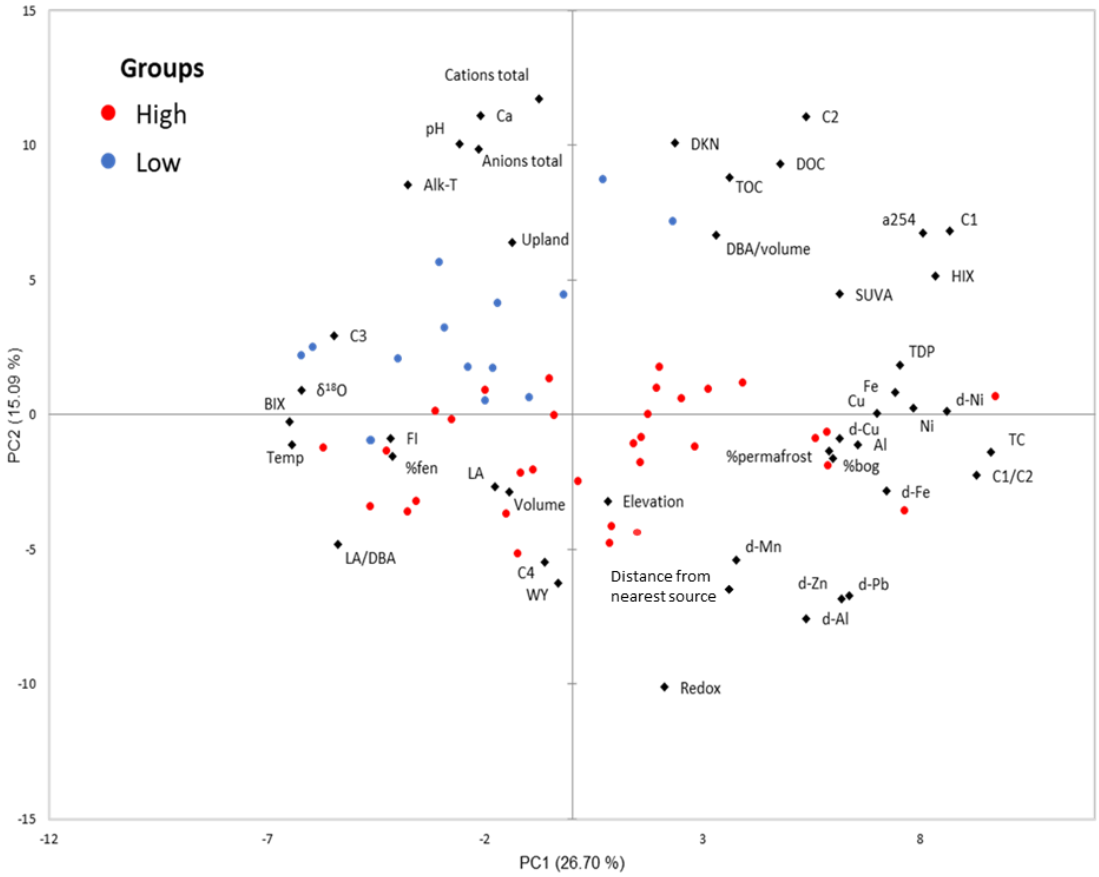

Figure B2. Biplot comparing principal component 1 (PC1) and principal component 2 (PC2) from the resulting principal component analysis (PCA) of the complete Acid Sensitive Lake (ASL) dataset, including all geochemical variables. Variables with the highest loading values are visible to improve legibility (black points). Factor scores have been categorized according to their H (red circles) and L (blue circles) lake subpopulation.

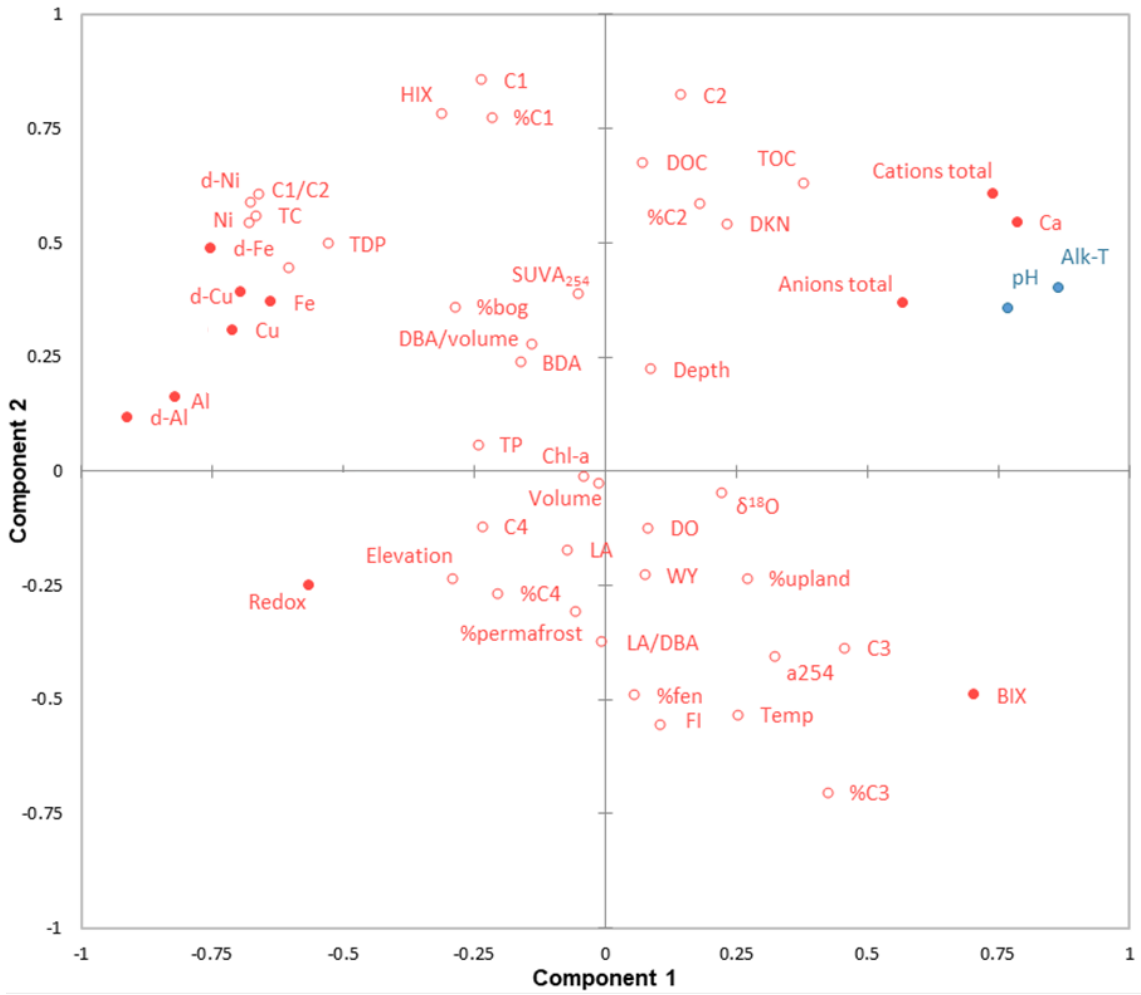

Figure B3. Correlation biplot displaying both X (red) and Y variables (blue) in relation to PLS components one and two. The filled red and outlined red points indicate X variables with high (≥ 1) and low (< 1) VIP scores, respectively.

Appendix B: Tables

Table B1. Summary of key variables included in the study. Variable abbreviations and units are displayed.

Variable	Abbreviation	Units
Temperature	Temp	°C
Redox potential	Redox	mV-1
Dissolved oxygen	DO	mg L^{-1}
pH	pH	pH units
Total alkalinity	Alk-T	mg L^{-1}
Sum of cations	Cation total	mEq l^{-1}
Sum of anions	Anion total	mEq l^{-1}
Ion deficit	Ion def	mEq l^{-1}
Dissolved inorganic carbon	DIC	mg C L^{-1}
Dissolved organic carbon	DOC	mg C L^{-1}
Chlorophyll - a	Chl-a	mg m^{-3}
Ammonia	NH_3	mg L^{-1}
dissolved Kjeldahl nitrogen	DKN	mg N L^{-1}
Total dissolved phosphorus	TDP	mg L^{-1}
Total phosphorus	TP	mg L^{-1}
True colour	TC	mg L^{-1} Pt
Oxygen-18 / oxygen -16 isotope ratio	$\delta^{18}O$	‰
Water yield	WY	mm
Lake inflow ratio	E/I	%
Lake elevation	Elevation	m
Lake surface area	LA	m^2
Lake volume	Volume	m^3
Lake depth	Depth	m
Drainage basin area	DBA	m^2
Lake catchment bog coverage	Bog	%
Lake catchment fen coverage	Fen	%
Lake catchment permafrost coverage	Permafrost	%

Table B2. Summary median water quality variable lake observations. The normalized median absolute deviation (NMAD; %) is displayed for each cohort.

	Lake region					
Metric	BM	SM	NE	WF	CM	S
pH	6.78 (0.93)	5.80 (0.63)	6.89 (0.72)	6.93 (0.95)	6.62 (0.41)	7.00 (0.17)
Alk-T (mg L^{-1})	9.77 (8.89)	3.63 (3.77)	35.1 (37.6)	20.10 (13.34)	15.5 (18.8)	16.98 (6.85)
Cation (meq L^{-1})	0.51 (0.33)	0.18 (0.09)	0.80 (0.62)	0.70 (0.49)	0.48 (0.29)	0.53 (0.13)
Anion (meq L^{-1})	0.35 (0.23)	0.09 (0.08)	0.74 (0.74)	0.51 (0.46)	0.36 (0.41)	0.40 (0.14)
Ion def (meq L^{-1})	0.17 (0.11)	0.10 (0.04)	0.16 (0.05)	0.15 (0.01)	0.17 (0.08)	0.14 (0.04)
DIC (mgC L^{-1})	2.23 (1.54)	1.24 (0.58)	5.06 (4.73)	4.03 (2.19)	<DL	<DL
Chl-a (mg m^{-3})	50.90 (42.5)	25.96 (26.98)	29.19 (25.35)	62.03 (97.49)	23.90 (16.8)	8.00 (9.2)
DO (mg L^{-1})	9.10 (0.61)	9.04 (0.25)	9.61 (0.88)	8.63 (0.76)	9.96 (0.9)	9.08 (0.55)
NH_3 (mg L^{-1})	0.05 (0.048)	0.06 (0.06)	0.05 (0.06)	0.04	0.02 (-)	-
DKN (mgN L^{-1})	0.71 (0.58)	0.48 (0.26)	0.68 (0.14)	0.87 (0.26)	0.60 (0.1)	0.52 (0.15)
TDP (mgP L^{-1})	0.05 (0.05)	0.01 (0.01)	0.01 (0.01)	0.01 (0.01)	0.01 (0.007)	< 0.01 (0.00)
TP (mgP L^{-1})	0.12 (0.19)	0.04 (0.02)	0.05 (0.04)	0.09 (0.12)	0.04 (0.01)	0.03 (-)
Fe (µg L^{-1})	1701.7 (1736.9)	483 (297.3)	629.8 (490.8)	415.3 (632.6)	793.2 (488.6)	713.6 (530.69)
d-Fe (µg L^{-1})	587.6 (522.6)	214.2 (225.1)	292.0 (279.4)	87.9 (162.80	457.2 (288.5)	410.8 (432.9)
TC (mg L^{-1} Pt)	161.0 (108.6)	104.9 (81.5)	113.4 (65.5)	83.4 (51.48)	151.0 (58.8)	85.0 (51.1)
DOC (mg C L^{-1})	20.5 (10.1)	14.3 (6.48)	22.1 (5.8)	26.3 (11.87)	25.0 (4.8)	21.0 (7.75)
a_{254} (m^{-1})	0.05 (0.05)	0.02 (0.01)	0.04 (0.03)	0.04 (0.00)	0.05 (0.02)	0.02 (0.02)
$SUVA_{254}$ L mg^{-1} m^{-1})	0.15 (0.14)	0.10 (0.04)	0.15 (0.16)	0.13 (0.00)	0.19 (0.07)	0.11 (0.06)
HIX	0.76 (0.09)	0.63 (0.08)	0.73 (0.08)	0.74 (0.05)	0.77 (0.04)	0.65 (0.12)
BIX	0.46 (0.06)	0.60 (0.07)	0.49 (0.10)	0.51 (0.05)	0.43 (0.01)	0.52 (0.11)
FI	1.15 (0.07)	1.31 (0.18)	1.18 (0.14)	1.15 (0.07)	1.11 (0.05)	1.15 (0.04)

Table B3. Variable factor loadings for the four principal components (PC1 – PC3) generated from the 2021 Acid Sensitive Lake data. Loading values > 0.8 or < - 0.8 indicate variables strongly associated with their respective principal component.

Variable	PC1 (26.7 %)	PC2 (15.1 %)	PC3 (10.3 %)	PC4 (9.4 %)
C1	0.86	0.51	0.01	-0.21
C2	0.54	0.83	-0.07	-0.17
C3	-0.54	0.22	-0.41	0.21
C4	-0.06	-0.41	-0.21	0.51
C1/C2	0.92	-0.17	0.11	-0.33
BIX	-0.78	0.20	0.05	0.38
FI	-0.41	-0.07	-0.36	0.24
HIX	0.83	0.38	0.01	-0.30
a_{254}	0.80	0.50	0.06	-0.01
$SUVA_{254}$	0.61	0.33	0.27	-0.29
TC	0.96	-0.10	-0.11	-0.09
TOC	0.36	0.66	-0.09	-0.24
DOC	0.48	0.70	-0.06	-0.23
Temp	-0.64	-0.08	-0.28	0.05
$\delta^{18}O$	-0.62	0.07	-0.54	0.16
TP	0.30	0.03	-0.38	0.70
TDP	0.75	0.14	-0.26	0.54
DKN	0.24	0.75	-0.20	0.02
Chl-a	0.10	0.13	-0.41	0.49
DO	-0.10	0.04	-0.11	0.22
pH	-0.26	0.75	0.34	0.29
Alk-T	-0.37	0.64	0.23	0.24
Redox	0.21	-0.76	0.02	0.13
Anions total	-0.21	0.74	0.18	0.28
Cations Total	-0.07	0.88	0.16	0.21
Ion Deficit	0.39	0.65	-0.09	-0.17
d-Al	0.53	-0.57	-0.25	-0.32
Al	0.65	-0.08	-0.30	0.59
Ca	-0.21	0.83	0.23	0.17
d-Cu	0.67	0.00	0.21	-0.12
Cu	0.70	0.03	0.24	-0.25
d-Fe	0.72	-0.21	0.18	-0.23
Fe	0.74	0.05	-0.24	0.58
d-Mn	0.38	-0.40	-0.26	-0.44
d-Ni	0.86	0.01	-0.03	0.47
Ni	0.78	0.02	-0.13	0.59
d-Pb	0.63	-0.50	-0.17	-0.19
d-Zn	0.61	-0.51	-0.31	-0.38

Table B3 Continued. Variable factor loadings for the four principal components (PC1 – PC3) generated from the 2021 Acid Sensitive Lake data. Loading values > 0.8 or < -0.8 indicate variables strongly associated with their respective principal component.

Variable	PC1 (26.7 %)	PC2 (15.1 %)	PC3 (10.3 %)	PC4 (9.4 %)
Depth	-0.01	-0.15	0.81	0.09
LA	-0.18	-0.20	0.58	0.47
BDA	0.14	0.06	0.47	0.14
Volume	-0.14	-0.21	0.67	0.28
LA / BDA	-0.53	-0.36	0.08	0.49
DBA / volume	0.33	0.50	-0.40	-0.42
Elevation	0.08	-0.24	-0.50	0.13
Nearest	0.17	-0.35	0.52	-0.09
%Bog	0.60	-0.12	0.60	0.12
%Fen	-0.41	-0.12	-0.60	-0.16
%Upland	-0.14	0.48	-0.06	-0.03
%Open	-0.16	0.02	-0.17	-0.08
%Permafrost	0.59	-0.10	0.62	0.11
WY	-0.03	-0.47	0.45	0.27

Appendix C

Chapter 4: Characterization of atmospheric water-soluble brown carbon in the Athabasca Oil Sands Region, Canada

Appendix C1: Mass Spectrometry analysis

Datasets were acquired using an Agilent 8800 triple quadrupole inductively coupled mass spectrometer, in the Water Quality Centre at Trent University (Table C1 & C2). A MicroMist nebulizer (nominal uptake rate 400 μL min^{-1}) and Scott double pass spray chamber was used for sample introduction. Calibration standards were prepared by serial dilution of a 100 ng mL^{-1} multi-element solution (HPS QCS 27) and 1000 ng mL^{-1} single element standards in 2% HNO_3. High purity water (18.2 MΩ) and nitric acid was used for the preparation of all solutions. The NIST SRM 1640a (Trace Elements in Natural Water), NRC SLRS-6 (River Water Certified Reference Material for Trace Metals) and CALA PT standards were used for QA/QC. The measured concentrations were within 5% of the certified values.

Appendix C: Figures

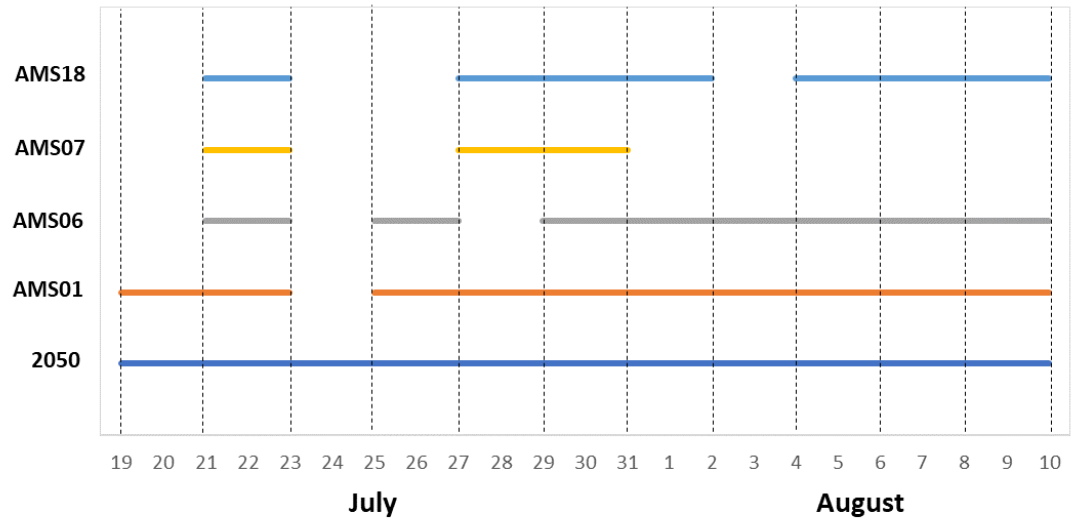

Figure C1: Temporal distribution of active sampler exposures (demarked by the vertical dotted lines) at each of the WBEA monitoring sites during the field study (July 19–August 10, 2023).

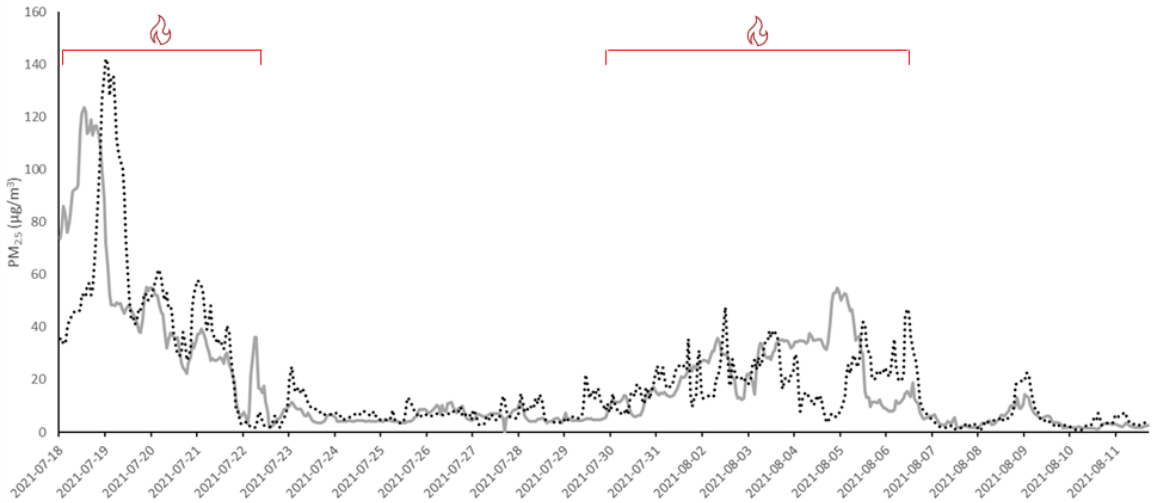

Figure C2: Hourly average $PM_{2.5}$ (µg m^{-3}) measured at a) AMS01 (black dotted line) and b) AMS18 (grey line) continuous monitoring stations during the study period (July 19–August 10, 2021). Approximated wildfire smoke events have been outlined in red.

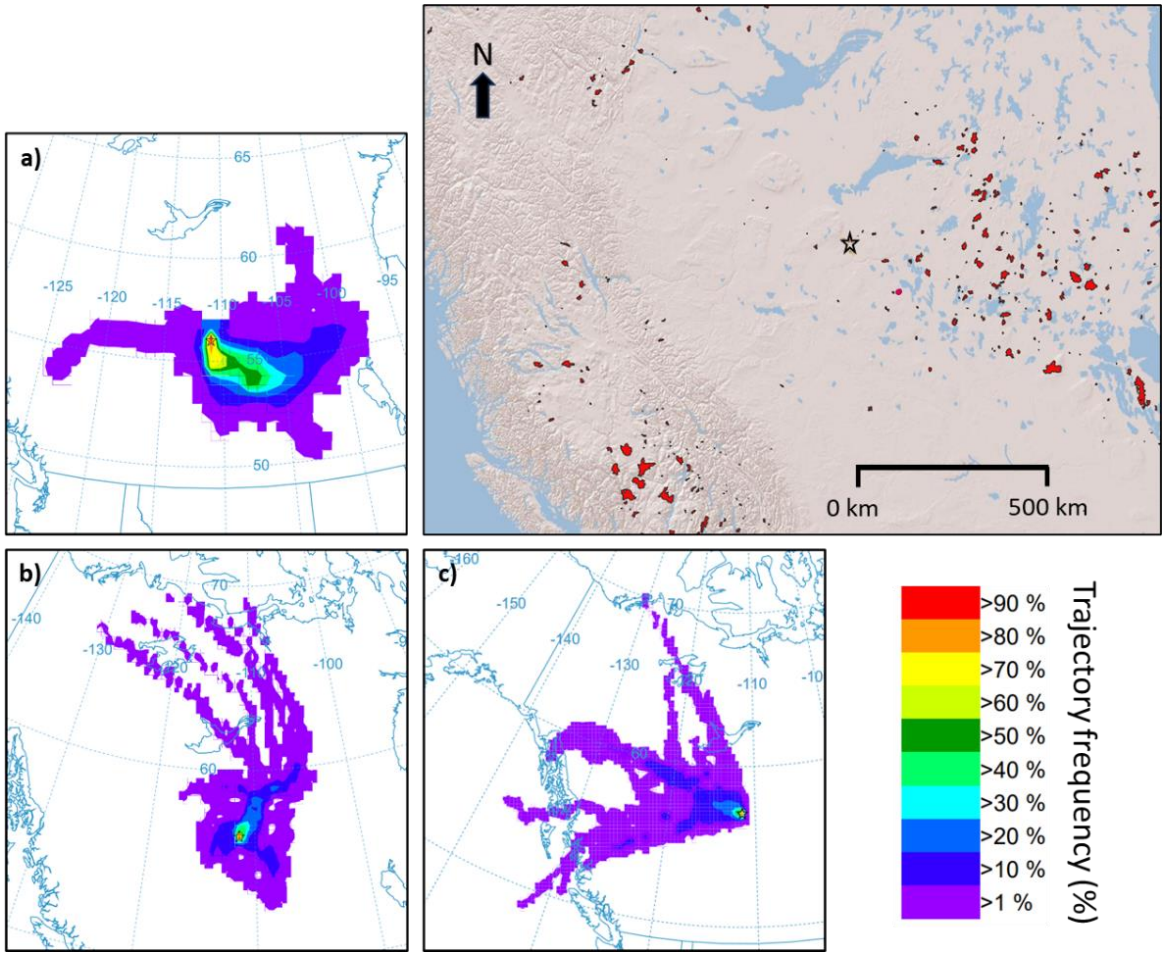

Figure C3. Back-trajectory (48 h) frequency (%) plots displaying atmospheric transport to AMS01 (black outlined star) during high $PM_{2.5}$ periods a) July 19 - 22, b) July 31 – August 7), and the low $PM_{2.5}$ period, c) July 23 – 30. The top-right map displays the spatial distribution of wildfire-affected areas (red polygons) throughout western Canada during the study period (July 19 – August 10) **(**ESRI 1995-2024**)**. Note that the spatial scale of the trajectory plots and wildfire map are not equal.

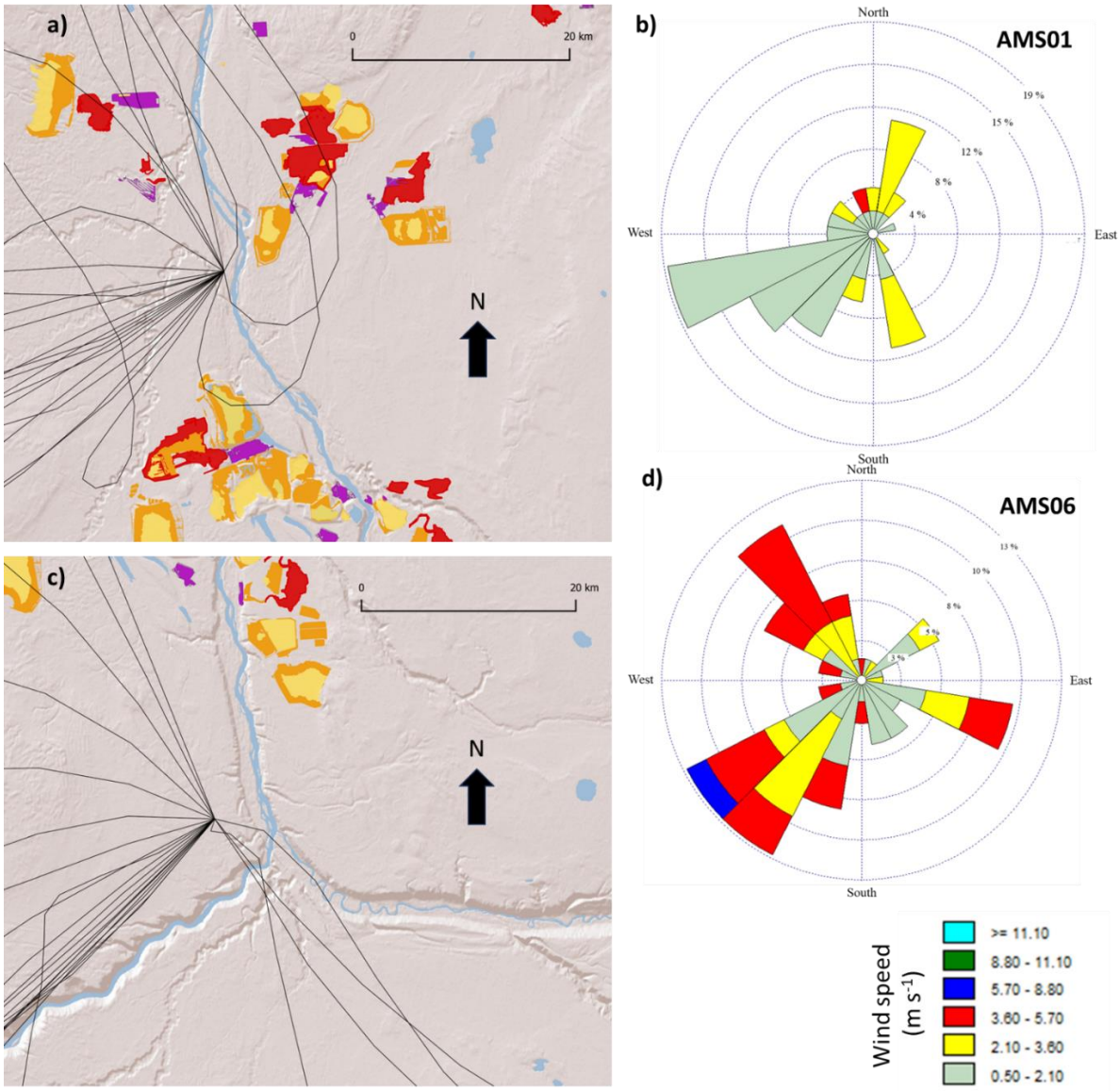

Figure C4. Comparison of HYSPLIT 48 h back-trajectories and continuous wind direction measurements corresponding to the July 25-27 and August 6-8 exposures at AMS01 (a & b) and AMS06 (c & d) continuous monitoring stations, respectively (ESRI 1995-2024**)**.

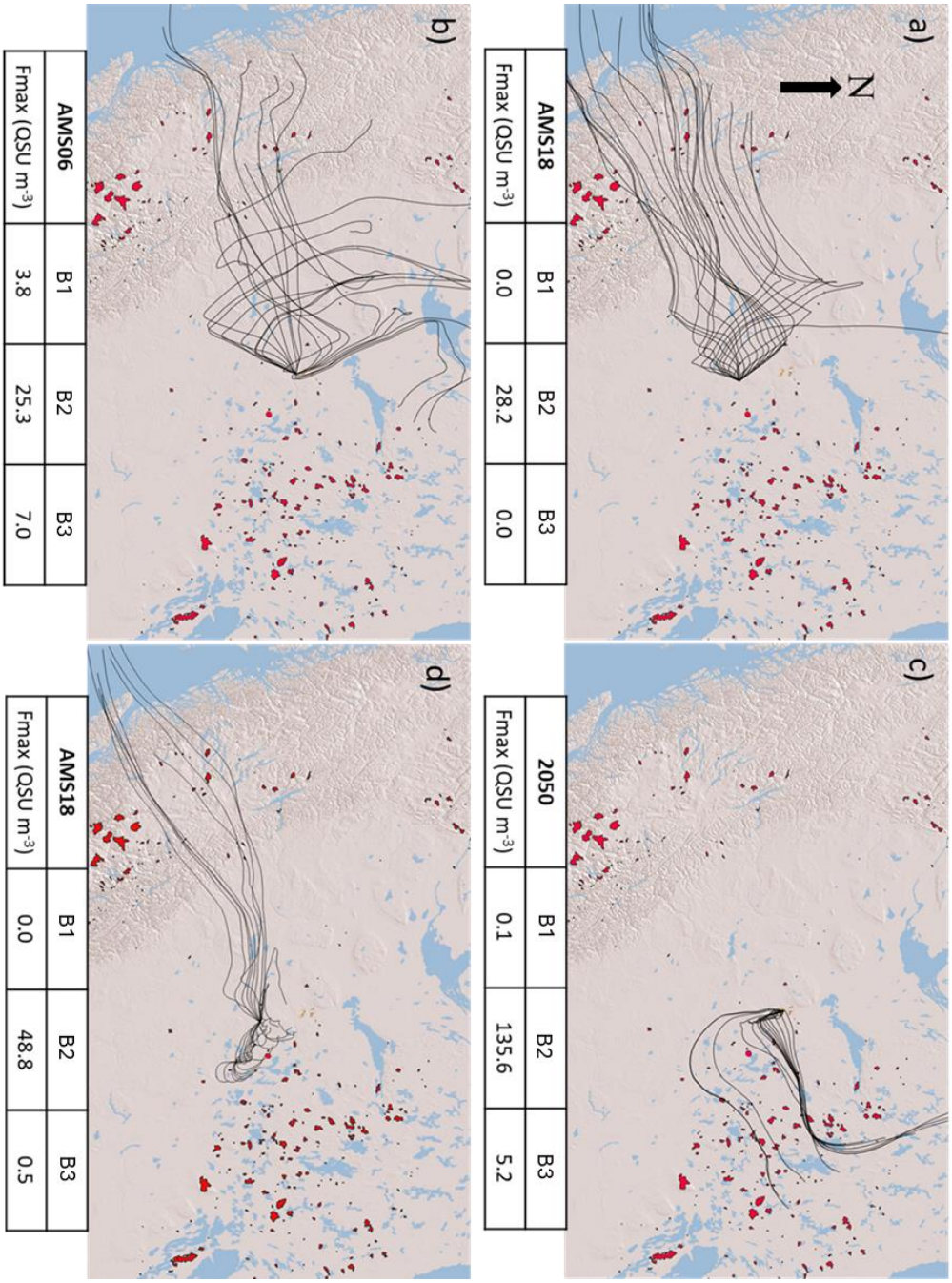

Figure C5. Spatial distributions of 48 h atmospheric back-trajectories (black lines) converging at sampling locations during selected exposure periods, including: a) AMS18; August 7-9, b) AMS06; July 21-23, c) DP2050; July 19-20, and d) AMS18; August 5-7. Normalized F_{MAX} values of C1 – C3 (QSU m^{-3}) measured during each exposure are shown beneath the corresponding trajectory plots (ESRI 1995-2024**)**.

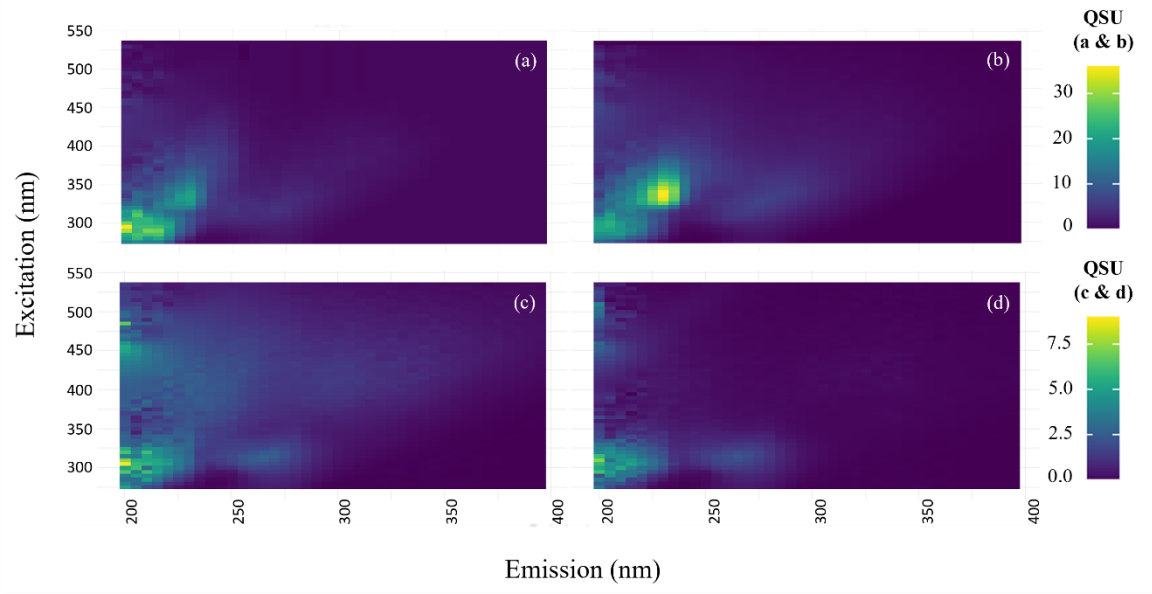

Figure C6. Visualization of the EEM scans produced from a) raw bitumen, b) dry MFT, and unpaved road dust from c) DP2050 and d) AMS01. Fluorescence intensity is displayed in QSU. Note that panels a and b follow a different colour-scale than panels c and d.

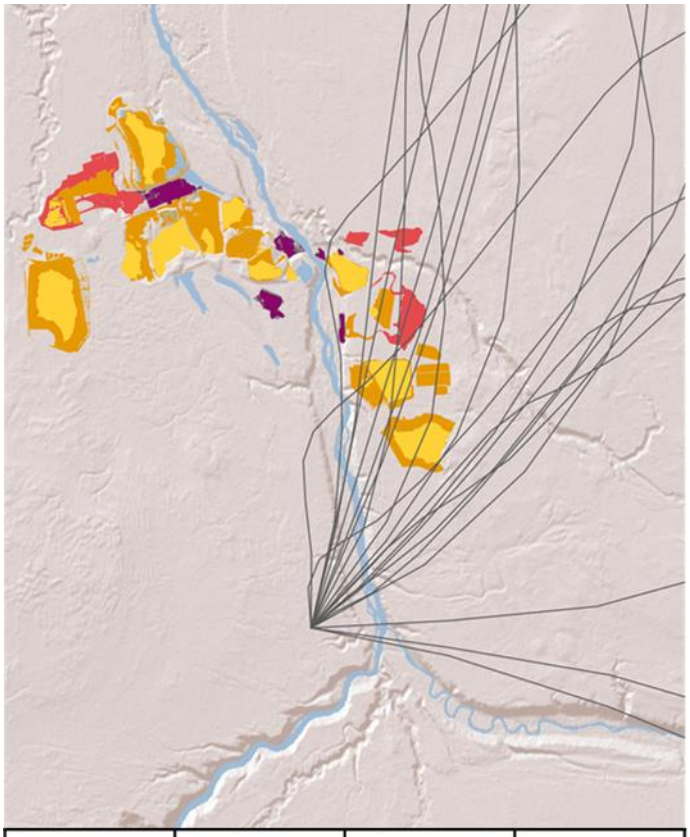

Fmax (QSU m^{-3})	B1	B2	B3
	40.7	53.9	36.0

Figure C7. Spatial distributions of 48 h atmospheric back-trajectories (black lines) converging at AMS06 during the August 4–6 exposure. F_{MAX} values of C1–C3 (QSU m^{-3}) measured during the corresponding exposure are shown. The spatial boundaries of various OS facilities, including wet tailings (yellow), dry tailings (orange), open mine pits (red), and plant sites (purple) are shown **(**ESRI 1995-2024**)**.

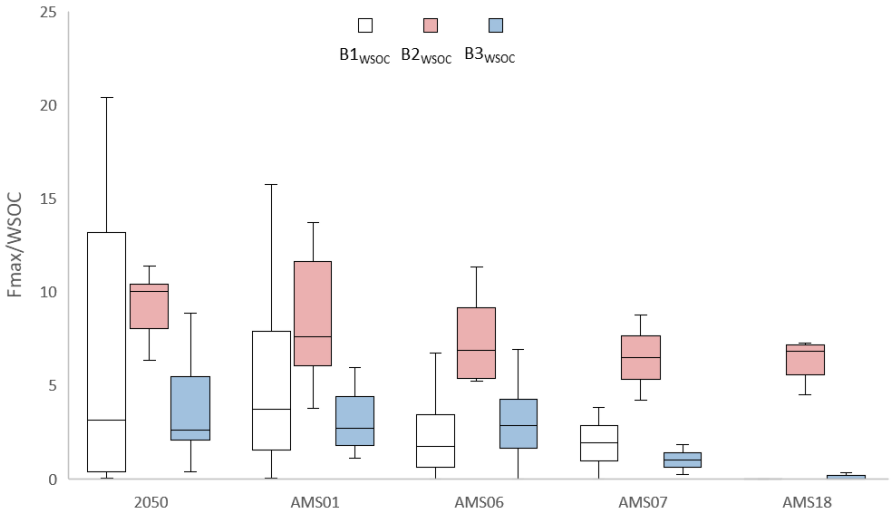

Figure C8. Distributions of WSOC-normalized component fluorescence ($B1_{WSOC}$–$B3_{WSOC}$) measured at each site during the study period (July 19–August 10, 2021).

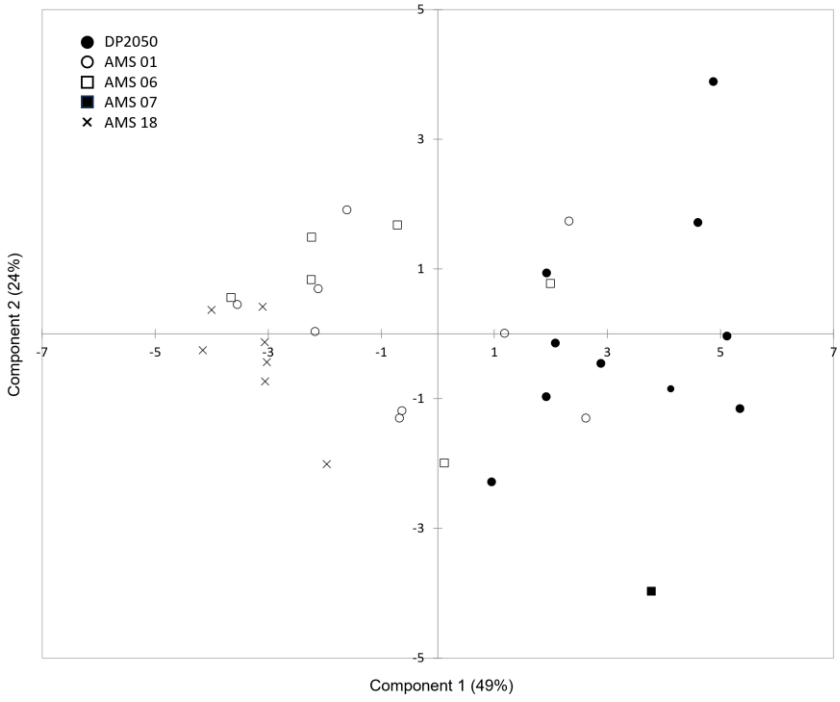

Figure C9. PLS-R Biplot displaying the distribution of observations relative to the first two modelled components. Observations are categorized according to site ID, including: AMS01 (open circle), DP2050 (full circle), AMS06 (open square), AMS07 (full square), AMS18 (x-mark).

Appendix C: Tables

Table C1. Instrument operating conditions and measurement parameters.

RF power	1550 W
Carrier gas flow rate[a]	1.05 L min^{-1}
Sampling depth[a]	10 mm
Extraction lens	X-type
Sampler and skimmer cone	Standard nickel

Table C2. Instrument tune mode and scan type used to measure each element.

Element	Tune Mode	Scan Type
Na	He	Single Quad
Mg	He	Single Quad
P	O_2	MS/MS
S	O_2	MS/MS
K	H_2	MS/MS
Ca	H_2	MS/MS
V	O_2	MS/MS
Cr	He	Single Quad
Mn	He	Single Quad
Fe	H_2	MS/MS
Zn	He	Single Quad
Sr	No gas	Single Quad

Table C3. Spearman correlation analysis comparing absorbance indices (Abs_{365}, MAE_{365}), modelled fluorescent components (B1-B3), trajectory frequencies (T_{OS}), and continuous pollutant species measured at the active sampling locations (excluding 2050). The correlation coefficient (R_S) for each significant correlation ($\alpha < 0.05$) is shown.

	T_{OS}	THC	TRS	SO_2	NO_2	NO	CO	$PM_{2.5}$
THC	0.87	-	-	-	-	-	-	-
TRS	0.92	0.85	-	-	-	-	-	-
SO_2	0.84	0.73	0.89	-	-	-	-	-
NO_2	0.9	0.91	0.88	0.82	-	-	-	-
NO	0.82	0.83	0.89	0.82	0.89	-	-	-
CO	0.5	0.47	0.63	0.65	0.66	0.54	-	-
$PM_{2.5}$	0.48	0.57	0.5	0.42	0.6	0.4	0.67	-
B1	0.77[a]	0.7	0.67	0.54	0.66	0.57	0.48	0.72
B2	0.62[a]	-	-	-	0.42	0.42	-	-
B3	0.88[a]	0.73	0.73	0.6	0.71	0.65	0.4	0.58
MAE_{365}	-	-	-	-	-	-	-	-
Abs_{365}	0.48[a]	-	-	-	-	0.36	-	-

[a] Correlation calculated using data from all stations, including DP2050.

Table C4. Spearman correlation analysis of modelled fluorescent components (B1-B3) against corresponding chemical and optical variables measured through the active sampler network. The coefficient (R_S) of each significant correlation ($\alpha < 0.05$) is shown.

Analyte	PARAFAC			Component / WSOC			Absorbance	
	B1	B2	B3	$B1_{WSOC}$	$B2_{WSOC}$	$B3_{WSOC}$	Abs_{365}	MAE_{365}
WSOC	-	0.70	-	-	-	-	0.55	-
DIC	-	0.80	-	-	-	-	0.57	-
TDN	-	0.44	-	-	-	-	0.39	-
NO_3^-	-	0.49	0.42	-	-	-	-	-
SO_4^{2-}	0.54	0.48	0.58	0.41	-	0.40	-	-
Cl^-	-	-	-	-	-	-	-	-
Na^+	0.62	0.61	0.75	0.57	-	0.60	0.36	-
Mg^{2+}	0.49	0.62	0.66	0.41	-	0.46	-	-
K^+	-	-	-	-	-	-	-	-
Ca^{2+}	0.35	0.74	0.57	-	-	-	0.54	-
P	-	0.71	0.55	-	-	-	0.55	-
S	0.62	0.56	0.71	0.65	0.36	0.68	-	-
V	0.52	0.65	0.69	0.39	-	0.45	0.52	-
Cr	-	0.72	-	-	-	-	0.57	-
Mn	0.37	0.63	0.57	-	-	-	-	-
Fe	0.36	0.40	0.33	-	-	-	0.42	-
Zn	-	-	-	-	-	-	-	-
Sr	0.62	0.63	0.79	0.56	0.47	0.60	0.42	-
Abs_{365}[a]	-	0.74	0.37	-	-	-	-	0.63
MAE_{365}[b]	-	-	-	-	0.57	0.36	0.63	-

[a] Reported as m^{-1}
[b] Reported as $m^{-2}gC^{-1}$

Appendix D

Chapter 5: Atmospheric deposition of chromophoric dissolved organic matter in the Athabasca Oil Sands Region, Canada, is strongly influenced by industrial sources during the winter months

Appendix D1: 45 metals in water and melt snow: NLET schema: TM2005/T45W and TM2005/D45W

A whole water sample was preserved in 0.2% HNO_3 (single sub-boiling grade) and before analysis brought up to 2 % acid by further addition of HNO_3. The sample was allowed to sit for 24 hrs. Forty milliliters (or 40 grams by weight) of the sample was placed in a 50 mL polypropylene tube. Two milliliters of 40% HCl (single sub-boiling grade) was added, and the sample mixed. The tubes were placed on a hotblock at 95 °C until the volume reduced to 8 mL. A watchglass was placed on the tube and the sample was allowed to reflux for 30 minutes at the same temperature. The sample was then cooled, and the volume brought back to 40 mL and well mixed. The sample was analyzed by inductively coupled argon plasma- collision/reaction cell mass spectrometer (CRC-ICP-MS) by discrete sampling pneumatic nebulization. Each respective element was measured at a specific mass to charge ratio, m/z value expressed in AMU (atomic mass units). The use of reaction and collision gases aid in the removal of interferences. Se(77) was analyzed in reaction gas [H_2] mode. Parameters analyzed in collision gas [He] mode included [Al(27), As(75), B(11), Ca(43), Co(59), Cr(52), Cu(65), Fe(56), Ge(74), K(39), Mg(26), Mn(55), Na(23), Ni (60), P(31), Sc(45), Sr(86), Ti(47), V(51), and Zn(66). The remaining elements, Ag(107), Ba(135), Be(9), Bi(209),Cd(111), Ce(140), Cs(133), Ga (71), In(115), La(139), Li(7), Mo(98), Nb(93), Pb(208),Pd(106), Pt(195), Rb(85), Rh(103), Sb (121), Sn(120), Te(128), Tl(205), U(238), W(184), Y(89), Zr(90)] were analyzed in normal mode. For dissolved analysis, the samples were filtered through a 0.45 um cellulose acetate filter paper, the

filtrate acidified to 2% (v/v) with HNO_3, allowed to sit for 24 hrs, and then analyzed by CRC-ICP-MS.

Appendix D2: Spatial variability of elemental and water chemistry variables within snowpack

Elevated concentrations and deposition loadings of POC, PON, DIC, major ions, most metals, and REEs were observed among near/mid-field snowpack sites in the study region (Table S2 and S5). Many of these analytes displayed a deposition gradient centered over OS operations, where loadings rapidly declined as a function of distance from the nearest industrial source (Figure S1 and S2). For example, average V loadings were 2599.4 μg m^{-2}, 249.4 μg m^{-2}, and 30.1 μg m^{-2} among near, mid, and far-field snow sites, respectively. Regional monitoring studies by Guéguen et al. (2016) and Gopalapillai et al. (2019) found that elemental species typically enriched within bituminous material (e.g., Al, Mo, Ni, V) displayed similar spatial gradients centered over OS facilities, as well as enhanced deposition loadings among near-field and mid-field snowpack sites.

Snowpack WSOC concentrations throughout the ASOR ranged from < 0.2 – 6.7 mg C L^{-1}, with a median value of 1.0 mg C L^{-1}; the corresponding WSOC loadings ranged from near 0 to 429.5 mg C m^{-2}, with a median value of 64.9 mg C m^{-2}. Snowpack WSOC loadings were relatively elevated among near-field sites (Table S5); however, notably high loads at the far-field location, ST-N, (Figure 5.3, Figure S2) suggested that both industrial and non-OS sources contributed to deposition.

Appendix D: Figures

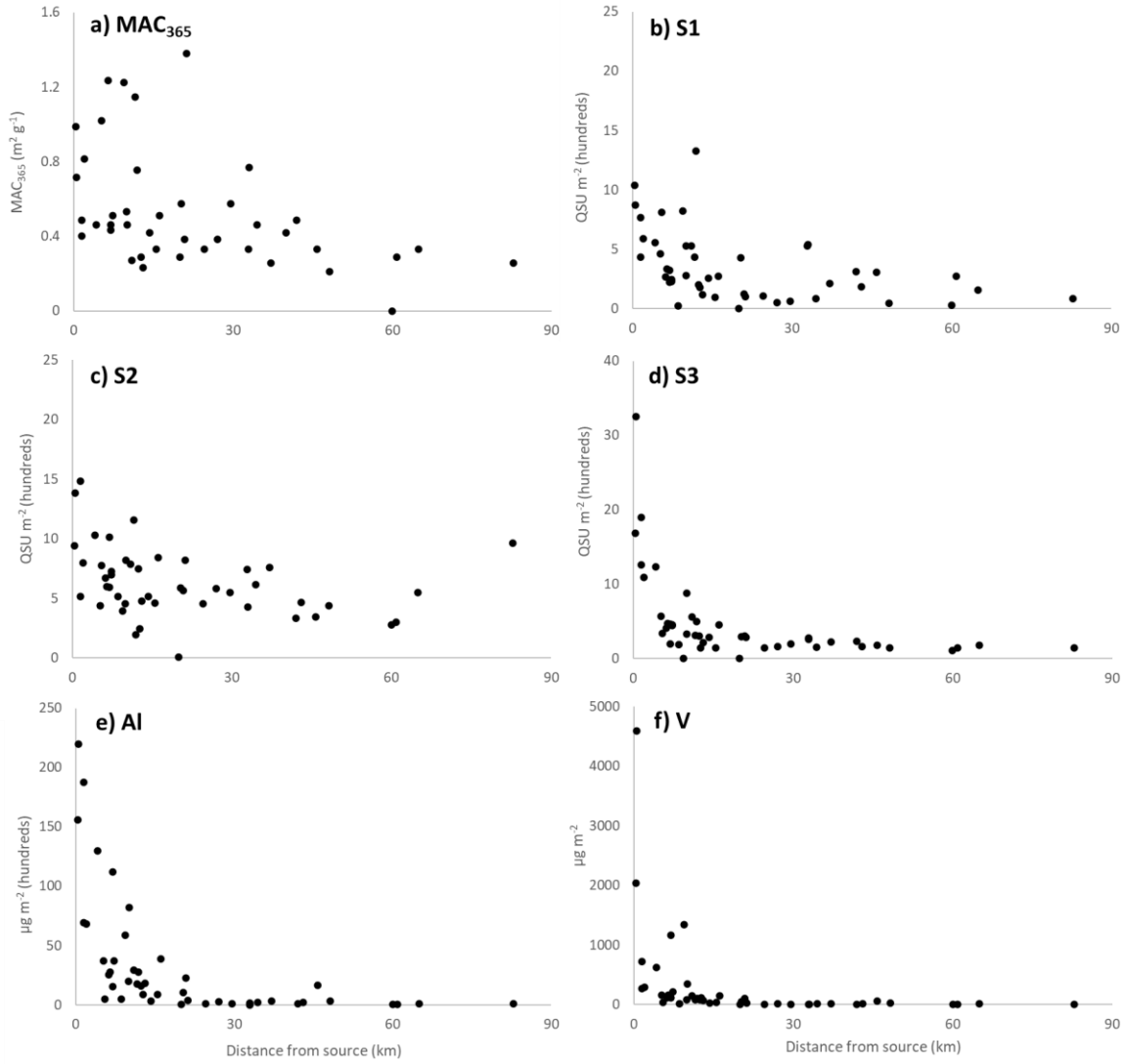

Figure D1. Measured snowpack loadings of of a) MAC_{365} (m^2 g^{-1}), b-d) S1-S3 (QSU m^{-2}), e) Al (µg m^{-2}, hundreds), f) V (µg m^{-2}) as a function of distance (km) from the nearest operational OS facilities.

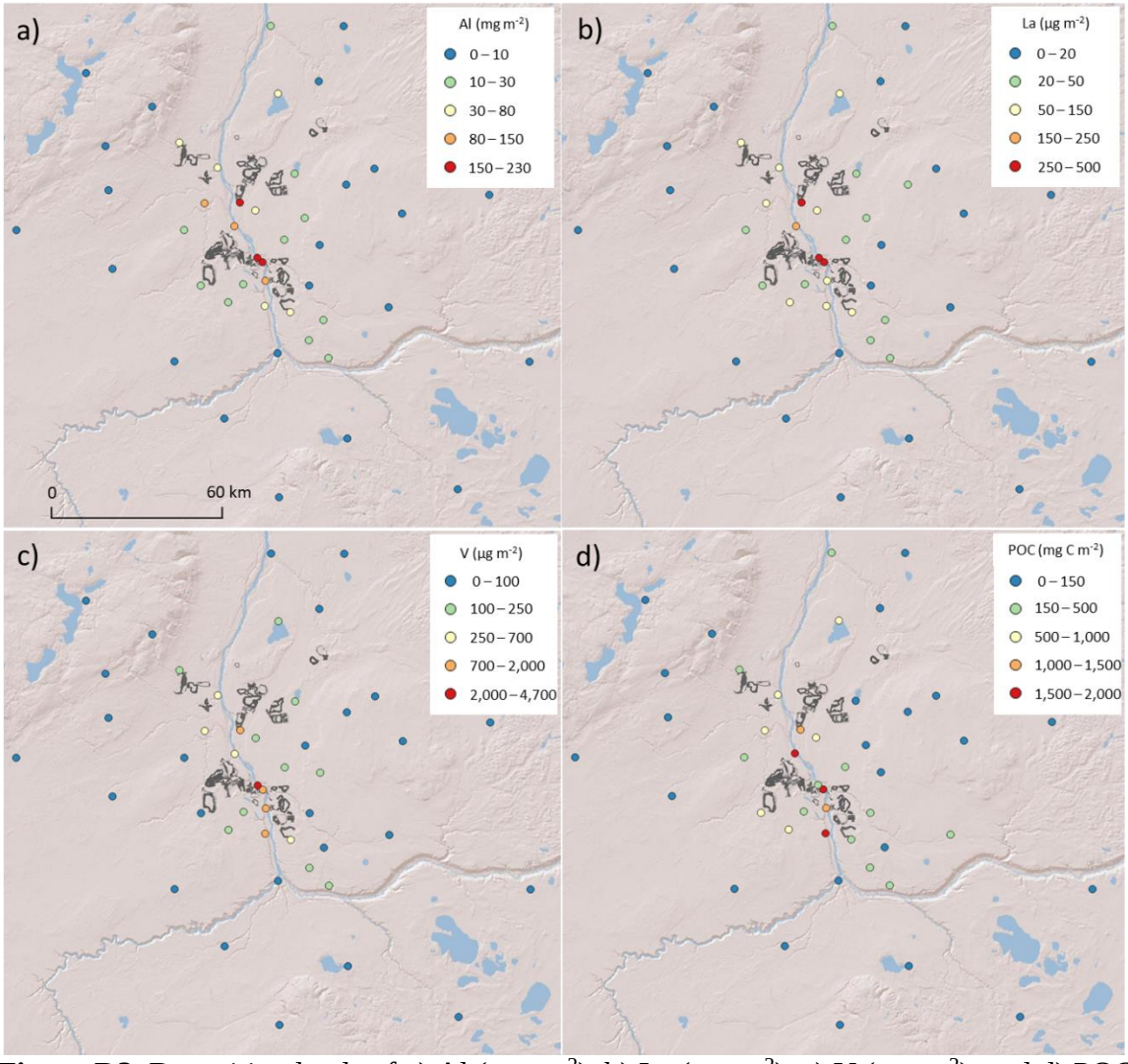

Figure D2. Deposition loads of a) Al (mg m^{-2}), b) La (µg m^{-2}), c) V (µg m^{-2}), and d) POC (mg C m^{-2}) measured at the snowpack sites (Spring 2023) throughout the AOSR. Grey outlined polygons represent OS facility boundaries.

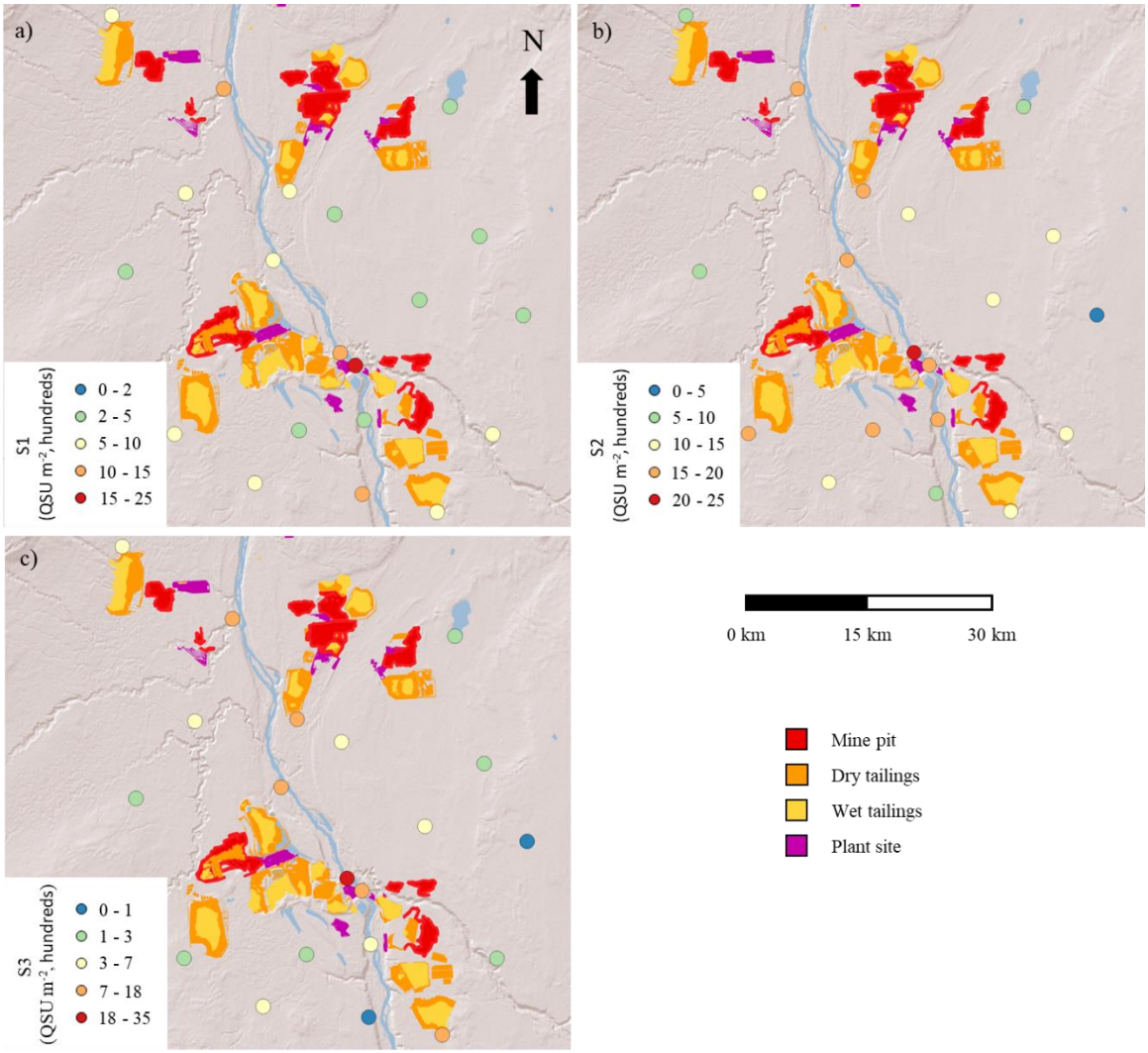

Figure D3. Deposition loadings of a) S1, b) S2, and c) S3 (QSU m^{-2}, hundreds) among snow sites located near the major Oil Sands facilities. Oil sands facility type is identified by the coloured polygons.

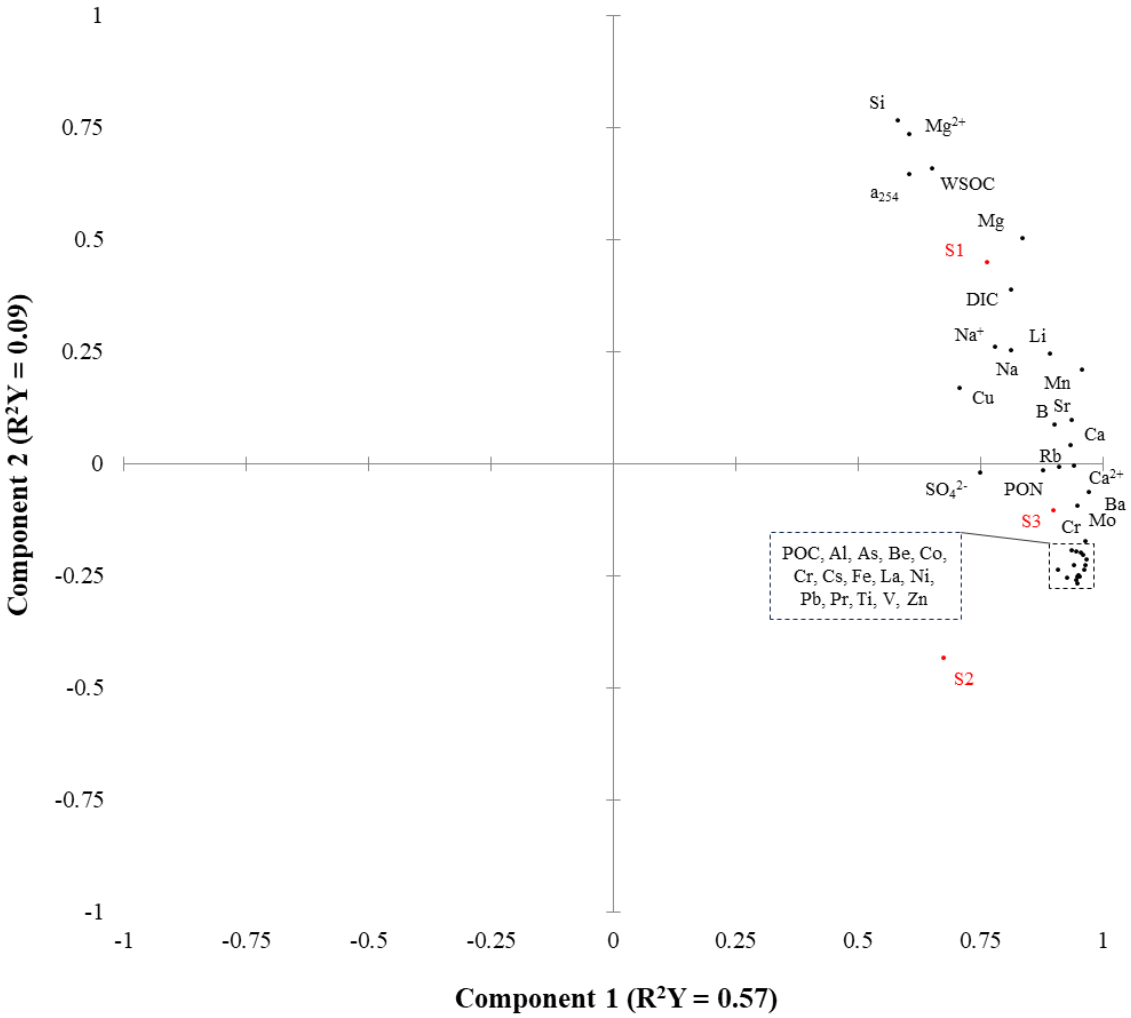

Figure D4. Correlation biplot displaying X (black) and Y (red) variables in relation to the first two partial least squares regression components generated from the 2023 snowpack dataset.

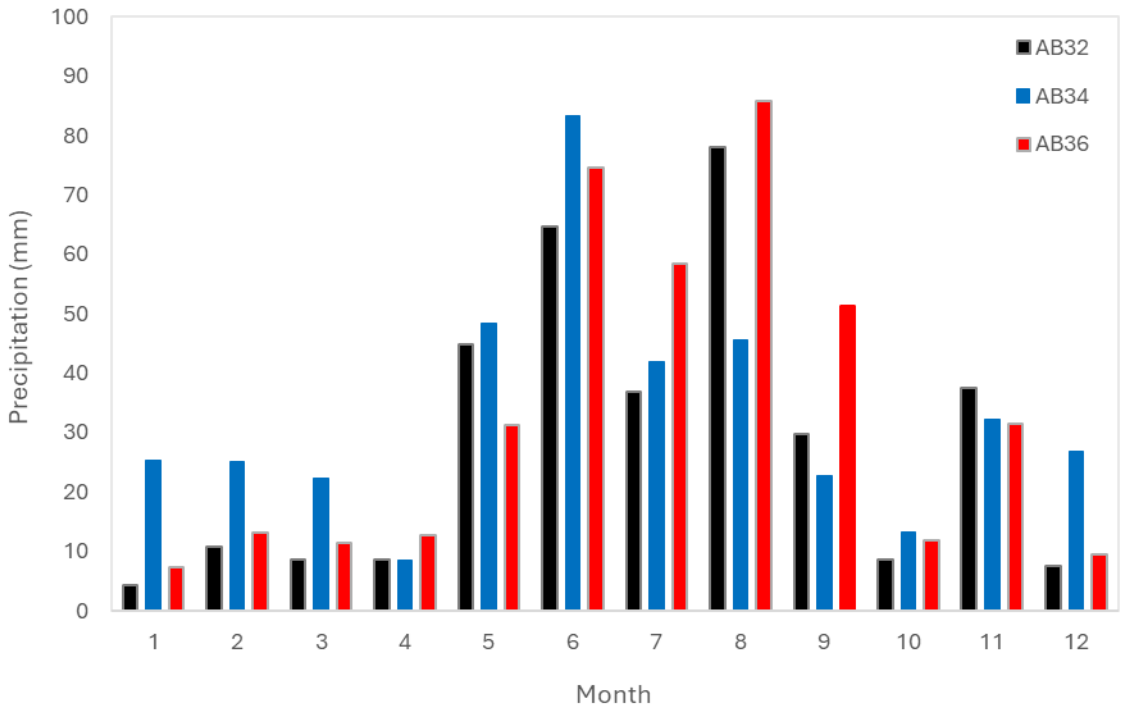

Figure D5. Monthly precipitation (mm) measured at the regional NADP monitoring stations (AB32, AB34, AB36) during the 2021 meteorological year.

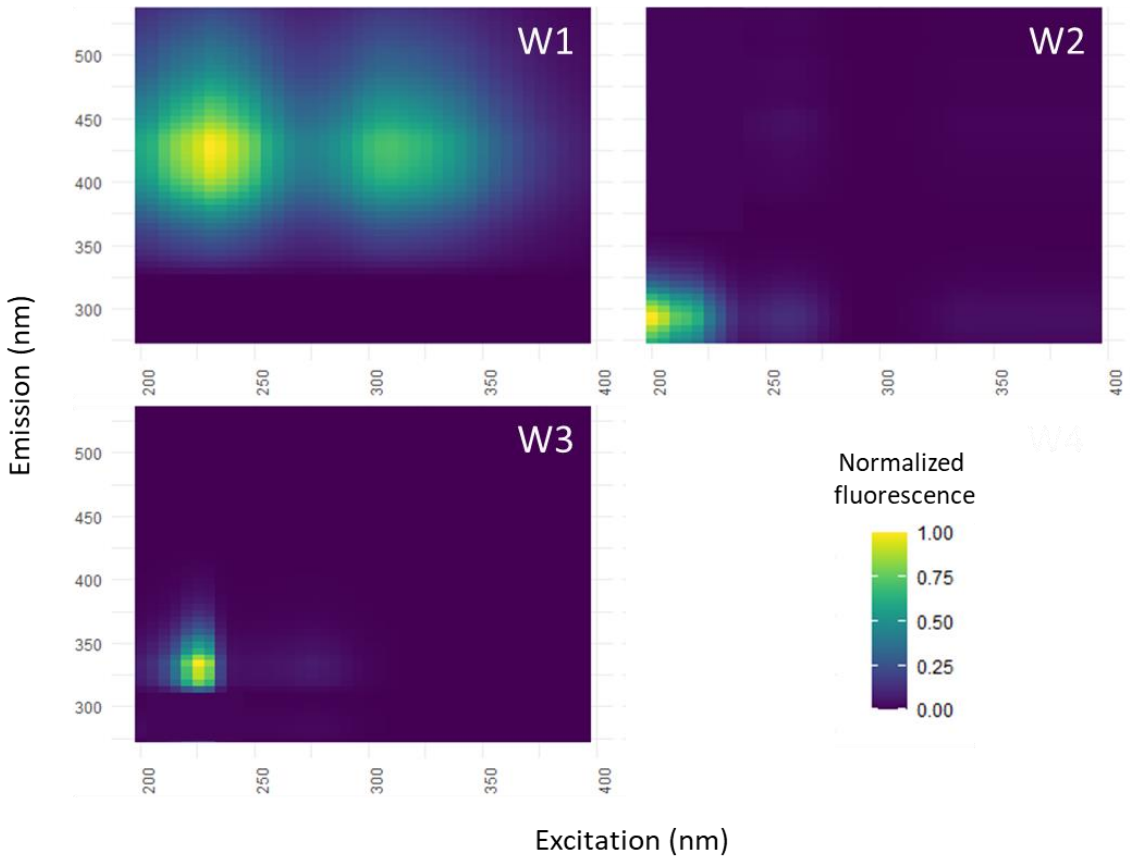

Figure D6. Visualization of the three PARAFAC components (W1–W3) generated from the weekly precipitation EEM samples. Emission intensity values are normalized according to maximum component fluorescence.

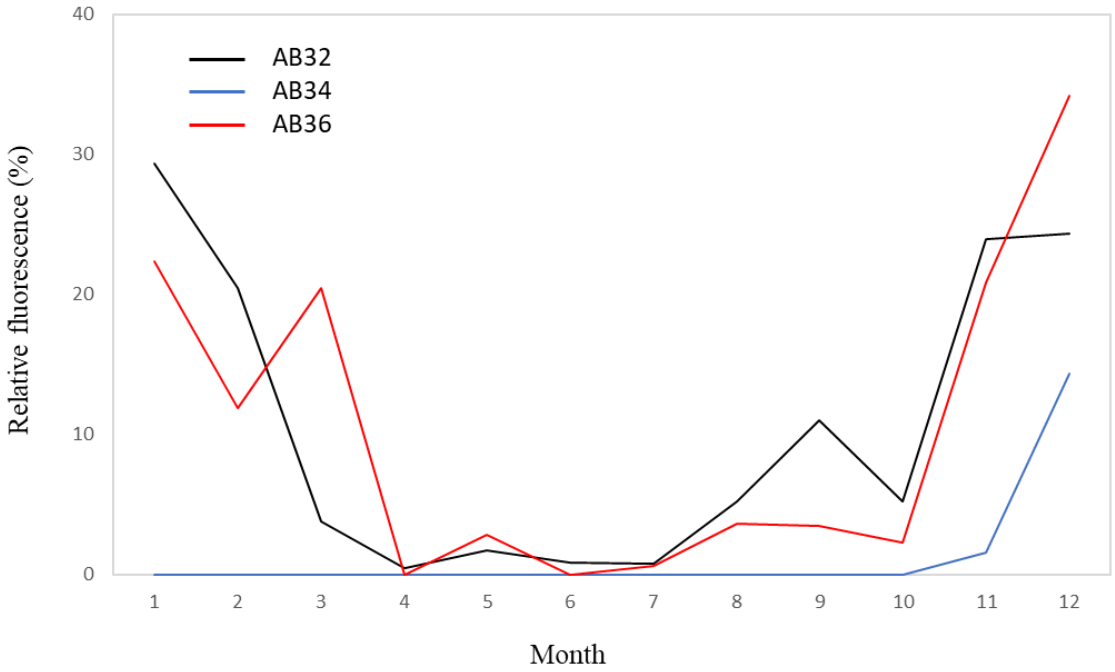

Figure D7. Monthly relative W3 fluorescence (%) measured at the regional NADP monitoring stations (AB32, AB34, AB36) during the 2021 meteorological year (January 2021 – December 2021).

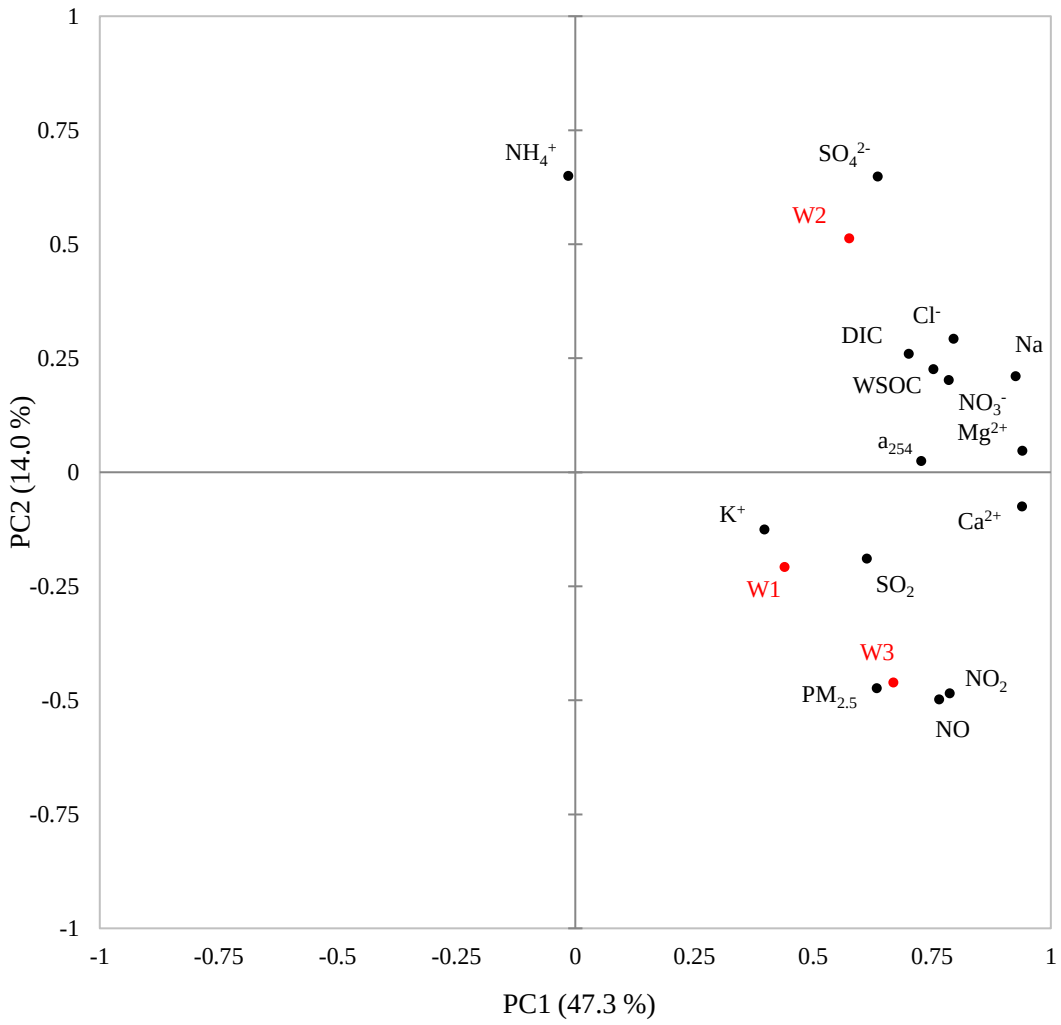

Figure D8. Principal component analysis biplot of wintertime (January – March 2021 and November – December 2021) weekly precipitation data displaying the factor loadings relative to principal component 1 ($PC1_{winter}$, 40.9%) and principal component 2 ($PC2_{winter}$, 20.2%).

Appendix D: Tables

Table D1. Identification and location of major AOSR oil sand production emission sources active during the winter (Landis et al., 2019c).

Facility	Latitude (°N)	Longitude (°W)
Suncor Upgrader Stack	57.003036	-111.476716
Suncor Millennium Mine	56.960700	-111.360025
Suncor Coke Storage	57.013372	-111.479297
Suncor Coke Reclamation	57.017717	-111.509058
Syncrude Upgrader Stack	57.047556	-111.618050
Syncrude Mildred Lake North	57.042776	-111.710675
Syncrude Aurora North Mine	57.315315	-111.507032
Syncrude Coke Storage	57.078019	-111.653875
Shell Muskeg Mine #1	57.277522	-111.528608
Shell Muskeg Mine #2	57.255994	-111.564344
Shell Jack Pine Mine	57.253569	-111.361223
Kearl Mine Area 1	57.396818	-111.131585
Kearl Mine Area 2	57.431361	-111.125275
Kearl Mine Area 3	57.396406	-111.038589
Canadian Natural Upgrader Stack	57.339853	-111.751458
Canadian Natural Horizon Mine	57.331233	-111.831839
Canadian Natural Coke Storage	57.360361	-111.719667

Table D2. Abbreviations and NLET method number corresponding to variables included in the study.

Variable name	Symbol	NLET method	Variable name	Symbol	NLET method
Absorbance coefficient	a_{254}	-	Calcium	Ca	2005[a]
Mass absorption cross section	MAC_{365}	-	Cesium	Cs	2005[a]
Fluorescent component 1	S1 & W1	-	Chromium	Cr	2005[a]
Fluorescent component 2	S2 & W2	-	Cobalt	Co	2005[a]
Fluorescent component 3	S3 & W3	-	Copper	Cu	2005[a]
S1(W1)/WSOC	$S1(W1)_{WSOC}$	-	Holmium	Ho	2005[a]
S2(W2)/WSOC	$S2(W2)_{WSOC}$	-	Iron	Fe	2005[a]
S3(W3)/WSOC	$S3(W3)_{WSOC}$	-	Iridium	Ir	2005[a]
pH	pH	1001	Lanthanum	La	2005[a]
Particulate organic carbon	POC	1090	Lead	Pb	2005[a]
Particulate organic nitrogen	PON	1090	Lithium	Li	2005[a]
Water soluble organic carbon	WSOC	1021	Magnesium	Mg	2005[a]
Dissolved inorganic carbon	DIC	1021	Manganese	Mn	2005[a]
Total dissolved nitrogen	TDN	1151	Molybdenum	Mo	2005[a]
Dissolved Kjeldahl nitrogen	DKN	1170	Neodymium	Nd	2005[a]
Calcium ion	Ca^{2+}	1062	Nickel	Ni	2005[a]
Magnesium ion	Mg^{2+}	1062	Potassium	K	2005[a]
Sodium ion	Na^{2+}	1062	Praseodymium	Pr	2005[a]
Potassium ion	K^{+}	1062	Rubidium	Rb	2005[a]
Chloride	Cl^{-}	1081	Samarium	Sm	2005[a]
Sulphate	SO_4^{2-}	1081	Selenium	Se	2005[a]
Nitrate	$NO3^{-}$	1081	Silica	Si	1062
Aluminum	Al	2005[a]	Sodium	Na	2005[a]
Antimony	Sb	2005[a]	Strontium	Sr	2005[a]
Arsenic	As	2005[a]	Tin	Ti	2005[a]
Beryllium	Be	2005[a]	Titanium	Sn	2005[a]
Boron	B	2005[a]	Vanadium	V	2005[a]
Cadmium	Cd	2005[a]	Zinc	Zn	2005[a]

[a] combined TM2005/T45 and TM2005/D45W NLET protocols

Table D3. Summary of median variable concentrations (and corresponding NMAD values [%]) measured across all (n = 45) and near-field (< 25 km from nearest source, n = 28) AOSR snowpack samples, respectively. Significant differences in variable concentrations between complete and near-field sample cohorts (Kruskal-Wallis, $\alpha < 0.05$) are identified. Variable reporting detection limits (RDL) are shown.

Analyte	Units	RDL	Complete (n = 45)		Near-field (n = 28)		Kruskal-Wallis ($\alpha < 0.05$)
			Median	NMAD (%)	Median	NMAD (%)	
SWE	kg m^{-2}	-	74.1	13.1	74.5	15.2	-
A_{365}	m^{-1}	-	2.72	64.0	3.83	74.9	Yes
MAC_{365}	m^2 g^{-1}	-	0.41	45.4	0.53	56.3	Yes
S1	QSU	0.28*	5.75	53.0	7.10	46.3	Yes
S2	QSU	0.74*	11.44	26.5	13.80	28.2	Yes
S3	QSU	0.15*	3.41	49.8	5.41	35.2	Yes
%S1	(%)	-	22.58	38.7	24.89	15.6	-
%S2	(%)	-	56.17	24.9	44.32	25.9	Yes
%S3	(%)	-	18.63	21.6	25.02	44.2	Yes
$S1_{WSOC}$	QSU mg C L^{-1}	-	4.74	54.4	7.42	34.9	Yes
$S2_{WSOC}$	QSU mg C L^{-1}	-	11.20	42.7	13.13	38.2	Yes
$S3_{WSOC}$	QSU mg C L^{-1}	-	3.55	31.7	8.81	31.4	Yes
pH	-	0	6.64	6.8	7.00	5.2	Yes
POC	mg C L^{-1}	0.0007	2.27	64.7	4.26	64.3	Yes
PON	mg N L^{-1}	0.0003	0.08	63.3	0.1	55.6	Yes
WSOC	mg C L^{-1}	0.2	1.00	38.5	1.2	41.7	Yes
DIC	mg C L^{-1}	0.2	1.45	52.6	1.70	70.6	Yes
TDN	mg N L^{-1}	0.015	0.27	25.7	0.28	43.6	-
DKN	mg N L^{-1}	0.014	0.09	40.0	0.10	66.8	-
Ca^{2+}	mg L^{-1}	0.01	1.09	67.7	1.55	74.8	Yes
Mg^{2+}	mg L^{-1}	0.01	0.19	76.0	0.24	62.5	Yes
Na^{2+}	mg L^{-1}	0.01	0.15	75.0	0.21	71.2	Yes
K^{+}	mg L^{-1}	0.03	0.10	75.8	0.12	74.9	Yes
Cl^{-}	mg L^{-1}	0.01	0.09	70.7	0.13	96.2	Yes
SO_4^{2-}	mg L^{-1}	0.01	0.64	68.0	0.91	68.7	Yes
$NO3^{-}$	mg L^{-1}	0.005	0.19	16.1	0.20	26.9	-
Al	µg L^{-1}	0.5	224.50	89.6	353.00	85.6	Yes
As	µg L^{-1}	0.01	0.14	84.1	0.22	90.6	Yes
Ba	µg L^{-1}	0.05	4.67	76.4	7.04	100.0	Yes
B	µg L^{-1}	0.5	1.30	68.8	2.30	90.3	Yes

* Method detection limit (MDL)

Table D3 continued. Summary of median variable concentrations (and corresponding NMAD values [%]) measured across all (n = 45) and near-field (< 25 km from nearest source, n = 28) AOSR snowpack samples, respectively. Significant differences in variable concentrations between complete and near-field sample cohorts (Kruskal-Wallis, $\alpha < 0.05$) are identified. Variable reporting detection limits (RDL) are shown.

Analyte	Units	RDL	Complete (n = 45)		Near-field (n = 28)		Kruskal-Wallis ($\alpha < 0.05$)
			Median	NMAD (%)	Median	NMAD (%)	
Cd	$\mu g\ L^{-1}$	0.001	0.01	40.0	0.01	63.6	-
Ca	$\mu g\ L^{-1}$	50	1360.00	64.3	1825.00	59.5	Yes
Ce	$\mu g\ L^{-1}$	0.001	0.76	90.0	1.37	86.8	Yes
Cs	$\mu g\ L^{-1}$	0.001	0.05	86.3	0.08	65.0	Yes
Cr	$\mu g\ L^{-1}$	0.02	0.53	68.7	0.85	68.0	Yes
Co	$\mu g\ L^{-1}$	0.002	0.24	88.7	0.39	84.6	Yes
Cu	$\mu g\ L^{-1}$	0.05	0.57	73.0	1.04	66.2	Yes
Ho	$\mu g\ L^{-1}$	0.001	0.01	92.9	0.01	86.2	-
Fe	$\mu g\ L^{-1}$	0.5	463.50	84.0	852.00	81.9	Yes
La	$\mu g\ L^{-1}$	0.001	0.33	89.8	0.59	86.8	Yes
Pb	$\mu g\ L^{-1}$	0.005	0.25	81.7	0.44	100.0	Yes
Li	$\mu g\ L^{-1}$	0.01	0.44	83.8	0.64	92.2	Yes
Mg	$\mu g\ L^{-1}$	5	365.50	64.0	492.00	57.5	Yes
Mn	$\mu g\ L^{-1}$	0.05	18.75	68.0	32.90	63.2	Yes
Mo	$\mu g\ L^{-1}$	0.005	0.08	73.0	0.17	61.4	Yes
Na	$\mu g\ L^{-1}$	5	162.00	84.5	240.00	100.0	Yes
Nd	$\mu g\ L^{-1}$	0.002	0.36	90.5	0.63	86.5	Yes
Ni	$\mu g\ L^{-1}$	0.02	0.57	80.1	1.28	71.8	Yes
K	$\mu g\ L^{-1}$	10	164.00	65.5	286.50	56.4	Yes
Pr	$\mu g\ L^{-1}$	0.001	0.08	91.2	0.16	86.6	Yes
Rb	$\mu g\ L^{-1}$	0.001	0.68	77.4	1.30	62.1	Yes
Sb	$\mu g\ L^{-1}$	0.001	0.01	62.5	0.02	45.0	-
Se	$\mu g\ L^{-1}$	0.01	0.01	50.0	0.02	50.0	-
Si	$mg\ L^{-1}$	0.01	0.09	70.4	0.13	76.9	Yes
Sm	$\mu g\ L^{-1}$	0.001	0.07	90.1	0.13	84.9	Yes
Sr	$\mu g\ L^{-1}$	0.05	3.53	61.6	5.56	66.0	Yes
Ti	$\mu g\ L^{-1}$	0.005	0.04	49.0	7.38	84.4	Yes
V	$\mu g\ L^{-1}$	0.01	1.06	86.3	1.79	81.0	Yes
Zn	$\mu g\ L^{-1}$	0.2	2.3	64.4	4.15	63.9	Yes

Table D4. Summary of the QA/QC data from the 2023 snowpack ICP-MS analysis. Instrument reporting detection limit (RDL), average relative percent difference (RPD, %) between duplicate samples, and average certified reference material recoveries (n = 10) are displayed for each target element.

Element	RDL µg L^{-1}	RPD %	Recovery %
Aluminum	0.5	19.0	93.1
Antimony	0.001	9.7	94.7
Arsenic	0.01	7.0	97.1
Barium	0.05	8.0	94.9
Boron	0.5	7.7	103.0
Cadmium	0.001	17.3	96.3
Calcium	50	4.3	93.7
Cerium	0.001	8.0	97.9
Cesium	0.001	12.3	98.1
Chromium	0.02	20.7	96.3
Cobalt	0.002	5.7	101.0
Copper	0.05	8.0	101.0
Holmium	0.001	3.3	94.1
Iron	0.5	13.7	98.7
Lanthanum	0.001	9.7	95.8
Lead	0.005	1.0	101.1
Lithium	0.01	10.7	97.0
Magnesium	5	4.0	95.1
Manganese	0.05	3.7	96.1
Molybdenum	0.005	8.7	93.8
Neodymium	0.002	5.7	94.4
Nickel	0.02	5.3	99.3
Potassium	10	6.3	95.4
Praseodymium	0.001	9.7	94.6
Rubidium	0.001	3.3	95.3
Samarium	0.001	10.3	94.0
Selenium	0.01	2.7	96.1
Sodium	5	4.3	95.2
Strontium	0.05	1.3	95.2
Titanium	0.05	8.7	99.2
Vanadium	0.01	11.7	95.6
Zinc	0.2	12.0	98.7

Table D5. Median deposition flux (and corresponding NMAD [%]) measured across all (n = 45) and near-field (< 25 km from nearest source, n = 28) AOSR snowpack samples, respectively. Significant differences in deposition flux between complete and near-field cohorts (Kruskal-Wallis, $\alpha < 0.05$) are identified.

Analyte	Units	Complete (n = 45)		Near-field (n = 28)		Kruskal-Wallis ($\alpha < 0.05$)
		Median	NMAD (%)	Median	NMAD (%)	
S1	QSU m^{-2}	405.77	49.1	498.15	44.2	Yes
S2	QSU m^{-2}	879.05	27.8	1050.34	25.2	Yes
S3	QSU m^{-2}	283.98	54.0	442.74	45.8	Yes
POC	mg C m^{-2}	168.87	74.1	329.33	58.4	Yes
PON	mg N m^{-2}	6.10	71.3	10.47	49.3	Yes
WSOC	mg C m^{-2}	81.28	42.5	91.79	38.7	Yes
DIC	mg C m^{-2}	101.63	38.5	124.28	48.1	Yes
TDN	mg N m^{-2}	18.62	22.8	20.54	17.4	-
DKN	mg N m^{-2}	6.77	37.5	7.49	66.9	-
Ca^{2+}	mg m^{-2}	83.84	77.4	127.32	51.0	Yes
Mg^{2+}	mg m^{-2}	13.91	78.3	17.29	58.8	Yes
Na^{2+}	mg m^{-2}	9.52	78.3	16.16	87.1	Yes
K^{+}	mg m^{-2}	5.60	58.8	6.83	100.0	Yes
Cl^{-}	mg m^{-2}	6.40	55.8	8.15	100.0	Yes
SO_4^{2-}	mg m^{-2}	50.30	59.4	64.02	49.6	Yes
$NO3^{-}$	mg m^{-2}	12.88	20.7	14.38	21.5	-
Al	µg m^{-2}	15293.34	91.1	27567.05	65.0	Yes
As	µg m^{-2}	9.97	86.4	16.93	57.4	Yes
Ba	µg m^{-2}	349.83	82.2	500.53	56.3	Yes
B	µg m^{-2}	102.16	77.6	173.39	74.2	Yes
Cd	µg m^{-2}	0.69	42.4	0.84	51.7	-
Ca	µg m^{-2}	93755.82	82.4	136948.21	43.4	Yes
Ce	µg m^{-2}	50.04	91.6	101.80	61.8	Yes
Cs	µg m^{-2}	3.72	88.1	6.43	58.8	Yes
Cr	µg m^{-2}	38.82	80.8	62.84	51.1	Yes
Co	µg m^{-2}	15.38	91.3	31.01	57.8	Yes
Cu	µg m^{-2}	42.85	80.1	72.68	56.4	Yes
Ho	µg m^{-2}	0.51	92.0	1.05	73.7	-
Fe	µg m^{-2}	31501.35	89.1	53208.43	64.1	Yes
La	µg m^{-2}	22.12	91.4	44.04	60.5	Yes
Pb	µg m^{-2}	16.79	85.3	32.69	69.5	Yes
Li	µg m^{-2}	28.63	92.4	49.62	52.3	Yes
Mg	µg m^{-2}	26181.88	82.1	36665.63	54.1	Yes
Mn	µg m^{-2}	1381.03	81.8	2434.27	61.6	Yes
Mo	µg m^{-2}	5.81	89.9	12.08	54.4	Yes

Table D5 continued. Median deposition flux (and corresponding NMAD [%]) measured across all (n = 45) and near-field (< 25 km from nearest source, n = 28) AOSR snowpack samples, respectively. Significant differences in deposition flux between complete and near-field cohorts (Kruskal-Wallis, $\alpha < 0.05$) are identified.

Analyte	Units	Complete (n = 45)		Near-field (n = 28)		Kruskal-Wallis ($\alpha < 0.05$)
		Median	NMAD (%)	Median	NMAD (%)	
Na	$\mu g\ m^{-2}$	10127.99	81.6	18614.507	87.4	Yes
Nd	$\mu g\ m^{-2}$	23.62	91.2	46.75	62.3	Yes
Ni	$\mu g\ m^{-2}$	43.03	88.0	94.07	68.6	Yes
K	$\mu g\ m^{-2}$	12709.48	81.0	20520.5	56.1	Yes
Pr	$\mu g\ m^{-2}$	5.85	91.5	11.63	62.4	Yes
Rb	$\mu g\ m^{-2}$	47.94	86.3	98.44	56.4	Yes
Sb	$\mu g\ m^{-2}$	0.84	63.9	1.30	70.2	-
Se	$\mu g\ m^{-2}$	0.94	52.7	1.46	51.0	-
Si	$\mu g\ m^{-2}$	6.56	74.0	7.88	68.6	Yes
Sm	$\mu g\ m^{-2}$	4.72	91.2	9.54	61.4	Yes
Sr	$\mu g\ m^{-2}$	238.66	83.4	398.98	54.8	Yes
Ti	$\mu g\ m^{-2}$	280.78	59.4	546.15	64.8	Yes
V	$\mu g\ m^{-2}$	74.07	87.3	115.99	64.7	Yes
Zn	$\mu g\ m^{-2}$	178.11	66.5	293.72	63.1	Yes

Table D6. Annual (January – December 2021) wet deposition (kg ha yr^{-1}) measured at the three National Atmospheric Deposition Program monitoring stations (AB32, AB34, AB36) and average ambient air pollutant concentrations ± standard deviation (ppm, ppb, µg m^{-3}) observed at corresponding Wood Buffalo Environmental Association monitoring stations.

		Monitoring station		
		AB32	AB36	AB34
	Latitude	57.1894	57.2592	55.6214
	Longitude	-111.6406	-111.0386	-111.1727
Deposition (kg ha yr^{-1}) (WSOC: g C m^2 yr^{-1})	Na^+	0.20	0.17	0.11
	Mg^{2+}	0.32	0.34	0.11
	K^+	0.14	0.10	0.13
	Ca^{2+}	2.52	2.53	0.65
	NH^{4+}	0.68	0.40	0.89
	Cl^-	0.18	0.18	0.18
	NO_3^-	2.11	1.77	2.12
	SO_4^{2-}	2.32	1.86	1.43
	WSOC[a]	0.38[a]	0.41[a]	0.29[a]
Concentration (ppb) (THC: ppm) $PM_{2.5}$: µg m^{-3})	SO_2	0.9 ± 2.4	0.8 ± 2.6	0.2 ± 0.7
	THC[b]	2.2 ± 0.3[b]	2.2 ± 0.4[b]	1.9 ± 0.1[b]
	NO	3.2 ± 8.8	0.3 ± 1.5	0.1 ± 0.3
	NO_2	8.1 ± 8.2	2.6 ± 3.6	1.2 ± 1.5
	$PM_{2.5}$[c]	6.8 ± 9.3[c]	5.3 ± 8.1[c]	5.0 ± 10.0[c]
	TRS	0.6 ± 0.3	-	0.1 ± 0.1

[a] Reported as g C m^2 yr^{-1}; [b] Reported as ppm; [c] Reported as µg m^{-3}

Table D7. Seasonal VWA ion concentrations (μeq L^{-1}, mg L^{-1}) measured at the three NADP stations (AB32, AB34, AB36) during the 2021 meteorological year.

Station		Total cation[a]	Ca^{2+}	SO_4^{2-}	NO_3^-
		μeq L^{-1}		mg L^{-1}	
AB32	Winter[b]	92.42	2.02	0.65	1.07
	Spring[c]	229.06	6.29	2.75	1.44
	Summer[d]	47.49	0.77	0.80	0.72
	Fall[e]	24.92	1.21	0.55	0.66
AB36	Winter	52.36	0.86	0.58	1.00
	Spring	101.85	1.83	0.85	0.70
	Summer	24.48	0.62	0.50	0.35
	Fall	38.56	0.68	0.43	0.40
AB34	Winter	9.25	0.10	0.15	0.63
	Spring	10.87	0.22	0.52	0.50
	Summer	13.83	0.21	0.45	0.56
	Fall	20.33	0.29	0.58	0.74

[a] Sum equivalence: Ca^{2+}, Mg^{2+}, K^+, Na^+, $NH4^+$; [b] December – February; [c] March – May; [d] June – August; [e] September – November

Table D8. Median monthly volume weighted average optical variables measured at each regional National Atmospheric Deposition Program station (AB32, AB34, AB36) during the 2021 meteorological year (January–December 2021). The normalized median absolute deviation (NMAD, %) value corresponding to each median is shown.

	AB32		AB36		AB34	
	Median	NMAD (%)	Median	NMAD (%)	Median	NMAD (%)
a_{254} (m^{-1})	2.4	28.7	1.5	53.2	1.2	57.1
W1 (QSU)	2.3	35.7	1.3	29.2	1.3	97.3
W2 (QSU)	17.2	41.4	19.3	31.8	16.8	25.1
W3 (QSU)	1.4	83.4	1.2	85.0	0.0	0.0
$W1_{WSOC}$	2.0	21.2	2.4	32.8	2.3	54.9
$W2_{WSOC}$	13.2	24.8	25.3	77.2	15.9	64.2
$W3_{WSOC}$	0.8	94.2	1.0	96.3	0.0	12.3

Table D9. Median monthly volume weighted average optical variables measured at each regional National Atmospheric Deposition Program station (AB32, AB34, AB36) during the snowfall months of 2021 (January–March & November - December 2021). The normalized median absolute deviation (NMAD, %) value corresponding to each median is shown.

	AB32		AB36		AB34	
	Median	NMAD (%)	Median	NMAD (%)	Median	NMAD (%)
a_{254} (m^{-1})	2.28	35.9	1.56	36.1	0.67	47.0
W1 (QSU)	2.17	26.2	1.78	22.6	0.66	74.6
W2 (QSU)	12.93	35.9	9.34	25.9	14.93	36.5
W3 (QSU)	4.45	71.8	3.21	75.2	0.00	0.0

Table D10. Spearman correlation coefficients (R_S) between NADP precipitation sample optical metrics, major ions, TC, TN, WSOC, and continuous air pollutant concentrations. Empty cells indicate an insignificant correlation ($\alpha > 0.05$).

	a_{254}	W1	W2	W3
Ca^{2+}	-	-	-	0.65
Mg^{2+}	-	-	-	0.67
K^{+}	-	-	-	-
Na^{+}	-	-	-	0.56
NH_4^{+}	-	-	-	-
NO_3^{-}	-	-	-	0.39
Cl^{-}	-	-	-	0.46
SO_4^{2-}	-	-	-	-
DIC	-	-	-	-
TDN	-	-	-	-
WSOC	0.74	0.64	0.49	-
SO_2	-	-	-	0.56
THC	-	-	-	0.58
NO	-	-	-	0.71
NO_2	-	-	-	0.73
NO_x	-	-	-	0.72
TRS[a]	-	-	-	0.80
$PM_{2.5}$	0.59	0.70	-	-

[a] TRS concentration data unavailable at Wapasu station (AB36)

Table D11. Summary of the proposed sources of each fluorophore measured within the regional snowpack (2023) and weekly precipitation (January – December 2021) samples.

Sample	Fluorophore	Potential Sources
Snowpack	S1	**Industry:** Disturbed overburden and surface materials
	S2	**Industry:** Specific sources uncertain
	S3	**Industry:** upgrader, tailings, mine dust, road emissions, vehicle exhaust
Weekly precipitation	W1	**Pyrogenic:** wildfire, **Industry:** Undefined, wintertime influence
	W2	**Pyrogenic:** wildfire
	W3	**Industry:** vehicle exhaust, road emissions

Appendix E

Chapter 6: Do industrial emissions influence chromophoric dissolved organic matter within lakes in the Athabasca Oil Sands Region, Canada?

Appendix E: Figures

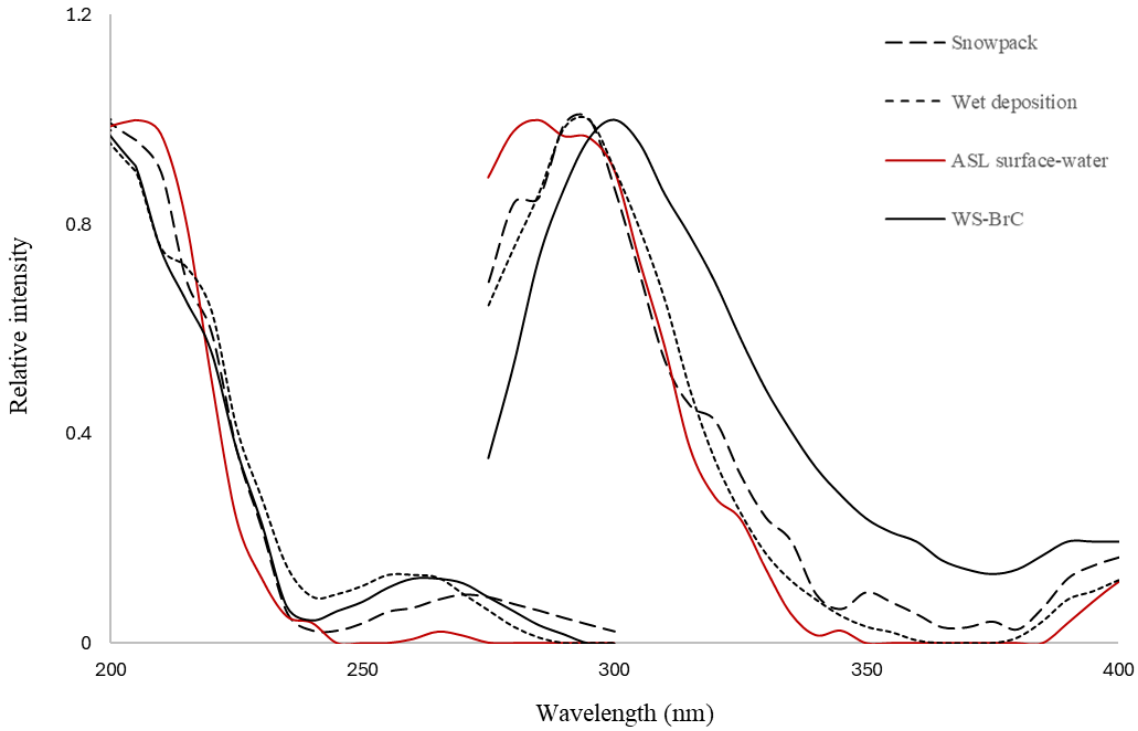

Figure E1. Comparison of normalized excitation (λ_{Ex}) and emission (λ_{Em}) spectra of individual fluorescent components observed in a) ASL surface-waters ($C4_{ASL}$: current study), b) atmospheric WS-BrC (B2: Blanchard et al., 2025a), c) snowpack (S2: Blanchard et al., 2025b), and d) NADP precipitation samples (W2: Blanchard et al., 2025b).

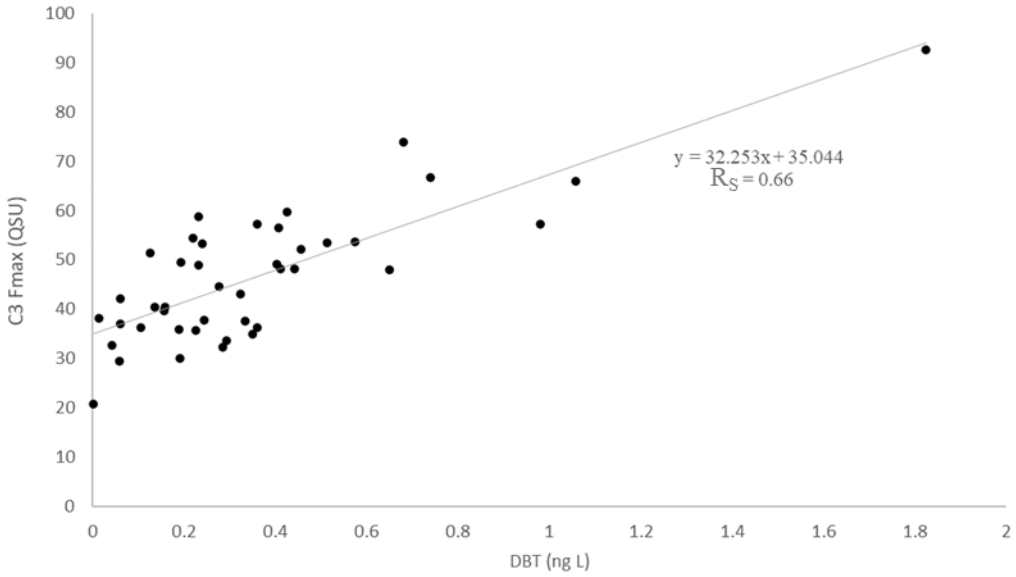

Figure E2. Comparison of DBT (ng L^{-1}) and C3 emission intensity (QSU) measured within ASL surface-waters in the AOSR. The line of best fit and corresponding Spearman correlation coefficient (R_S) is displayed.

Appendix E: Tables

Table E1. Identification and Location of Major AOSR Oil Sand Production Emission Sources in 2014 (Landis et al., 2019c).

	Facility	Latitude (°N)	Longitude
1	Suncor Upgrader Stack	57.003036	-111.476716
2	Suncor Millennium Mine	56.960700	-111.360025
3	Suncor Coke Storage	57.013372	-111.479297
4	Suncor Coke Reclamation	57.017717	-111.509058
5	Syncrude Upgrader Stack	57.047556	-111.61805
6	Syncrude Mildred Lake North	57.042776	-111.710675
7	Syncrude Aurora North Mine	57.315315	-111.507032
8	Syncrude Coke Storage	57.078019	-111.653875
9	Shell Muskeg Mine #1	57.277522	-111.528608
10	Shell Muskeg Mine #2	57.255994	-111.564344
11	Shell Jack Pine Mine	57.253569	-111.361223
12	Kearl Mine Area 1	57.396818	-111.131585
13	Kearl Mine Area 2	57.431361	-111.125275
14	Kearl Mine Area 3	57.396406	-111.038589
15	Canadian Natural Upgrader	57.339853	-111.751458
16	Canadian Natural Horizon Mine	57.331233	-111.831839
17	Canadian Natural Coke Storage	57.360361	-111.719667
18	Hammerstone Quarry	57.192628	-111.555453
19	Athabasca Creek Quarry	57.286486	-111.599471